Experimental and modelling studies of process intensification for the solvent-antisolvent precipitation of nanoparticles in a spinning disc reactor.

by

Sahr Sana

Thesis submitted for the degree of Doctor of Philosophy in the Faculty of Engineering of the Newcastle University.

School of Engineering
Newcastle University
Newcastle upon Tyne, UK.

December 2019.

Abstract

Solvent-antisolvent precipitation is a key process in pharmaceuticals industries. This research concerns solvent-antisolvent precipitation of starch nanoparticles in the spinning disc reactor (SDR), based on a combination of both experimental and modelling studies. The SDR's ability to use surface rotation to improve micromixing within thin liquid films, as well as its capability to exhibit near plug flow characteristics is the primary motivation to investigate this process intensification technology for solvent-antisolvent precipitation.

One of the objectives of this study is to highlight and understand interactions of the disc surface topography with conditions such as flowrate, solvent-antisolvent ratio and disc speed and their impact on the mixing and precipitation processes.

Smaller nanoparticles with narrow particle size distributions (PSDs) were produced as flow rate increased from 6 to 18 mL/s (248 to 175 nm) and disc speed increased from 400 to 1200 rpm (234 to 175 nm). This is attributed to increased shear and instabilities within the liquid film, enhancing mixing as the liquid travels outwards on the disc surface. Increasing the antisolvent to solvent ratio from 1:1 to 9:1 also caused a reduction in size (276 to 175 nm), as greater supersaturation was generated at reduced solubilities, causing nucleation to dominate over particle growth. The disc texture did not significantly affect nanoparticle size; however, particles produced on the grooved disc were of narrower PSD with higher yields.

Nucleation rates were determined for the precipitation of starch nanoparticles in the SDR. Nucleation rates increased with an increase in flow rate and disc speed but were a weak function of antisolvent to solvent ratio. The nucleation rate was greater on the grooved surface at the poorer precipitation conditions, as the precipitation then relied primarily on better mixing through the eddies generated by the grooved surface. A maximum nucleation rate of 6.44×10^{16} mL^{-1} s^{-1} was estimated at conditions of 1200 rpm, 9:1 ratio and 15 mL/s, on the smooth disc.

Finally, experimentally obtained nucleation kinetics along with growth kinetics have been applied to formulate a predictive PSD model, combining the population balance equations (PBE) with a micromixing model. The model uses Hounslow's discretisation method to solve the PBEs, accounting for nucleation, growth, and agglomeration in the SDR. Validation of the simulated PSDs has been done through comparison against experimental results. The modelled PSDs are in good agreement with the experimental results.

Acknowledgements

I am profoundly grateful to my supervisors, Dr Kamelia Boodhoo and Dr Vladimir Zivkovic for their guidance and encouragement throughout the course of the PhD. I am especially indebted to Kamelia, without whom this PhD would not have been possible, and for this reason I cannot imagine a better supervisor!

I would also like to thank the technical staff, Rob Dixon and Iain Strong in particular for their assistance with equipment and experimental setup. A special thanks to Kathryn White (EMRS) and Maggie White (ACMA) for their assistance in analyses. Thank you also to Nichola and Jade for their support.

Finally, I would like to thank my parents for their support and encouragement; my sisters, Rabab and Alisha for always being there for me, and my childhood friend Saubia for her countless trips to Newcastle! A warm thanks to Tolu, Felix and Maria, for making my time at Newcastle enjoyable.

Contents

List of Figures

List of Tables

Nomenclature

S	Supersaturation (-)
C	Solute concentration (g solute / g solvent)
C^*	Equilibrium concentration (g solute / g solvent)
ΔG	Gibbs free energy (kJ mol^{-1})
k	Boltzmann constant (1.38×10^{-23} m^2 kg s^{-2} K^{-1})
N_A	Avogadro's constant (6.022×10^{23} mol^{-1})
T	Temperature (K)
D	Stokes-Einstein diffusion coefficient (m^2 s^{-1})
J	Nucleation rate (particles. mL^{-1} s^{-1})
k_b	Nucleation rate coefficient (particles. mL^{-1} s^{-1})
b	Nucleation rate order (-)
G	Growth rate (m s^{-1})
k_g	Growth rate coefficient (m s^{-1})
g	Growth rate order (-)
Q	Volumetric flow rate (m^3 s^{-1})
u_{av}	Average velocity (m s^{-1})
r	Radial position from centre of disc (m)
r_c	Critical radius (m)
D_i	Impeller diameter (m)
t_{res}	Liquid residence time on disc (s)
t_{ind}	Induction time (s)
t_{micro}	Micromixing time (s)
L	Particle size (m)
V	Volume (m^3)
V_s	Volume of segregated liquid (m^3)
$\dot{m}$	Mass flow rate (kg s^{-1})
k_v	Volume shape factor (-)
n	Population density function (m^{-4})
N_p	Power number (-)
N	Impeller rotation (s^{-1})
N	Particle number per volume suspension (m^{-4})
W	Stability ratio (-)

A_H	Hamaker constant (J)
H	Surface to surface distance of particles (m)
e	Elementary electric charge (1.602×10^{-19} C)
I	Ionic Strength (kmol m^{-3})

Greek symbols

ω	Angular velocity (rad s^{-1})
ν	Kinematic viscosity (m^2 s^{-1})
μ	Dynamic viscosity (Pa s)
ρ	Density (kg m^{-3})
δ	Liquid film thickness (m)
φ_m	Molar volume (m^3 mol^{-1})
σ	Relative supersaturation (-)
τ	Mixing time scale (s)
γ	Interfacial tension between solid surface and supersaturated solution (J m^{-2})
$\dot{\gamma}$	Shear rate (s^{-1})
$\dot{\mu}_3$	3rd moment – volume of solid per unit volume of suspension (m^3/m^3)
β	Collision rate (m^3 s^{-1})
α	Weighting factor (-)
Φ	Particle to particle interaction potential energy (J)
ε	Specific energy dissipation rate (W/kg)
ε	Relative permittivity (-)
ε_0	Electric field constant (8.854 x 10^{-12} $\mathrm{C^2J^{-1}m^{-1}}$)
ψ_0	Surface potential (V)
κ	Inverse Debye length ($\mathrm{m^{-1}}$)

Dimensionless numbers

Da	Damköhler number, $Da = \frac{t_{micro}}{t_{ind}}$ (-)
Sc	Schmidt number, $Sc = \frac{\nu}{D}$ (-)
Re	Reynolds number, $Re = \frac{2Q}{\pi\nu r}$ (-)
Re_ω	Rotational Reynolds number, $Re_\omega = \frac{\omega r^2}{\nu}$ (-)
Ro	Rossby number, $Ro = \frac{u_i}{\omega r}$ (-)
Ta	Taylor number, $Ta = \frac{4\omega^2 r^4}{\nu^2}$ (-)

Ek	Ekman number, $Ek = \frac{\nu}{\omega\delta^2}$ (-)

Subscripts

i	Inner disc radius or interval class bin (PBE)
o	Outer disc radius
AGG	Agglomeration
NCG	Nucleation and growth

Chapter 1. Introduction

1.1. Background

The concept of process intensification emerged in the late 1970s, when Imperial Chemicals Industries (ICI) came up with a strategy to reduce major capital costs without compromising plant output. Although the key aim was to reduce plant size in order to cut down on capital cost, soon the many other benefits of process intensification (PI) became apparent. Since then PI has grown and numerous innovative apparatus and techniques have been developed and implemented across the globe. Two of the ways to intensify a process include: developing a more energy efficient process through improved heat transfer that could lead to reduced energy costs; and switching from batch to continuous to reduce inventory, hence resulting in a safer and more sustainable process. A simple definition of process intensification according to Stankiewicz and Moulijn (2000) is, "any chemical engineering development that leads to a substantially smaller, cleaner and more energy efficient technology is process intensification".

The spinning disc reactor (SDR) is a process intensification technology that has been shown to enhance mixing through subjecting the liquid to high centrifugal forces, creating highly sheared, thin, and unstable films. The thin liquid film generated on the surface of the disc can exhibit near plug flow characteristics with negligible radial dispersion (Mohammadi and Boodhoo, 2012). The SDR has previously been used in many applications, including catalytic reactions (Vicevic et al., 2007), polymerisation reactions (Boodhoo and Jachuck, 2000) and reactive crystallisation (Cafiero et al., 2002). There is not much evidence of solvent-antisolvent precipitation processes carried out in an SDR, and research is limited to one publication for the production of curcumin nanoparticles (Khan and Rathod, 2014).

1.2. Research motivations

The use of nano- and micro-sized particles to gain enhancements in physical and chemical operations is on the increase, particularly in the pharmaceuticals industry. Previous methods to produce smaller sized particles have involved the ‘milling’ of larger particles, a top-down process. However, the many drawbacks of milling, such as a wide particle size distribution, presence of impurities and it being a costly process has directed industries towards the bottom-up approach where particles are generated from the atomic level (Thorat and Dalvi, 2012). One such method of precipitation is solvent-antisolvent precipitation, which is the focus of this work. In previous studies, solvent-antisolvent precipitation has been carried out

in a variety of reactors, from stirred tank reactors to narrow channel reactors with the purpose of achieving better mixing and a controlled particle size distribution. Another way to achieve these goals would be through process intensification. Process intensification approaches for precipitation processes may be classified under four domains (Wang et al., 2018):

1. Space domain, which focusses on limiting spatial gradients such as concentration and momentum to increase control over the final product.
2. Time domain, which may involve switching from batch to continuous.
3. Function domain, which implements synergistic effects.
4. Energy domain, which introduces the use of external fields such as ultrasound or microwaves to encourage nucleation.

The spinning disc reactor takes advantage of both the spatial and time domain to intensify precipitation processes, as the thin films generated in the SDR encourage plug flow, intensifying heat and mass transfer rates and improving micromixing. Furthermore, the residence time on the disc is short and controllable through the conditions imposed in the reactor (Boodhoo, 2013). These characteristics are extremely fundamental in precipitation processes, particularly in antisolvent precipitation, as adequate mixing is crucial for the incorporation of antisolvent into the solute/solvent mixture. Additionally, reduced residence times in the SDR limit particle growth.

Starch nanoparticles have a wide range of applications in various industries, especially in the pharmaceuticals industry where they have been used as drug carriers. Current methods of starch nanoparticle production mainly consist of acid hydrolysis, which is prone to issues such as low yields and negative environmental impact (Sun et al., 2014). Furthermore, acid hydrolysis promotes digestibility of starch nanoparticles through the formation of a certain crystalline polymorph, which is undesirable if the nanoparticles are to be used as drug carriers (Srichuwong et al., 2005). The solvent-antisolvent precipitation of starch nanoparticles is currently carried out through a fed-batch set-up, limited to dropwise addition of the antisolvent in order to deal with the high viscosities of the starch solution and avoid agglomeration of the nanoparticles (Hebeish et al., 2014). There is therefore much scope for improvement of such a precipitation process. Previous solvent-antisolvent precipitation studies have demonstrated that particle size and morphology are influenced by a number of conditions including flow rate, antisolvent to solvent ratio, solute concentration

and mixing intensity (Sinha et al., 2013). Therefore, by employing continuous flow intensified technologies which can optimise such parameters in an efficient manner, solvent-antisolvent precipitation can be more effectively conducted.

1.3. Aims and objectives

This research aims to investigate solvent-antisolvent precipitation in an SDR. To date, the extent of research on this particular process in the SDR has been limited. The present work looks into producing starch nanoparticles as the model system due to its wide range of applications, and to improve on limitations presented by the current procedures. Ethanol has been selected as the antisolvent and sodium hydroxide as the solvent. Experimental and modelling studies are carried out as part of this research, with the following objectives:

1. Study of effect of various parameters for the solvent-antisolvent precipitation of starch nanoparticles in an SDR.

   The research intends to look into factors that could affect the precipitation process. The factors to be studied include total flow rate of solute/solvent and antisolvent streams, solvent-antisolvent ratio, solute concentration, and disc rotational speed. The effect of these parameters on the particle size distribution and the morphology of the particles will be studied, as well as the yield generated. Additionally, the influence of the disc surface is to be explored as the surface of the disc has previously shown to affect the hydrodynamics in the spinning disc reactor, thus affecting precipitation and particle formation (Mohammadi, 2014).

2. Investigation of precipitation kinetics for starch nanoparticles precipitation.

   A number of mechanisms occur during a precipitation process, including nucleation and particle growth. To ensure the production of small sized particles with a narrow size distribution, it is important that the dominating mechanism is homogeneous nucleation (Beck et al., 2010). The study of precipitation kinetics allows us to investigate the conditions at which homogeneous nucleation prevails, and how factors such as mixing, and supersaturation affect the kinetics of the process. For the parameters mentioned in the previous objective, the aim is to characterise the solvent-antisolvent precipitation of starch nanoparticles through an estimation of nucleation and growth kinetics, with particular focus on determining induction times in the SDR which has never been done before.

3. To model the solvent-antisolvent precipitation process.

   A population balance equation approach will be adopted to develop a predictive model using the precipitation kinetics determined as part of objective 2. The model will be used to validate the experimental results and gain a better understanding of the solvent-antisolvent precipitation process.

1.4. Research approach

The work conducted as part of this research has been split into three parts. The first part of the research is concerned with the precipitation of starch nanoparticles in the SDR using the solvent-antisolvent precipitation method. Sodium hydroxide was identified as a suitable solvent and ethanol as the antisolvent. Preliminary experiments have been conducted in a semi-batch set-up to get an awareness of the conditions that affect starch nanoparticles, as well as the limitations and boundaries in such a set-up. Following this, intensification in the SDR has been carried out using various combinations of carefully selected operating parameters, including disc surface. The effect of these parameters was studied using particle size, size distribution, morphology and yield as a basis of analysis.

The second part of the research focuses on the precipitation kinetics of starch nanoparticles precipitation in the SDR. One novel aspect of this section of the study is the ability to measure induction time in the SDR which has been carried out using a high-speed camera system, allowing the prediction of the radial point at which nucleation occurs on the disc.

The key focus of the final part of the research is the modelling of the solvent-antisolvent precipitation of starch nanoparticles in the SDR. Population balance modelling has not yet been carried out for solvent-antisolvent processes in the SDR. The precipitation kinetics determined earlier as part of the current work have also been incorporated into the model which has been solved using MATLAB software. Additionally, a micromixing model has been applied as an alternative over computational fluid dynamics (CFD) based models.

1.5. Thesis layout

Chapter 1 presents a brief background to the research, with particular focus on the motivations for undertaking this study. This is followed by aims and objectives and an outline of the approach and methodology applied to undertake the research.

Chapter 2 provides a review of the current literature available on the major topics covered in this work. A detailed background on the formation of nanoparticles through the process of

precipitation is given, deliberating on mechanisms including nucleation, growth and agglomeration, with particular attention on the solvent-antisolvent method of precipitation. The current method of starch nanoparticles formation is evaluated, and areas of application are discussed. Further review of literature focuses on the conditions that affect the quality of particles produced, delving into technologies applied in precipitation processes with emphasis on process intensification (PI) technologies. The hydrodynamics of the spinning disc reactor and areas which the SDR has been applied to until present are reviewed. Finally, the importance of mixing in precipitation processes is discussed.

Chapter 3 provides details of the equipment and the methodologies applied in this work. Details of analytical techniques used to characterise the starch nanoparticles are also presented in this chapter.

The results and discussions for the solvent-antisolvent precipitation of starch nanoparticles in an SDR are given in Chapter 4. In the first section within this chapter, experimental results are presented in the form of size distributions and TEM images to determine the effect of operating parameters such as flow rate, disc rotational speed and antisolvent to solvent ratio. The effect of disc surface texture is also analysed. In addition, comparison of the SDR technology with the semi-batch results are detailed within this chapter. Following this, empirical correlations based on multiple linear regression analysis are formulated to investigate the interaction between parameters (flow rate, disc speed and antisolvent to solvent ratio) affecting particle size during precipitation in the SDR.

The second section of the chapter concentrates on the precipitation kinetics where induction times are estimated and compared for a range of conditions in the SDR and applied in calculating nucleation rates. Interfacial tension and critical radii values are also obtained and discussed in the context of corresponding literature values in order to gain a better understanding of the kinetics.

Chapter 5 is concerned with the development of a mathematical model using MATLAB. A brief review on the significance of population balance modelling as well as the possible methods available for solving population balance equations (PBEs) are presented within this chapter. Two distinct methods are applied to obtain solutions to the PBEs, namely, the Lax-Wendroff method and Hounslow's method of discretisation. The particle size distributions obtained from these methods are analysed and compared with experimental results.

Finally, the conclusion and recommendations for future work derived from this research are stated within Chapter 6.

Chapter 2. Literature review

This chapter provides an overview of the current literature relevant to this research. Firstly, the chapter presents an insight into the precipitation process and the many stages involved in precipitation, including nucleation and particle growth. This is followed by a review of solvent-antisolvent precipitation, focusing on the conditions which influence particle formation.

Starch nanoparticles are selected as the model system to evaluate solvent-antisolvent precipitation in the spinning disc reactor (SDR), and so the areas of application and current production methods are reviewed within this chapter.

The final part of this chapter focuses primarily on process intensification (PI) technologies and the application of PI in solvent-antisolvent precipitation processes. The application of the SDR in various processes is assessed and the hydrodynamics are discussed. Following this, the significance of mixing in the SDR with respect to solvent-antisolvent precipitation is presented.

2.1. Precipitation process

The process of precipitation involves various steps, generally falling under two broad categories: nucleation and the growth phase. The most vital step in the precipitation process is the creation of supersaturation, as particles can neither form nor grow unless the solution is supersaturated. A pictorial outline of the mechanisms involved is shown in Figure 2-1 below.

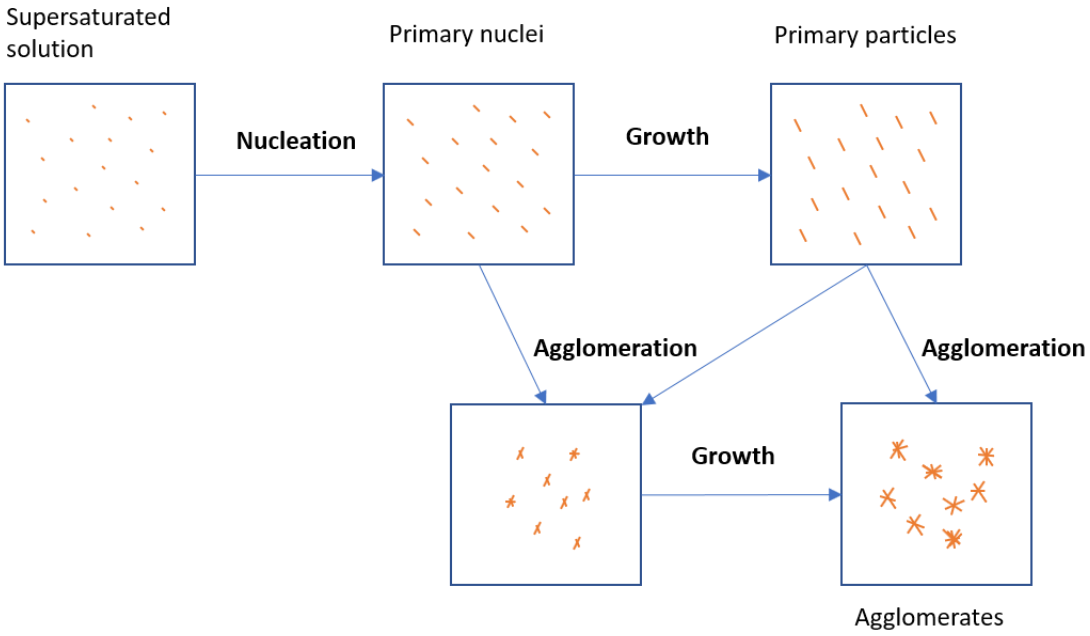

Figure 2-1: Precipitation mechanism showing nucleation, growth and agglomeration of particles.

2.1.1. Supersaturation

The driving force for precipitation is supersaturation which by definition is the state of thermodynamic equilibrium between the solution and the solute, and below this threshold solid formation is impossible (Green and Perry, 2007). Supersaturation can be expressed in many different ways but prominent amongst these are the concentration driving force, ΔC, the supersaturation ratio, S, and the absolute or relative supersaturation, σ, defined through the following equations (Mullin, 2001):

$$\Delta C = C - C^* \tag{2-1a}$$

$$S = \frac{C}{C^*} \tag{2-1b}$$

$$\sigma = \frac{\Delta C}{C^*} = S - 1 \tag{2-1c}$$

where, C is the solution concentration and C^* is the equilibrium concentration. An alternative way to express the driving force for precipitation is through the difference in chemical potentials of the solution and the precipitated particles. This method of expressing supersaturation is however not easy to apply. Therefore, if the concentration of the solution and the equilibrium saturation concentration are known, the supersaturation can be obtained through the concentration driving force as expressed in Equation 2-1a (Jones, 2002).

Supersaturation can be achieved by cooling, solvent evaporation, addition of an antisolvent to lower solubility, or by producing a substance with lower solubility through a chemical reaction. Jones (2002) explained the significance of a solubility curve in determining the method of precipitation. A steep curve indicates a strong temperature dependence and so cooling precipitation can be used. A solution with a flat equilibrium line can be precipitated through an evaporative process. However, if any of these processes are inefficient, producing low yields, then antisolvent precipitation can be carried out. Alternatively, a solute can also be produced via a chemical reaction. A solubility – supersolubility phase diagram (Figure 2-2) taken from Jones (2002) has been modified to help understand the process of precipitation, as well as aid in selecting the most suited method for a certain substance. The solubility curve is divided into three regions: the undersaturated region, metastable region and the labile region. In the undersaturated region there is no particle formation as particles tend to dissolve in the solution. On the other hand, the metastable and labile regions fulfil the supersaturation requirement and particle formation can occur, with spontaneous nucleation occurring in the labile region.

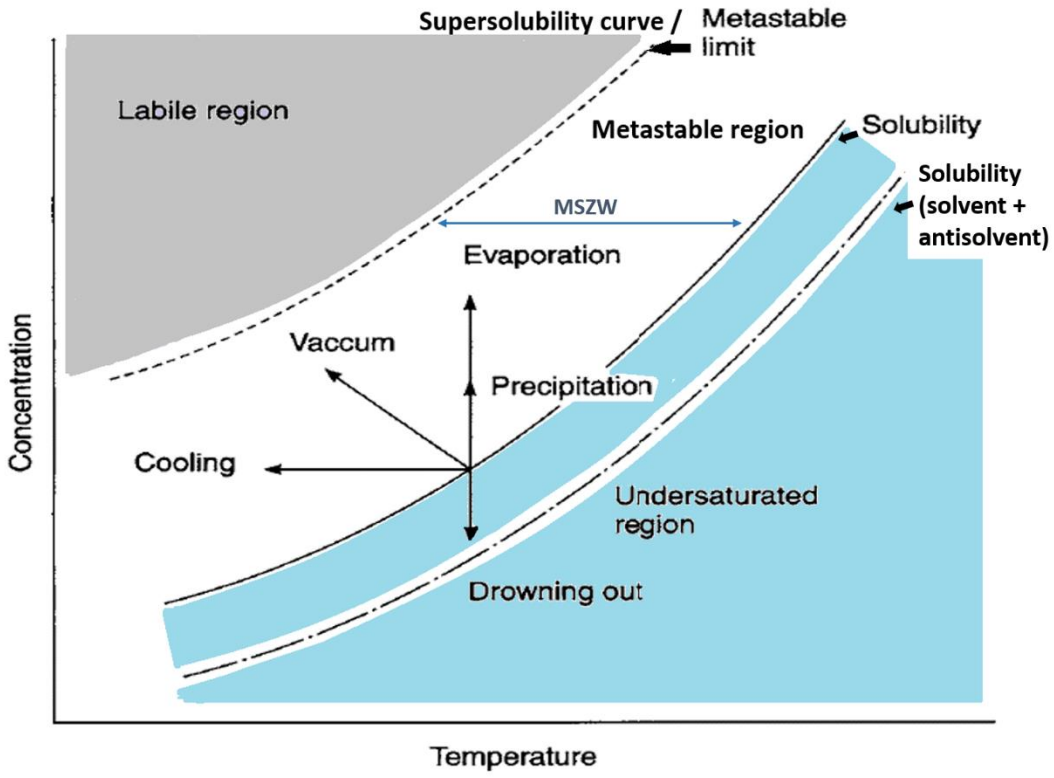

Figure 2-2: Solubility curve adapted from Jones (2002), showing the labile (grey), metastable (white), and undersaturated (blue) regions.

In the figure above, the metastable region is a zone of supersaturation, enclosed by the solubility and supersolubility curves. The supersolubility curve is essentially the metastable boundary separating the metastable zone from the labile zone where supersaturation is spontaneous. The metastable zone width (MSZW) is the maximum allowable supersaturation beyond which nucleation is spontaneous (Mullin, 2001).

2.1.2. Nucleation

Nucleation is the formation of a new solid phase known as a nucleus. The precipitation process centres around nuclei and for precipitation to begin a number of nuclei must be present. Nucleation can be split into two categories: primary and secondary nucleation. Primary nucleation occurs when there are no previously present particles in the solution to influence nucleation, whereas secondary nucleation is induced by particles already present in the solution. Primary nucleation is further divided into two categories, namely homogeneous nucleation and heterogeneous nucleation.

2.1.2.1. *Homogeneous Nucleation*

Homogeneous nucleation is a spontaneous process highly dependent on supersaturation. The relationship between supersaturation and nucleation rate is displayed in Figure 2-3, showing that nucleation rate, *J*, is a function of supersaturation, *S* (Mullin, 2001). Nucleation rate is defined as the number of nuclei formed per unit time per unit volume. As supersaturation increases there is an increase in the nucleation rate, however further increase in supersaturation beyond the metastable limit leads to a reduction in the nucleation rate. This may be the result of the solution being too viscous for nucleation to occur (Mullin, 2001), or caused by phase separation of the solution, known as oiling out (Tung et al., 2008c).

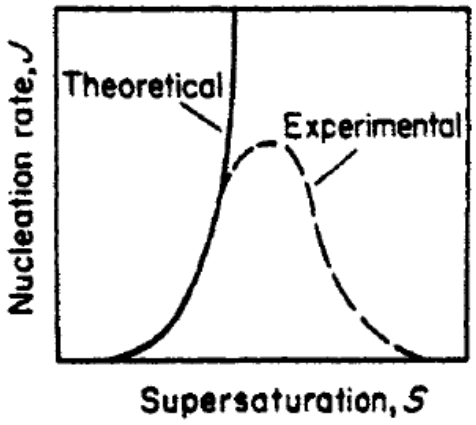

Figure 2-3: A plot of supersaturation against nucleation rate (Mullin, 2001).

The initiation of nucleation results from molecular additions to a critical cluster, x:

$$x + x \leftrightarrow x_2$$

$$x_2 + x \leftrightarrow x_3$$

$$x_{n-1} + x \leftrightarrow x_n$$

High supersaturation conditions are required for the assembly of stable nuclei. Many clusters formed are short lived unstable sub-nuclei which re-dissolve into the solution. However, under average supersaturation, a nucleus may become stable if it grows beyond a critical size. The process can be explained in terms of free energy change.

The overall free energy, *ΔG* between a solid solute particle and the solute in solution can be defined as the sum of the excess free energy between the surface of a particle and the bulk of a particle, ΔG_s (positive), and the excess free energy between a particle of infinite size and the solute in solution, ΔG_V (negative):

$$\begin{aligned} \Delta G &= \Delta G_s + \Delta G_V \\ &= 4\pi r^2 \gamma + \frac{4}{3}\pi r^3 \Delta G_v \end{aligned} \tag{2-2}$$

Where, ΔG_v is the free energy change of the conversion per unit volume, and *γ* is the interfacial tension between the solid surface and the supersaturated solution. From Equation 2-2 the minimum size of a stable nucleus, known as the critical size, r_c can be determined by setting $\frac{d\Delta G}{dr} = 0$:

$$r_c = \frac{-2\gamma}{\Delta G_v} \tag{2-3}$$

This relationship can be explained through the free energy diagram for nucleation, presented in Figure 2-4 (Mullin, 2001). The total free energy passes through a maximum at the critical radius, r_c, at which the energy corresponding to the critical nucleus is given by:

$$\Delta G_{crit} = \frac{4}{3}\pi\gamma r_c^2 \tag{2-4}$$

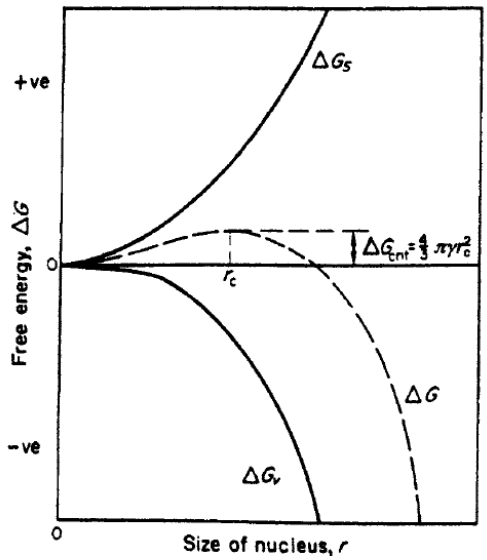

Figure 2-4: Free energy diagram explaining the critical nucleus (Mullin, 2001).

As supersaturation increases the free energy curve is lowered due to a decrease in the entropy of phase transformation, subsequently reducing the critical radius value beyond which the particle is stable (Tung et al., 2008b).

The rate of nucleation, J, can be expressed in the form of the Arrhenius equation (Mullin, 2001).

$$J = Ae^{-\Delta G/kT} \tag{2-5}$$

where *A* is a rate constant, and *k* is the Boltzmann constant. Equation 2-5 can be further expressed in terms of supersaturation, *S,* and interfacial tension, γ:

$$J = Ae^{\left[-\frac{16\,\pi\gamma^3{\varphi_m}^2}{3\,k^3T^3(ln\,S)^2}\right]} \tag{2-6}$$

Detailed explanation of how Eq. 2-6 is obtained is given in Mullin (2001).

2.1.2.2. *Heterogeneous Nucleation*

Nucleation may be affected by the presence of impurities or foreign entities in the system. Heterogeneous nucleation is a weak function of supersaturation and strongly dependent on the presence of foreign particles.

For heterogeneous nucleation, the overall free energy change for the formation of a critical nucleus is expressed as:

$$\Delta G'_{crit} = \varphi \Delta G_{crit} \tag{2-7}$$

Where φ is a factor less than 1 since the presence of impurities increases nucleation rate. It has been reported by Mersmann (1999) that the presence of foreign particles reduced energy required for nucleation by 10% of the homogeneous nucleation value.

As mentioned earlier, interfacial tension is a key influencing factor for nucleation rate. Resolving interfacial tension for three phases in contact gives an expression for the contact angle which corresponds to the wetting angle in liquid-solid systems. The wetting angle, θ, can then be used to express the factor φ; Volmer (1939) found that the decrease in free energy depended on the contact (or wetting) angle of the solid phase (Myerson and Ginde, 2002).

$$\varphi = \frac{(2 + cos\theta)(1 - cos\theta)^2}{4} \tag{2-8}$$

At a wetting angle of θ=180°, φ=1, $\Delta G'_{crit}=\Delta G_{crit}$, therefore, nucleation is not influenced by the presence of the foreign particle. For wetting angles between θ=0° and θ=180°, $\Delta G'_{crit}<\Delta G_{crit}$ which implies that heterogeneous nucleation is more spontaneous than homogeneous nucleation as less overall free energy is required and this is presented in Figure 2-5 (Mullin, 2001).

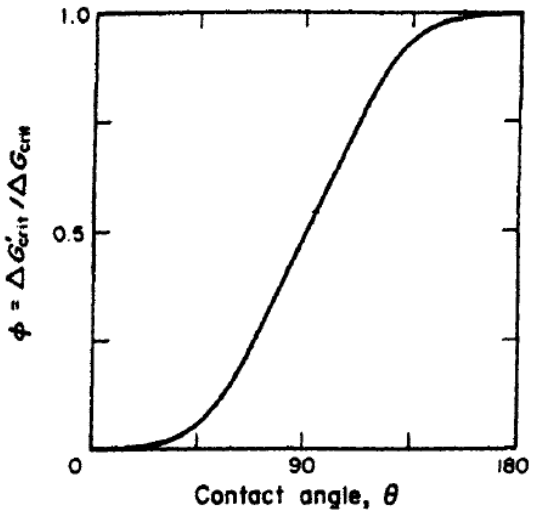

Figure 2-5: A plot between contact angle and free energy factor (Mullin, 2001).

2.1.2.3. *Secondary Nucleation*

The formation of new particles can be influenced by the prior presence of solute particles in the saturated solution, known as secondary nucleation. Many theories have been proposed

for the mechanism of secondary nucleation. Those found in literature include (Mason and Strickland-Constable, 1966):

1) Initial breeding – this involves dust from solid surfaces being formed and acting as nucleation sites.
2) Needle breeding – high levels of supersaturation may lead to dendrite structures being formed and as these particles break off, they are able to serve as new nucleation sites.
3) Collision breeding – the interaction between particles with one another or with the vessel causes abrasion of the particles, resulting in particles with round edges that serve as nucleation sites.

The above mechanisms come under the 'true nucleation' category (Söhnel, 1992), although, there are other secondary nucleation mechanisms including contact nucleation and seeding. Contact nucleation is the formation of nucleation sites formed as a result of the collisions between particles, particle-stirrer collisions or collisions between particles and vessel wall. However, this differs from collision breeding since contact nucleation involves microabrasion of the particles as opposed to the macroabrasion during collision breeding. The seeding method is most frequently carried out in industrial precipitation processes and involves inoculating a supersaturated solution with nuclei of the species to be precipitated.

2.1.2.4. *Induction Periods*

Induction period is defined as the time elapsed between the onset of supersaturation and the appearance of the first particles. It is the sum of the time required to reach steady state nucleation, t_r, the time required for formation of a stable nucleus, t_n, and the time needed for the nucleus to grow to a detectable size, t_g (Mullin, 2001):

$$t_{ind} = t_r + t_n + t_g \tag{2-9}$$

These time periods are impossible to isolate but the factors that affect them can be explored further. The relaxation time is dependent on the viscosity of the solution mixture and so the diffusivity; at high viscosities, diffusivity is low and t_r is high. The final quantity, t_g, depends on the size at which the nuclei can be detected and hence is difficult to predict. Despite the induction period being affected by external factors it is still frequently used as a fundamental method to predict the mechanism of nucleation. The following assumption can be made, providing nucleation is of a true homogeneous nature (Mullin, 2001):

$$t_{ind} \propto J^{-1}$$

A plot of log t_{ind} versus (log S)$^{-2}$ should ideally produce a straight line with a gradient of interfacial tension, γ according to the following relationship which is obtained from Eq. 2-6:

$$\log t_{ind} \propto \left[\frac{\gamma^3}{T^3(\log S)^2}\right]$$

However, when Söhnel and Mullin (1978) determined experimentally the relationship between induction period and supersaturation for $CaCO_3$, the plot presented in Figure 2-6 showed two straight lines with different slopes. The change of slope indicates the transformation from homogeneous to heterogeneous nucleation. At low supersaturation, heterogeneous nucleation dominates whereas homogeneous nucleation is the dominant mechanism at higher supersaturations.

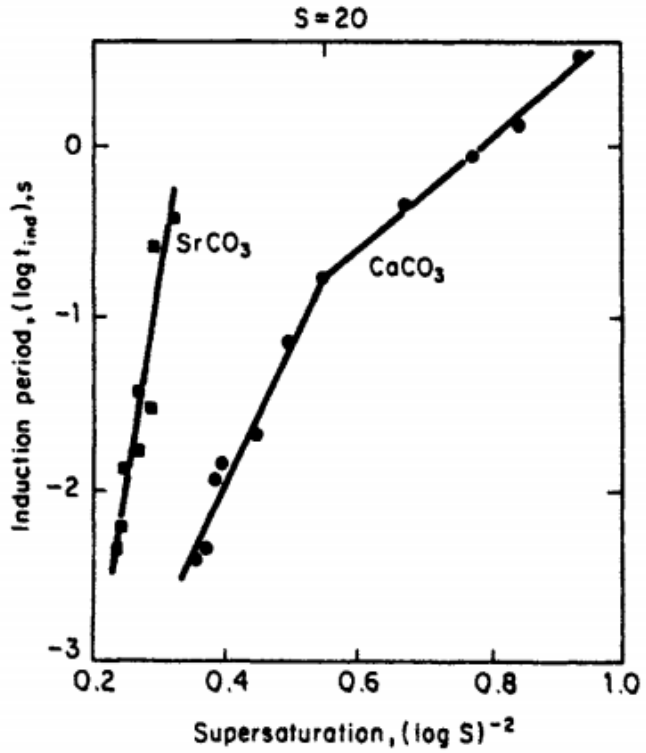

Figure 2-6: Induction period as a function of supersaturation for $CaCO_3$ (Söhnel and Mullin, 1978).

2.1.2.5. *Measuring Nucleation Rate*

Knowledge of the particle count and induction time are required to determine the nucleation rate. The particle count is the number of particles per unit volume and is obtained through simple particle counting methods. Some of those mentioned in literature include, microscopic methods such as a haemocytometer (Cafiero et al., 2002, Mohanty et al., 1988), number based size distribution methods such as electro-zone sensing and light

obscuration (Roelands et al., 2004). Another method estimates the number of particles as the ratio of mass of precipitated particles over the mass of one particle (Ramisetty et al., 2013). The haemocytometer procedure involves manual counting under the microscope which can be a time-consuming task. However, together with image analysis software counting can be automated (Blandin et al., 2001). Determining particle count by weighing mass of precipitated solute is susceptible to increased errors if the particles are unevenly sized or agglomerated. Similarly, with the size distribution based technique of measuring particle count, it is preferred that the particles are spherical as non-spherical particles may lead to errors (Roelands et al., 2004).

Among the numerous methods of detecting induction time, thus the onset of nucleation mentioned in literature, some of the more prominent ones are: focused beam reflectance measurement (FBRM) (Ó'Ciardhá et al., 2011), attenuated total reflectance-Fourier transform-infrared (ATR-FTIR) (O'Grady et al., 2007), optic probe (Zhi et al., 2011, Chaitanya and Sarkar, 2014), turbidity probe (Parisi and Chianese, 2013, Zhang et al., 2015) and visually (Chianese et al., 1995). The FBRM detects the point at which particles become apparent in solution, the FTIR detects the reduction in concentration, whereas the optic probe and the turbidity probe detect changes in optical properties at the point of nucleation. Kubota (2008) argues that the detection method is significant, stating that a more sensitive measuring equipment would detect nucleation at a lower number density, resulting in a lower induction time. However, when the induction time becomes very small and comparable to the mixing time, detection may seem difficult. Carosso and Pelizzetti (1984) measured the induction time for the precipitation of barium sulphate using a stopped flow mixing system with a laser beam passing through the mixing chamber to measure the deflection of the beam caused by the formation of particles. This method allowed induction times of 5 to 30 ms to be measured. The investigators further calculated the interfacial tension for their system and derived an expression for induction time as a function of supersaturation.

McCarthy et al. (2007) used the model from Carosso and Pelizzetti (1984) to compare theoretical induction time with the induction time measured in the narrow channel reactor for the reactive precipitation of barium sulphate. The induction time was measured by visually monitoring the onset of turbidity in a clear channel, a method first carried out by Nielsen (1961). The authors stated that the range of predicted induction times were much

greater than the highest measured induction time. The authors concluded that mixing in the narrow channels played a vital role in reducing the induction time.

However, for continuous systems such as the spinning disc reactor determining the induction time can be substantially difficult. Cafiero et al. (2002) adopted the expression suggested by Carosso and Pelizzetti (1984) to estimate a value for the theoretical induction time for barium sulphate. The authors assumed the model suitable for estimating the precipitation of barium sulphate in the spinning disc reactor as homogeneous nucleation does not depend on the reactor geometry but only the operating temperature which disagrees with the findings of McCarthy et al. (2007) for the narrow channel system as reactor geometry influences mixing.

2.1.3. Particle growth

Once the stable nuclei have been formed, the solution desupersaturates and this initiates the formation of particles. Over the past century many mechanisms of particle growth have been proposed. A few of these have, however, fallen into disuse. For example, the theories based on the concept of surface energy, which proposes that particles assume a shape that has minimum surface energy (Mullin, 2001). Another theory is the adsorption layer theory, which suggests that a loosely adsorbed layer of particles is formed at the particle surface, establishing a dynamic equilibrium between the layer and solution (Mullin, 2001).

The most widely mentioned theory is the diffusion theory, which is a two-step process involving diffusion from the solution to the particle surface, and the integration of the molecules into the crystal lattice through a surface reaction process. This was first proposed by Berthoud (1912) and Valeton (1924), whereas prior to that it was believed that precipitation is the reverse of dissolution, disregarding the integration process (Mullin, 2001). The two kinetic processes occur consecutively, reaching a steady state where the rates of the two processes are equal. The two driving forces can be expressed as:

$$\frac{dm}{dt} = k_d A\,(C - C_i)$$
$$\frac{dm}{dt} = k_r A\,(C_i - C^*) \qquad (2\text{-}10)$$

where m is the mass of solid deposited in time, t, k_d is the mass transfer coefficient, k_r, the reaction rate, C is the concentration in the bulk, C_i is the concentration of the solute at the interface and C^* is equilibrium concentration.

However, it is not possible to measure C_i, the concentration at the interface, so an overall driving force is considered:

$$\frac{dm}{dt} = K_g A\,(C - C^*)^g \tag{2-11}$$

where K_g is the overall particle growth coefficient, and g is the overall order of the growth process.

2.1.4. Secondary processes

The basic three steps of supersaturation, nucleation and particle growth may be followed by various succeeding steps, considerably affecting the final product. A few of the processes that generally occur are aging, agglomeration, breakage and ripening.

Aging is a slow process leading to particle modification in the microscopic, sometimes macroscopic level and could either consist of physical or chemical changes. Aging may involve recrystallization to more stable, compact forms. Söhnel and Mullin (1982) reported the transformation of vaterite to stable calcite during calcium carbonate precipitation.

A lot of confusion and disagreement is apparent in defining the terms agglomeration and aggregation, and are often seen to be used interchangeably (Nichols et al., 2002). However, to avoid such confusion the term agglomeration will be used in this report, as was done by Mullin (2001) in his textbook for crystallisation. Agglomeration is the clustering of particles to form larger particles. The process of agglomeration depends on interparticle collisions that may result in the permanent attachment of particles, given the forces of attraction such as van der Waals forces can overcome the repulsive forces (Söhnel, 1992). To distinguish between the types of collision, agglomeration can be further divided into two categories: perikinetic and orthokinetic as proposed by Smoluchsowki (1918), (Mullin, 2001). Perikinetic agglomeration occurs in static fluid, where particle collision depends on Brownian motion. On the other hand, orthokinetic agglomeration occurs in agitated systems. In addition to collision frequency, the rate of agglomeration depends on countless other factors, including particle size, concentration, fluid temperature, pH and viscosity (Mersmann, 2001).

Agglomerated particles can also undergo a process known as breakage. This is a result of interaction between particles and with foreign bodies such as an impeller or the vessel wall, breaking up the agglomerates. Agglomeration and breakage are fundamental processes in the determination of the particle size distribution (Karpinski and Wey, 2002).

Ripening, also known as Ostwald ripening, is the dissolution of smaller particles to form larger ones. As both ripening and agglomeration result in an increase particle size and a reduction in the number of particles, it is often difficult to distinguish between the two (Karpinski and Wey, 2002). The process of ripening is driven by the difference in solubilities between the small and large particles. The system aims to reach a minimum total surface free energy and in order to do so, solute from the small particles is deposited onto the surface of the larger particles, eventually reaching a thermodynamic state of equilibrium (Söhnel, 1992).

2.2. Solvent-antisolvent precipitation

Precipitation can occur by adding a second solvent known as an antisolvent to the solute-solvent mixture. The antisolvent reduces solubility, generating supersaturation. This is highlighted in Figure 2-2 where the solubility curve for the solvent-antisolvent system is lower than the system with only the solvent. The method is particularly useful for highly soluble solutes. An advantage of this method is that it can be carried out at ambient temperatures, requiring no heating or cooling. This makes antisolvent precipitation an attractive option for heat sensitive solutes, or systems that can be unstable at changing temperatures (Doki et al., 2002). It is also a low energy demanding process as it may be carried out at ambient temperatures, proving to be a low cost option. Oosterhof et al. (2001) successfully carried out antisolvent precipitation at ambient temperature of anhydrous sodium carbonate which is usually carried out at extremely high temperatures and involves many steps, saving energy as a result. Another advantage of antisolvent precipitation is the ability to control formation of polymorphs by favouring a certain crystalline structure (Takiyama et al., 2010). This property makes antisolvent precipitation the preferred method in pharmaceutical manufacture. However, the solvent-antisolvent mixture needs to be separated as a final step, is highly dependent on mixing and may lead to agglomeration if the system is not adequately mixed (Takiyama et al., 1998).

There have been plenty of studies looking at the factors affecting antisolvent precipitation. One such factor is supersaturation. Toth et al. (2005) established that antisolvent

precipitation is highly dependent on initial supersaturation, and by changing three parameters: solution concentration, solubility and operational time, a range of particle sizes can be produced. Granberg et al. (1999) studied the effect of solvent composition on an antisolvent precipitation process. The study showed that by increasing initial supersaturation, nucleation rate increased. However, when initial supersaturation was kept constant, the solvent composition had no effect on precipitation. The authors concluded that supersaturation and not solvent-antisolvent composition defined induction time, and the antisolvent only had an influence on solubility and crystal properties but not the kinetics of the process.

Conditions such as increasing solute concentration or reducing solubility by adding antisolvent increase the degree of supersaturation, thereby increasing nucleation rate and reducing particle growth, producing particles of smaller sizes (Takiyama et al., 1998, Holmbäck and Rasmuson, 1999, Kim, 2006, Hash and Okorafor, 2008). However, smaller particles are likely to undergo agglomeration, resulting in a wider particle size distribution (PSD). Fujiwara et al. (2002) stated that agglomeration was more likely to occur in particles smaller than 100 microns. Similarly, Granberg et al. (1999) reported an increase in initial supersaturation increased agglomeration in particles. Yu et al. (2005) studied agglomeration in paracetamol particles at a range of antisolvent feed rates, the results indicated that an increase in antisolvent addition produced high supersaturation, increasing the production of fine particles that promote agglomeration. However, despite the production of large particles, the authors concluded that an increase in antisolvent had an overall effect of moving the PSD towards smaller sizes.

2.2.1. Solvent/Antisolvent selection

The antisolvent precipitation process highly depends on the choice of solvent and antisolvent, as well as the ratio between the two. In order to obtain supersaturation and thus a high particle yield, the antisolvent chosen must be miscible with the solvent, the solute should be insoluble in the antisolvent and soluble in the solvent, and the solvent-antisolvent mixture should be readily separable (Mullin, 2001).

Antisolvent precipitation has been applied to a range of areas, including the precipitation of both organic and inorganic substances. Hence the solvents need to be selected based on the solubility properties of the substance being precipitated. The terms salting-out or drowning-out are often used interchangeably with antisolvent precipitation. The distinguishing factor

for the two terms is generally the type of antisolvent used. The precipitation of an inorganic salt using an organic antisolvent is known as salting-out. On the other hand, in the precipitation of pharmaceuticals or organic substances, water is used as the antisolvent and the process is known as drowning-out (Wey and Karpinski, 2002). This is based on the principle of 'like dissolves like'.

2.2.2. Precipitation of starch nanoparticles

Starch is a biopolymer made up of two polymers, amylose and amylopectin. Starch nanoparticles have many medical and industrial applications, such as polymer drug carriers and reinforcements in nanocomposites. Starch nanoparticles can be produced through a variety of methods, including both top-down and bottom-up approaches. The preferred method of production is acid hydrolysis, a top down process. However, acid hydrolysis is a time consuming process which results in low yields (Hebeish et al., 2014). Other methods of producing starch nanoparticles include enzymatic hydrolysis, ultrasonication, reactive extrusions and gamma irradiation (Kim et al., 2015).

The nanoparticles formed through each method differ in size and morphology, as well as the yields obtained. The ratio of amylose and amylopectin also affects the characteristics of the starch nanoparticles, as does the system used to precipitate out the starch nanoparticles (Dufresne, 2015). Often sodium hydroxide is used as the solvent to dissolve starch by breaking the hydrogen bonds between water-starch and starch-starch molecules to form sodium starch alkoxide (starch-O-Na) (Chin et al., 2014). An alternative to the alkali sodium hydroxide is dimethylsulphoxide (DMSO), which has the advantage of being applicable for the use in drug carrier systems that are sensitive to pH (Wu et al., 2016).

Ethanol and other alcohols have been used as antisolvents in previous studies for the precipitation of starch. Wu et al. (2016) investigated the effect of the antisolvent on the starch nanoparticles. Several alcohols were used in this study, with the results indicating that shorter chain alcohols produced smaller sized nanoparticles. This was linked to the difference between the dielectric constants of the solvent, DMSO, and the antisolvent. Furthermore, changing the antisolvent to solvent ratio had a small effect on particle size, where an increase in antisolvent resulted in a slight decrease in particle size but had a profound impact on the morphology of the particles. Similar results were obtained by Chin et al. (2011) where sodium hydroxide was used as the solvent and ethanol as the antisolvent. The particle sizes obtained were in the range between 300 nm and 400 nm. The

concentration of the starch molecule and the surfactants used also affect the size and morphology of the particles obtained (Hebeish et al., 2014).

The precipitation of starch nanoparticles has only been carried out using low material concentrations as a way to avoid agglomeration of particles, and have involved dropwise addition of either the antisolvent to the solvent (Hebeish et al., 2014), or the solvent to the antisolvent (Chin et al., 2011). No continuous flow systems have yet been studied for the precipitation of starch nanoparticles.

2.3. Process intensification

Process intensification (PI) work first gained attention in the late 1970s by Colin Ramshaw's group in Imperial Chemicals Industries (ICI), UK (Reay et al., 2008). Inspired by NASA's work on rotating boilers, ICI used rotational movement and centrifugal forces to develop a Higee distillation unit (Ramshaw, 1983, Reay et al., 2008). Since then several new concepts and technologies have been developed in the name of PI.

Although there is no single clear definition of process intensification, the concept of PI is often based around the following principles (Baldea, 2015, Reay et al., 2008):

- Reduction in equipment size
- Reduction in capital and production cost
- Improved process safety
- More environmentally favourable
- Increased energy efficiency
- Improved product quality

In addition, Van Gerven and Stankiewicz (2009) suggested the following four principles:

1. Maximising process kinetics to achieve greater conversion and selectivity.
2. A similar processing experience offered to all reacting species, encouraging plug flow.
3. Improved mass and heat transport through the optimisation of driving forces and increased specific surface area.
4. Use of multifunctional devices to promote synergy.

Stankiewicz and Moulijn (2000) whose definition of PI focuses on the novelty aspect of the technology provide a PI toolbox (Figure 2-7). The toolbox is divided into two distinct categories, process intensifying equipment and process intensifying methods. Process

intensifying equipment are devices that provide enhanced mixing and, or heat and mass transfer. Process intensifying methods on the other hand could be for example, the integration of reaction and separation processes, or the use of alternative energy sources such as microwaves.

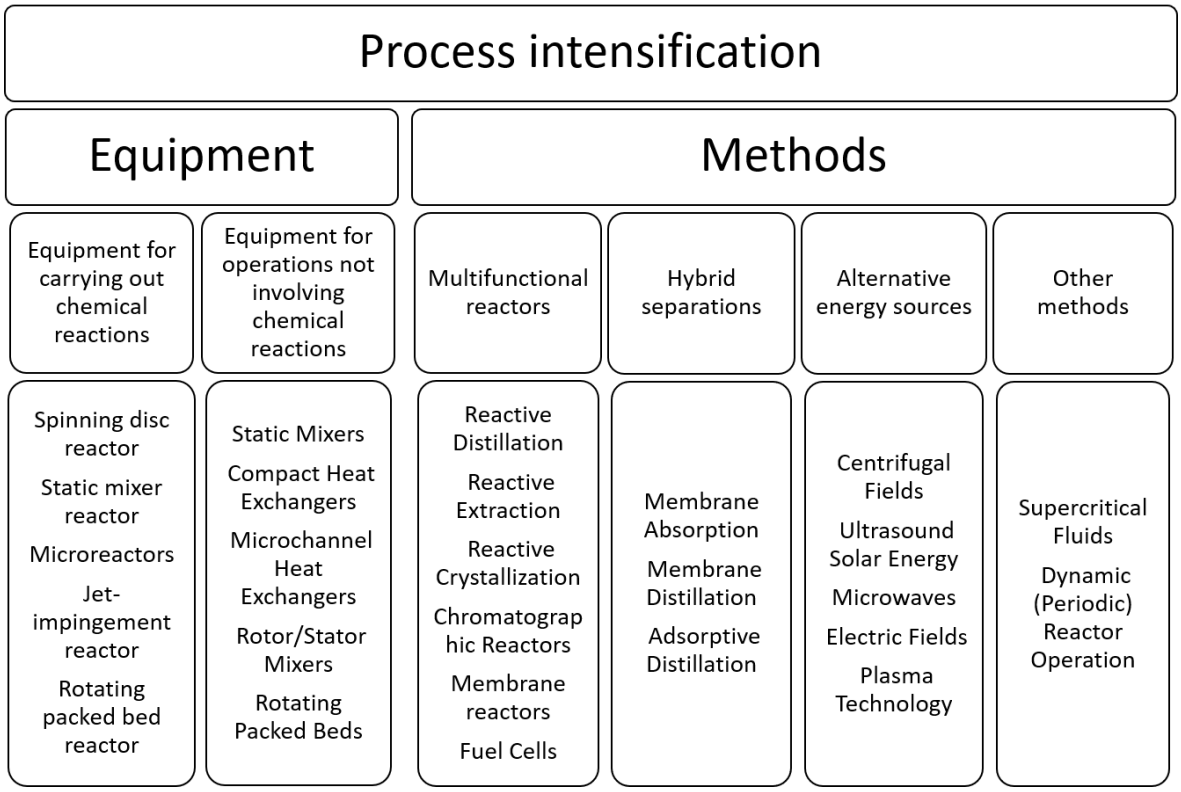

Figure 2-7: PI toolbox (Stankiewicz and Moulijn, 2000).

2.3.1. Process Intensification of solvent-antisolvent precipitation processes

Mullin (2001) described several industrial crystallisers including unstirred vessels, agitated vessels and fluidised beds. However, a lot of these experience issues such as large particle sizes, particle breakage and broad particle size distributions due to varying residence times within the crystallisers.

Numerous mixing devices have been studied for precipitation processes that provide intensified mixing with low mixing times. One way to achieve reduced mixing times is through impingement mixing. Confined impinging jet reactors (CIJR) have been widely used for the production of small particles with a narrow size distribution, particularly for the production of drug nanoparticles (Dong et al., 2011). Dong et al. (2010), carried out antisolvent precipitation in a static mixer, concluding that static mixing has a high potential for continuous and large-scale antisolvent precipitation within the pharmaceutical industry. Microchannel reactors have also been investigated for precipitation processes. The small

reactor channels offer high velocities and energy dissipations by reducing the diffusion length between the solvent and antisolvent (Zhao et al., 2007). Two known microreactor designs are the Y-shape mixer and the T-mixer. Kim (2006) investigated antisolvent precipitation in a T-mixer, they determined that a T-mixer generated high supersaturation with micromixing effects. Wong et al. (2004) demonstrated the micromixing effects of a T-mixer, concluding that mixing times are within the millisecond range. However, in comparison to high-gravity (Higee) technology the T-mixer is inferior when it comes to enhancing micromixing efficiency (Yang et al., 2015).

Oscillatory baffled reactors (OBR) are a type of process intensification equipment consisting of equally spaced out baffles in a cylindrical tube (Wang et al., 2017). Their ability to maintain plug flow and provide rapid mixing, as well as their ease in scalability make OBRs a popular choice for precipitation processes (Brown et al., 2014, Jiang and Ni, 2019). Lawton et al. (2009) carried out the continuous cooling crystallisation of an active pharmaceutical ingredient in an OBR and were able to reduce processing time from 9 hours and 40 minutes in a batch system to 12 minutes in the OBR. Although, studies involving cooling precipitation processes in the OBR are more common (Brown et al., 2014, Lawton et al., 2009, McGlone et al., 2015), a few antisolvent precipitation processes have also been carried out in the OBR (Brown et al., 2015, Brown and Ni, 2011).

High-gravity (Higee) process intensification technology has more recently been introduced to precipitation processes. The technology is essentially a rotating packed bed reactor (RPB) in which the centrifugal force creates a high gravity environment intensifying mixing, with enhanced heat and mass transfer properties (Kuang et al., 2015). High gravity reactive precipitation (HGRP) process involves precipitation through the chemical reaction route. Chen et al. (2004) successfully prepared nanodrugs through HGRP, identifying rotating speed, liquid flow rate and reactant concentration as key factors. High gravity antisolvent precipitation (HGAP) process combines the antisolvent precipitation method with the RPB. Zhao et al. (2009) prepared drug nanoparticles through the HGAP process, stating that the antisolvent precipitation is most promising of all methods, with low cost and time saving properties as well as ease for scale up. Kuang et al. (2015) investigated the production of another drug nanoparticle through the HGAP method, the effect of mixing and rotating speed on the size of particles and the particle size distribution were investigated. The results achieved showed a vast reduction in mean particle size, as well as enhanced product quality.

2.3.2. The Spinning Disc Reactor

Like rotating bed reactors, the spinning disc reactor is also a type of Higee equipment as the centrifugal force created by the reactor generates high gravity fields. The centrifugal force produced by the disc create high shear and instabilities within the liquid film, generating waves and ripples that intensify mixing and, heat and mass transfer rates (Cafiero et al., 2002). Along with increasing mixing and mass transfer rate, the disc also reduces the chances of agglomeration by providing a high surface area to volume ratio (Tai et al., 2008). Other advantages of SDRs include: ease of scale-up, low fluid residence times in comparison to stirred tanks, and small reactor hold up making it better suited to hazardous processes (Oxley et al., 2000). An illustrative sketch of the SDR is presented in Figure 2-8, showing the flow of liquid film on the disc (Reay et al., 2008).

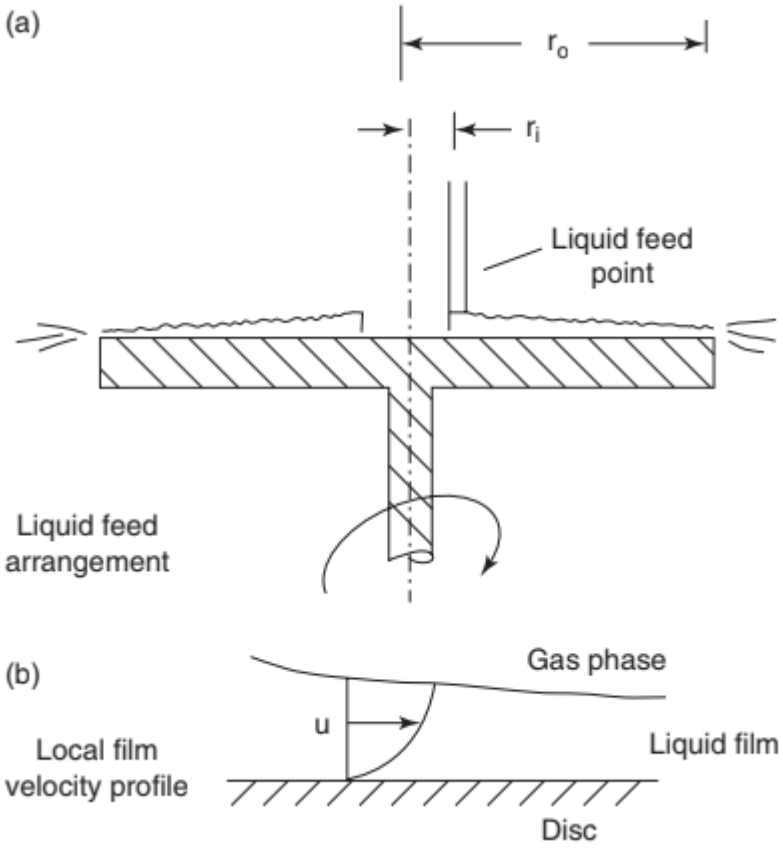

Figure 2-8: A) Sketch of SDR, B) Liquid film flow on disc (Reay et al., 2008).

A range of processes have been carried out in a spinning disc reactor, including polymerisation reactions (Boodhoo et al., 2006, Dobie et al., 2013), reactive precipitation (Cafiero et al., 2002, Mohammadi, 2014, Tai et al., 2007, Chin et al., 2008, Ahoba-Sam et al., 2018, D' Intino et al., 2014, Teychené and Biscans, 2008, de Caprariis et al., 2012, Dabir et al., 2015), acid-base neutralisation reactions (Ghiasy et al., 2013) and catalytic reactions (Oxley

et al., 2000, Vicevic et al., 2007). The thin liquid film generated on the surface of the disc can exhibit near plug flow characteristics, increasing the probability of homogenous axial mixing on the disc. Mohammadi and Boodhoo (2012) studied the conditions on the spinning disc reactor at which near plug flow behaviour is observed. The findings suggested that plug flow was more likely to be established at a higher degree of turbulence in the film created at increased disc speeds and liquid flow rate, lower liquid viscosities and with discs of a textured surface. This behaviour can be explained by increased surface waves resulting in uniform velocity and reduced radial dispersion as well as better transverse mixing across the film.

Reactive precipitation in the SDR has been studied on various occasions. Mohammadi (2014) studied the formation of TiO_2 precipitation in an SDR. Key findings suggested that high rotational speed, flow rate and a grooved disc surface were favoured for the formation of smaller sized nanoparticles with high yields. A comparison with a conventional stirred tank reactor indicated improved particle characteristics. Cafiero et al. (2002) carried out the precipitation of barium sulphate in an SDR. Initial supersaturation and disc rotational speed were amongst the conditions studied. They concluded that at a lower specific dissipation rate the number of crystals obtained were comparable to that of a T-mixer at the same initial supersaturation. Dehkordi and Vafaeimanesh (2009) as well as Jacobsen and Hinrichsen (2012) also precipitated barium sulphate in a spinning disc reactor, expanding on the findings of Cafiero et al. (2002) by studying the impact of parameters such as disc diameter, disc texture and feed location. Jacobsen and Hinrichsen (2012) found that increasing the number of feed location from one to multiple feed points decreased particle size.

Oxley et al. (2000) experimented with a few reactions in the SDR to assess its viability for commercial processing. Important amongst these was the antisolvent precipitation of an active pharmaceutical ingredient (API). The experiment faced issues with particle adhesion to the disc surface, which was corrected with PTFE coating, allowing the progression of the study. The process produced fine particle sizes and a very narrow particle size distribution. Although the particles produced were mainly of a small size, ranging from 1-15 µm, amongst these were also agglomerated and larger particles generally produced at higher rotational speeds. The authors found, that at high rotational speeds the PTFE coating affected the wettability of the disc, creating instabilities which caused the liquid film to break down into

rivulets. Consequently, the poor mixing resulted in the production of agglomerated particles. In addition to exploring disc rotational speed, other parameters reportedly studied were temperature, feed rate and solvent-antisolvent ratio. However, there is no further mention of the effect of these variables on the precipitation process.

Khan and Rathod (2014) studied the solvent-antisolvent precipitation of curcumin nanoparticles in the spinning disc reactor, in contrast to the conventional semi-batch process. Parameters studied included flow rate, antisolvent to solvent ratio, disc rotational speed and solute concentration. For each of these parameters, the effect on the particle size distribution was determined and based on this the conclusions drawn suggested: high antisolvent flow rate, increased ratio of antisolvent in feed, high disc rotational speed and a grooved disc with a large diameter produced smaller particles. However, the authors have only focused on the size of the particles produced, and not the actual kinetics of the antisolvent precipitation process on the SDR, which indicates a gap for further research.

2.3.2.1. *Hydrodynamics of the Spinning Disc Reactor*

Figure 2-9 shows a schematic diagram of an SDR. The liquid fed at the centre of the rotating disc flows outwardly towards the periphery as a continuous film. As the disc rotates at high speeds, the liquid is subjected to the centrifugal force that stretches and distorts the film, creating an extremely thin and unstable film, generally around 50 microns for water (Reay et al., 2008).

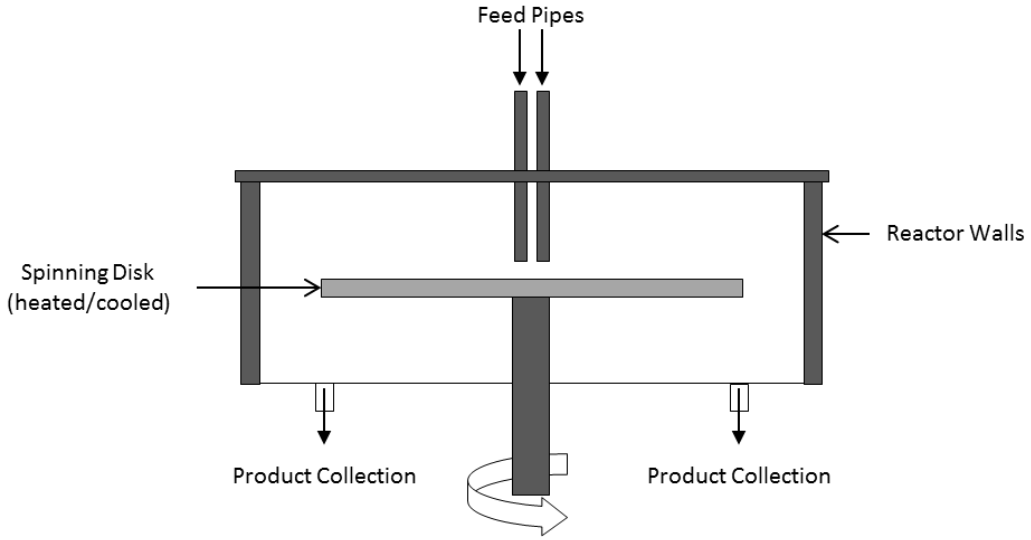

Figure 2-9: A schematic diagram of a spinning disc reactor.

The performance of the SDR is highly dependent on the hydrodynamics of the liquid film it generates. The flow of thin liquid films can be described by the Navier-Stokes equations,

however, as it may be difficult to handle the full set of Navier-Stokes equations, a simplified model based on the Nusselt (1916) theory for flow of a condensate film may be considered for the characterisation of the liquid film in an SDR (Reay et al., 2008). Assuming no shear at the gas-liquid interface, wave free film and no-slip condition at the disc-liquid interface, the average film velocity, u_{av} is expressed as:

$$u_{av} = \left[\frac{Q^2\omega^2}{12\pi^2\nu r}\right]^{1/3} \tag{2-12}$$

where Q is volumetric flow rate, ω the angular velocity, and ν is the kinematic viscosity of the liquid, respectively.

The film thickness is expressed as (Boodhoo, 2013):

$$\delta = \left[\frac{3Q\nu}{2\pi\omega^2 r^2}\right]^{1/3} \tag{2-13}$$

Further manipulation of the above equations leads to the equation for the residence time on the disc, t_{res}:

$$t_{res} = \frac{3}{4}\left(\frac{12\pi^2\nu}{Q^2\omega^2}\right)^{1/3}\left(r_0^{4/3} - r_i^{4/3}\right) \tag{2-14}$$

where r_o is the outer disc radius and r_i is the inner disc radius.

Since many assumptions have to be made in order to apply the Nusselt theory to the spinning disc, the Nusselt theory is not the most accurate model. Burns et al. (2003) compared the film thickness experimentally obtained with that obtained using the Nusselt model. The technique to obtain film thickness involved measuring electrical resistance between two electrodes placed at a distance on the disc surface and relating the measured resistance with film height. The authors found that the experimentally determined film thickness was not consistent with that predicted by the Nusselt model, with the Nusselt model becoming more relevant after a 'spin-up' zone. Further experiments conducted involved using liquids of different viscosity to determine the effect of viscous and inertial forces on film thickness and its deviation from the Nusselt model, expressed through the Eckman number, *Ek*. A plot of Eckman number against the ratio of measured film thickness to Nusselt film thickness showed that at high *Ek* values the measured film thickness was

close to the predicted Nusselt film thickness, whereas at lower values of *Ek*, the measured film thickness deviated significantly from the Nusselt film thickness. In conclusion, the average film thickness obtained experimentally was lower than the predicted Nusselt film thickness.

On the contrary, Espig and Hoyle (1965) measured the maximum liquid film thickness on a rotating disc to be 40% larger than the Nusselt model prediction, explaining the difference a result of waves being present on the disc which are not considered in the Nusselt model.

The extremely unstable liquid film flowing on the disc surface develops to generate a series of ripples and waves of a chaotic nature. Plenty of studies have been carried out to investigate flow instabilities and flow regimes. One such study was carried out by Thomas et al. (1991). The authors conducted a photographic study for flow visualisation on a spinning disc, establishing the existence of two flow regimes: wavy-laminar and radial-wave. At lower rotational speeds, the wavy laminar flow occurred, which transitioned into the radial-wave flow regime as the rotational speed increased. As the flow evolved from wavy-laminar to radial-wave, V-shaped waves were observed between the two regimes. Charwat et al. (1972) investigated the waves on a spinning disc at various flow rates and rotational speeds. The authors identified four different wave forms on the disc. Initially, a smooth film flow was observed at the lower flow rate and disc speed. As disc speed and flow rate increased, waves began appearing on the surface of the disc. Concentric waves were seen near the centre of the disc and decayed towards the edge. These waves occurred as the stream coming out of the nozzle entrained the surrounding air and according to the authors the waves were not due to surface instabilities. A decrease in flow rate and an increase in disc rotational speed led to the formation of spiral waves at a radius away from the centre of the disc, eventually decaying close to the edge. A further increase in flow rate and rotational speed gave rise to extreme instability, causing spiral waves to break up into wavelets. The findings were in agreement with the work of Woods (1995), who carried out a study of flow of thin liquid films over a rotating disc.

A more recent study was conducted by Ozar et al. (2003) using a collar to generate the flow as opposed to the impinging jet used in previous studies. Visualisation experiments and film thickness measurements were conducted at a variety of liquid flow rates and rotational speeds. As the discs rotational speed increased, the initial wavy-laminar flow transitioned to spiral-wavy flow. The film thickness was measured upstream and downstream of the

hydraulic jump which showed a trend of an increase, followed by a decrease depending on the position on the disc. The authors revealed that the liquid film was affected by three forces, namely: frictional, inertial and centrifugal. Near the centre of the disc, inertial and frictional forces dominated, and the centrifugal force was dominant near the edge of the disc. In between was the transition region where all three forces prevailed. The study concluded that an increase in Reynolds number caused the inertial forces to dominate, shifting the maximum film thickness towards the edge of the disc. On the other hand, an increase in rotational speed caused the centrifugal forces to dominate, shifting maximum film thickness towards the inlet. The observations and results achieved by the authors in this study were in accordance with the conclusions made by Thomas et al. (1991) for maximum film thickness.

The onset of wave formation can be defined in terms of Reynolds number:

$$Re = \frac{2Q}{\pi \nu r} \tag{2-15}$$

The Reynolds criteria at which flow transition from laminar to turbulent occurs is defined as the following (Boodhoo, 1999):

$Re < 16$: smooth laminar flow

$16 \leq Re < 40$: small amplitude waves

$40 \leq Re < 80$: sinusoidal waves replaced by regular waves

$80 \leq Re < 1000 - 2000$: wavy-laminar flow

$Re \geq 1000 - 2000$: turbulent flow regime

Charwat et al. (1972) studied the nature of waves in a rotating disc as well as the effect of liquid physical properties on film flow. The authors found that surface tension and viscosity affect the formation of waves, where an increase in viscosity alters the critical Reynolds number so that the rate of wave formation is reduced. On the contrary, Leneweit et al. (1999) questioned the generation of waves, presuming perturbations were a result of 'entrance effects'. The instabilities at various input flow rates, nozzle diameters and inlet heights were examined at different flow rates.

Aoune and Ramshaw (1999) carried out a heat and mass transfer test in a spinning disc reactor to determine the effect of instabilities and ripples on transfer rates. The absorption

of oxygen into thin films of water and a viscous solution of propylene glycol were analysed, using the Nusselt theory for heat transfer predictions and the Higbie model for mass transfer predictions. The results showed discrepancies between the experimental data and the predicted data, especially in the case of mass transfer coefficients which were hugely underestimated by the Higbie model, as the presence of waves were neglected. However, the Nusselt model was in better agreement with the experimental data for the viscous solution. The study concluded that the spinning disc provided an intense mixing environment caused by wave formation, highlighting the need for better predictive models for thin liquid films that also account for instabilities within the film.

The Nusselt model, and thus Equations 2-12 to 2-14 are valid only if Coriolis forces are negligible. Coriolis forces comes into play when the radial velocity term, v_r is of a considerable magnitude. This generates acceleration in the angular direction opposite to rotation, known as Coriolis acceleration, and is defined as (Boodhoo, 2013):

$$a_{Cor} = 2v_r\omega \tag{2-16}$$

When centrifugal acceleration dominates, Coriolis acceleration is considered to be negligible. This is true when the following condition is satisfied (Emslie et al., 1958):

$$\nu \gg \omega\delta^2$$

This is particularly true for high viscosity liquids and distances away from the centre of the disc where film thickness is at a minimum (Boodhoo, 1999). Ghiasy et al. (2012) carried out visual analysis of flow in an SDR under centrifugal and Coriolis regimes, concluding that increased disc speeds reduced Coriolis effects as radial mixing is reduced. In addition, at greater viscosities, Coriolis effects disappeared.

2.3.3. Mixing

Like many process intensification technologies, enhanced mixing is a fundamental characteristic of the spinning disc reactor. Mixing introduces uniformity in a mixture with the aim to either reduce temperature gradients, concentration gradients or viscosity gradients. In the case of antisolvent precipitation reducing non-homogeneity amongst the solvents and eliminating stagnant zones is the key focus. Mersmann (1999) states the importance of mixing in the precipitation of sparingly soluble solutes, as low micromixing times assist in generating maximum supersaturation in a short time. For this reason, the role and significance of mixing in the SDR as well as in precipitation processes have been explored.

Mixing is affected by the amount of energy put into a system in the form of mechanical energy, as an increase in this energy increases the turbulent kinetic energy dissipation rate. The turbulent energy dissipation rate has an impact on the mixing time and length scales and hence the mixing mechanism. Generally, an increase in turbulent energy results in the breakdown of larger eddies into smaller eddies and eventually to those at the molecular scale. This introduces homogeneity and enhances the rate of heat and mass transfer. There are three levels of mixing: macromixing, mesomixing and micromixing (Boodhoo and Harvey, 2013). These mixing mechanisms are summarised in Figure 2-10.

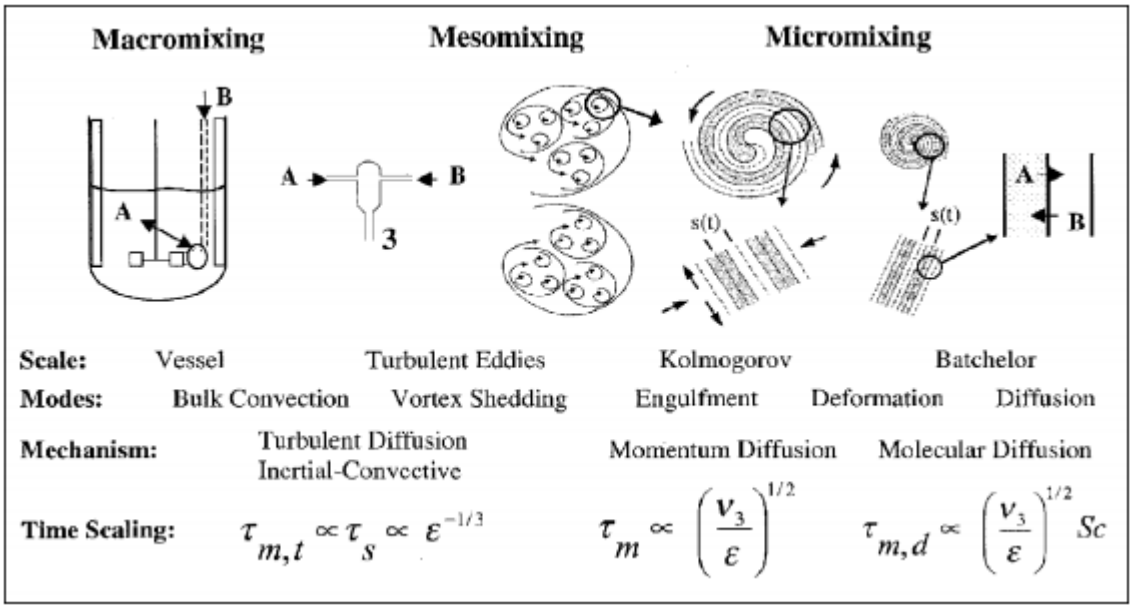

Figure 2-10: Mixing mechanisms (Johnson and Prud'homme, 2003).

Macromixing is the process of large-scale mixing at reactor scale, involving bulk or convective movement of the liquid. In a continuous system, the residence time distribution (RTD) is affected by the process of macromixing. RTD is defined as the time spent by species in a reactor, displayed as a distribution, as all entities spend a distinctive time in the reactor. Macromixing can be described through mean circulation time, τ_c, in a stirred tank reactor of volume, *V*, and volumetric flow rate leaving the impeller blades, Q_c:

$$\tau_c = \frac{V}{Q_c} \tag{2-17}$$

Mesomixing is the intermediate level of mixing characterised by turbulent dispersion and inertial convection mechanisms. The first involves the early dispersion of a feed plume into its surrounding liquid, with a time scale equivalent to that of the feed pipe diameter. The second mechanism concerns the inertial-convective decay of large turbulent eddies into

smaller eddies, analogous to energy dissipation from larger eddies to smaller eddies, eventually being transformed into internal energy. The turbulent dispersion time scale, τ_D, is given by Eq. 2-18 and is dependent on the pipe radius, r_{pipe}.

$$\tau_D = \frac{Q_f}{uD_{turb}} \quad (if\ r_{pipe} \ll L_D) \tag{2-18}$$

$$\tau_D = \frac{{r_{pipe}}^2}{D_{turb}} \quad (if\ r_{pipe} \approx L_D\ or\ r_{pipe} > L_D)$$

where, $D_{turb} = 0.12\varepsilon^{1/3}{L_D}^{4/3}$ and L_D is the length scale for dispersion

The inertial-convective time scale is expressed as:

$$\tau_S = A\left(\frac{L_C}{\varepsilon}\right)^{1/3} \tag{2-19}$$

where, A is a constant dependent on the turbulence level of the system, L_C is the inertial-convective mesomixing length scale and ε is the turbulent energy dissipation rate.

The smallest scale of mixing is known as micromixing where, unlike the other two scales, mixing takes place at the molecular level. At this level, the fluids are completely homogenised with no segregated zones. It is often referred to as the Kolmogorov scale or the Batchelor scale. The fluid elements are subject to engulfment, deformation and diffusion during the micromixing process. Chemical processes such as precipitation are dependent on interactions between molecules. These interactions are made possible through the molecular diffusion which occurs during micromixing. Micromixing time scales are estimated through expressions given in Equation 2-20 and 2-21. Equation 2-20 represents the time scale due to engulfment and can be used up until values of $Sc \approx 10^3$, beyond that $\tau_{Ds} > \tau_e$, and micromixing is governed through the process of shear deformation and diffusion (Eq. 2-21 (Boodhoo, 2013).

$$\tau_e = 17.2\left(\frac{\nu}{\varepsilon}\right)^{0.5} \tag{2-20}$$

$$\tau_{Ds} \approx 2\left(\frac{\nu}{\varepsilon}\right)^{0.5} arcsinh\ (0.5\ Sc) \tag{2-21}$$

where, Sc is the Schmidt number, $Sc = \nu/D$, and D is diffusivity

Chen et al. (2006) studied the characteristics of micromixing in an RPB, whilst comparing it to the SDR. The authors concluded that the SDR could provide better micromixing at lower liquid flow rates, since the liquid was being equally distributed on the disc surface, achieving thinner liquid films and hence better mixing at the micro-level. At low liquid flow rates, the packing was not completely wet in the RPB and so micromixing was not as effective. However, as the liquid flow rate increased, efficiency of micromixing in the SDR decreased and increased in the RPB. Similarly, at low liquid flow rates the SDR produced smaller particles through reactive precipitation but as liquid flow rate increased, the particle sizes increased. Chen et al. (2006) concluded the SDR is more suitable for low liquid flow rates and the RPB is more suitable for high liquid flow rates. This conclusion is in line with the more recent findings of Boodhoo and Al-Hengari (2012).

Jacobsen and Hinrichsen (2012) summarised the benefits of an SDR for the production of barium sulphate via reactive precipitation. By controlling the disc speed, the authors were able to control the degree of micromixing. A decrease in particle size and a narrower distribution was obtained with increased micromixing. The authors concluded that, for the processes studied, the SDR was able to provide high micromixing efficiency as well as the resistance to fouling.

To a large extent, antisolvent precipitation depends on micromixing between the solvent/solute and the antisolvent, as insufficient mixing could lead to zones of high local supersaturation, producing a broad particle size distribution. Takiyama et al. (1998) stated that antisolvent precipitation is highly dependent on mixing and may lead to agglomeration if the system is not adequately mixed. To characterise the relationship between mixing and precipitation, the dimensionless Damköhler number, *Da,* is used. It is defined as the ratio between mixing time and induction time (Equation 2-22). For nucleation to be the dominating process, *Da* must be less than 1. This would denote rapid supersaturation and uniform micromixing, producing smaller particles with narrower size distributions.

$$Da = t_{micro}/t_{ind} \tag{2-22}$$

2.4. Summary

Solvent-antisolvent precipitation involves the addition of a second solvent, the antisolvent, to reduce solubility and generate supersaturation. Supersaturation drives the precipitation process, governing both nucleation and particle growth. Solvent-antisolvent precipitation is

also affected by operating conditions such as agitation rate, flow rate, antisolvent to solvent ratio and the solute concentration. Furthermore, enhanced micromixing is required between the solvent and the antisolvent to establish mixing in the molecular level and reduce local supersaturation. These conditions affect the morphology, size and size distribution of the particles obtained.

For the selected starch nanoparticles system, previous solvent-antisolvent precipitation studies have been carried out at limited flow rates and solute concentrations to avoid agglomeration in the semi-batch systems, where mixing is insufficient. Continuous flow systems have not been studied for the solvent-antisolvent precipitation of starch nanoparticles.

There is evidence suggesting the SDR is capable of generating intensified micromixing through the thin films created on the surface of the disc. This creates potential for better mixing between the solvent and antisolvent for the precipitation of starch nanoparticles. Additionally, plug flow is generated at high disc speeds and flow rates, resulting in uniform velocity and reduced radial dispersion on the disc. Residence times on the disc are also low, hence limiting growth of particles on the disc. Finally, solvent-antisolvent precipitation studies in the SDR are limited, and do not cover precipitation kinetics, hence representing a substantial gap within literature.

Chapter 3. Experimental set-up and procedures

This chapter presents the equipment and methodology employed to conduct the present research project.

3.1. Spinning disc reactor (SDR) set-up and procedure

A schematic diagram of the experimental set-up is given in Figure 3-1. The set-up consists of a number of components, details of which are presented further within this section.

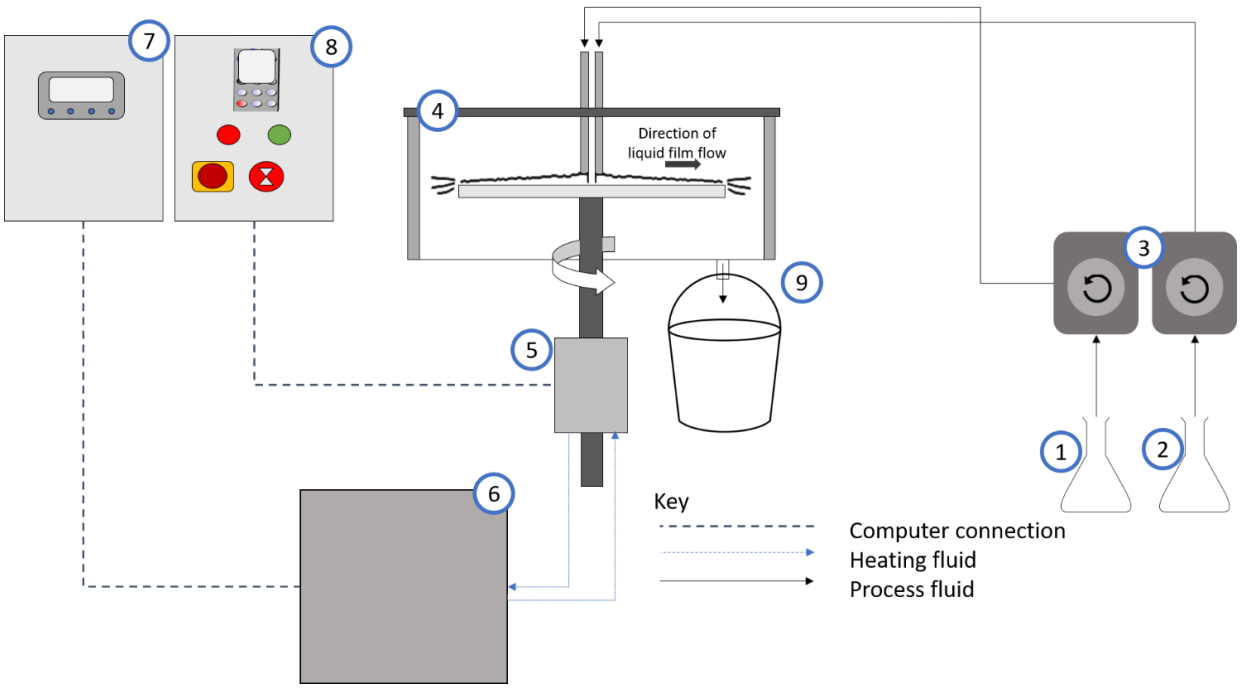

Figure 3-1: Schematic of experimental set-up for SDR. 1) solute/ solvent feed 2) antisolvent feed 3) peristaltic pumps 4) SDR 5) motor 6) heating tank 7) temperature control unit 8) SDR rotational control unit 9) product outlet and receiver.

Figure 3-2 shows a schematic diagram of the spinning disc reactor used in this research. The reactor consists of a 30 cm diameter stainless steel disc (grooved or smooth) encased in a reactor housing which contains the flow of liquid exiting from the edge of the spinning disc. The temperature on the surface of the disc is regulated through water circulation underneath the disc at a maintained temperature of 25 °C. The water is held in a tank equipped with thermocouples. The temperature of the water is controlled and monitored by a temperature control unit. When operational, the disc is covered with a lid and secured with bolts. Samples are received from a product collector at the bottom of the reactor. An image of the rig, showing the SDR, heating tank and the sample collector is presented in Figure 3-3.

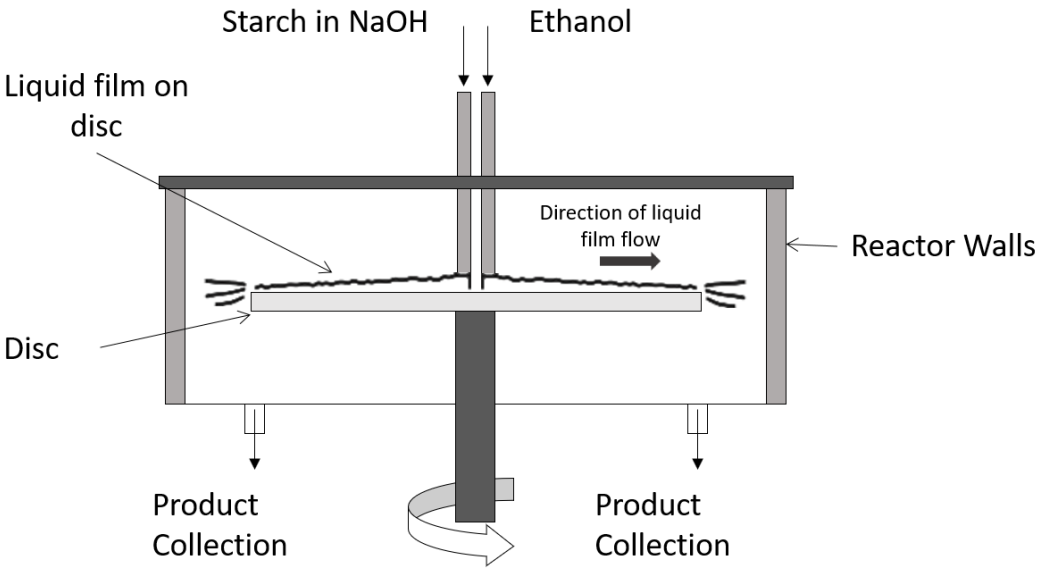

Figure 3-2: Schematic diagram of the spinning disc reactor.

Figure 3-3: SDR set-up.

The rotational speed of the disc is adjusted using the control unit shown in Figure 3-4. A calibration graph to relate frequency (Hz) with revolutions per minute (rpm) is given in Figure 3-5.

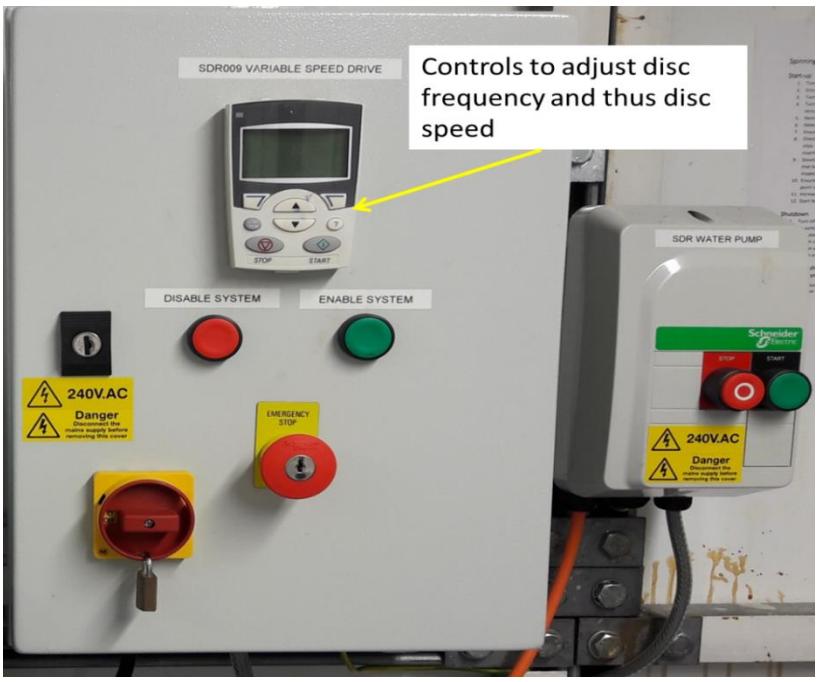

Figure 3-4: SDR control unit.

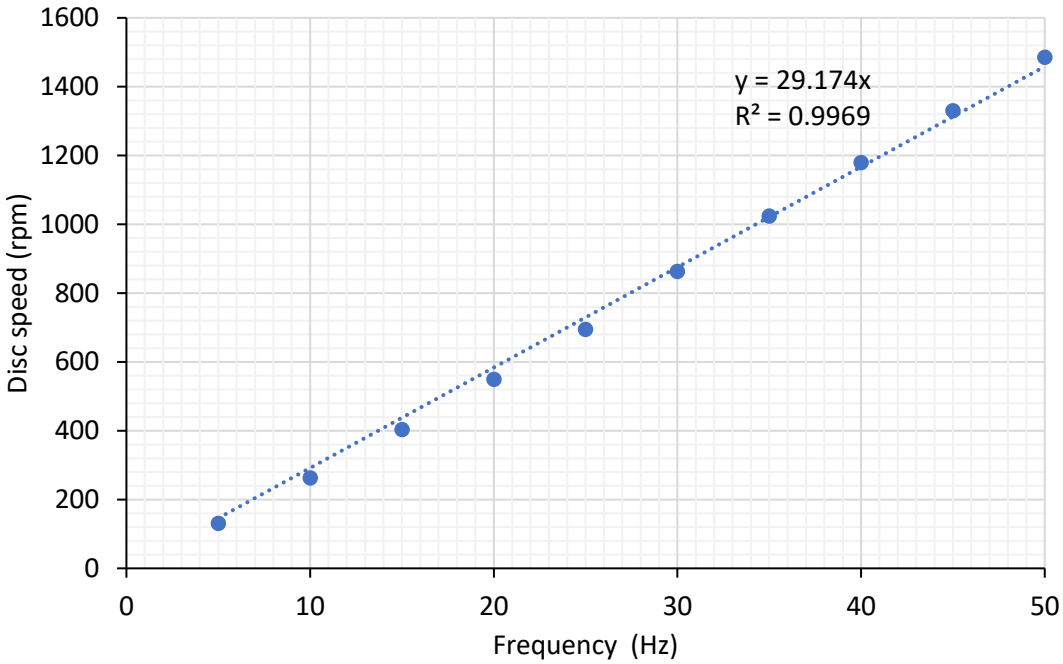

Figure 3-5: SDR calibration graph for disc speed.

3.1.1. Peristaltic pumps

The flow rates of the individual starch/NaOH and ethanol feed streams to the disc were provided by Watson Marlow 323E and Watson Marlow 505S peristaltic pumps, respectively, which fed the solvent and antisolvent to single point feed distributors situated 2.3 cm above the centre of the disc. Tubing compatible with the materials were used. Silicone tubing of

8 mm internal diameter (i.d.) was used to transport the ethanol, and Marprene tubing with 4.8 mm internal diameter was used for the starch/sodium hydroxide solution. Pulse dampeners were connected between the pump and disc feed inlet to reduce pulsation. The calibration graphs obtained are given in Figure 3-6 for ethanol and Figure 3-7 for starch/sodium hydroxide. The measurements were repeated 4 times to obtain the flow rate at each pump setting. The standard error bars are presented in the calibration graphs.

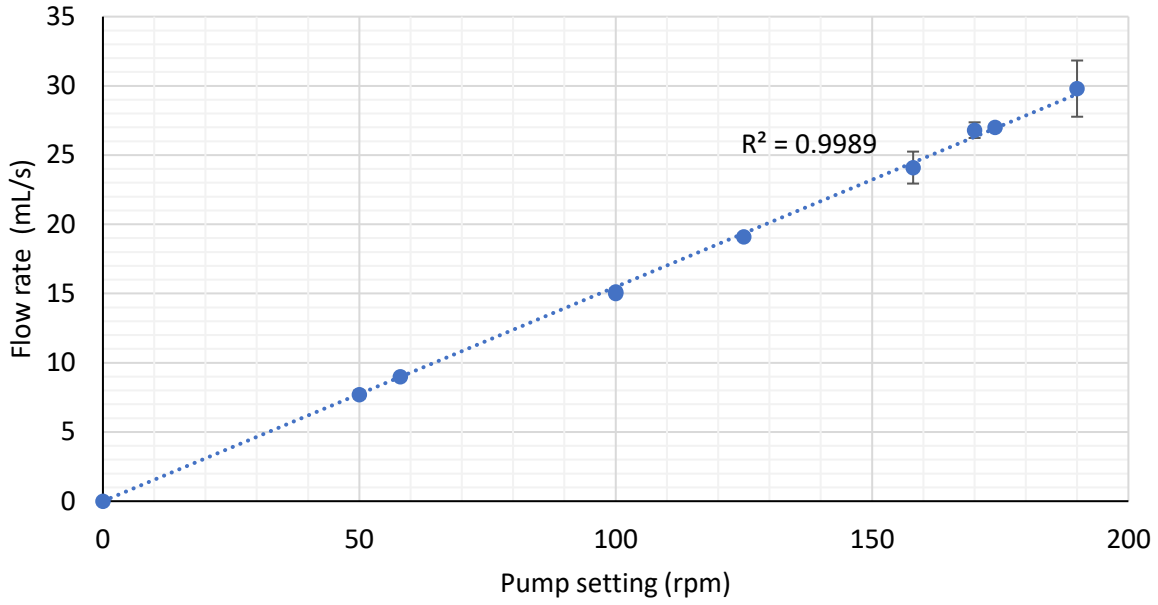

Figure 3-6: Pump calibration for ethanol with 8 mm i.d silicone tubing.

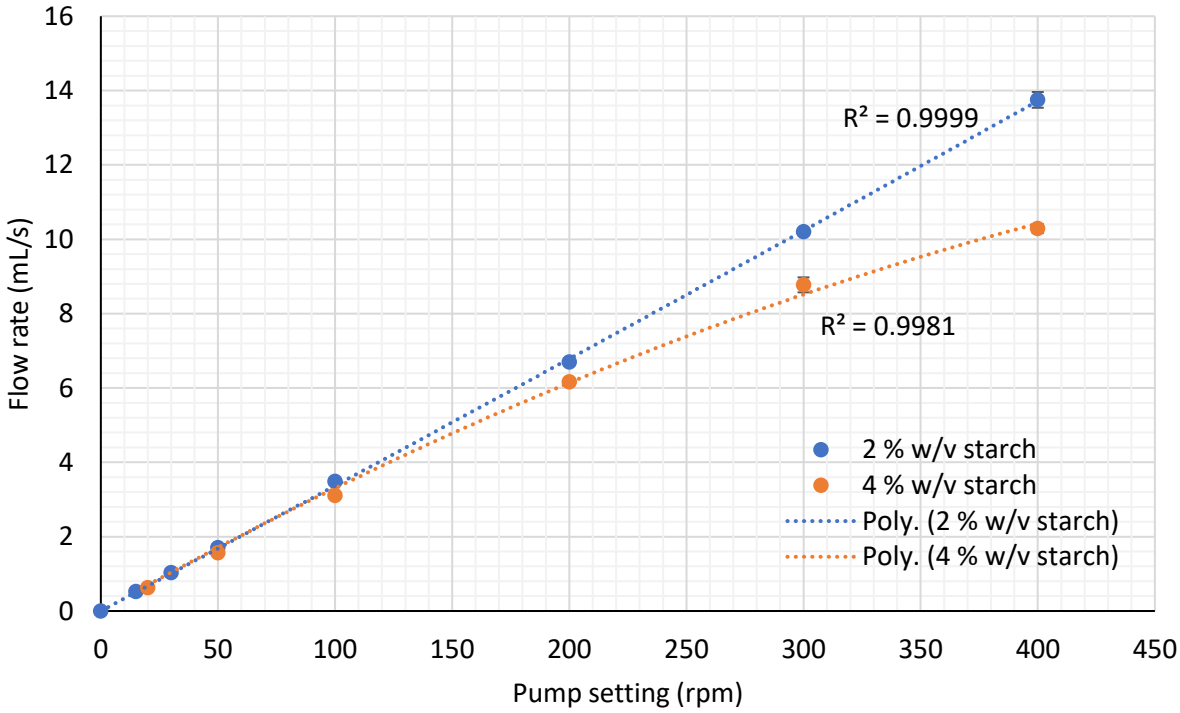

Figure 3-7: Pump calibration for starch/NaOH solution with 4.8 mm i.d Marprene tubing.

3.1.2. Liquid feed distributor

The liquids are supplied to the surface of the spinning disc through a liquid feed distributor (Figure 3-8). The distributor consists of two stainless steel tubes; one to deliver the solute/solvent mixture and the other to deliver the antisolvent. The internal diameter of each tube is 1.5 mm.

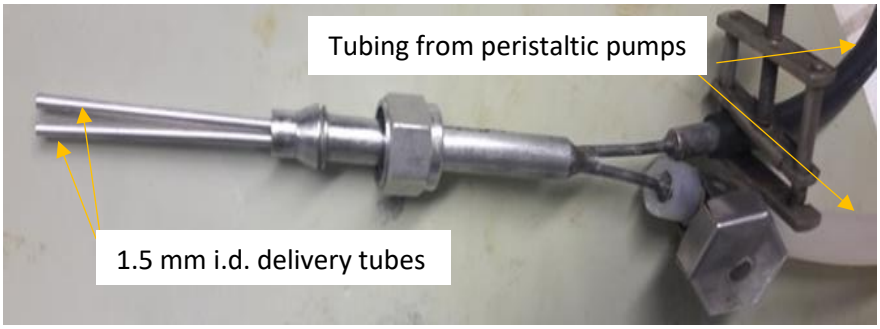

Figure 3-8: Liquid feed distributor.

3.1.3. Methodology

A full factorial design for experiments at 2 % w/v starch in the SDR, consisting of 3 factors and 3 levels was created using the operating conditions given in Table 3-1. The values for total flow rate and antisolvent to solvent ratio were selected based on the minimum and maximum allowed flow rate for each pump from the calibration data (Figures 3-6 and 3-7). Although lower flow rates were achievable, it was important to consider the effect of pulsation at lower pump speeds. Repeat runs were included to test the validity of the experiments. The design of experiments including the Individual flow rates of the solvent and antisolvent streams are given in Appendix A.

Table 3-1: Operating conditions for SDR experiments.

Factor	Low	Centre	High
Disc rotational speed (rpm)	400	800	1200
Total flow rate (mL/s)	6	12	18
Antisolvent to solvent ratio (vol/vol basis)	1:1	5:1	9:1

The reagents, sodium hydroxide in pellet form and 99.8 % absolute ethanol were purchased from Fisher Scientific, UK. Corn starch was purchased from Sigma Aldrich. To form a 2 % w/v starch solution, 16 g starch was dissolved in 800 mL of 0.5 M sodium hydroxide solution. This was changed accordingly to make the 4 % w/v solution. A 20 % w/w concentration (based on starch weight) of Tween 80 was added to the starch solution to act as the surfactant in order

to prevent agglomeration of starch. The solutions were prepared at a temperature of 25 °C and were monitored and controlled using a hot plate during the runs. To prevent vaporisation of the solvent the vessel was kept covered at all times. The solvent and antisolvent were delivered to the disc with the aid of the peristaltic pumps. The temperature of the disc was controlled by pumping water at 25 °C to the disc. The disc was run for 60 seconds. A sample was first collected after 20 s of running the feed to the disc, which allowed time for the disc to equilibrate. Further samples were taken at 40 s and then at 60 s from the start of the runs. Once collected, the samples were quenched in deionised (DI) water to halt the precipitation process.

Experiments were conducted on a stainless-steel grooved disc with 8 concentric grooves and repeated on a stainless-steel smooth disc as shown in Figure 3-9.

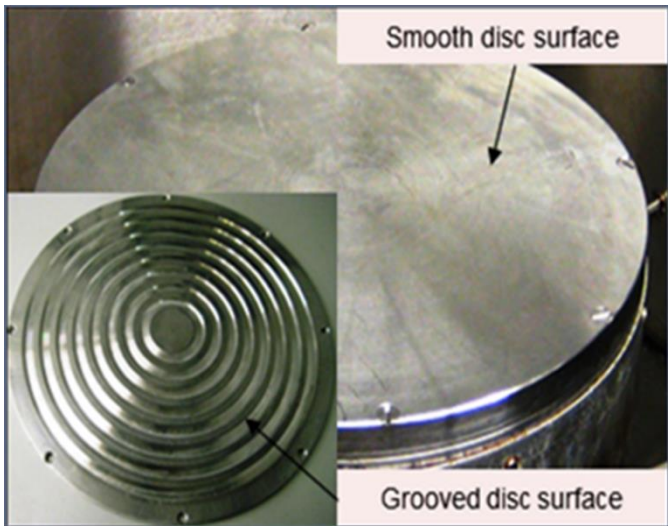

Figure 3-9: The grooved and smooth disc surfaces used in SDR experiments.

3.2. Semi-batch reactor (SBR) set-up and procedure

For benchmarking experiments in the semi-batch reactor, a reactor vessel of 6.6 cm diameter and a marine propeller impeller of 3.5 cm diameter was used, as shown in Figure 3-10. The temperature was maintained at 25 °C by circulating water through the jacketed reactor vessel. 100 mL solutions of 1 % w/v and 2 % w/v starch in 0.5 M sodium hydroxide solution were prepared and a total of 100 mL ethanol antisolvent was added to the starch solution at flow rates of 1 mL/s and 12 mL/s. Samples from the vessel were collected immediately after the ethanol had been added. The particles remained in suspension under continuous agitation and samples were collected through tubing immersed into the liquid,

with the other end connected to a syringe pump set to withdraw samples. The samples collected were then quenched in DI water to prevent further precipitation.

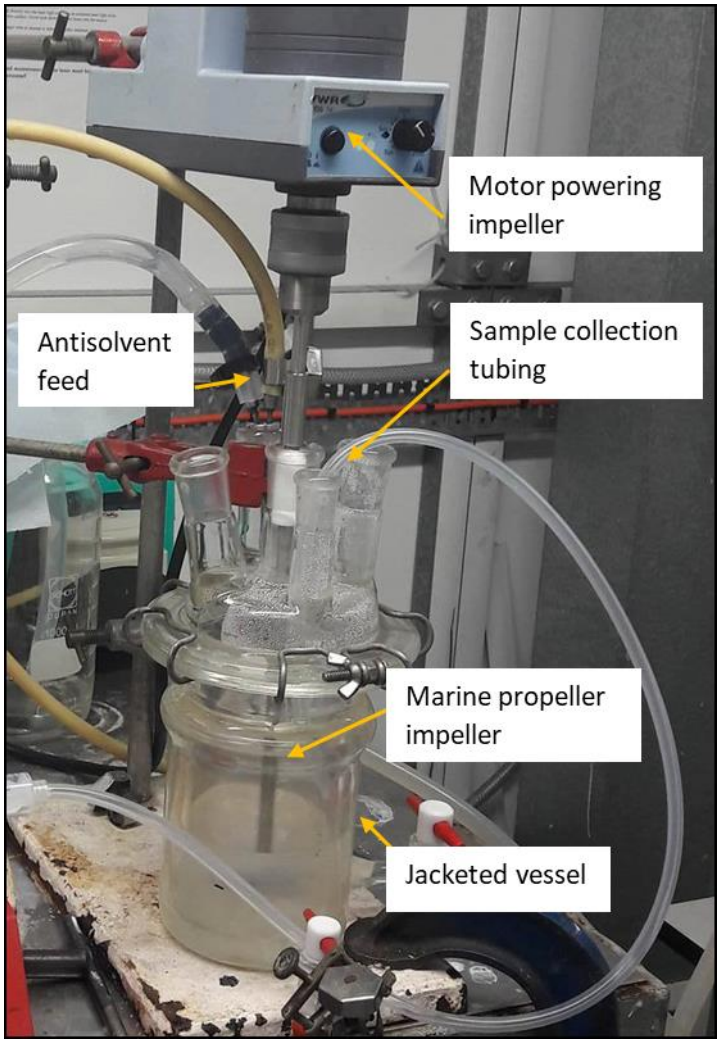

Figure 3-10: Semi-batch set-up.

3.3. Particle characterisation techniques

Samples of starch nanoparticles from the disc were analysed using Dynamic Light Scattering (DLS - Mode Nano ZS Malvern instruments, UK) technology to obtain particle size and size distributions. The size measurements were all carried out at 25 °C. Each sample measurement was performed in triplicates, with the average of the size distribution measurements and the mean peak sizes being reported for the primary peak. Although in many cases a smaller second peak corresponding to agglomeration is present, the focus here is on the first peak for analysing the size of the particles, and for this reason the agglomeration peak will be ignored in analysing the results, unless specified. A typical PSD showing both peaks is shown in Figure 3-11. The width of the size distribution is represented

by a Polydispersity Index (PdI) value. Again, this has been calculated for the single peak of interest, and not for the entire distribution, unless specifically indicated.

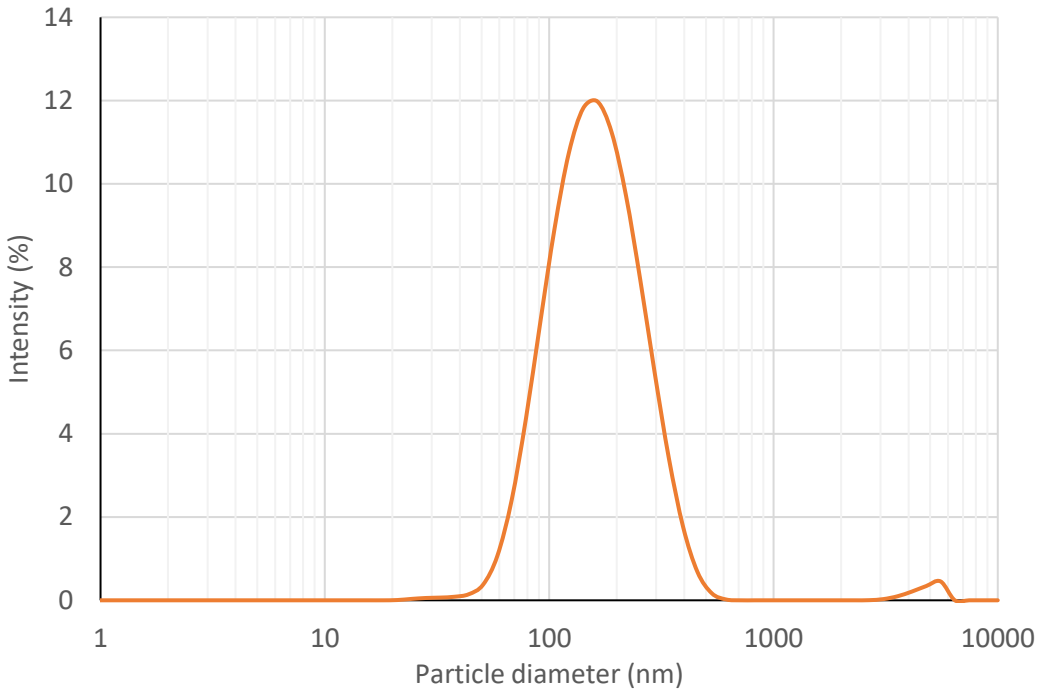

Figure 3-11: Overall PSD showing the primary peak and an agglomeration peak.

Transmission electron microscopy (Philips CM100 100kV TEM, FEI) of the samples was also performed for a realistic quantification of the actual particle size as well as for studying the morphology and the presence of any agglomeration amongst the nanoparticles. Images were taken with an Optronics AMT40 CCD camera, 1824x1824 pixel (Deben UK) using 400 mesh copper grids (Gilder Grids UK) with negative staining.

To estimate particle yield, a small volume of the sample, roughly 14 mL was collected 30 s into the run. The sample was then subjected to centrifugation at 1000 rpm for 2 minutes to separate and remove the supernatant. This was repeated 5 times and washed with ethanol to remove the NaOH and water in between centrifuging. The particles were then left to dry under vacuum at 35 °C. The particles were weighed to estimate yield using Equation 3-1. An example calculation for yield is given in Appendix B, and yield has been reported as an average of three samples. Particle count was obtained through a similar method. To obtain the number of particles per mL, the average size of a particle was taken from the TEM measurements and together with starch density, the mass of a single particle was estimated. Equation 3-2 was then applied to estimate particle count. Again, a sample calculation is included in Appendix B.

$$Yield\ (\%)\ =\ \frac{Mass\ of\ dried\ product}{Mass\ of\ starch\ in\ original\ solution} \times 100 \qquad (3\text{-}1)$$

$$Particle\ count\ (no./mL)\ =\ \frac{Mass\ of\ dried\ product}{Mass\ of\ single\ particle} \qquad (3\text{-}2)$$

3.4. Solubility measurement

Mixtures of 0.5 M NaOH and ethanol were created at concentrations ranging from 0.05 g ethanol/g NaOH to 5 g ethanol/g NaOH. An excess amount of starch was added to each sample and left for 24 hours to dissolve under constant stirring at 25 °C. A Buchner funnel attached to a vacuum pump was used to separate the undissolved starch. The arrangement for solubility experiments is shown in Figure 3-12. Grade 542 Whatman® quantitative filter paper placed in the funnel retained the starch, which was then subjected to drying in a vacuum oven at 35 °C. The mass of the starch was measured every hour until the mass remained at a constant value. The experiments were repeated twice to obtain an average solubility value. The solubility was calculated by means of Equation 3-3. A sample calculation is given in Appendix B, with results presented in Appendix C.

$$Solubility\ (g\ starch/g\ NaOH) = \frac{Initial\ mass\ of starch\ (g) - Mass\ of\ starch\ retained\ (g)}{Mass\ of\ 0.5\ M\ NaOH\ solution\ (g)} \qquad (3\text{-}3)$$

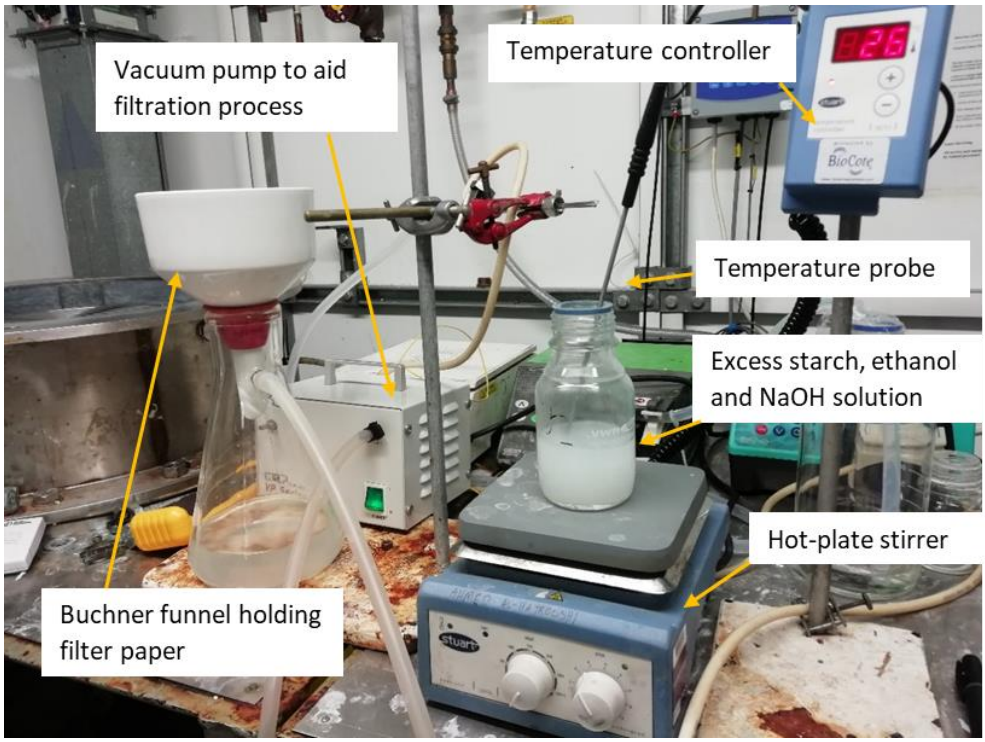

Figure 3-12: Set-up for solubility experiments.

3.5. High speed camera visualisation measurements for nucleation rate determination

Induction time in the SDR has been estimated through visualisation experiments. Photron SA5 high speed camera system (Frame rate 2000 fps, shutter speed 1/30 s) focused towards the surface of the disc was used to capture and locate the first appearance of the particles. A schematic showing the set-up for the camera is shown in Figure 3-13. A spotlight was also used, focusing on the disc surface to adjust brightness and increase the quality of the images. The captured image was analysed to estimate the radial distance of these particles from the centre of the disc. This distance was then used in an altered version of the residence time equation to estimate the induction time (Equation 3-4).

$$t_{ind,SDR} = \frac{3}{4}\left(\frac{12\pi^2\nu}{\omega^2 Q^2}\right)^{1/3}\left(r_{ind}^{4/3} - r_i^{4/3}\right) \quad (3\text{-}4)$$

where t_{ind} is the induction time, and r_{ind} is the radial distance from the centre at which nucleation becomes apparent.

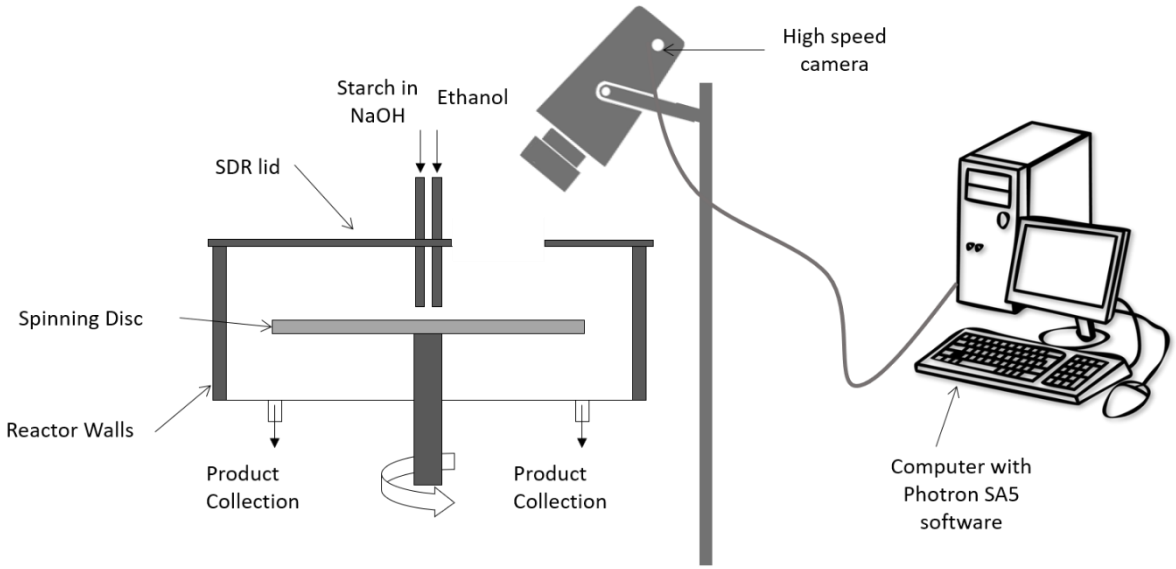

Figure 3-13: Schematic of high-speed camera focusing on SDR for visualisation experiments.

Chapter 4. Results

The current procedure of producing starch nanoparticles through the solvent-antisolvent precipitation method has many limitations, as has been highlighted within the literature review (chapter 2). One such limitation is the reduced flow rate and low starch concentrations used in semi-batch systems to avoid agglomeration of the precipitated nanoparticles (Hebeish et al., 2014). The SDR has thus been proposed to counteract these shortcomings. Flow systems have not yet been investigated for the solvent-antisolvent precipitation of starch nanoparticles, demonstrating this as one of the novel elements within this work.

This chapter is divided into two sections. The first section focuses on the solvent-antisolvent precipitation of starch nanoparticles in the SDR. Various operating conditions such as total flow rate, disc rotational speed, antisolvent to solvent ratio, disc surface texture, and starch concentration are investigated, evaluating the effect of these conditions on the size, size distribution, morphology and yield of the starch nanoparticles. A comparison between the SDR and a conventional semi-batch system is also presented within this section. Additionally, the interaction between the parameters studied and particle size is explored to formulate empirical relationships through multiple linear regression analysis.

The second part of this chapter studies the precipitation kinetics for the solvent-antisolvent precipitation of starch nanoparticles in the SDR. A novel method using a high-speed camera system, as described in the previous chapter, is applied to estimate induction time. The conditions affecting induction time and nucleation rate are also assessed. Furthermore, nucleation and growth kinetics are estimated, which will be applied in the next chapter to aid in the generation of a mathematical model.

4.1. Production of starch nanoparticles

4.1.1. Solvent-antisolvent precipitation in the SDR

4.1.1.1. Effect of total flow rate on nanoparticle size distribution

The effect of total flow rate on starch nanoparticle size distribution at a constant disc speed of 1200 rpm and a 9:1 antisolvent to solvent ratio on the grooved disc is presented in Figure 4-1. From the plot, it is observed that an increase in total flow rate causes a decrease in both the average size of particles and the polydispersity index. This is evident through the size distribution peak at 175 nm (± 14.96 nm) and a PdI value of 0.204 (± 0.040) at 18 mL/s flow rate, whereas the mean size and PdI value obtained at 6 mL/s are 248 nm (± 43.03 nm) and

0.302 (± 0.039), respectively, as can be seen in Figure 4-1(B). However, this decline in particle size flattens out between 12 mL/s and 18 mL/s, as no further reduction in nanoparticle size is noticed. This is a possible result of the agglomeration of smaller particles as more particles are generated at the higher flow rate. Such behaviour has also been observed by Fujiwara et al. (2002) and Yu et al. (2005) upon the generation of small particles which agglomerated. Furthermore, as smaller sized particles are formed, the surface area is increased for the same volume of particles, therefore, the coverage by the surfactant may not be sufficient, considering the same concentration of surfactant has been used for all experimental conditions. Hence, greater free surface is available for smaller particles to agglomerate. Similar trends occur at all disc speeds and antisolvent to solvent ratios. The TEM images in Figure 4-2 presents a comparison between particles produced with a flow rate of 6 and 18 mL/s. This analysis confirms that higher flow rate produced smaller sized particles. Average size of particles at 18 mL/s from TEM analysis was found to be 13.3 nm, whereas at 6 mL/s the average size was higher at 30.3 nm. As mentioned earlier, there is slight agglomeration amongst smaller particles noticeable in the TEM image for particles generated at 18 mL/s. It should also be noted that the difference in particle sizes from DLS and TEM is a result of larger particles scattering more light in the DLS technique which shifts the peaks towards the larger end of the size distribution, whereas the TEM shows the true particle size (Hagendorfer et al., 2012). Comparison of TEM and DLS trends with respect to the experimental conditions on a grooved disc are presented in Appendix D.

The smaller sized particles are formed as the high flow rate causes an increase in liquid shear on the disc which promotes formation of instabilities within the liquid film (Ozar et al., 2003). The effect of the experimental conditions on shear rate, including flow rate, are given in Appendix E. The increased instabilities within the film then enhances micromixing between the solvent and antisolvent which aids in the production of uniformly high supersaturation, causing nucleation of starch nanoparticles. The spinning disc reactor does not increase supersaturation itself, as supersaturation and nucleation processes are independent of reactor geometry (McCarthy et al., 2007). However, it does prevent high local supersaturation through effective mixing of the solvent and antisolvent streams flowing on the disc, thereby ensuring uniform supersaturation across the film layer. Within this ideal uniform mixing environment, more successful collisions between molecules can occur to form the critical nucleus required for particle nucleation to take place, thus increasing

nucleation rate in this way. An increase in nucleation rate means that supersaturation is reduced primarily by nucleation which contributes to the formation of reduced particle size (Tung et al., 2008a). Growth of particles and even agglomeration may be further reduced as the residence time decreases with an increase in flow rate, according to Eq. 2-14.

The decrease in particle size distribution width at increasing flow rates, as indicated by the lower PdI values suggest superior transverse mixing occurs across the film thickness with reduced radial mixing, leading to a narrow residence time distribution and thus a narrow particle size distribution. This effect of flowrate on residence time distribution has been quantitatively demonstrated in an earlier study (Mohammadi and Boodhoo, 2012). The results obtained are in agreement with prior solvent-antisolvent precipitation work done in the SDR, where increasing flow rate has resulted in smaller sized particles (Khan and Rathod, 2014).

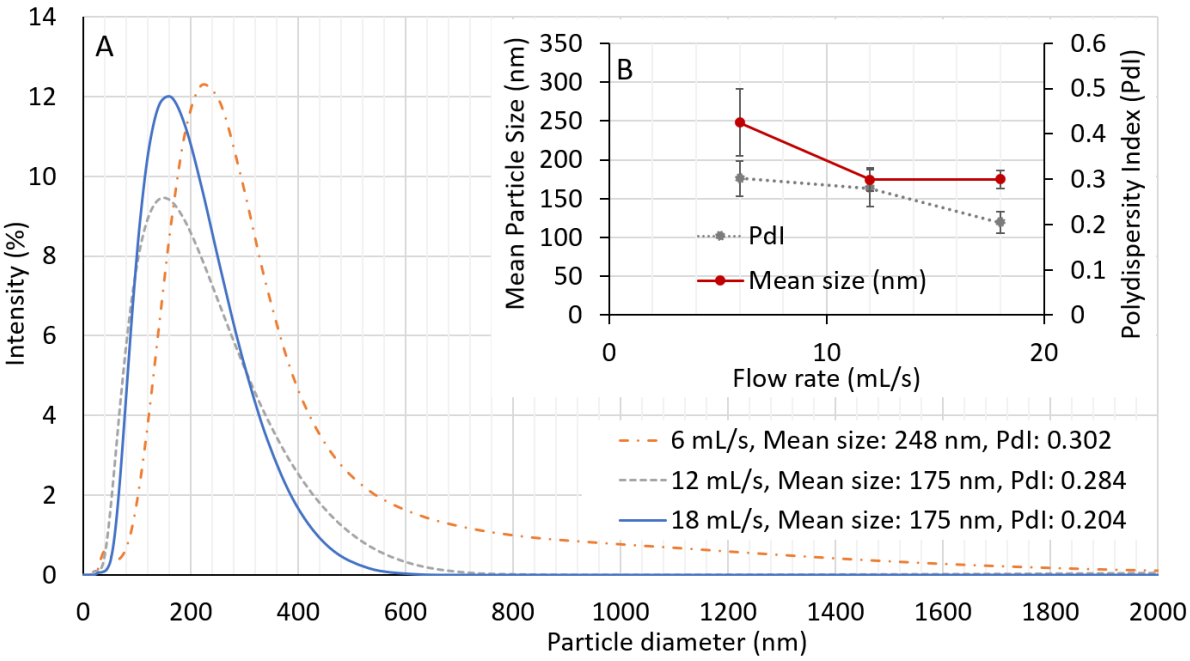

Figure 4-1: Effect of flow rate at 1200 rpm, 9:1 antisolvent to solvent ratio, on the grooved disc A) PSD, B) plot of mean particle size and PdI.

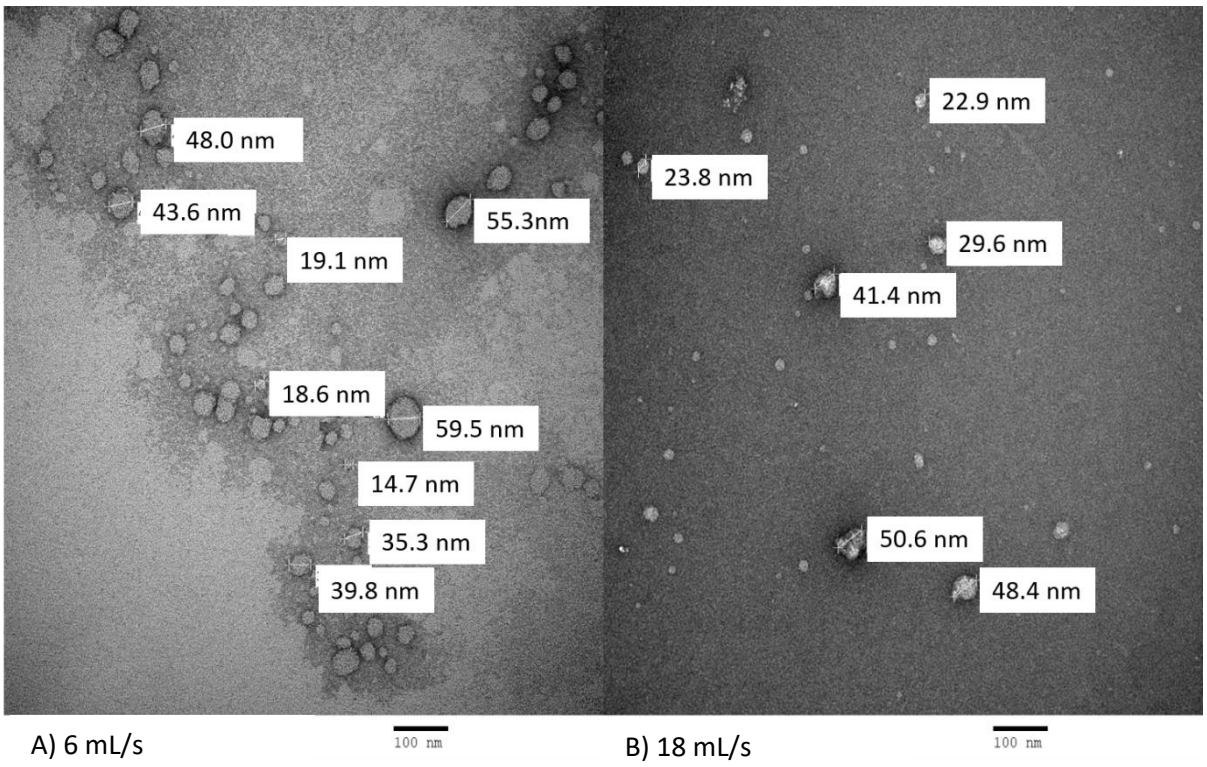

Figure 4-2: TEM images for A) 6 mL/s, and B) 18 mL/s at 1200 rpm and 9:1 ratio.

4.1.1.2. Effect of disc rotational speed on nanoparticle size distribution

A similar effect as flow rate has been observed for disc rotational speeds investigated at 400, 800 and 1200 rpm, presented in the PSD profiles in Figure 4-3(A). At higher disc speeds, there is a reduction in both mean particle size and PdI as shown in Figure 4-3(B). An increase in disc rotational speed increases mixing and contact between antisolvent and starch solution due to reduced film thickness and higher shear rate, which leads to an increase in nucleation rate and decrease in particle growth. Furthermore, the disc speed has also been shown to influence plug flow behaviour (Mohammadi and Boodhoo, 2012), with flow approaching plug flow at higher disc rotational speeds and at high flow rates. Plug flow conditions aid in mixing between the solvent and antisolvent as well as reduce backmixing on the disc, decreasing the variation between particles thus leading to a much narrower size distribution. These results agree with previous work done on solvent-antisolvent precipitation, where an increase in rotational speed resulted in smaller particles (Khan and Rathod, 2014).

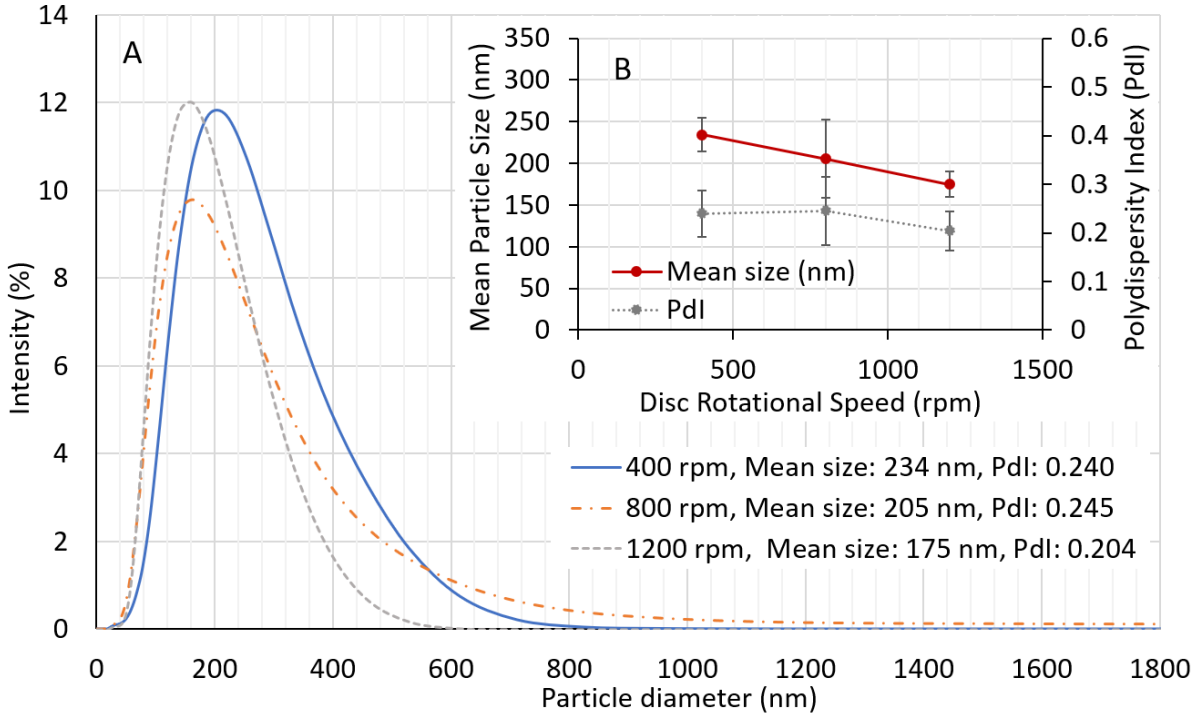

Figure 4-3: Effect of disc rotational speed at 9:1 antisolvent to solvent ratio and 18 mL/s flow rate on the grooved disc, a) PSD, b) plot of mean particle size and PdI.

It has, however, been observed that the combination of low antisolvent to solvent ratio of 1:1 and a high flow rate of 18 mL/s on the grooved surface resulted in the production of larger and agglomerated particles. This is evident in the size distribution seen in Figure 4-4, showing the sharp increase in mean particle size at 1:1 and 18 mL/s compared to the corresponding values at 9:1 antisolvent to solvent ratio and 18 mL/s shown in Figure 4-1. The particle size increases with further increase in disc speed. This could be explained by poor mixing between the two inlet streams at much higher solvent flow rates, or more specifically the occurrence of back-mixing in the region of the inlet tubes, causing precipitation to take place within the central region of the disc. This phenomenon is evident in Figure 4-5, showing the accumulation of starch in the central region and forming a colloidal substance above the surface of the disc. In effect, when the flow rates of the two inlet streams are similar as when the antisolvent to solvent ratio is 1:1, it is more challenging to incorporate the large quantity of solvent/solute stream within the antisolvent stream, more so under the less than ideal mixing conditions in the inner zones of the disc. This phenomenon has also been experienced in past studies (Khan and Rathod, 2014, Chen et al., 2006). If such low antisolvent to solvent ratios are to be used, it may be more advantageous to introduce the antisolvent stream onto the spinning disc away from the central region where more stable and improved hydrodynamic conditions prevail (Mohammadi et al., 2014).

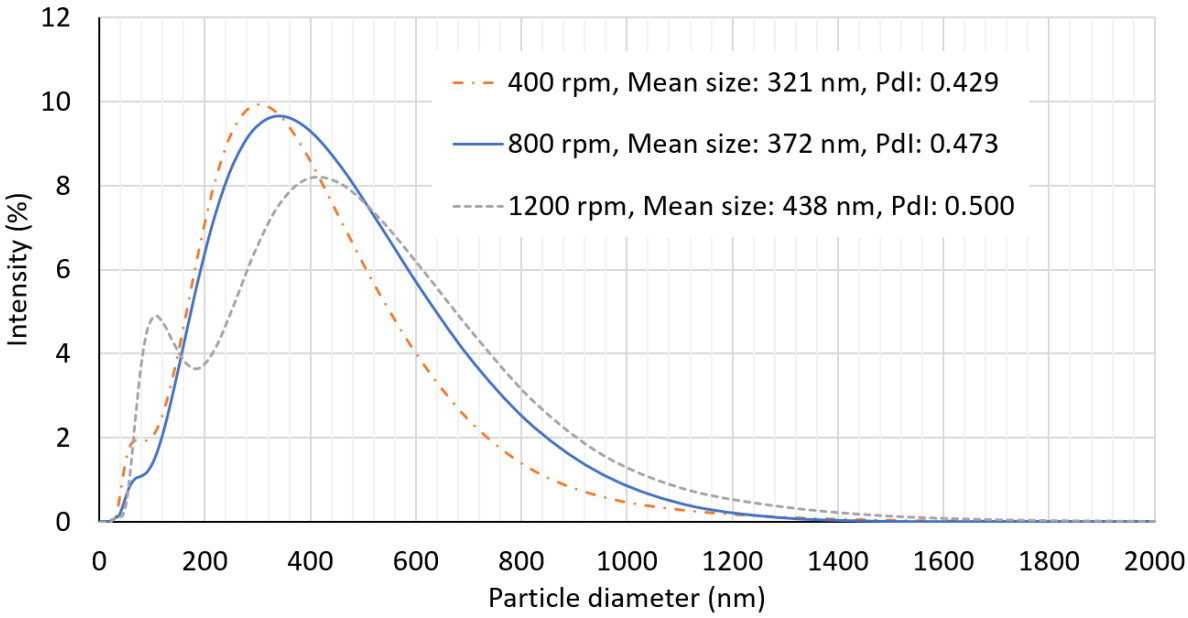

Figure 4-4: Effect of disc rotational speed on PSD of starch nanoparticles at 1:1 antisolvent to solvent ratio and 18 mL/s.

Figure 4-5: Image of SDR showing back-mixing phenomenon at 18 mL/s, 1200 rpm and 1:1 ratio.

4.1.1.3. Effect of antisolvent to solvent ratio on nanoparticle size distribution

Figure 4-6(A) shows the particle size distribution profiles at selected antisolvent to solvent ratios of 1:1, 5:1 and 9:1, at constant conditions of 12 mL/s total flow rate and a disc rotational speed of 1200 rpm. An antisolvent to solvent ratio of 9:1 shows a peak of lowest

mean size at 175 nm, whereas the PdI value increases with the ratio as shown in Figure 4-6(B). An increase in antisolvent to solvent ratio causes an increase in supersaturation through reduction of starch solubility. The generated supersaturation is then consumed by nucleation processes, generating smaller sized particles. The increase in PdI, on the other hand, is likely to be a consequence of greater chances of agglomeration between the small size primary nuclei occurring as a result of more particles of smaller size being produced at the highest ratio. However, the overall PdI, which is a combination of the PdIs of the main peak, and a much smaller, less intense peak of higher particle size corresponding to agglomerated particles, as depicted in Figure 4-7, shows that there is more overall agglomeration at the low antisolvent to solvent ratio of 1:1. Agglomeration at 1:1 ratio may be the result of the entrapment of solvent between particles in close proximity to each other as incorporation of the higher amount of solvent/solute stream within the antisolvent stream becomes more difficult. Table 4-1 presents the individual and overall PdI values for the three antisolvent to solvent ratios, along with the Z-averages.

Although previous work focusing on solvent-antisolvent precipitation of starch nanoparticles has been carried out in a semi-batch system, it has been limited to 1:1 ratio of antisolvent to solvent and resulting particle sizes produced have been between 130 to 140 nm (Hebeish et al., 2014). However, in this present study an average particle size of 11.45 nm has been obtained for 1:1 antisolvent to solvent ratio at 18 mL/s and 1200 rpm. For such a small particle size to be produced in a semi-batch system, further downstream processing would be required, such as milling, which may consume a significant amount of energy. Therefore, the bottom up approach adopted here in producing these particles would be more beneficial on a practical level, especially if conditions can be tailored to the particle size requirements.

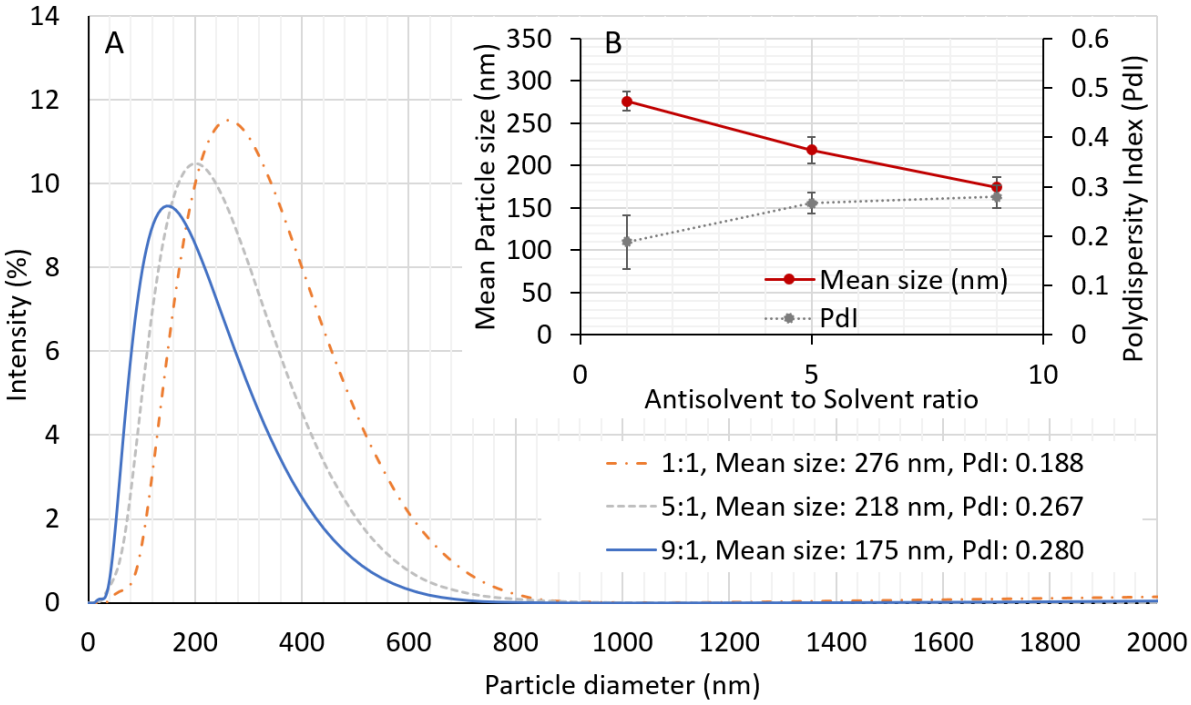

Figure 4-6: Effect of antisolvent to solvent ratio at 12 mL/s and 1200 rpm on the grooved disc, A) PSD, B) plot of mean particle size and PdI.

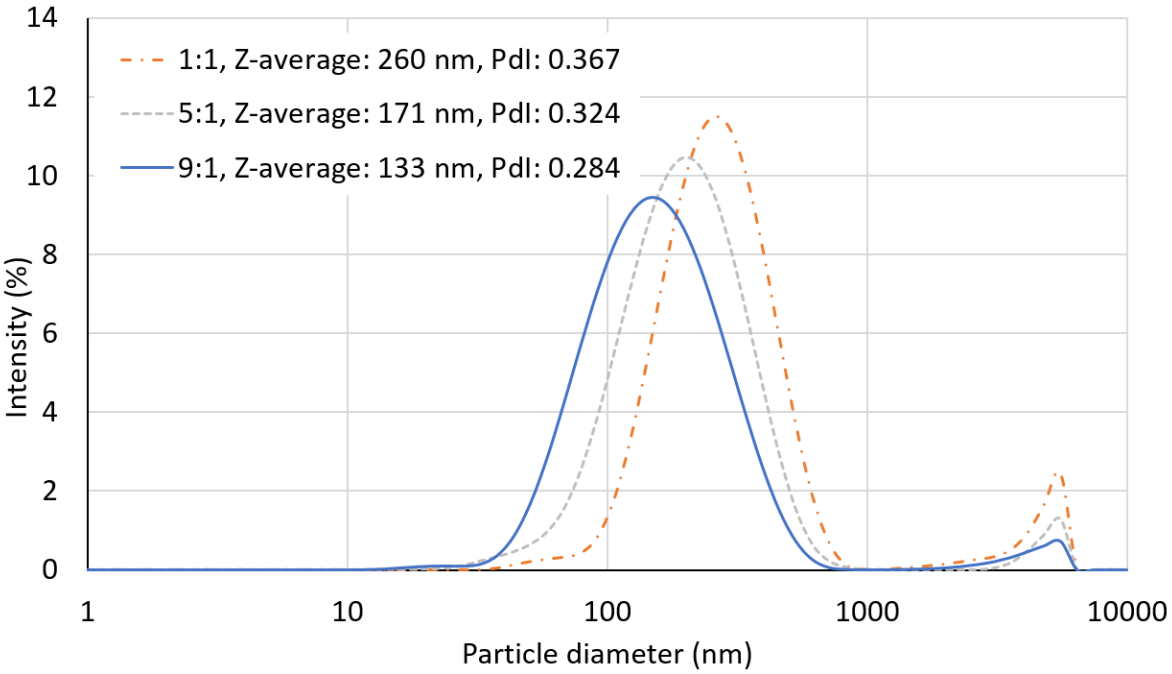

Figure 4-7: Overall PSD showing effect of antisolvent to solvent ratio at 12 mL/s and 1200 rpm.

Table 4-1: Particle sizes and PdI values for different antisolvent to solvent ratios at 12 mL/s and 1200 rpm.

Antisolvent to solvent ratio	Mean peak 1 (nm)	Mean peak 2 (nm)	Z-average (nm)	PdI of peak 1	PdI overall
1:1	276	4813	260	0.188	0.367
5:1	218	4952	171	0.267	0.324
9:1	175	3789	133	0.280	0.284

4.1.1.4. Comparison between smooth and grooved disc surfaces

Figure 4-8 compares the smooth and grooved discs for the production of starch nanoparticles. The trend followed in the smooth disc is similar to that observed on the grooved disc for the conditions studied, and for reasons discussed earlier.

Figure 4-8(A) shows the effect of increasing flow rate, which suggests the production of smaller sized starch nanoparticles on the grooved disc up until 12 mL/s. However, after that there is not much more of a reduction in particle size as the flow rate is increased to 18 mL/s. On the other hand, for the smooth disc the particle size continues to decrease to produce slightly smaller sized particles than on the grooved surface. This is also true for the effect of rotational speed presented in Figure 4-8(B). For the conditions of 18 mL/s flow rate, 9:1 ratio and 1200 rpm disc speed, the PSD in Figure 4-9 reveals a lower particle size on the smooth disc surface, however the size distribution is narrower with the grooved disc, resulting in a lower overall PdI. The TEM images in Figure 4-10 for these conditions confirm the presence of more agglomeration amongst particles produced on the smooth disc.

Figure 4-8(C) shows the effect of antisolvent to solvent ratio for smooth and grooved disc surfaces. There is not a significant difference between particle sizes obtained on the smooth and grooved discs, particularly at the higher ratios of 5:1 and 9:1. This is most likely due to supersaturation being a more important factor than surface texture, and the supersaturation generated is the same for both surfaces at a given antisolvent to solvent ratio.

The lower PdI on the grooved disc is the consequence of increased plug flow, associated to the narrower residence time distribution. It is a result of the textured surface generating turbulent eddies within the liquid film as it travels along the grooved surface. Furthermore, a grooved surface also promotes surface wetting and promotes the flow of a continuous film

when compared to a smooth surface (Mohammadi and Boodhoo, 2012). All these hydrodynamic effects prevalent on the grooved disc in contrast to the smooth disc provide the best conditions for controlling the PdI, resulting in better quality starch particles upon precipitation.

The effect of the texture of the disc surface on mean particle size and its interactions with total flow rate, disc rotational speed and antisolvent to solvent ratio are presented in Figure 4-11, as well as the interactions between other parameters. The interactions plot summarises and agrees with the results so far. The interaction between total flow rate and the antisolvent to solvent ratio especially at high flow rates and low antisolvent to solvent ratio is particularly evidenced by the reverse trend observed at these values. Generally, when comparing the particle sizes obtained on the smooth and grooved disc for the same conditions, the particles produced on the smooth disc are smaller. However, looking at the error bars in Figure 4-8, they tend to overlap in a few areas which suggests that the effect of disc surface on particle size is not as profound as it is on the width of the particle size distribution.

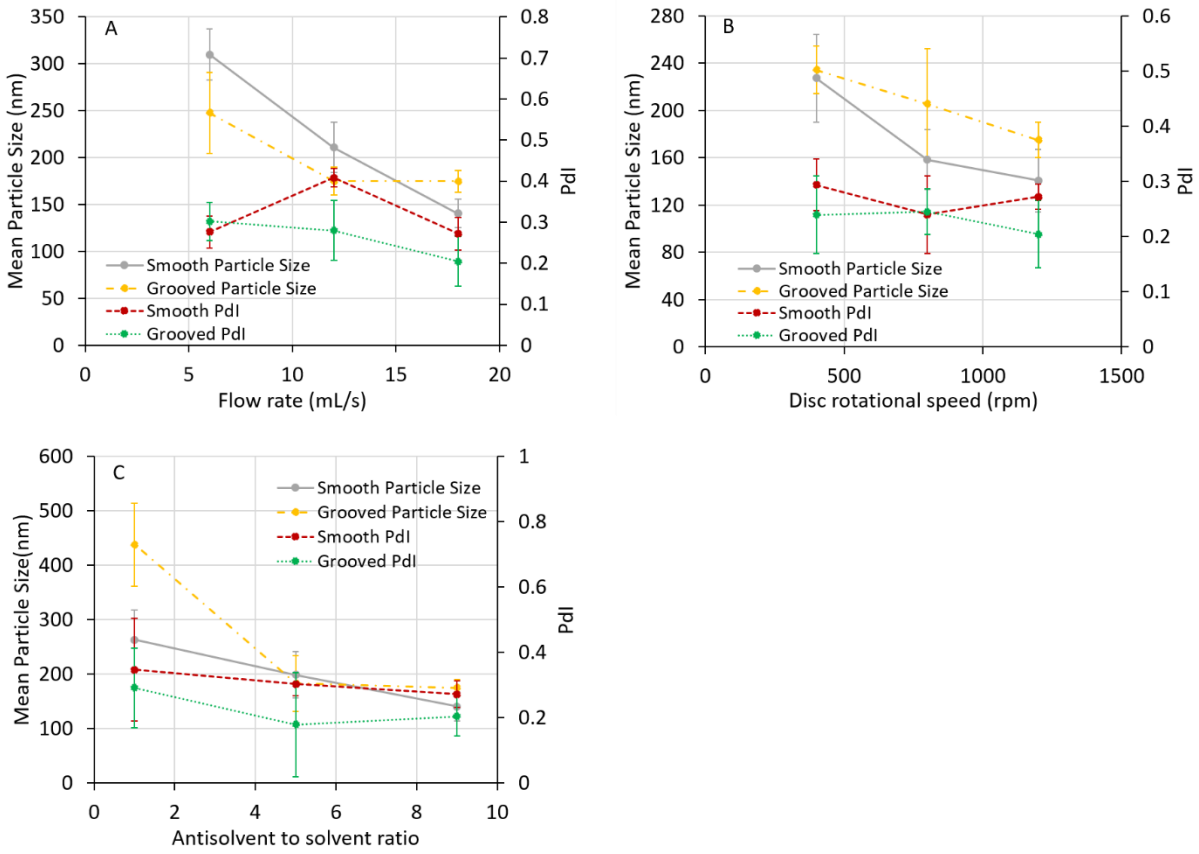

Figure 4-8: Comparison between smooth and grooved disc for the effect of A) flow rate (1200 rpm, 9:1 ratio), B) disc rotational speed (18 mL/s, 9:1 ratio), C) antisolvent to solvent ratio (1200 rpm, 18 mL/s).

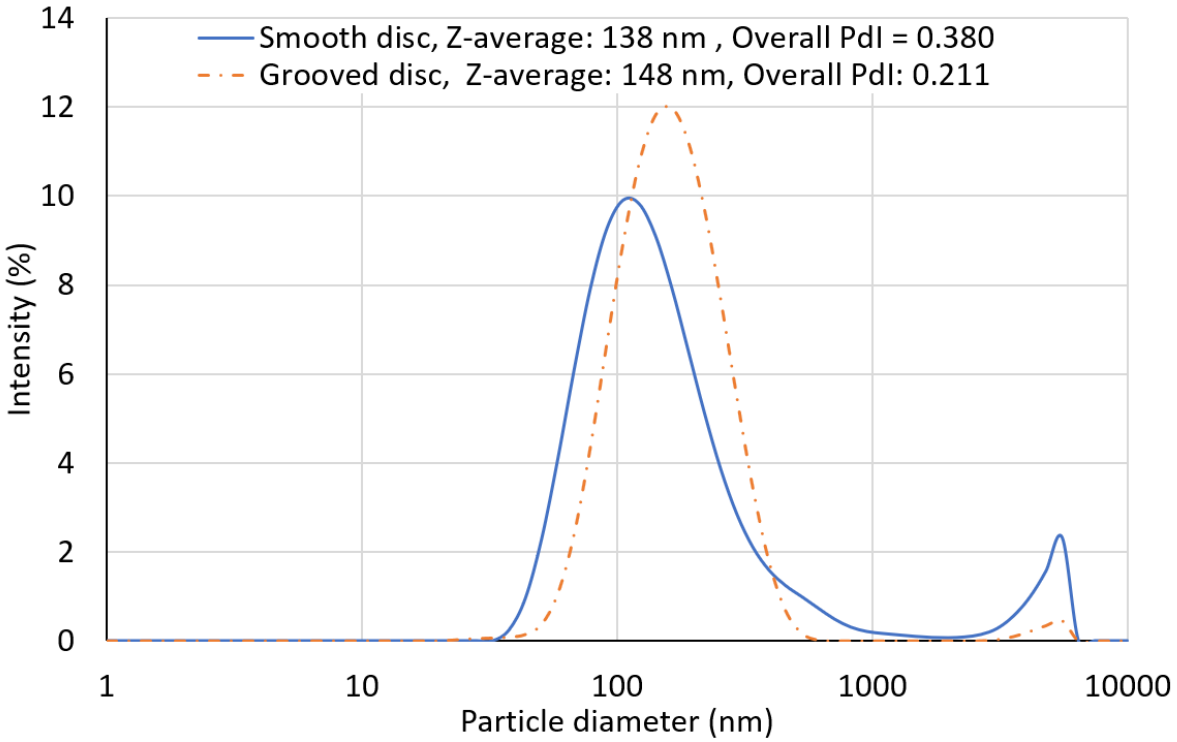

Figure 4-9: PSD comparing smooth and grooved disc surfaces at 18 mL/s, 9:1 ratio and 1200 rpm.

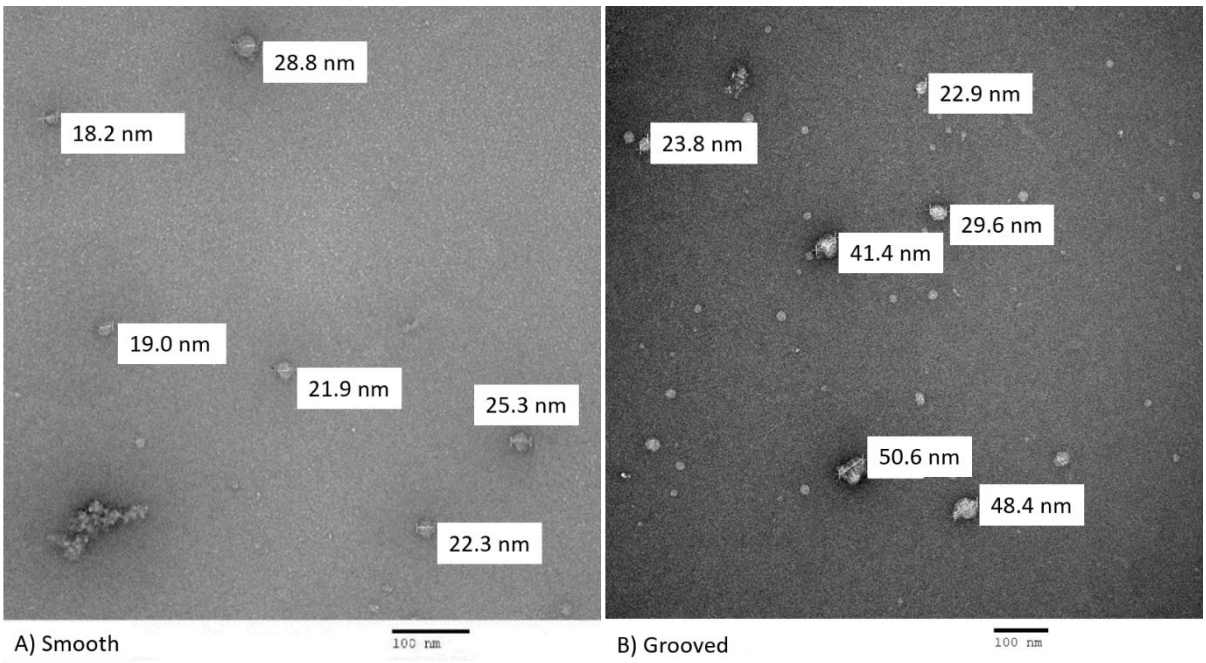

Figure 4-10: TEM image at 18 mL/s, 9:1 ratio and 1200 rpm for A) smooth and B) grooved surfaces.

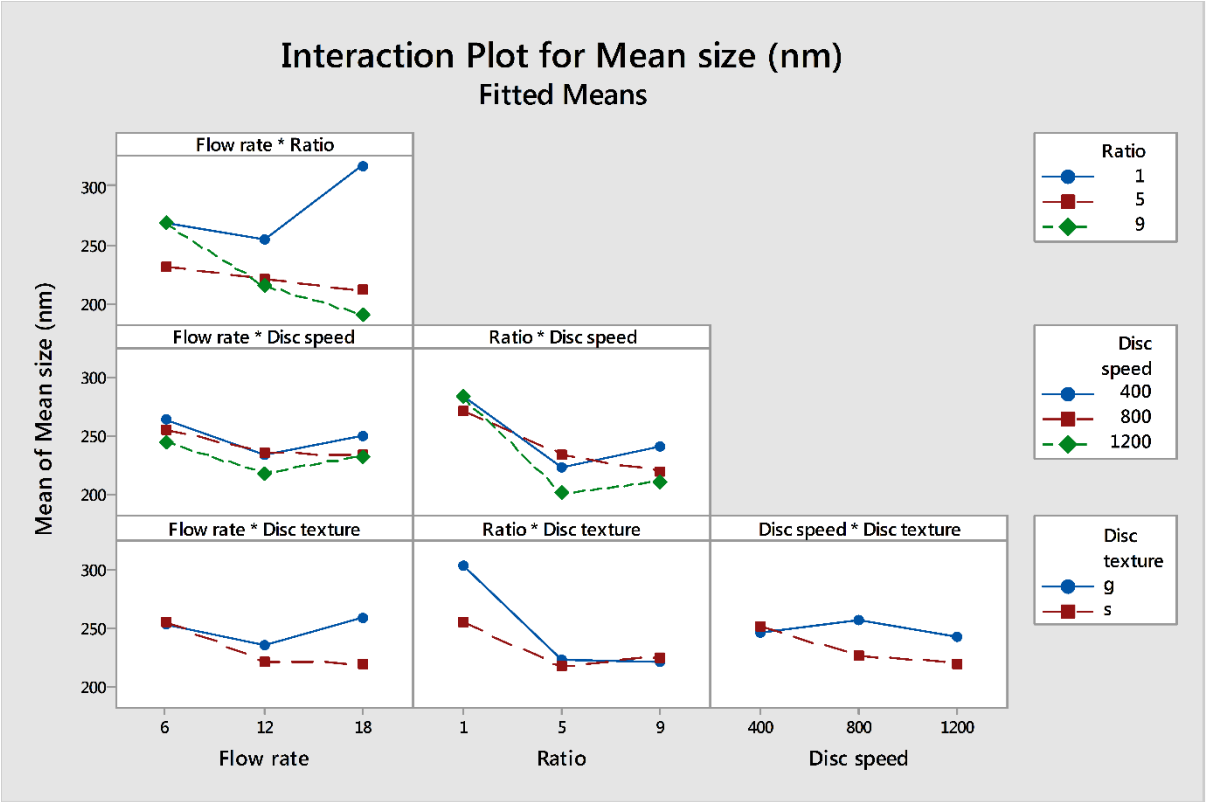

Figure 4-11: Interactions plot showing effect of interactions between parameters on particle size obtained from the DLS.

4.1.1.5. Yield

Figure 4-12 shows the effects of flow rate, disc speed, and antisolvent to solvent ratio on particle yield for both smooth and grooved disc surfaces. As discussed earlier, increased flow rates, higher disc speeds and increased proportion of antisolvent promote nucleation due to better mixing conditions. This generally translates into higher yields of particles under these conditions, especially so on the grooved disc.

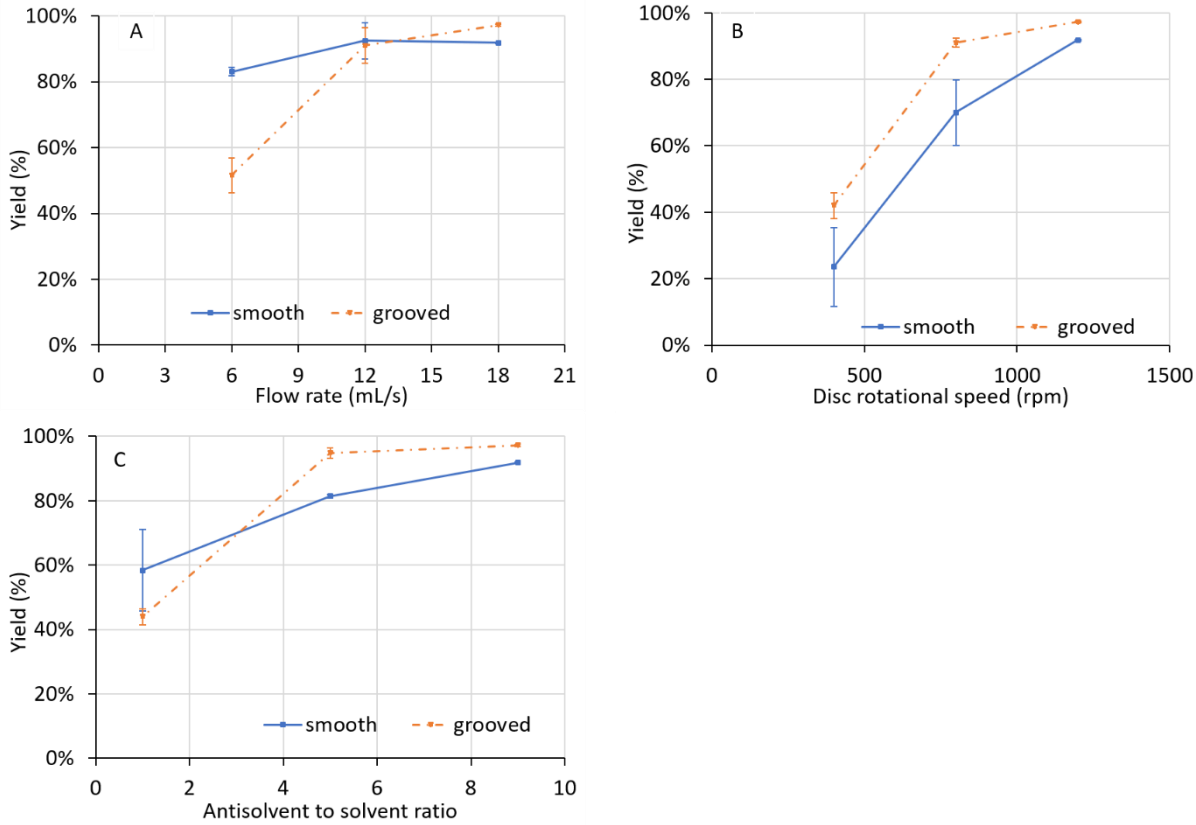

Figure 4-12: Yields for smooth and grooved discs for the effect of A) flow rate (1200 rpm, 9:1 ratio), B) disc rotational speed (18 mL/s, 9:1 ratio), C) antisolvent to solvent ratio (1200 rpm, 18 mL/s).

4.1.1.6. Effect of starch concentration on precipitation of starch nanoparticles

A number of experiments were repeated using 4 % w/v starch solution to evaluate the effect of concentration on particle size and the size distribution of precipitated starch nanoparticles. Figure 4-13 presents the size distributions for 2 % w/v and 4 % w/v starch on both grooved and smooth disc surfaces at 6 mL/s, 1200 rpm and 9:1 ratio. The PSDs indicate the precipitation of smaller sized particles at the 4 % w/v concentration. In comparison, Figure 4-14, which displays the PSDs at conditions of 18 mL/s, 1200 rpm and 9:1 ratio, shows smaller sized particles produced at 2 % w/v. An increase in particle size at 4 % w/v is observed as flow rate is increased. Additionally, at the lower flow rate, for both 2 % w/v and 4 % w/v, nanoparticles produced on the grooved disc are smaller than those on the smooth disc (Figure 4-13), whereas the opposite is true at the higher flow rate of 18 mL/s (Figure 4-14).

Hebeish et al. (2014) reported an increase in particle size as concentration of starch in solution was increased. A range of starch concentrations up to 10 % w/v were studied and it was established that as a result of high viscosity impeding penetration of the solute/solvent by the antisolvent, the starch nanoparticles were produced of larger sizes with high PdI

values. The study was carried out in a semi-batch set-up, however, due to the high shear in the SDR and the shear thinning behaviour exhibited by the starch solutions at the high shear rates, the viscosity is no longer an issue at high concentrations. Furthermore, an increase in solute concentration results in greater supersaturation, promoting the production of smaller sized particles in sparingly soluble systems such as the starch system (Mersmann, 1999). This explains the resultant smaller sized starch nanoparticles at 4 % w/v concentrations shown in Figure 4-13.

Figure 4-14 can be explained with the aid of Figure 4-15 which focuses on the entire PSD, including the agglomeration peak for the conditions of 18 mL/s, 1200 rpm and 9:1 ratio, on the grooved disc. The PSD shows a sharper agglomeration peak at the 4 % w/v concentration and combined with the smaller peak around the 50 nm mark points towards the possibility of smaller sized particles being produced at 4 % w/v, agglomerating to a larger extent, and shifting the peak towards the right side of the PSD. This would be a result of the greater supersaturation generated at the high solute concentration as well as the intense shear generated at the high flow rate, heightening micromixing between the solute/solvent and antisolvent.

A similar effect as flow rate on particles produced with 4 % w/v starch is observed as disc rotational speed and antisolvent to solvent ratio are increased. Figure 4-16 summarises the influence of the experimental conditions on mean particle size. An opposite trend for the 4 % w/v concentration is observed in comparison to 2 % w/v regardless of disc texture. That is, as the conditions for precipitation increase, particle size distributions indicate larger sized particles are generated at 4 % w/v starch concentrations. However, as no TEM images were taken at the 4 % w/v concentration, one can only speculate that the cause of this is greater agglomeration due to increased supersaturation and micromixing conditions. Furthermore, a large concentration of smaller particles would suggest a higher surface area for the surfactant to cover, and as the concentration of surfactant is kept constant, this would result in low surface coverage, thus promoting agglomeration of the nanoparticles.

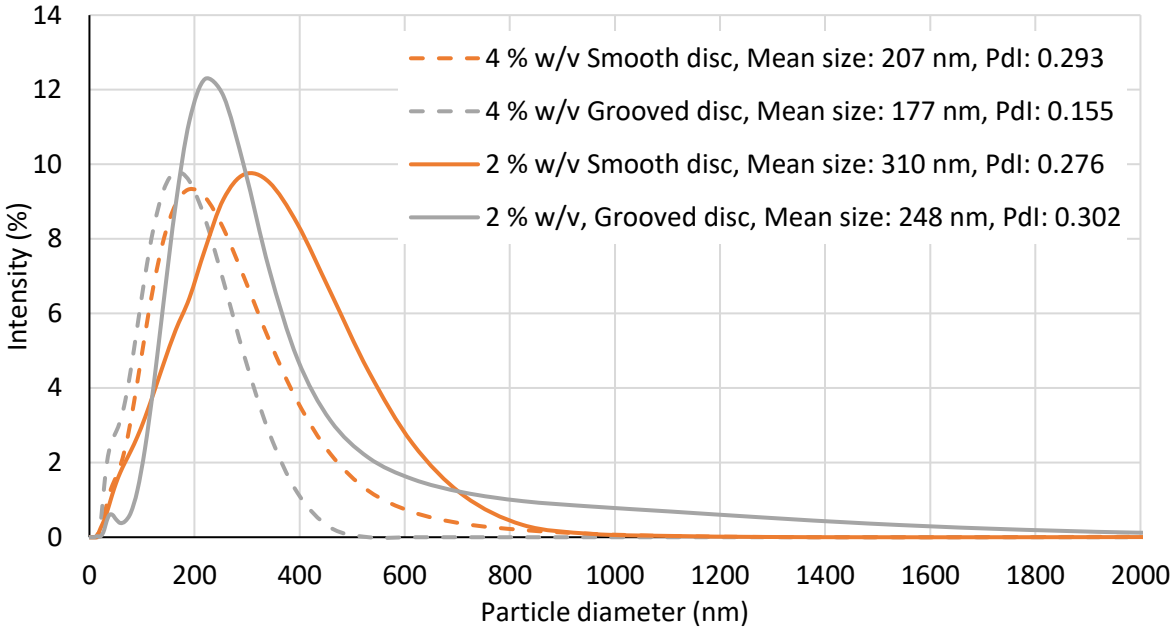

Figure 4-13: Effect of concentration at 6 mL/s, 1200 rpm and 9:1 ratio for both grooved and smooth disc surfaces.

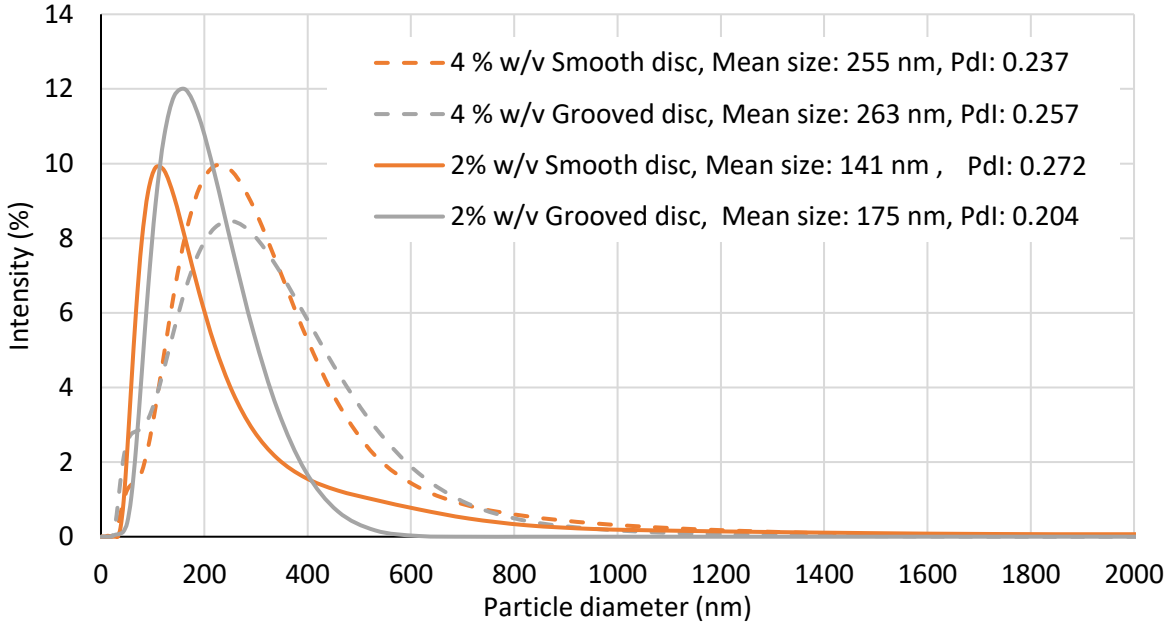

Figure 4-14: Effect of concentration at 18 mL/s, 1200 rpm and 9:1 ratio for both grooved and smooth disc surfaces.

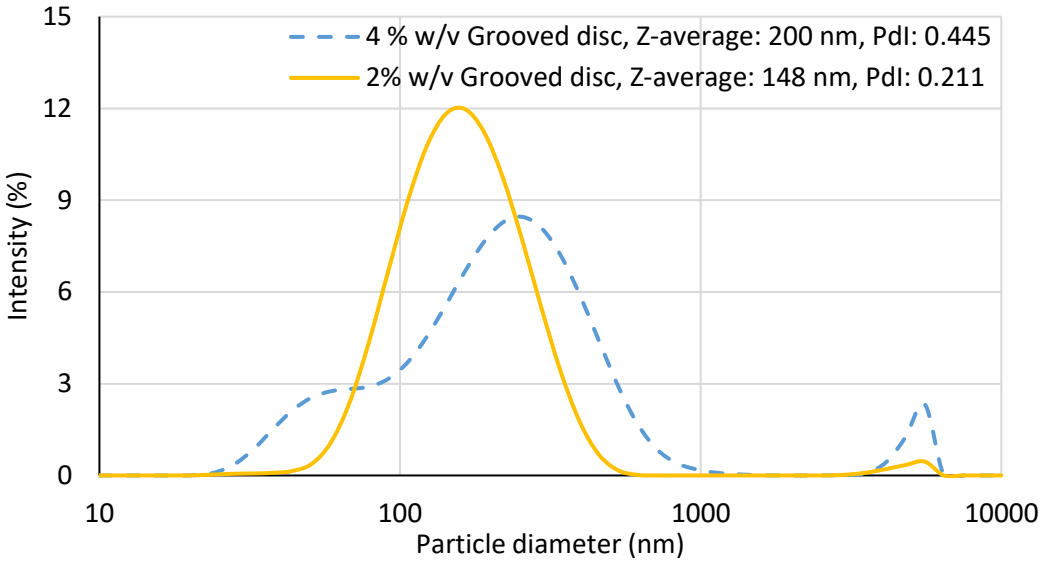

Figure 4-15: PSD showing effect of concentration at 18 mL/s, 1200 rpm, 9:1 ratio on the grooved disc.

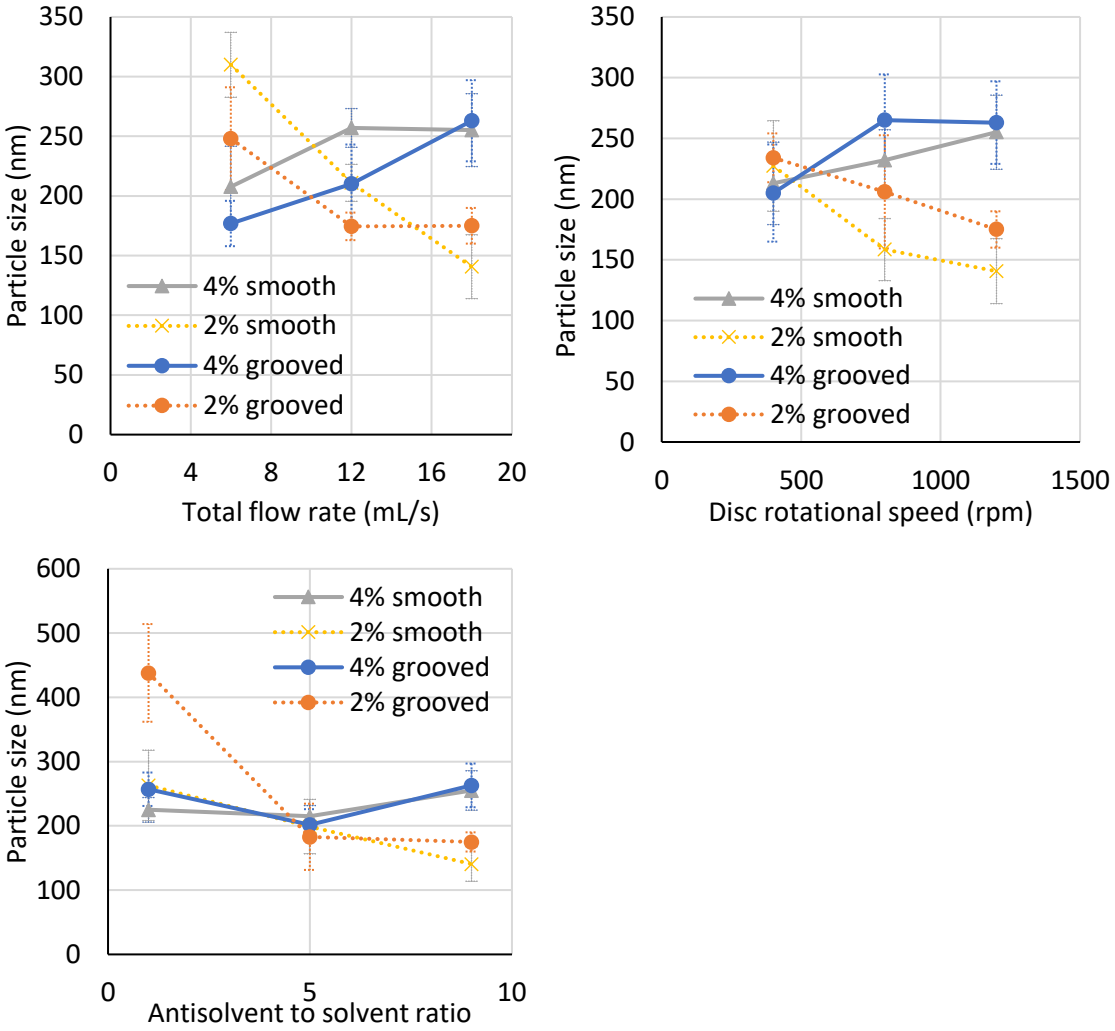

Figure 4-16: Particle sizes for 2 % w/v and 4 % w/v starch with the effect of A) flow rate at 9:1 ratio and 1200 rpm, B) disc speed at 9:1 ratio and 18 mL/s, and, C) antisolvent to solvent ratio at 18 mL/s and 1200 rpm.

4.1.2. Comparison between SDR and SBR

To benchmark the SDR process, experiments were carried out in a semi-batch setup with the results for the SBR process presented in Appendix F.

When comparing the SBR with the SDR process, it is evident from the size distributions displayed and discussed earlier that the particle sizes are smaller and size distributions narrower when carrying out the process in an SDR arrangement. The basis of comparison for the two systems presented here would be on the grounds of similar power dissipation, which is at the highest power dissipation in the SBR and the lowest in the SDR. For the SBR system the highest dissipation rate was found to be at 800 rpm agitation rate and 1 mL/s ethanol addition rate, with the dissipation rate being 0.8 W/kg at both starch concentrations of 1 and 2 % w/v. For the SDR process the condition with the lowest dissipation rate (18 W/kg) was at low disc rotational speed and low total flow rate, hence the results at 2 % w/v, 6 mL/s, 1:1 ratio and 400 rpm on the SDR are used for comparison with the SBR.

Figure 4-17 shows a comparison between TEM images of starch nanoparticles from two semi-batch processes (800 rpm agitation rate and 1 mL/s ethanol addition rate) and from the SDR process (2 % w/v, 6 mL/s total feed flow rate, 1:1 ratio and 400 rpm). The particles produced in the semi-batch system, shown in Figure 4-17(A) and 4-17(B), are larger, more irregular in shape, as well as agglomerated. The SDR processed particles in Figure 4-17(C), however, are smaller, less agglomerated and more spherical in shape. The particle sizes from the two systems are evidently different which is a result of poor mixing occurring in the SBR, particularly at lower agitation rates and high antisolvent addition, leading to agglomerated and larger sized particles. Figure 4-18 shows the size distributions obtained from the TEM images for both SDR and SBR processes. The size distribution shows smaller sized particles with a narrow size distribution for the SDR process.

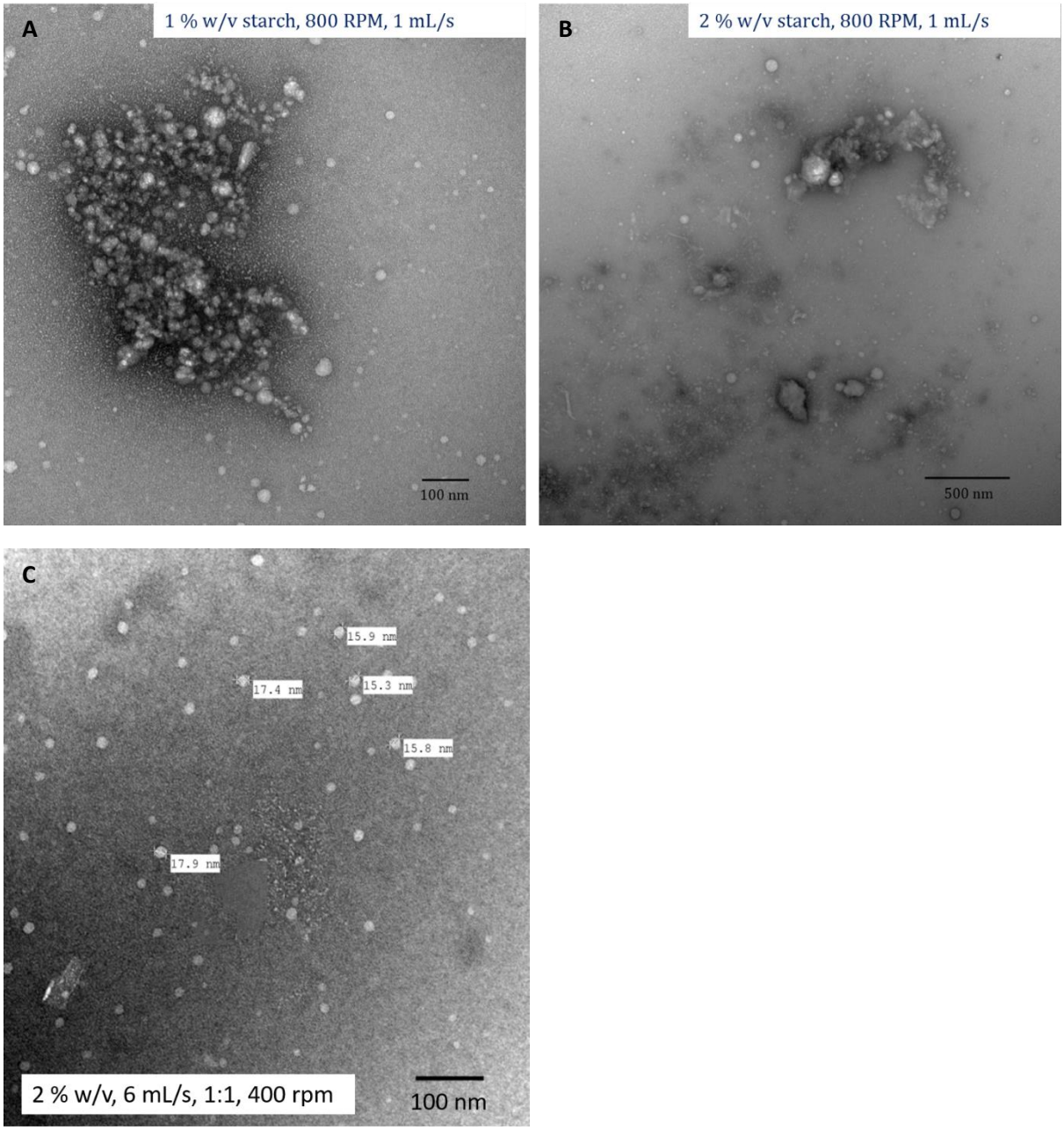

Figure 4-17: TEM images of starch nanoparticles from, SBR runs at conditions of A) 1 % w/v, 1 mL/s ethanol addition rate, 800 rpm, B) 2 % w/v, 1 mL/s ethanol addition rate, 800 rpm and, C) SDR run at 2 % w/v, 6 mL/s total feed flow rate, 1:1, 400 rpm.

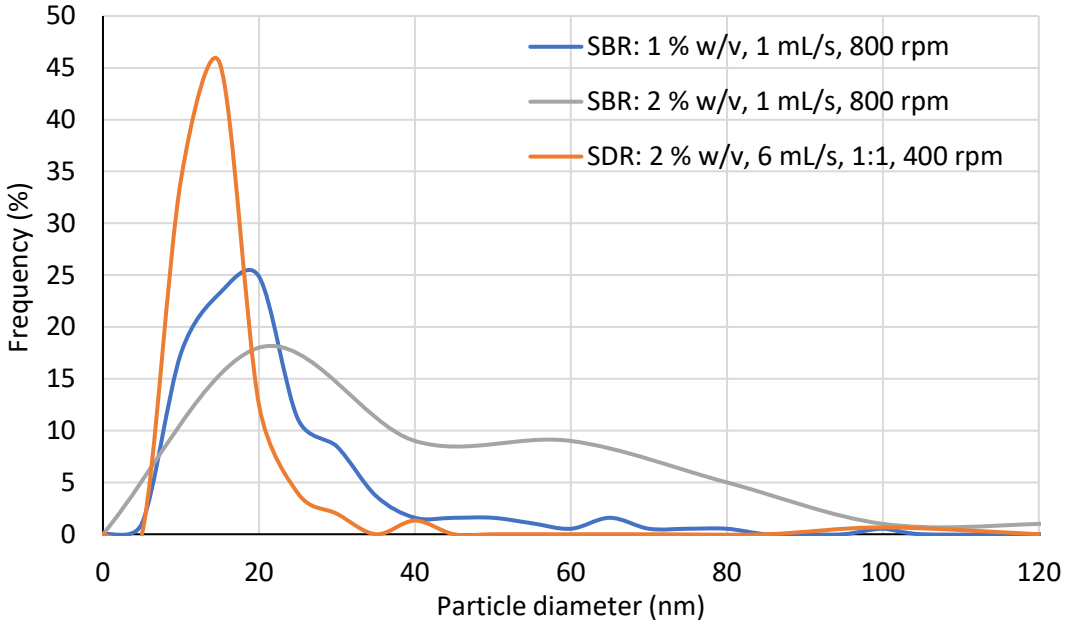

Figure 4-18: PSD from TEM images (Figure 4-17) for SBR at 1 % w/v and 2 % w/v starch concentrations (1 mL/s ethanol addition rate, 800 rpm) – dissipation rate of 0.8 W/kg; and SDR (2 % w/v, 6 mL/s total feed flow rate, 1:1, 400 rpm) experiments – dissipation rate of 18 W/kg.

The particle sizes obtained through each of the systems can be plotted against power dissipation for further comparison. This is given in Figure 4-19.

The equation for power dissipation in an agitated vessel is given by Eq. 4-1.

$$\varepsilon_{local} = \emptyset \frac{N_p N^3 D_i^5}{V} \tag{4-1}$$

where, N_P is power number taken from Furukawa et al. (2012), N is the impeller rotation speed, D_i is the impeller diameter, and $\emptyset$ is the relative power dissipation dependent on vessel injection point, considered to be 1 in this case as the injection point is near the impeller (Assirelli et al., 2002).

For the spinning disc reactor the equation for power dissipation rate is as follows:

$$\varepsilon = \frac{1}{2t_{res}}((r^2\omega^2 + u^2)_o - (r^2\omega^2 + u^2)_i) \tag{4-2}$$

Where u is average velocity and t_{res} is the residence time in the SDR and is expressed as:

$$t_{res} = \left(\frac{81\pi^2\nu}{16\omega^2 Q^2}\right)^{1/3}\left(r_0^{4/3} - r_i^{4/3}\right) \tag{4-3}$$

It should be noted that the power consumption model for the SDR is for a smooth surface which means the disc characteristics and film interactions with the grooves on the grooved

disc may not have been accounted for in the power dissipation model. Additionally, Eq. 4-2 is at steady state where little energy is consumed in keeping the disc rotating at a certain speed against air drag.

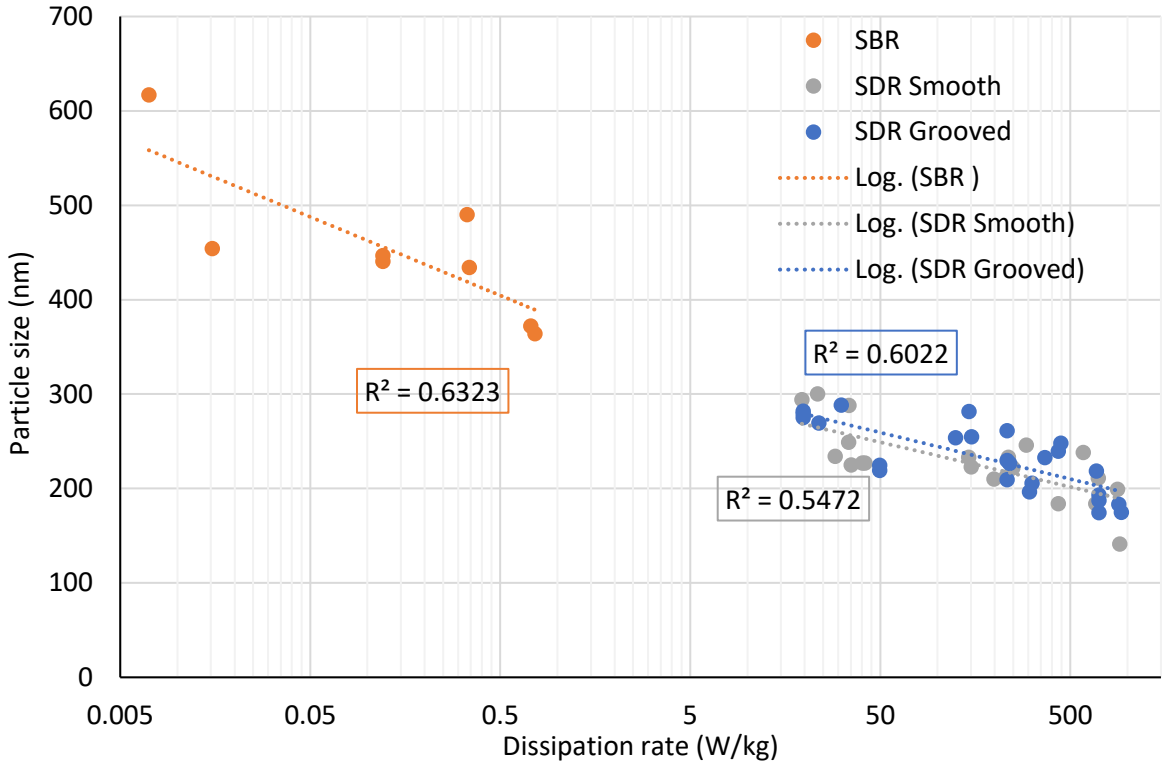

Figure 4-19: Plot of power dissipation vs. particle size of starch nanoparticles for the SBR and SDR.

The plot in Figure 4-19 shows that energy dissipation rate is higher for SDR experiments, with energy dissipation for SBR lying between 0.01- 0.8 W/kg, and between 20 and 1000 W/kg for the SDR. A higher energy dissipation rate means more energy available to be passed onto the liquid being processed in order to achieve better mixing. But it is important that the benefits of the high dissipation rate exceed the drawbacks of high energy consumption. In this case, the starch nanoparticle sizes obtained in the SDR are much smaller than those obtained in the SBR system. It should be pointed out that the bearings in the SDR are designed so that there is negligible resistance through air drag acting on the rotating disc, hence less energy is consumed in keeping the disc rotating. The agitator, however, in the SBR system is surrounded by bulk liquid, exerting a higher drag force on the impeller and requiring a larger energy input for its rotation. Furthermore, semi-batch setups are known to struggle to homogeneously circulate the energy supplied, often leading to local energy dissipation (Lafficher et al., 2018). The energy dissipation rate is related to micromixing time through the following relationship for both reactor systems (Baldyga et al., 1995):

$$t_{micro} = 17.2\left(\frac{\nu}{\varepsilon}\right)^{0.5} \quad (4\text{-}4)$$

The equation assumes micromixing is governed through the process of engulfment, which is valid when the Schmidt number ($Sc = {}^{\nu}/_{D}$), Sc < 10^3, as is the case for the current system (Boodhoo, 2013). The molecular diffusion coefficient, *D*, is approximately 10^{-10} m^2/s for the current system and has been estimated from the Stokes-Einstein equation ($D = \frac{kT}{6\pi\mu r}$), assuming *r* is equivalent to the value of a stable nuclei.

The values for micromixing time in the SDR are plotted against dissipation rate in Figure 4-20. A decrease in micromixing time is apparent as dissipation rate increases. In comparison, the micromixing time in the SBR ranges from 0.06 s to 0.6 s, which is an order of magnitude higher than the micromixing times estimated for the SDR. These results are presented in Figure 4-21. For a precipitation process, the mixing time is of great importance as $t_{micro} < t_{ind}$ suggests a low Damköhler number (Eq. 2-22), indicating a well-mixed system which promotes the production of smaller sized particles with a narrow size distribution, The induction times measured for the SDR system are estimated to lie between 0.03 to 0.15 s (section 4.4.1), however, the induction times in the SBR are not known, though the large micromixing times in the SBR indicate that larger induction times would be required to maintain a well-mixed system. A further comparison between micromixing time and induction times in the SDR are presented in Figure 4-22. The graphs show that micromixing time is a function of flow rate (Fig. 4-22 (A)), disc rotational speed (Fig. 4-22(B)), and antisolvent to solvent ratio (Fig. 4-22(C)), with rotational speed having a greater impact on micromixing, indicated by the more profound decline in micromixing time as disc speed is increased. As micromixing time is more than an order of magnitude lower than the induction time, homogeneous nucleation would be the dominant nucleation mechanism (Aguiar et al., 2003).

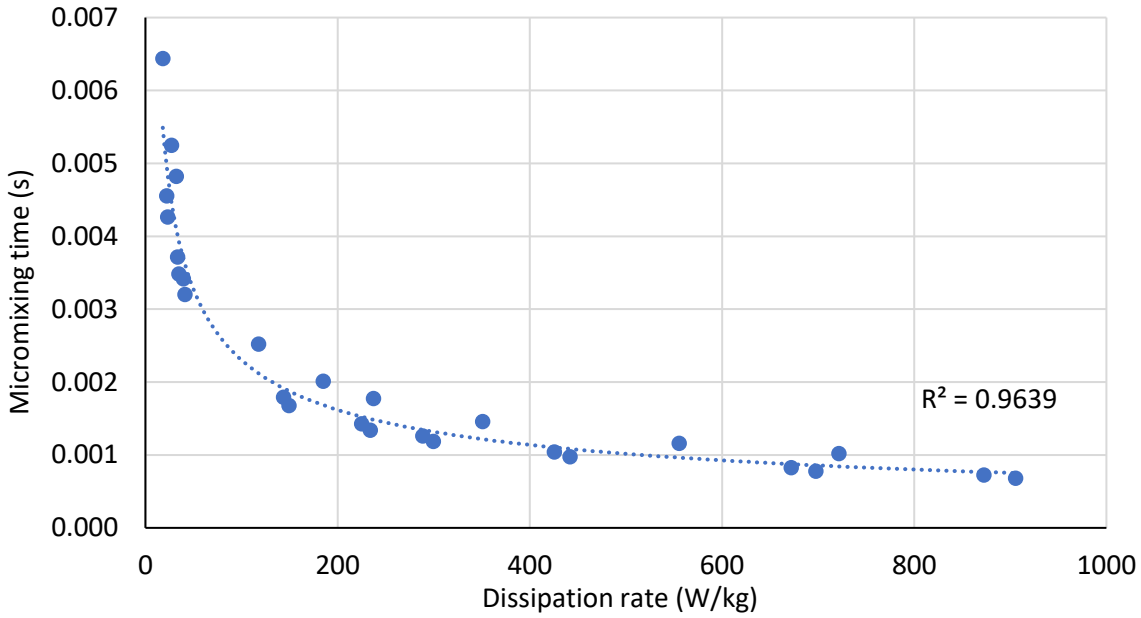

Figure 4-20: Micromixing time against dissipation rate for the SDR.

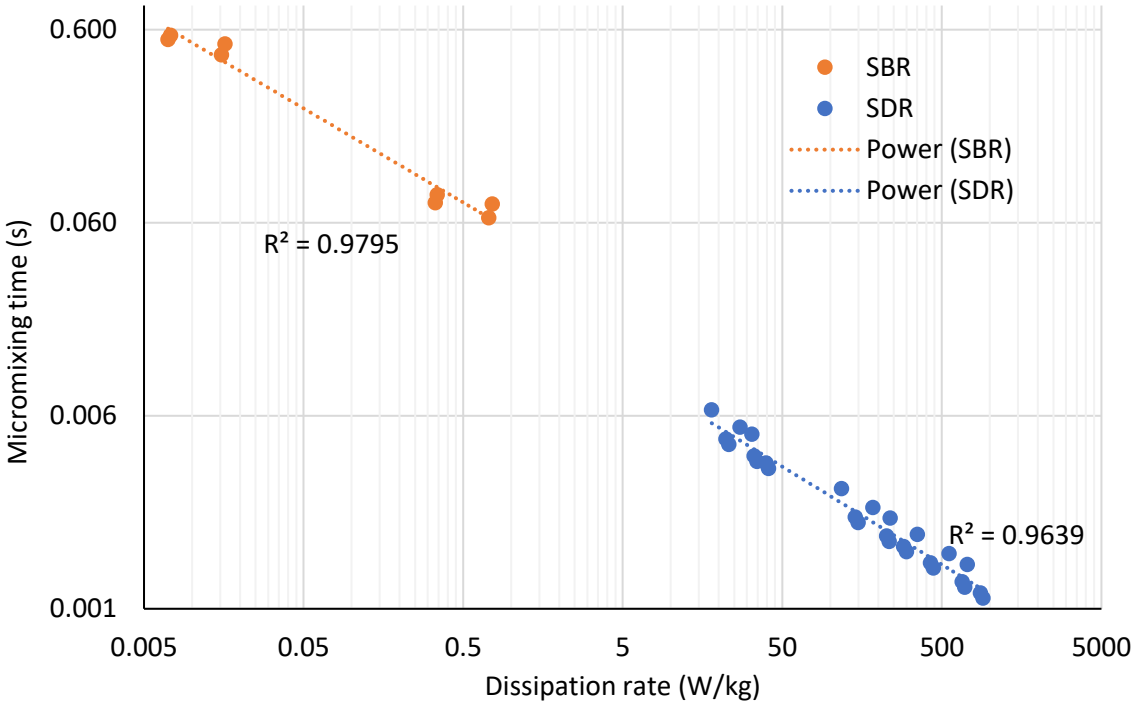

Figure 4-21: Micromixing time comparison for SBR and SDR.

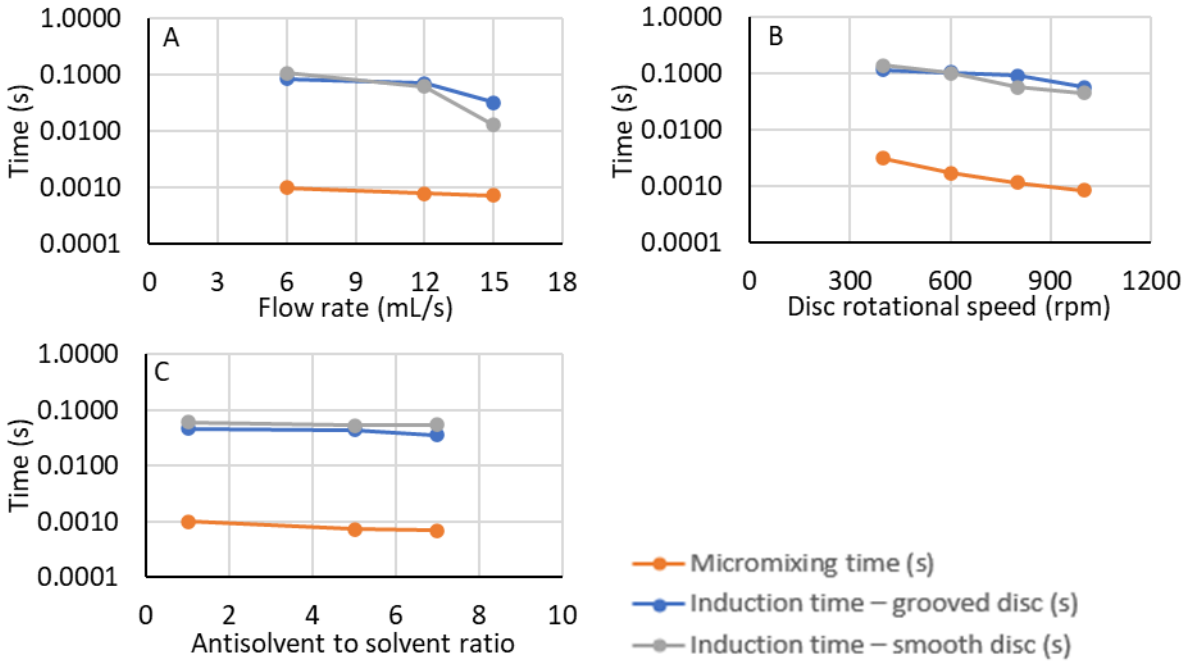

Figure 4-22: Comparison between induction times and corresponding micromixing times for smooth and grooved discs, showing the effect of A) flow rate (1200 rpm, 9:1), B) disc rotational speed (18 mL/s, 9:1), and C) antisolvent to solvent ratio (18 mL/s, 1200 rpm).

4.1.3. XRD analysis

Figure 4-23 shows the XRD plots for native corn starch along with the starch nanoparticles produced through solvent-antisolvent precipitation in the SDR. The latter set of results are reported for 9:1, 5:1 and 1:1 antisolvent to solvent ratios. For the native starch sample, peaks are present at 2θ= 15°, 17°, 18°, 20° and 23°. The XRD pattern corresponds to A-type crystallinity (Qin et al., 2016). Upon precipitation, the peaks at 15°, 17°, 18° and 23° disappear. The disappearance of these characteristic peaks has been related to the gelatinisation of starch in sodium hydroxide, causing disruption of starch's crystalline structure, as well as the reduction in particle size as ethanol is added for precipitation, causing a decline in crystallite size (Hu et al., 2016). The formation of the broad diffraction peaks at 20° and 13° in the precipitated nanoparticles reveals the V-type diffraction pattern corresponding to the reduction in crystallinity, and the transformation of the double helix originating from the native starch into a single helix. The single-helixed structure is an 'inclusion complex' made up of amylose and the antisolvent, ethanol (Qin et al., 2016). The extent of crystallinity possessed by the nanoparticles affect a number of physical properties. Bel Haaj et al. (2016) compared starch nanocrystals with starch nanoparticles, finding that starch nanocrystals retain greater thermal and colloidal stability. However, starch nanoparticles have a lower impact on transparency of a nanocomposite film than starch nanocrystals and have lower viscosities. Such properties would establish their suitability for

certain applications. In addition, starch nanoparticles have limited ionic strength in comparison to starch nanocrystals which make them ideal for food and drug delivery systems (Jiang et al., 2016). Furthermore, starch nanoparticles possess greater resistance to digestion as the presence of the V-type polymorph impedes digestion, whereas the A-type structure found in nanocrystals is readily digestible (Srichuwong et al., 2005). This property makes them able to survive acidic conditions, thus further demonstrating their suitability to drug delivery systems (Liu et al., 2016a, Ali Razavi and Amini, 2016, Le Corre and Angellier-Coussy, 2014).

As displayed in Figure 4-24, the degree of crystallinity is affected by the antisolvent to solvent ratio as the intensity of the V-type peaks falls with an increase in the amount of ethanol. The peak at a 1:1 ratio has a greater intensity in comparison to 9:1 ratio, however at a 5:1 ratio the peak at 20° is level with the peak at 1:1. The ethanol is said to induce the formation of the V-type complex (Liu et al., 2016b). However, it is also essential that the amylose content is sufficient for its formation (Cheetham and Tao, 1998). Despite there being a higher proportion of ethanol at the 9:1 ratio, the amylose content is limited, whereas at the lower antisolvent to solvent ratios there is adequate amounts of both the amylose and the ethanol to form the inclusion complex.

Peaks beyond 2θ= 28° correspond to impurities such as sodium carbonate. Carbon dioxide reacts with water in the atmosphere to form carbonate ions. The carbonate ions are then able to combine with any unwashed sodium ions present in the sample, producing sodium carbonate. The impurities have all been quantified separately and the presence of the internal reference material, silicon, has been accounted for through the Rietveld Refinement method. Results show that above 70 wt. % of each sample contribute to starch alone. XRD patterns are not affected by disc speed or flow rate, and so the influence of these are not discussed further.

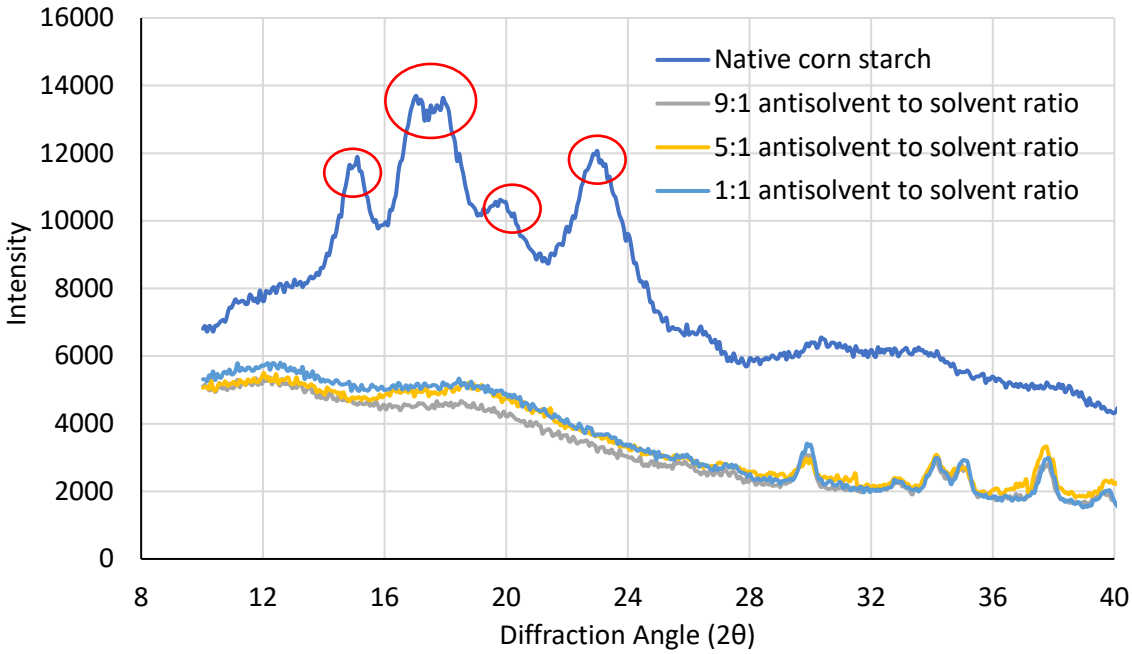

Figure 4-23: XRD plots for native corn starch and starch nanoparticles produced in the SDR at 9:1, 5:1 and 1:1 antisolvent to solvent ratios. With key peaks highlighted for native starch.

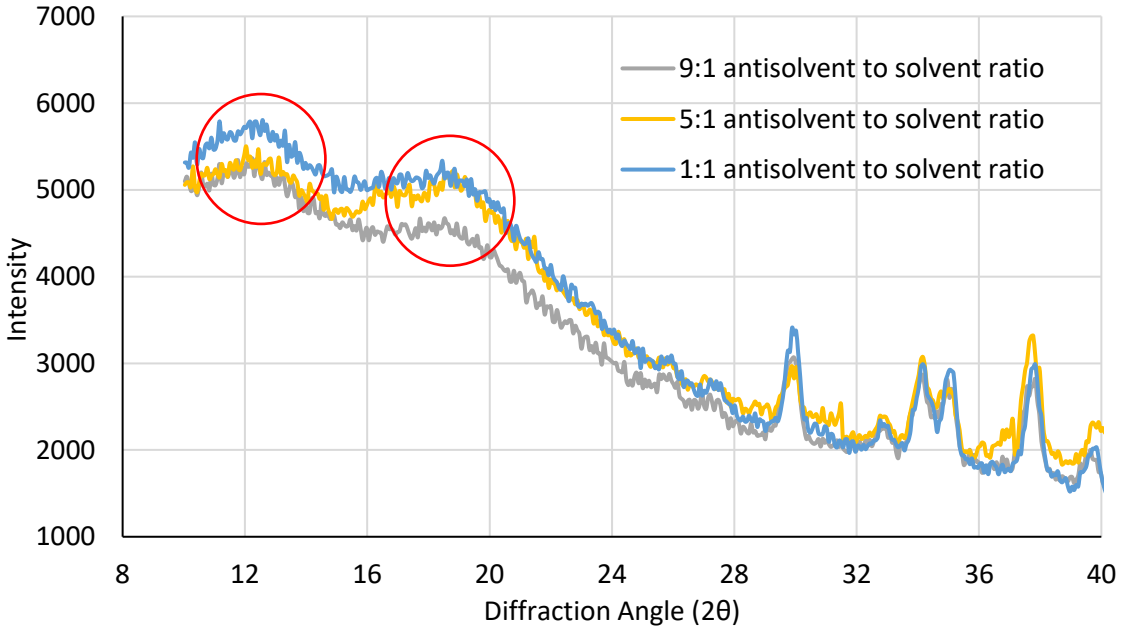

Figure 4-24: XRD plots for starch nanoparticles produced in the SDR at 9:1, 5:1 and 1:1 antisolvent to solvent ratios, with V-type peaks highlighted.

4.2. Dimensionless model for solvent-antisolvent precipitation in the SDR

Earlier in Chapter 4.1, the effects of certain experimental conditions on particle size were presented. To summarise, the results showed a reduction in particle size as flow rate, disc rotational speed and antisolvent to solvent ratio increased. The interactions of these single variables have been further analysed through empirical correlations consisting of the relevant dimensionless numbers derived to predict starch nanoparticle size for smooth and

grooved discs. In this section, various dimensionless numbers relevant to the SDR and the solvent/antisolvent process are first introduced, followed by the development of the empirical correlation using experimental results.

Reynolds number for thin film flow in the SDR is typically defined as (Boodhoo, 1999):

$$Re = \frac{2Q}{\pi \nu r} \tag{4-5}$$

It is commonly used to characterise liquid flow in the SDR as it is a function of flow rate and disc radius. This particular definition of Reynolds number, however, does not encompass the rotational aspect of the SDR. For this reason, another dimensionless number will also be incorporated into the model to characterise rotation of the disc, such as the Taylor number, *Ta:*

$$Ta = \frac{4\omega^2 r^4}{\nu^2} \tag{4-6}$$

The Taylor number is a ratio of inertial to viscous forces. Saw et al. (1985) used the Taylor number along with the Reynolds number to develop a predictive model for liquid film thickness. This was further applied by Khan (1986) and by Mohammadi (2014) who proposed that particle size is directly proportional to the dimensionless form of liquid film thickness. Their models assumed negligible Coriolis forces, provided Re^2/Ta is less than unity. As Re^2/Ta is in the range of 10^{-11} to 10^{-9} for the present work, the effect of Coriolis forces may be assumed to be negligible. Alternatively, the Rossby number has been used in previous work to characterise liquid flow on a spinning disc (Basu and Cetegen, 2006, Leneweit et al., 1999, Scheichl and Kluwick, 2019). It is defined as the ratio of inertial to Coriolis force. The Rossby number is presented in Eq. 4-7, where u_i is the inlet velocity calculated from total flow rate of the antisolvent and solvent/solute streams. The Rossby number is estimated to lie in the range of 0.045 to 0.405 for the operating conditions used in the present work, indicating dominance of Coriolis forces over inertial when $Ro < 1$, whereas centrifugal forces dominate when $Ro \ll 1$ (Leneweit et al., 1999). The Rossby number is often expressed as a product of the Ekman number, *Ek*, as presented in Eq. 4-8 (Rauscher et al., 1973). It implies that for a small Ro value, *Ek* will be large in order to maintain an order of magnitude of 1. In circumstances where $Ro \ll 1$, the Ekman number is significantly greater to satisfy Eq. 4-8, implying negligible Coriolis forces. Based on this, the *Ro* values in the present work are

considered to be within the region where Coriolis forces are negligible, as *Ek*>>1 at the outer region of the disc (Prieling, 2013).

$$Ro = \frac{u_i}{\omega r} \tag{4-7}$$

$$Ek.Ro \sim \mathcal{O}(1) \tag{4-8}$$

where $Ek = \frac{\nu}{\omega \delta^2}$

The rotational Reynolds number is another dimensionless number which may be used to describe the rotational aspect of flow on the film. Similar to the conventional Reynolds number, it is expressed in the following form:

$$Re_\omega = \frac{\omega r^2}{\nu} \tag{4-9}$$

The rotational Reynolds number provides an alternative over the conventional Reynolds number for characterising flow regime in the reactor as *Re* does not take angular velocity into consideration (Shevchuk, 2015). Similarly, Re_ω does not include flow rate in its expression. Ozar et al. (2003) states that both flow rate and disc speed play a major role in flow transition from laminar to turbulent. Rotational Reynolds number criteria for categorising flow regimes are as follows (Shevchuk, 2015):

$Re_\omega < 10^4$	Laminar regime
$10^4 \leq Re_\omega < 10^5$	Flow instabilities increase and flow is in transition to turbulent regime
$Re_\omega \geq 10^5$	Turbulent regime

Finally, previous dimensionless forms for film flow in a spinning disc reactor have focused on rotational speed and liquid flow (Khan, 1986, Mohammadi, 2014). However, in the present study, antisolvent to solvent ratio is as fundamental as the previous two parameters. To capture antisolvent to solvent ratio in a dimensionless form, the dimensionless supersaturation ratio term has been applied (Eq. 2-1b), reproduced below:

$$S = \frac{C}{C^*} \tag{4-10}$$

The regression models have been generated using the dimensionless forms mentioned. A comparison between three different models is highlighted. Starch nanoparticle sizes used to derive the empirical model are those obtained through the DLS instrument and are intensity-based means to maintain consistency with earlier chapters and reduce conversion errors.

The particle size for starch nanoparticles can be represented through Eq. 4-11 for the Taylor number. This particular form of linear multiple regression has been selected for simplicity and as it has been used previously in precipitation systems to predict particle size (Mohammadi, 2014, Valente et al., 2012).

$$Particle\ size\ (\text{microns}) = A\ Re^{a} Ta^{b} S^{c} \tag{4-11}$$

where *A* (microns), *a*, *b* and *c* are coefficients of the regression model. The units for particle size are in microns to avoid large values of coefficient *A* and to keep all coefficients roughly of similar magnitudes. Furthermore, with coefficient *A* and particle size being in microns ensures dimensional agreement is preserved.

The following models have been generated for the smooth and grooved discs:

Smooth disc $$Particle\ size\ (\text{microns}) = 10^{0.35} Re^{-0.08} Ta^{-0.06} S^{-0.03} \tag{4-12}$$
$$R^2 = 0.933,\ R^2\ (\text{adj.}) = 0.913$$

Grooved disc $$Particle\ size\ (\text{microns}) = 10^{0.28} Re^{-0.26} Ta^{-0.04} \tag{4-13}$$
$$R^2 = 0.930,\ R^2\ (\text{adj.}) = 0.909$$

The model is applicable for the following range at radial distances of 15 cm from the centre:

$$8.21 \leq Re \leq 52.36$$

$$3.69 \times 10^{11} \leq Ta \leq 1.50 \times 10^{13}$$

$$116 \leq S \leq 1074$$

Figure 4-25 displays a comparison between the experimental data and data predicted from the models given in Equations 4-12 and 4-13. The negative sign of the coefficients in Eqs. 4-12 and 4-13 indicate a negative correlation between the dimensionless parameters and particle size, that is, an increase in Reynolds number would lead to a reduction in particle size. This would occur at high flow rates or low viscosities as described in Equation 4-5. Similarly, the Taylor number is greater at higher disc rotational speeds, leading to a reduction in particle size. An increase in initial supersaturation ratio also results in smaller particles. Furthermore, the values of the coefficients in Equations 4-12 and 4-13 give an idea of how strongly each dimensionless number affects particle size, which suggests that Reynolds number is more influential than the other two parameters for both discs, with it being more of an influence on particle size on the grooved disc. This indicates that according to this correlation flow rate has a greater impact on particle size, particularly for the smooth

disc. Whereas there is no significant difference in the effect of the Taylor number between the two discs, with the coefficient being only slightly larger for the smooth disc. Supersaturation has the least impact on particle size, based on the small magnitude of the coefficient. For the grooved disc, however, the exponent for *S* was determined to be less than 0.01, therefore has been disregarded, assuming that supersaturation has very little to no effect on particle size. This may be caused by the supersaturation values used in this study being towards the higher end, and perhaps a larger range of values, particularly lower values of S, would give a different result. Additionally, ideal mixing conditions provided by the grooves could have contributed through the uniform distribution of supersaturation at all values of supersaturation. It is also worth noting that extreme results have been removed, specifically, particle size attained at 1:1 ratio and 18 mL/s, signifying the occurrence of backmixing have been regarded as outliers, thus distorting the results. R^2 and adjusted R^2 values are also presented in Eqs. 4-12 and 4-13 for the regression models. The values are greater than 0.9, indicating a good fit between the predictive model and the experimental results. The confidence intervals (CI) displayed in the plots have been obtained to demonstrate the upper and lower limits of the regression model at a 95 % confidence level. This tells us it is 95 % certain that the regression model lies within this interval and as most points lie within the bounds of the confidence interval, it can be concluded that the regression model is a good fit to predict particle size.

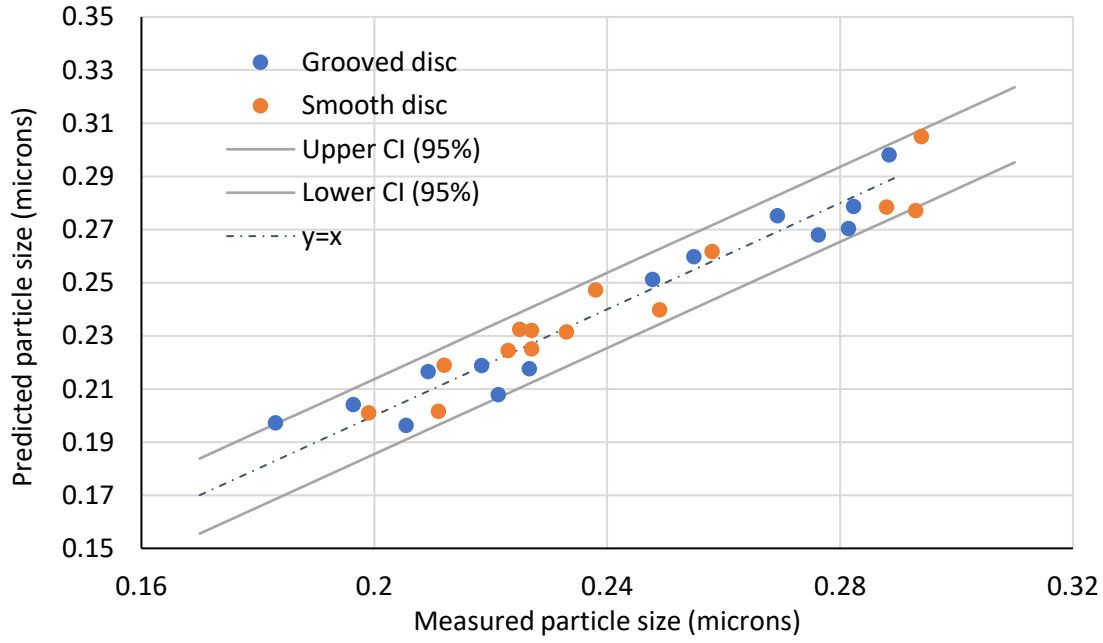

Figure 4-25: Comparison between predicted particle size and experimental particle size for smooth and grooved discs using Ta.

Similarly, a regression model with the rotational Reynolds number representing disc speed has been generated, again with *Re* and *S* characterising flow rate and antisolvent to solvent ratio. The particle size is represented in the following form:

Smooth disc $$Particle\ size\ (\text{microns}) = 10^{0.32} Re^{-0.08} {Re_\omega}^{-0.13} S^{-0.03} \quad (4\text{-}14)$$

$$R^2 = 0.933,\ R^2\ (adj.) = 0.913$$

Grooved disc $$Particle\ size\ (\text{microns}) = 10^{0.24} Re^{-0.26} {Re_\omega}^{-0.08} \quad (4\text{-}15)$$

$$R^2 = 0.930,\ R^2\ (adj.) = 0.909$$

Eq. 4-14 and 4-15 are valid for the following conditions at radial distances of 15 cm from the centre:

$$8.21 \leq Re \leq 52.36$$

$$3.04 \times 10^5 \leq Re_\omega \leq 1.94 \times 10^6$$

$$116 \leq S \leq 1074$$

Figure 4-26 compares particles sizes predicted from Eq. 4-14 and 4-15 to the measured particle sizes. According to the range of rotational Reynolds numbers encountered in the SDR, the flow is primarily in the transitional or turbulent regime. Though the conventional Reynolds number, *Re*, suggests the flow regime falls between laminar and wavy-flow regimes. It is apparent from Eq. 4-14 and 4-15 that the rotational Reynolds number, hence disc rotational speed is more significant in the smooth disc, whereas *Re,* hence flow rate is more influential in the grooved disc. An explanation for this would be that in the presence of grooves the flow regime is more likely to transition into turbulent flow at lower values of Re_ω (Shevchuk, 2015). This would mean that the grooved disc is capable of achieving greater turbulence at lower disc rotational speeds, hence the grooved disc is influenced less by disc speed and more by flow rate. Although these results are somewhat different to the model derived using the Taylor number, which suggests Reynolds number, hence flow rate is more significant on both discs, it is worth noting how close the values of the coefficients for *Re* and *Ta* are in Eq. 4-12. Additionally, similar to the previous model, the exponent for *S* is considerably low, particularly for the grooved disc, and hence has been disregarded, indicating that supersaturation has little influence on particle size for the reasons provided earlier. For this reason, it is not possible to assume which of the two models represent the starch nanoparticle system better, especially since the R^2 and R^2 adjusted (Eqs. 4-14 and 4-

15) are also above 0.9 for this model, yet again indicating a good fit. Similarly, CI displayed in the plot is narrow with all points lying within that region.

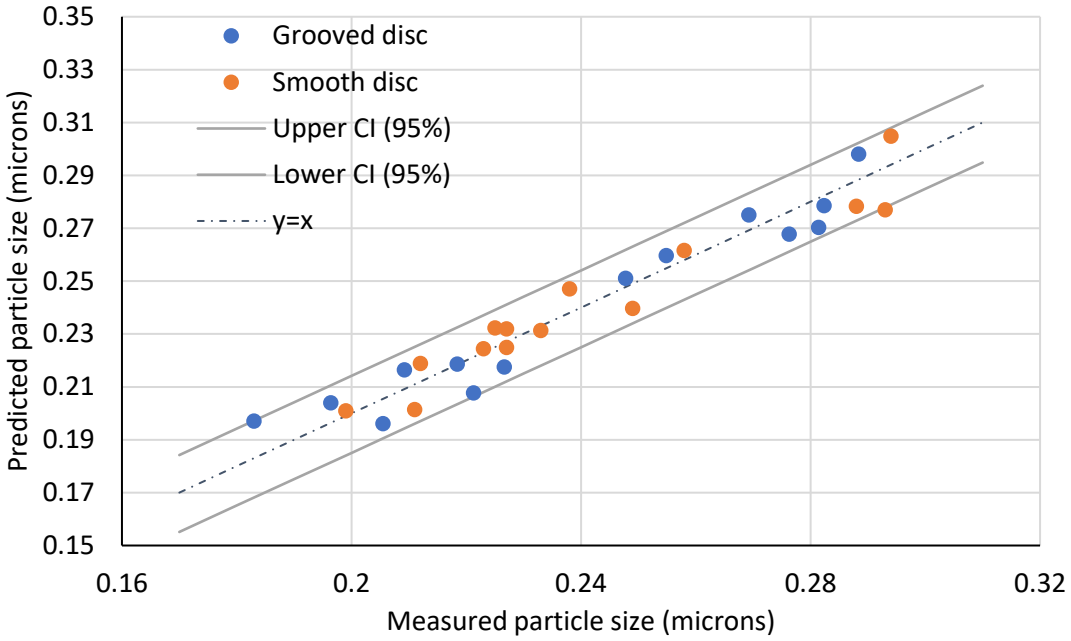

Figure 4-26: Comparison between predicted particle size and experimental particle size for smooth and grooved discs using Re_{ω}.

Finally, a regression model has been generated using the Rossby number to characterise disc rotation. As the Rossby number is a function of both inlet velocity and angular velocity (Eq. 4-7), the Rossby number will be applied in this next model to characterise both flow rate and disc rotational speed. The following models have been obtained for the smooth and grooved discs at a 15 cm radial distance from the centre.

Smooth disc $$Particle\ size\ (\text{microns}) = 10^{-0.37} Ro^{0.03} S^{-0.08} \quad (4\text{-}16)$$

$$R^2 = 0.778,\ R^2\ (adj.) = 0.734$$

Grooved disc $$Particle\ size\ (\text{microns}) = 10^{-0.36} Ro^{-0.06} S^{-0.12} \quad (4\text{-}17)$$

$$R^2 = 0.854,\ R^2\ (adj.) = 0.830$$

The model is applicable for the following range:

$$0.045 \leq Ro \leq 0.405$$

$$116 \leq S \leq 1074$$

Figure 4-27 shows a comparison between the predicted and measured particle size values using the models given in Equations 4-16 and 4-17. The values of R^2 and R^2 adjusted (Eqs. 4-16 and 4-17) for the current regression model are lower in comparison to the previous two

models. One reason for this would be that an increase in the number of independent variables in a multiple regression model usually tends to increase R^2 values, bringing them closer to 1.

In Eq. 4-17, the coefficient for the Rossby number has a negative sign for the model predicted for the grooved disc, implying that as the Rossby number increases, particle size decreases. An increase in *Ro* would be influenced by greater flow rate, which agrees with the previous model, suggesting that disc rotational speed has less of an effect on particle size on the grooved disc. On the smooth disc the opposite is true, indicated by the positive coefficient for the Rossby number, representing a greater dependence of particle size on disc rotational speed. A decrease in the Rossby number, caused by an increased disc rotational speed, would produce smaller sized particles on the smooth disc. However, because both flow rate and disc speed parameters are represented by the single dimensionless number, it is difficult to speculate the exact relationship between the parameters and *Ro*. Furthermore, unlike the previous two models, here supersaturation appears to have more of an impact on particle size, as implied by the larger coefficient.

At large flow rates and low disc rotational speeds, the Rossby number increases towards a value of 1. At such conditions, Coriolis forces start coming into play, deviating from the Nusselt model (Ghiasy et al., 2013). However, the highest value for the Rossby number is 0.405, which is still smaller than 1, meaning that centrifugal forces are dominating.

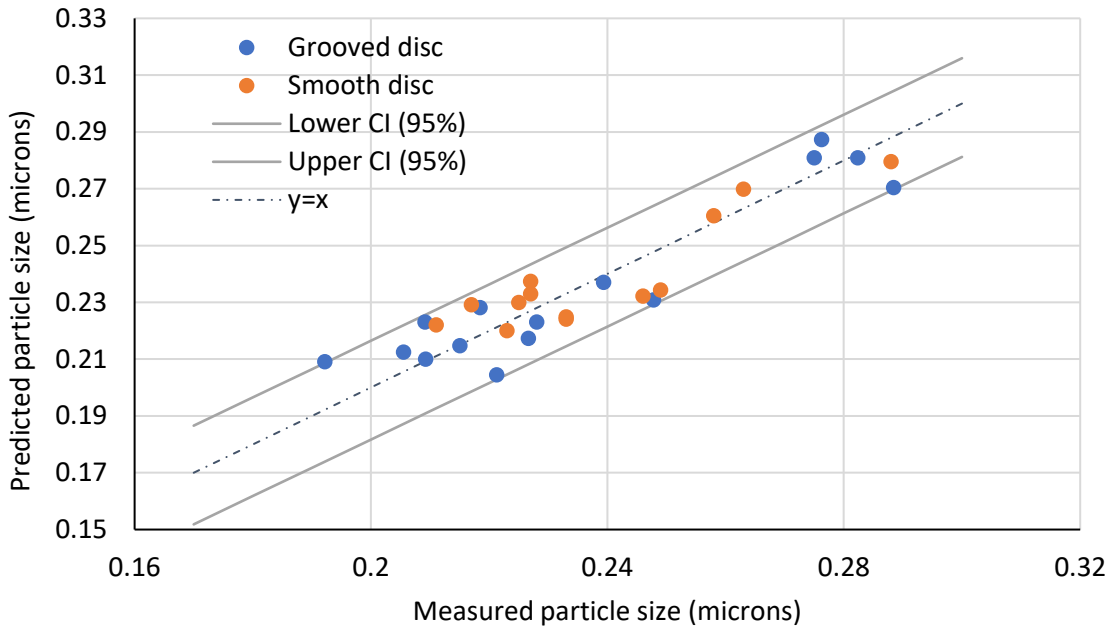

Figure 4-27: Comparison between predicted particle size and experimental particle size for smooth and grooved discs using Ro.

All three models show good correlation between the predicted and measured particle size values at the 95 % confidence interval. The Rossby number, however, only considers the liquid at the entrance of the SDR and does not take account of the viscous forces on the disc, whereas both, the Taylor number and the rotational Reynolds number, as well as Reynolds number for flow rate, incorporate the effect of shear through the viscosity term. Furthermore, above the stated range of Rossby numbers studied Coriolis forces may begin to dominate and for the Nusselt model to be valid Coriolis forces must be negligible, which is true for the experimental conditions studied as $\nu \gg \omega\delta^2$ (Appendix G), where δ is the film thickness (Boodhoo, 1999). The empirical models using *Ta* and Re_ω provide a better fit of the data as indicated by the R^2 which are above 0.9 for both discs. Finally, the dimensionless quantities have been estimated for radial distances close to the edge of the disc, and as conditions, such as film thickness, vary along the radius of disc, the dimensionless numbers would be affected by the radius, *r*. However, as nanoparticle samples have been collected at the edge of the disc, the effect of radial distance on the dimensionless correlations have not been investigated further.

4.3. Summary

This section demonstrated the solvent-antisolvent precipitation of starch nanoparticles in a spinning disc reactor. The impact of operating conditions such as total flow rate, antisolvent to solvent ratio and disc rotational speed were investigated. It has been observed that an

increase in flow rate, antisolvent to solvent ratio and disc speed all caused a reduction in particle size. Yield experiments also showed a similar trend of increased flow rate, disc speed and antisolvent to solvent ratio resulting in higher yields; more so on the grooved disc. It may be deduced that disc speed and total flow rate increase shear and instabilities within the liquid film, enhancing mixing between solvent and antisolvent, thus producing smaller sized starch nanoparticles with narrow PSDs. In addition to this, the increased antisolvent to solvent ratio decreases solubility and promotes nucleation through increased supersaturation. Increasing starch concentration from 2 % w/v to 4 % w/v showed a reduction in particle size at lower disc speeds and flow rates. However, increasing disc rotational speed and flow rate caused an increase in particle size, indicating greater agglomeration as a result of amplified supersaturation and mixing conditions.

Comparisons between the smooth and grooved surfaces were made to investigate their impact on particle size, PdI and yield. It was noticed that, although the smooth surface resulted in slightly smaller particles in some cases, the smooth surface of the disc did not have an extreme effect on particle size, and thus it would be reasonable to conclude that the disc surface does not significantly affect the mean size of the starch nanoparticles. In contrast, the disc surface was found to have a more significant impact on PdI value, caused by increased plug flow on the grooved disc, which resulted in narrower size distributions.

Furthermore, comparisons were made between starch precipitation in the SDR and a semi-batch set-up. Results showed a decrease in particle size and a narrower size distribution as well as less agglomeration amongst starch nanoparticles produced in the SDR. Power dissipation was calculated to be greater in the SDR which translated into a greater degree of micromixing between the solvent/solute and the antisolvent. For this reason, the micromixing time was an order of magnitude smaller in the SDR. The smaller micromixing time suggested a lower Damköhler number, hence homogeneous nucleation being the dominant mechanism in starch precipitation. Finally, XRD patterns of the precipitated starch nanoparticles indicated a decline in crystallinity, with the particles being of an amorphous nature. The intensities of the XRD peaks were affected by the antisolvent to solvent ratio alone and not the operating conditions of the SDR such as flow rate or disc speed.

Empirical correlations have been developed relating the size of starch nanoparticles produced in the SDR to the key parameters: flow rate, disc rotational speed and antisolvent to solvent ratio. Dimensionless numbers have been applied to characterise these

parameters. Three linear regression models have been proposed through combinations of: Reynolds number, Taylor number, rotational Reynolds number, Rossby number and dimensionless supersaturation demonstrating good correlation between measured and predicted particle sizes for starch nanoparticles. Correlations obtained using the Taylor number and rotational Reynolds number to characterise disc speed have provided the best results.

4.4. Precipitation kinetics

4.4.1. Induction time

Induction time was acquired visually by means of a high-speed camera system. Figure 4-28 shows an example image captured by the high-speed camera. The particles appearing on the disc are highlighted in the image. The particles highlighted here are most likely agglomerates of approximately 50 microns in size, or a build-up of particles on the disc as they precipitate at the specified locations. The starch nanoparticles produced in the system are in the nanometre range, thus undetectable by the naked eye or indeed to the camera system as the absolute limit for visible light optical detection is in the order of 200 nm (Chen et al., 2011). However, magnification was limited as the images required had to cover most of the disc surface. An assumption has been made that nucleation occurs between the feed pipe inlet and these radial distances, r_{ind} as shown in Figure 4-28, before the particles accumulate and become visible. Induction time is the sum of the time required for the formation of a stable nucleus and the time for the particle to grow to a detectable size (Myasnikov et al., 2013). This has been highlighted earlier in the form of Eq. 2-9. There is no universal method of determining induction time, and so, the more sensitive the detection device, the lower the determined induction time (Kubota, 2008). A theoretical value for induction time depends solely on chemical parameters, such as concentration, solubility and supersaturation, but ignores reactor geometry and mixing conditions, and hence it is expected that the conditions in the SDR would impact induction time. In the present work, it can be said that the estimated induction time is the maximum induction time. However, no such estimation of nucleation has ever been made using the SDR for any crystallisation system, up until the time of this research.

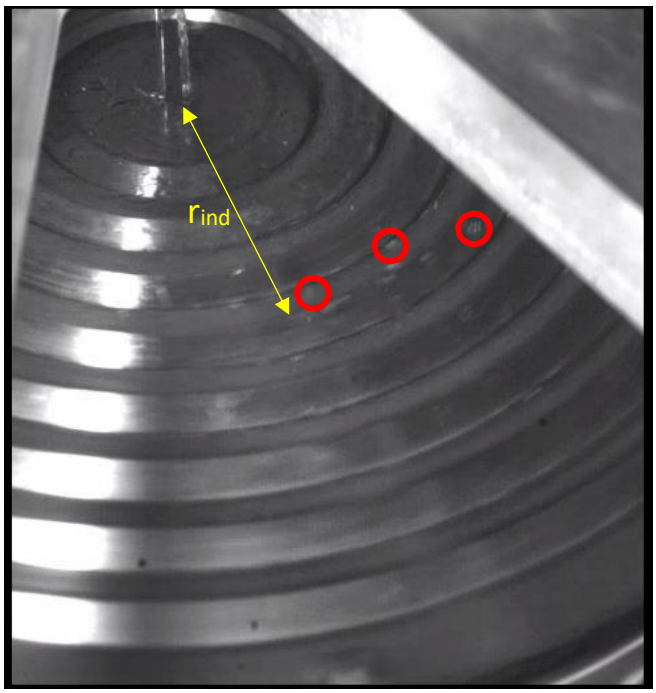

Figure 4-28: Example image from high-speed camera for induction time estimation.

Table 4-2 presents the estimated values of induction time for both grooved and smooth disc surfaces, using Equation 4-18.

$$t_{ind,SDR} = \frac{3}{4}\left(\frac{12\pi^2\nu}{\omega^2 Q^2}\right)^{1/3}\left(r_{ind}^{4/3} - r_i^{4/3}\right) \quad (4\text{-}18)$$

where r_{ind} is the radial distance from the centre at which induction is observed as shown in Figure 4-28.

Table 4-2: Radial positions observed via high-speed camera system and the respective induction time estimations for grooved and smooth discs at various operating conditions (additional experiments)*

Total flow rate (mL/s)	Disc speed (rpm)	Antisolvent to solvent ratio	Radial position of induction – grooved disc (cm)	Induction time – grooved disc (s)	Radial position of induction – smooth disc (cm)	Induction time – smooth disc (s)
18	400	9:1	6.0	0.118 ± 0.0054	7.0	0.144 ± 0.0254
*18	600	9:1	6.9	0.107 ± 0.0012	7.0	0.109 ± 0.0118
18	800	9:1	7.2	0.093 ± 0.0100	5.1	0.059 ± 0.0018

*18	1000	9:1	5.6	0.058 ± 0.0032	4.8	0.046 ± 0.0033
18	1200	9:1	ND	ND	ND	ND
*15	1200	9:1	3.6	0.032 ± 0.0018	2.0	0.013 ± 0.0027
12	1200	9:1	5.8	0.070 ± 0.0065	5.3	0.062 ± 0.0024
6	1200	9:1	4.9	0.090 ± 0.0037	5.7	0.106 ± 0.0102
*18	1200	7:1	4.2	0.036 ± 0.0032	5.8	0.055 ± 0.0036
18	1200	5:1	4.9	0.044 ± 0.0025	5.6	0.053 ± 0.0147
18	1200	1:1	4.6	0.047 ± 0.0008	5.0	0.062 ± 0.0049

ND – not determined due to experimental/measurement limitations

Generally, with a few exceptions, induction time appears to be lower on the grooved disc for identical operating conditions in the SDR, which may be the result of increased formation of eddies as turbulence increases in the presence of the grooves. The increased turbulence on the disc enhances mixing and the contact between the solvent/solute and the antisolvent, causing induction to occur earlier. It is worth noting that at the conditions of 18 mL/s, 1200 rpm and 9:1 ratio, induction time could not be estimated using the visualisation method. A reason for this could be that induction time is exceedingly low and possibly occurs within the central region of the disc, and as a result of the high disturbance in that region caused by liquid entering onto the disc surface at a high flow rate, nucleation would go undetected by the visualisation method. In addition to the high flow rate, the high disc rotational speed makes it difficult to capture a clear image of particles on the disc in order to calculate induction time. Consequently, further experiments were conducted at conditions less extreme than 18 mL/s, 1200 rpm and 9:1 ratio. These results are also displayed in Table 4-2, marked with an asterisk. At the higher flow rates and a constant ratio of 9:1, the induction times on the smooth disc are lower. This is due to discontinuity of the liquid film in

presence of the grooves which prevents efficient mixing between the liquid streams in the spinning disc reactor. This phenomenon is discussed further in section 4.4.2.

To investigate reproducibility of the data, conditions of 6 mL/s and 12 mL/s (1200 rpm and 9:1 ratio) were repeated twice on the grooved disc. Errors of 11 % and 5 % were estimated for 6 mL/s and 12 mL/s runs, respectively. As these errors are not significantly large, it may be assumed that the reproducibility of the induction time experiments is fairly good. However, to get a better idea of what conditions affect these errors, further repeats are suggested.

The shear generated in the spinning disc reactor is influenced by flow rate and disc rotational speed, as shear increases with an increase in both the flow rate and disc speed. Furthermore, increased shear has a shear thinning effect on the starch solution which leads to a reduction in viscosity, hence making mixing of antisolvent within the solute/solvent mixture easier (see Appendix E). The effect of shear rate on induction time is presented in Figure 4-29. The plots show a decline in induction time as shear rate increases and enhances mixing between the solvent/solute and antisolvent. A power trend has been fitted to the data with relatively good fit (R^2 between 0.87 and 0.88), and all points lie within 25 % of upper and lower limits once 5 outliers have been removed. The outliers removed from the plot are primarily from the grooved disc and are linked to the conditions where induction time on the grooved disc tends to be exceedingly greater than that on the smooth disc. An explanation for this has been given in detail in the next section. A similar plot was presented by Liu and Rasmuson (2013), demonstrating the inverse relationship between shear and induction time of butyl paraben precipitation in a Taylor-Couette.

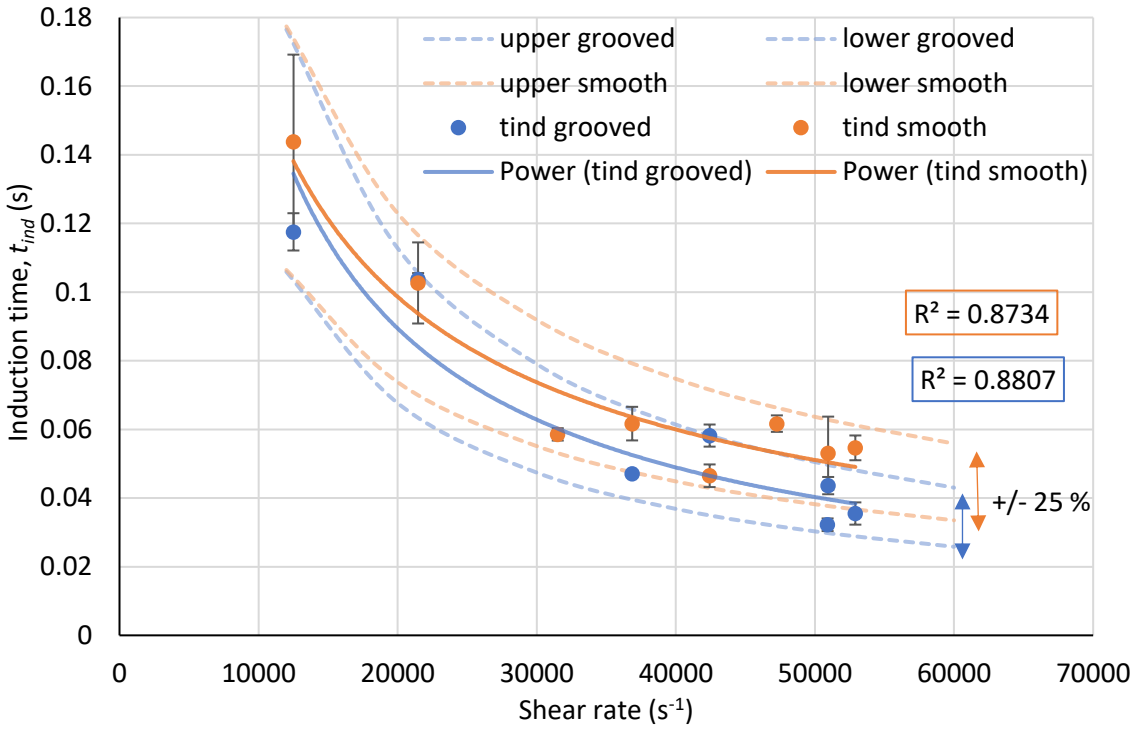

Figure 4-29: Induction time for grooved and smooth discs as a function of shear rate.

4.4.1.1. Interfacial tension and critical radius

The critical radius is defined as the minimum size of a particle nucleus at which the particle is stable (Mullin, 2001). It is a function of nanoparticle/solution interfacial tension, the value of which can be found through a plot of ln (induction time) vs (ln supersaturation)$^{-2}$ (Myerson, 2002),shown in Figure 4-30. However, to find interfacial tension from such a plot, the condition of true homogeneous nucleation must be fulfilled. Homogeneous nucleation occurs at high values of supersaturation whereas heterogeneous nucleation is said to occur at lower supersaturation values. Hence, the data is restricted to the range of supersaturation values where only homogeneous nucleation occurs. Such a plot for this system is shown in Figure 4-31, where the gradient is equal to:

$$\frac{16\pi\gamma^3\varphi_m^2}{3k^3T^3} \qquad (4\text{-}19)$$

where, γ is interfacial tension, φ_m is molar volume calculated using an average value of 692 g/mol for the molecular weight of starch (Sigma Aldrich, UK), and *k* is the Boltzmann constant.

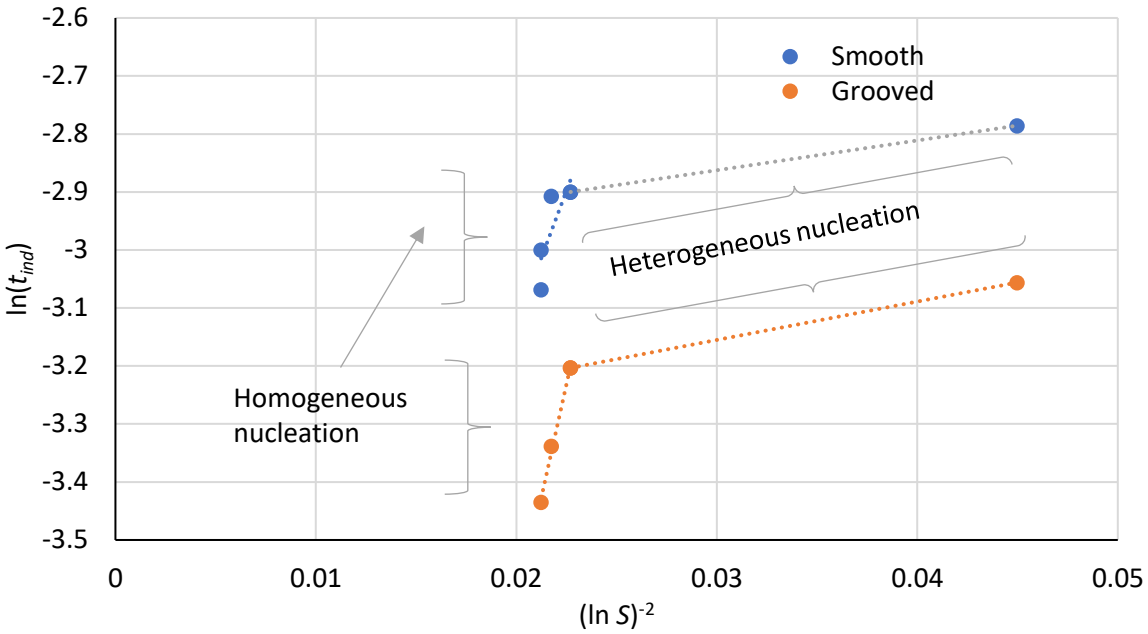

Figure 4-30: Plot of ln (induction time) vs ln (supersaturation)$^{-2}$ showing homogeneous and heterogeneous nucleation of starch nanoparticles (1200 rpm, 18 mL/s).

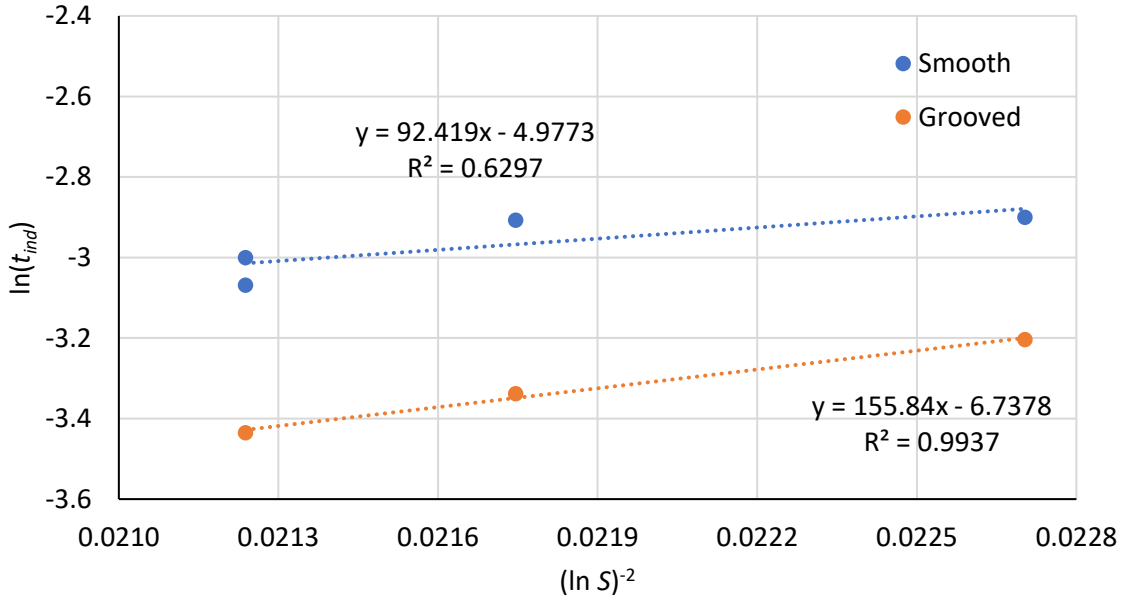

Figure 4-31: Plot of ln (induction time) vs ln (supersaturation)$^{-2}$ for the estimation of interfacial tension.

The interfacial tension has been estimated from Equation 4-19 as 10.33 mJ/m^2 for the grooved disc and 8.68 mJ/m^2 for the smooth disc. The value for interfacial tension estimated on a grooved disc is greater than that obtained for the smooth disc. This may suggest that more work is required to form the interface of the new phase on the grooved surface. This difference may be caused by the slightly smaller sized particles formed on the smooth surface. Additionally, the R^2 value for the smooth disc data is smaller than that for the grooved disc, which could be improved if the number of data points from which the

interfacial tension has been calculated was greater. Nevertheless, the interfacial tensions for the disc surfaces is not significantly different and will be used for further calculations.

Values of interfacial tension for a starch-NaOH-ethanol system are not available in literature and interfacial tension for starch nanoparticles has only been reported for an oil-water medium, ranging from 18 mJ/m^2 to 39 mJ/m^2 for 100 nm sized particles, with interfacial tension varying as a function of particle concentration and size (Pei et al., 2017). The more concentrated and smaller the particle, the lower the interfacial tension. In addition, the values reported are for an emulsion system, naturally having greater interfacial tension due to the immiscible nature of oil and water. A number of factors impact the interfacial tension, the key influencer being solubility. Omar et al. (2006) studied the effect of various solvents on solid-liquid interfacial tension of paracetamol. They found that interfacial tension increased with decreasing solubility, as at a constant supersaturation, reducing solubility by using a less polar solvent resulted in larger induction times for homogeneous nucleation thus increasing the value of interfacial tension. Many precipitation systems compare well to these estimates, especially polar substances such as urea in an ethanol-water system for which interfacial tension has been estimated to be between 4.2 - 8.9 mJ/m^2 (Lee et al., 1976). Granberg et al. (2001) found the interfacial tension for paracetamol at various acetone-water mixtures to be between 1-3 mJ/m^2. The interfacial tension for L-asparagine monohydrate has been reported to be 10.3 mJ/m^2 for a water/2-propanol solvent/antisolvent precipitation system (Lindenberg and Mazzotti, 2011). Mahajan and Kirwan (1994) also estimated the interfacial tension of L-aspargine through nucleation kinetics in a similar solvent/antisolvent system. The estimated value was slightly lower, around 6.1 mJ/m^2. Lindenberg and Mazzotti (2011) considered this discrepancy a result of different reactor systems and experimental procedures such as sampling. Kuldipkumar et al. (2007) estimated the interfacial tension for Tolazamide crystals in a buffer solution lay between 1.94 to 2.80 mJ/m^2, further reporting values for asparagine as 4.4 mJ/m^2.

Two simplified theoretical models for interfacial tension have been proposed by Bennema and Söhnel (1990) and Mersmann (1990):

$$\gamma = kT{\varphi_m}^{-2/3}0.25(0.7 - ln\, x^*) \qquad (4\text{-}20)$$

$$\gamma = 0.414\, kT\, (c_s N_A)^{2/3} \ln\left(\frac{c_s}{c_{eq}}\right) \qquad (4\text{-}21)$$

where x^* is equilibrium solubility, c_s is solute concentration and c_{eq} is the equilibrium concentration.

Using Eq. 4-20, the interfacial tension range for the starch system in the present work is estimated as 23 mJ/m^2 to 26 mJ/m^2 for x^* values between 7x10^{-10} and 6x10^{-9}. Using Mersmann's correlation in Eq. 4-21, the estimated interfacial tension lies between 19 mJ/m^2 to 20 mJ/m^2.

The values predicted from the empirical correlations are over twice the size of the values obtained from the experimental results. Similar results have been reported by researchers in previous works. Granberg et al. (2001) used Eqs. 4-20 and 4-21 to predict the interfacial tension of paracetamol in acetone-water mixtures, concluding that the experimentally obtained values were lower than those predicted from these equations. Similarly, Dalvi and Yadav (2015) found that the two equations estimated values of interfacial tension as an order of magnitude higher than the experimental values for curcumin in aqueous ethanol solutions. The empirical relationships derived by Bennema and Söhnel (1990), and the Mersmann (1990) equation are primarily for inorganic solutes in water with solid-liquid interfacial tensions lying between 10-30 mJ/m^2, thus not entirely useful for starch nanoparticles in ethanol/sodium hydroxide solutions.

As the interfacial tension has been estimated, the critical radius for each of the experimental conditions can be determined using the following equation:

$$r_c = \frac{2\gamma\varphi_m}{kT\ lnS} \tag{4-22}$$

The critical radii for the different conditions on the SDR are presented in Table 4-3.

Table 4-3: Critical radii for grooved and smooth discs.

Flow rate (mL/s)	Disc rotational speed (rpm)	Antisolvent to solvent ratio	Critical radius – grooved (nm)	Critical radius – smooth (nm)
18	400	9:1	0.551	0.463
18	600	9:1	0.551	0.463
18	800	9:1	0.551	0.463
18	1000	9:1	0.551	0.463
18	1200	9:1	0.551	0.463

15	1200	9:1	0.551	0.463
12	1200	9:1	0.551	0.463
6	1200	9:1	0.551	0.463
18	1200	7:1	0.558	0.469
18	1200	5:1	0.570	0.479
18	1200	1:1	0.809	0.680

As a result of the higher interfacial tension estimated for the grooved disc, the critical radii are also higher than the critical radii on the smooth disc. Critical radii values stated in literature are of a similar range, for example Granberg et al. (2001) found that the critical radius for paracetamol ranged from 0.5 to 2.5 nm. Furthermore, the equation for critical radius shows that it is dependent on supersaturation alone, and not on other conditions such as flow rate or disc speed. Shear rate is also not considered in the critical radius calculation. Theoretically, higher shear rate would increase the size of the critical radius, as shear influences the total free energy for nucleation. An increase in shear causes elastic deformation of the nucleus, as a result of which the free energy due to deformation increases. This then shifts the size of the critical nucleus to a greater value which would mean the critical size of the nucleus would be expected to be larger than the values presented in Table 4-3 (Mura and Zaccone, 2016).

4.4.2. Nucleation rate

Nucleation rate is defined as the number of nuclei formed per unit volume per unit time. It is a function of particle count and induction time expressed through the following equation:

$$Nucleation\ rate\ (mL^{-1}s^{-1}) = \frac{Particle\ count\ (mL^{-1})}{Induction\ time\ (s)} \quad (4\text{-}23)$$

Figure 4-32 shows the effect of flow rate on nucleation rate. Nucleation rate increases with an increase in flow rate. This is caused mostly by an increase in shear rate which lowers induction time. Furthermore, at higher flow rates, instabilities increase and waves on the surface of the liquid film are formed, which enhances mixing between the antisolvent and solute/solvent streams. Better mixing between the liquids causes more successful collisions by particles to form nuclei, hence resulting in a higher nucleation rate. This phenomenon is also observed with increasing disc rotational speed, presented in Figure 4-33. An increase in disc rotational speed causes an increase in nucleation rate, with the highest escalation in nucleation rate occurring from 600 to 800 rpm, above which the increase in nucleation rate

with respect to disc speed slows down. This could be explained by the effect of shear on the formation of the critical nuclei. As mentioned earlier, under shear the transport of molecules towards the nucleus increases which increases the rate of formation of nuclei. However, by further increase in shear, deformation of nuclei occurs, causing the critical radius value to increase as the energy barrier increases as a result of that deformation. This results in slower nucleation. Such an occurrence often leads to the presence of a maximum nucleation rate (Mura and Zaccone, 2016, Yang et al., 2016). Nucleation rate is a weak function of antisolvent to solvent ratio as shown in Figure 4-34. There is an initial increase in nucleation rate as the greater amount of antisolvent added reduces solubility of starch in NaOH and increases supersaturation. The increased supersaturation then results in nucleation dominating over the growth of the particles. There is, however, a decrease in nucleation rate at the highest antisolvent to solvent ratio of 7:1, particularly evident for the grooved disc. This could be explained through the TEM images shown in Figure 4-35 which indicates the presence of agglomerates as antisolvent to solvent ratio is increased from 5:1 to 9:1. The formation of agglomerates is facilitated by the production of smaller nanoparticles at higher supersaturations, as has been highlighted in section 4.1.1. This may lead to a cluster of particles being picked up as one single particle, thus reducing the estimated values of particle count and nucleation rate.

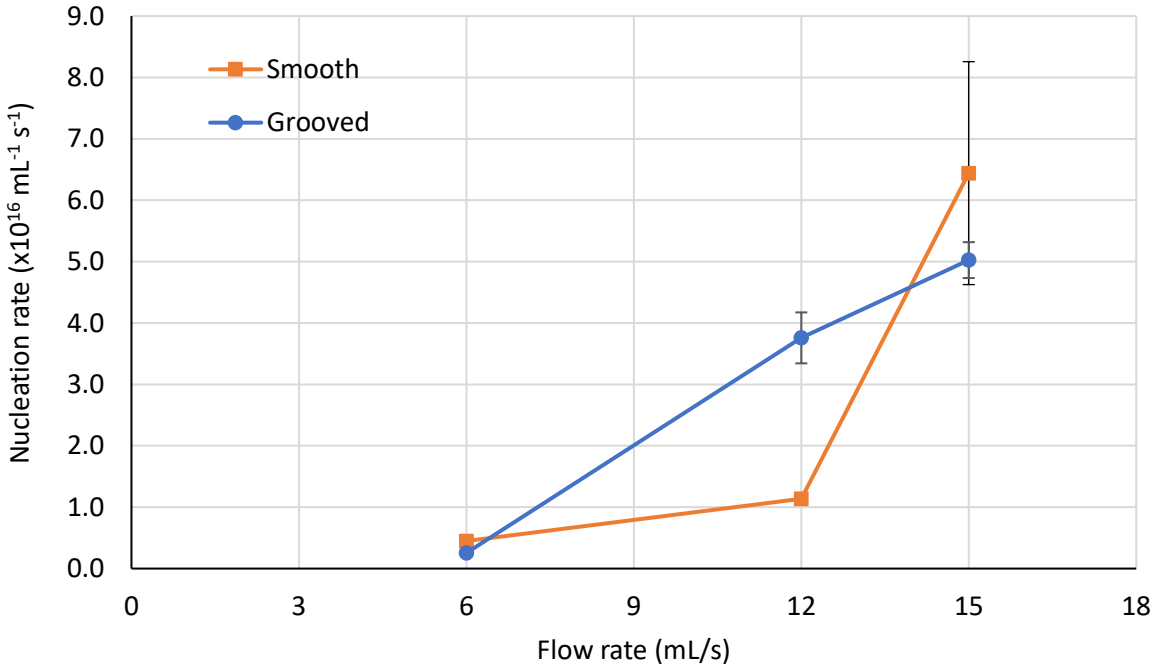

Figure 4-32: Effect of flow rate on nucleation rate (1200 rpm and 9:1 ratio).

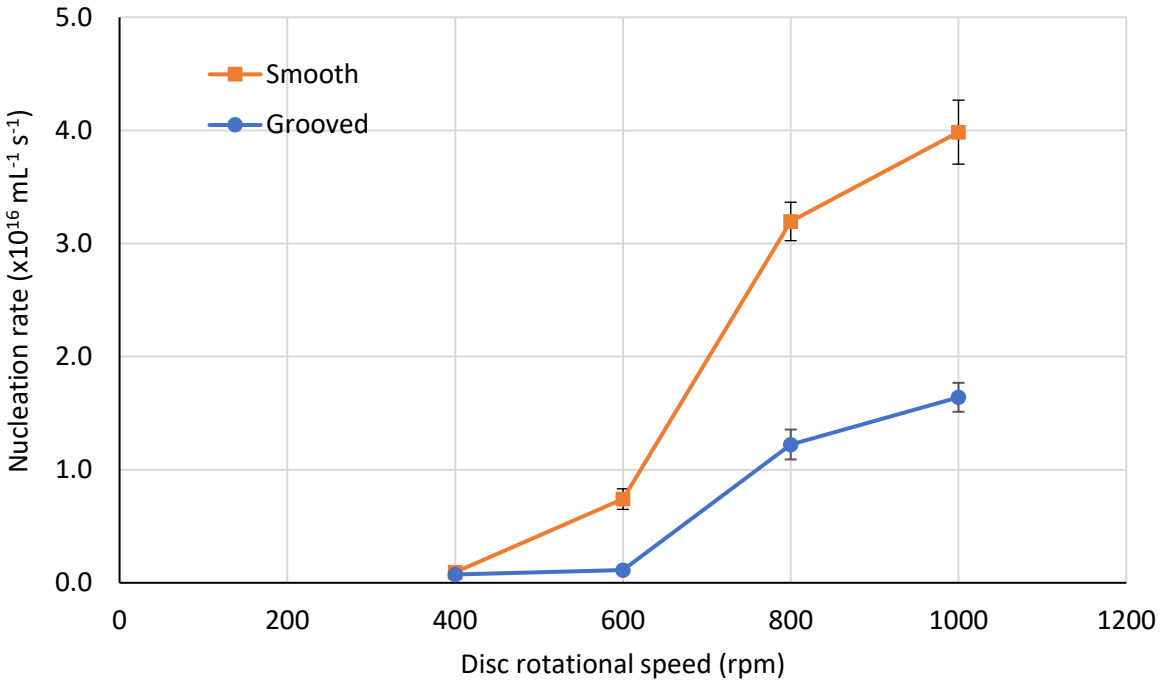

Figure 4-33: Effect of disc rotational speed on nucleation rate (18 mL/s, 9:1 ratio).

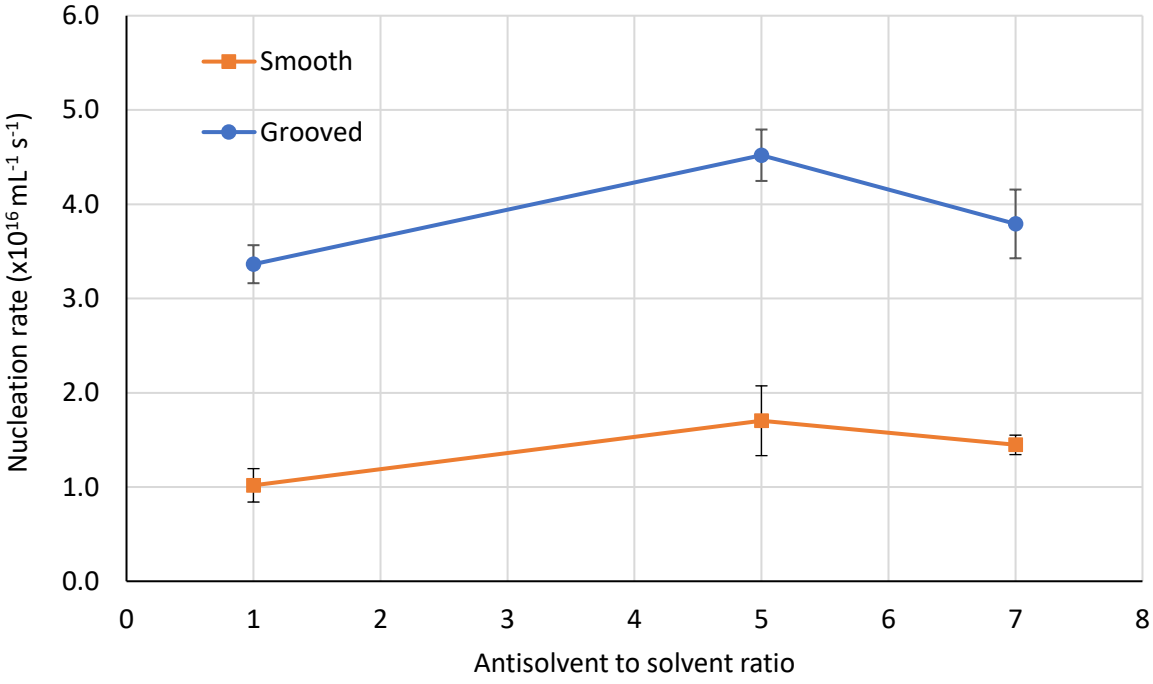

Figure 4-34: Effect of antisolvent to solvent ratio on nucleation rate (18 mL/s, 1200 rpm).

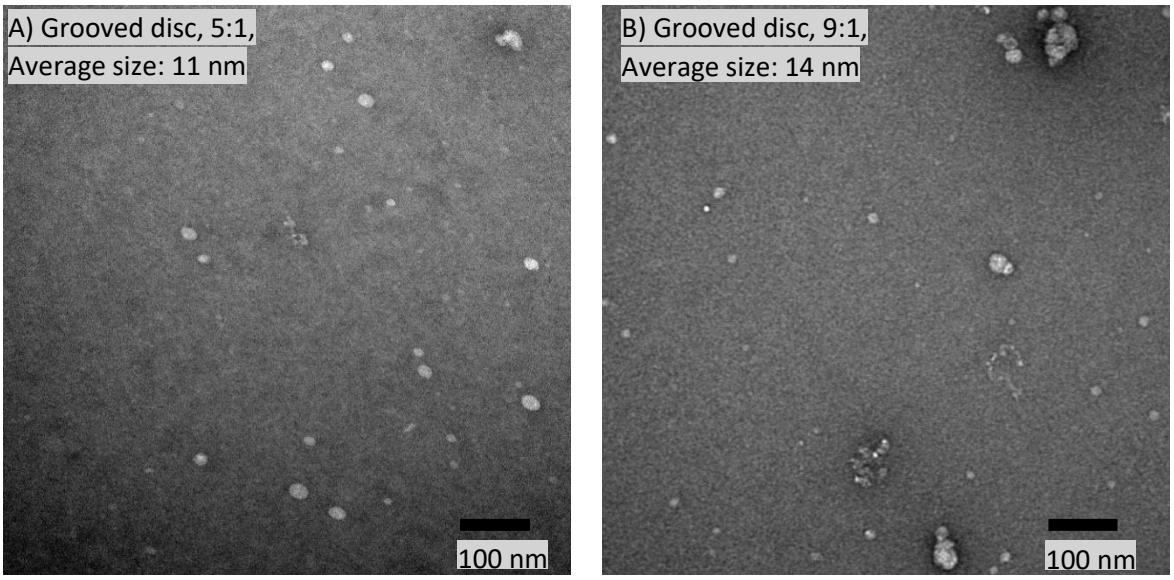

Figure 4-35: TEM images showing effect of antisolvent to solvent ratio at 18 mL/s, 1200 rpm A) 5 to 1 ratio and B) 9 to 1 ratio.

For the constant antisolvent to solvent ratio of 9:1, increasing flow rates and disc rotational speeds, the smooth disc provides lower induction times and higher nucleation rates in comparison to the grooved disc, as has been shown in Figures 4-32 and 4-33. This is due to liquid 'jumping' off the grooves upon entry onto the disc instead of flowing along the disc, which leads to nucleation occurring further along the disc radius. Such an occurrence has been explained by Mohammadi and Boodhoo (2012) and also by Burns et al. (2003). It has been attributed to situations where the liquid is in the 'spin-up zone' with the liquid not being fully attached to the surface of the disc. These situations are observed when inertial forces dominate over viscous forces. For example, low disc rotational speeds, high liquid flow rate and low viscosity, would give rise to such behaviour. This would explain why nucleation rate is lower on the grooved disc at 15 mL/s, as indicated in Figure 4-32.

In contrast, at lower antisolvent to solvent ratios, flow rates and disc rotational speeds, the nucleation rate was faster on the grooved disc, shown in Figure 4-34. An explanation for this would be that due to low supersaturation, nucleation predominantly relies on better mixing between the solvent/solute and the antisolvent to promote nucleation. In such conditions the grooved disc has advantage over the smooth disc, as the grooved surface enhances the formation of eddies and increases turbulence within the liquid film, providing more efficient mixing leading to successful collisions between particles for the formation of starch nuclei.

The results presented in Figs. 4-32 to 4-34 for nucleation rate compliment the results for particle size shown earlier in Fig. 4-8 (section 4.1). At higher nucleation rates, smaller

particles are produced as supersaturation is reduced through nucleation. Looking back at Fig. 4-8, at conditions of greater antisolvent to solvent ratio, flow rates and disc rotational speeds, particle sizes obtained were smaller on the smooth disc, corresponding to greater nucleation rates obtained on the smooth disc (Figs. 4-32 and 4-33). Whereas, for conditions of low antisolvent to solvent ratio, flow rate and disc speed, smaller sized particles were generated on the grooved disc, comparable to the high nucleation rates obtained on the grooved disc (Figs. 4-32 and 4-34).

It should also be noted that the equation for residence time, adapted for the estimation of the induction time (Eq. 4-18), assumes fully synchronised flow on the disc which usually occurs near the edge of the disc, away from the centre. However, the observed particles are appearing in the inner region, hence the radial distance used to estimate induction time is taken from the inner region of the disc. To validate this method, the spin-up radius was estimated at the experimental conditions using the method developed by Burns et al. (2003), also applied by Ghiasy et al. (2013). The method and results are explained in Appendix H. The calculations showed that a majority of the conditions gave rise to an induction radius beyond the spin-up radius, hence the flow can be assumed to be fully synchronised and the equation for residence time is valid for the purpose of estimating induction time.

There is no mention of nucleation rate for starch nanoparticles in literature, therefore comparisons to other precipitation systems have been made. Firstly, Cafiero et al. (2002) measured nucleation rate for barium sulphate produced in a spinning disc reactor, which was approximately 1.25×10^{12} cm^{-3} s^{-1}, which compared well to a theoretical nucleation rate of 2.48×10^{13} cm^{-3} s^{-1}. The theoretical nucleation rate has been calculated through the following equation (Dalvi and Yadav, 2015):

$$J = A_{hom} S \, e^{-B_{hom}/(lnS)^2} \tag{4-24}$$

$$A_{hom} = \left(\frac{4\pi}{3\varphi_m}\right)^{1/3} \left(\frac{\gamma}{kT}\right)^{1/2} DC^* N_A \tag{4-25}$$

$$B_{hom} = \frac{16\pi {\varphi_m}^2 \gamma^3}{3k^3 T^3} \tag{4-26}$$

where *C** is the equilibrium concentration and *D* is Stokes-Einstein diffusion coefficient.

Applying this theory to the current system of starch in ethanol/sodium hydroxide solution in the present work, yields values in the range of 1.65×10^{21} mL^{-1} s^{-1} and 7.65×10^{22} mL^{-1} s^{-1}, with the value decreasing at lower values of supersaturation and on a grooved surface as a result of the high interfacial tension predicted earlier. For a 9:1 antisolvent to solvent ratio, on a smooth disc, the nucleation rate estimated from Eqs. 4-24 to 4-26 is 7.65×10^{22} mL^{-1} s^{-1}. This predicted value is substantially higher than the nucleation rates estimated experimentally for a similar supersaturation, which is approximately an average value of 2.5×10^{16} mL^{-1} s^{-1}, bearing in mind that disc speed and flow rate are not considered in approximating the theoretical nucleation rate. One reason behind the lower experimental nucleation rate value could be the result of particle agglomeration in the experimental study, seemingly reducing the number of particles counted. Another more likely possibility is the induction time being measured at positions further along on the disc rather than at the true nucleation point caused by limitations of the camera system, leading to a maximum induction time. Besides this, the interfacial tension values used in the theoretical estimation of nucleation rate are obtained from Figure 4-31 and are likely to involve errors due to the limited number of data points available for the estimation of interfacial tension.

4.4.3. Nucleation and Growth kinetics

Nucleation and supersaturation can be related through the simple rate equation (Lindenberg and Mazzotti, 2011, Schall et al., 2018):

$$J = k_b S^b \qquad (4\text{-}27)$$

where k_b is the nucleation rate constant, and b is the nucleation rate order.

Figure 4-36 shows a logarithmic plot of nucleation rate versus supersaturation for both, grooved and smooth disc textures at 18 mL/s and 1200 rpm. The supersaturation, S in the Fig. 4-36 and Eq. 4-27 is the initial supersaturation based on the assumption that supersaturation is at first depleted by nucleation alone. From the plot it may be established that the grooved disc promotes the nucleation of starch nanoparticles at a faster rate than the smooth disc. This is contradictory to the results obtained earlier in section 4.4.1.1, where critical radii for the grooved disc were estimated to be greater than those for the smooth disc. A greater critical radius would mean more molecules would need to come together to form a cluster of a size larger than the critical radius, hence the nucleation process would be expected to be slower. However, the enhanced nucleation rate on the grooved surface could

possibly be the result of more collisions per unit time due to the grooves creating a more turbulent environment (Mohammadi and Boodhoo, 2012).

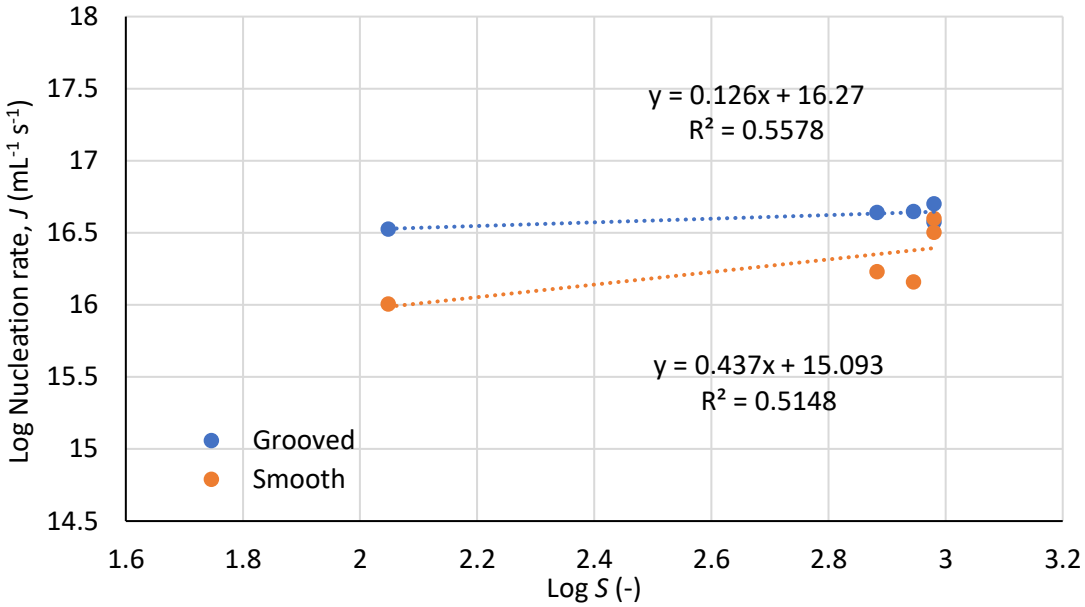

Figure 4-36: Nucleation rate as a function of supersaturation in log-log plot to obtain nucleation kinetics using Eq. 4-27 (18 mL/s, 1200 rpm).

Nucleation kinetics from Figure 4-36 have been estimated as the following:

For grooved disc: $k_b = 1.86 \times 10^{16}$ (particles. $\mathrm{mL^{-1}s^{-1}}$), $b = 0.126$

For smooth disc: $k_b = 1.24 \times 10^{15}$ (particles. $\mathrm{mL^{-1}s^{-1}}$), $b = 0.437$

The R^2 values apparent in Figure 4-36 are fairly low, a probable cause of which may be the high errors associated with the estimation of nucleation rate as discussed earlier in Section 4.4.2. The nucleation parameters can be compared with data present in literature. The nucleation rate order, *b*, has been reported to fall within the range -0.34 ≤ *b* ≤ 10.85 (Morris et al., 2015), where a negative sign indicates an inverse relationship between supersaturation and nucleation rate. This is often the case when nucleation is controlled by secondary mechanisms such as microabrasion. Typically, values of *b* > 1 indicate a strong relationship between nucleation rate and supersaturation (Chemaly et al., 1999). For the current system, the rate order for the smooth disc is slightly higher than it is for the grooved disc. This may suggest that precipitation on the smooth disc is more strongly dependent on supersaturation in comparison to precipitation on the grooved disc, despite the greater rate of formation of particles on the grooved disc. However, the rate order, *b*, being less than unity for this system indicates low dependency of nucleation rate on supersaturation, and

the possibility that other factors may play a greater role on influencing nucleation rate. Looking back at Figure 4-29 in Section 4.4.1, there is a strong correlation between induction time and shear rate which would suggest that increased shear influences a higher nucleation rate, possibly more so than supersaturation. However, Figure 4-36 depicts nucleation kinetics under conditions of the maximum shear rate (between 36,000 and 54,000 s^{-1}), achieved in this study through constant flow rate and disc speed of 18 mL/s and 1200 rpm, respectively. For this reason, it is difficult to speculate whether the kinetics remain constant upon changing shear. Figure 4-36 is reproduced alongside a linearised log-log plot of nucleation rate against shear rate in Figure 4-37, at constant supersaturation of 1074 (9:1 AS/S ratio). The plot shows nucleation rate is influenced more strongly by shear rate than it is by supersaturation. As the current data is limited to large shear rates at conditions of high liquid flow rate and disc rotational speed, it would seem apt to assume uniform supersaturation is obtained on the surface of the disc. However, it is likely that at lower shear rates, poorer mixing would be observed because of which nucleation rate would be more dependent on local supersaturation. Nevertheless, studies focusing on shear induced nucleation are limited (Nappo et al., 2018), and further in depth understanding of the effect of shear and hydrodynamics on nucleation at a molecular level is needed, which is outside the scope of this research.

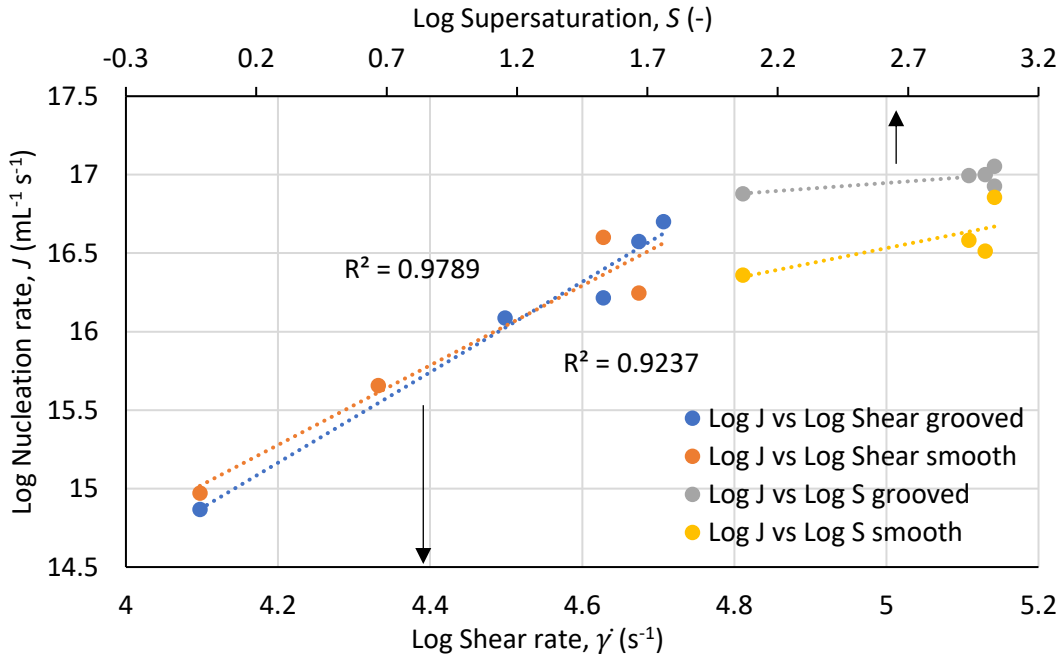

Figure 4-37: Effects of shear rate and supersaturation on nucleation rate on smooth and grooved discs.

Similarly, the equation for growth rate is (Myerson, 2002, Lindenberg and Mazzotti, 2011):

$$G = k_g(S-1)^g \quad (4\text{-}28)$$

$$S - 1 = \Delta C/C^* \quad (4\text{-}29)$$

$$\Delta C = C - C^* \quad (4\text{-}30)$$

where k_g is growth rate constant, g is the growth rate order, (S-1) is the relative supersaturation, ΔC is the supersaturation driving force and C^* is the equilibrium concentration.

For the calculation of growth rate, it has been assumed that growth is occurring only after nucleation and not simultaneously. In reality, this is not the case as nucleation and growth occur at the same time. However, at high supersaturations, nucleation dominates over growth. Bearing this in mind, this assumption can be made based on the high levels of supersaturation in this system. The diameter of the starch nuclei from which the particles grow is assumed to be equivalent to the size of the critical nucleus. A logarithmic plot of growth rate against relative supersaturation is given in Figure 4-38.

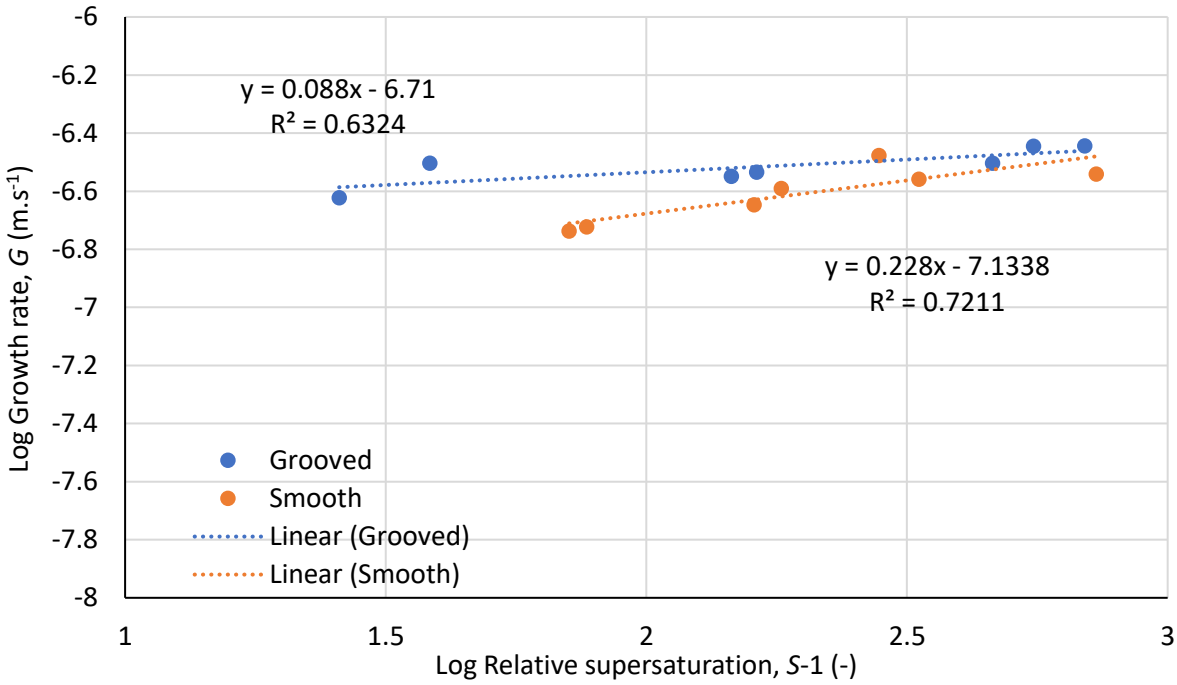

Figure 4-38: Growth rate as a function of supersaturation in log-log scale for the estimation of growth kinetics using Eq. 4-28.

The growth kinetics calculated from Figure 4-38 are as follows:

For grooved disc: $k_g = 1.95 \times 10^{-7}\ (\mathrm{m.s^{-1}})$, $g = 0.088$

For smooth disc: $k_g = 7.35 \times 10^{-8}\ (\mathrm{m.s^{-1}})$, $g = 0.228$

These results imply that growth rate is slightly higher on the grooved disc, particularly at low values of supersaturation, highlighted by the large k_g value. This result compliments the high interfacial tension estimated for the grooved disc earlier in section 4.4.1.1, as a high interfacial tension attracts particle growth (Kuldipkumar et al., 2007). The growth rates displayed in Fig. 4-38 cover a range of experimental conditions, unlike the nucleation rate plot in Fig. 4-36, which is for conditions of constant flow rate and disc speed. However, to gain a better understanding of the link between nucleation and growth, Table 4-4 presents nucleation and growth rate values at a constant disc rotational speed and flow rate of 1200 rpm and 18 mL/s, respectively. The data in the table shows that a greater nucleation rate results in lower supersaturation values after nucleation, leading to reduced growth rate. This trend is particularly evident when comparing the grooved disc with smooth disc, as nucleation rate is higher on the grooved disc at the conditions given in Table 4-4.

Table 4-4: Comparison between nucleation and growth rates for smooth and grooved discs at various initial supersaturations (18 mL/s and 1200 rpm).

Antisolvent to solvent ratio	Initial Supersaturation	Nucleation rate, J ($mL^{-1}\ s^{-1}$)	Supersaturation after nucleation	Growth rate, G ($m.s^{-1}$)
Grooved disc				
1	112	$3.36x10^{16}$	63	$4.04x10^{-7}$
5	763	$4.52x10^{16}$	39	$3.13x10^{-7}$
7	881	$3.79x10^{16}$	164	$2.92x10^{-7}$
9	955	ND	27	$2.39x10^{-7}$
Smooth disc				
1	112	$1.02x10^{16}$	54	$4.09x10^{-7}$
5	763	$1.70x10^{16}$	142	$4.31x10^{-7}$
7	881	$1.45x10^{16}$	281	$3.34x10^{-7}$
9	955	ND	78	$1.89x10^{-7}$

The growth order rates are within the range of values found published in literature between $-0.3 \leq g \leq 2.29$ (Morris et al., 2015). The growth kinetics for this system, captured by k_g and g, are typically in the lower end, which may be due to the SDR environment, specifically the low residence times limiting the growth of the starch nanoparticles. Furthermore, the value

of *g* depicts the dominating growth mechanism, for example, if *g*=1 growth is diffusion-controlled, between *g*=1-2 for the screw-dislocation model, and beyond *g*=2 polynuclear growth occurs (Myerson, 2002, Shiau, 2018). With *g* <1, mass transfer rate is slower in the diffusion-controlled mechanism (Omar, 2006). In addition, as supersaturation is high in the present system, growth will be controlled by the diffusion mechanism (Xiang et al., 2010, Lindenberg and Mazzotti, 2011).

4.4.4. Summary of precipitation kinetics

Induction times for starch precipitation in a spinning disc reactor have been estimated by means of a high-speed camera. The high-speed camera system assisted in establishing radial distances from the centre of the disc at which induction occurs, where induction is regarded as the time between the onset of supersaturation and the appearance of the first particles. A graph of induction time against supersaturation was plotted to calculate solid-liquid interfacial tension on the smooth and grooved disc surfaces. The interfacial tensions determined in this way were slightly lower than the values calculated using theoretical correlations suggested by Bennema and Söhnel (1990) and Mersmann (1990), but nevertheless compared favourably to the values published in literature for a number of different particles precipitated in various solvent/antisolvent mixtures. Interfacial tension values were further used in estimating the critical radius and theoretical nucleation rates. Values of critical radii compared well with published data for other systems, although, the values are expected to be greater when considering the effect of shear on the disc. Theoretical nucleation rates were calculated, however, these values were a few orders of magnitude greater than the experimentally obtained nucleation rates. Furthermore, disc speed and flow rates are not taken into consideration for the calculation of critical radius or theoretical nucleation rate, although an increase in shear as a result of high disc speeds and flow rates, as well as increased micromixing, were found to impact nucleation rate. Finally, nucleation and growth kinetics for the current system have been determined and are found to be within the range established in the wider literature for precipitated particles.

Chapter 5. Population balance modelling

Population balance models are often used for the optimisation of reactor design and operating conditions as well as for the control of precipitation systems (Aamir et al., 2009, Chiu and Christofides, 2000, Mesbah et al., 2009, Shi et al., 2006). The population balance equation (PBE), which describes the evolution of particles through space and time was introduced simultaneously by Randolph (1964) and Hulburt and Katz (1964). It is presented in Equation 5-1 below for a well-mixed system (Hounslow et al., 1988). It describes the nucleation, growth, agglomeration and breakage of the particles, as well as the motion the particles undergo. Often a particle characteristic such as shape or size of the particles is used as the internal coordinate (Eitzlmayr, 2010). Here the equation is in terms of the particle size, *L*.

$$\frac{\partial n}{\partial t} + \frac{\partial (Gn)}{\partial L} = B - D \tag{5-1}$$

The first term in Eq. 5-1 accounts for nucleation; the second for growth, where *n* is the number density and *G* is particle growth rate; *B* and *D* are the birth and death rates respectively, accounting for particle agglomeration and breakage.

There are many ways in which the PBE can be solved, coupled with either computational fluid dynamics (CFD), a micromixing model, or both (Schwarzer et al., 2006, Marchisio et al., 2003). This section will focus on the common few. The simplest solution is an analytical one, based on a number of assumptions, one being, negligible agglomeration and breakage. With the inclusion of agglomeration and breakage in the model, the solution to the PBE becomes progressively more difficult. Omar and Rohani (2017) have carried out an in-depth review of the population balance solution methods.

5.1. Methods of solving PBEs

5.1.1. Analytical solution

The most popular analytical solution is that for a continuous mixed suspension mixed product removal (MSMPR) crystalliser (Mullin, 2001). Assumptions made include, a) steady-state operation, b) no crystal seeds, c) size-independent growth, d) negligible breakage and agglomeration. Additionally, the residence time,τ, of all species is the same. This leads to a simple solution presented in following equation:

$$n = n^0 \exp\left(-\frac{L}{G\tau}\right) \tag{5-2}$$

where n^0 is the nuclei population density ($n^0 = B/G$) and L is particle size.

Equation 5-2 has been extended and applied to multiple MSMPR units in series to increase total residence time, allowing nucleation to occur in the earlier stages and growth to dominate in the latter stages (Alvarez et al., 2011)

5.1.2. Discretisation methods

The discretisation method, also known as the class method, is the preferred method of solving PBEs, as it is able to preserve population distributions whilst including breakage and agglomeration terms. It is beneficial for precipitation systems which feature changing distributions. Discretisation methods involve the breakdown of the internal coordinate, often particle size or volume, into discrete bins or classes. The classes can either be equidistant or non-equidistant. To increase accuracy of the results, a substantial number of classes are required, making it computationally expensive and time consuming, especially for precipitation processes where nucleation is in the nanometer range and growth in the micrometer range (Omar and Rohani, 2017). A number of discretisation methods have been formulated, including, the method of characteristics (Kumar and Ramkrishna, 1997, Lim et al., 2002, Mahoney et al., 2002, Jiang et al., 2014), finite difference method (Bennett and Rohani, 2001, John et al., 2009, Sheikhzadeh et al., 2008) and the finite element method (Nicmanis and Hounslow, 1998, Rigopoulos and Jones, 2003, Tsang and Rao, 1990).

5.1.3. Method of moments

The method of moments is preferred over the discretisation method when CFD is involved (Marchisio et al., 2003, Rane et al., 2014). The standard method of moments (SMOM) is the foundation for the other method of moments (Zauner and Jones, 2002, Rohani and Bourne, 1990). It is defined in the form of the following equation:

$$m_k = \int_0^\infty L^k \, n(L) \, dL \tag{5-3}$$

where m_k is the kth moment.

However, the SMOM fails in instances where size-dependent growth rate expressions and certain agglomeration kernels are included (Falola et al., 2013). In such situations, other methods such as extended method of moments (EMOM) (Falola et al., 2013) and quadrature method of moments (QMOM) are favoured (Marchisio and Fox, 2005, Marchisio et al., 2003).

5.1.4. Monte Carlo method

Monte Carlo methods are highly adaptable to a range of PBEs, including agglomeration and breakage. The method involves the input of randomly generated numbers and events to devise a solution based on the random events. The solution, although highly accurate and robust, may be computationally expensive as a large range of particles need to be tracked using a very small time-step (Lin et al., 2002, Maisels et al., 2004, Omar and Rohani, 2017).

5.2. Solution to mathematical model for starch nanoparticles in SDR

Two methods have been explored as part of this study: the Lax-Wendroff method (Bennett and Rohani, 2001), which assumes negligible agglomeration and breakage; and a discretised method suggested by Hounslow et al. (1988), which takes agglomeration and breakage into account.

5.2.1. Lax-Wendroff method

A combination of Lax-Wendroff and Crank-Nicholson to solve the population balance equation was first introduced by Bennett and Rohani (2001). Alvarez and Myerson (2010) further explored the method for a plug flow crystalliser. Some of the assumptions they made also hold true for the SDR, especially since the SDR exhibits plug flow behaviour (Mohammadi and Boodhoo, 2012). Assuming there is no radial dispersion and that growth rate is independent of particle size, and finally that agglomeration and breakage is not significant, Equation 5-1 can be written as Equation 5-4 at steady state. The latter condition has been based on the short residence times provided by the SDR, making the possibility of agglomeration low (Mohammadi, 2014).

$$u_{av}\frac{\partial n(L,r)}{\partial r}+G\frac{\partial (n)}{\partial L}\ =\ 0 \qquad (5\text{-}4)$$

where *r* is the radial position along the radius of the SDR and u_{av} is the average film flow velocity in the SDR, expressed previously in Eq. 2-12 and reproduced below:

$$u_{av}\ =\left(\frac{Q^2\omega^2}{12\pi^2 r\nu}\right)^{1/3}$$

The boundary condition relating the population density with nucleation rate is defined as:

$n\,(0,\,r) = B_0\,(r)/G(r)$

where B_0 is the nucleation rate at size, L=0 and radial distance, r (Alvarez and Myerson, 2010).

The initial condition is $n(L, 0) = 0$, that is, no solids are present at the entrance of the disc ($r = 0$) (Lindenberg et al., 2008). As the particles form and undergo growth, the rate of gain of mass by the solid following the depletion of solute from the solution is given in the form of the following mass balance (Alvarez and Myerson, 2010):

$$u_{av}\frac{dC}{dr} = -3\rho_s k_v G \int L^2 n\, dL \tag{5-5}$$

Eqs. 5-4 and 5-5 along with the equations determined earlier for nucleation rate, J and growth rate, G, reproduced below for the smooth disc (Eqs. 5-6 and 5-7), were discretised into length steps (ΔL) and radial steps along the reactor (Δr). The population balance was solved as a series of multistage SDR units through expansion of the Taylor Polynomial, where the number density calculated at the exit of the previous stage (n^i) became the basis of the next unit (n^{i+1}). 100 SDR units were selected on the basis of increased accuracy of the model, whilst limiting computational time. Similarly, particle length was discretised into 100 length steps from 0 to 100 nm. The script for the MATLAB code is given in Appendix I.

$$J = 1.24 \times 10^{15}\, S^{0.437}\ (\text{particles.mL}^{-1}\text{s}^{-1}) \tag{5-6}$$

$$G = 7.35 \times 10^{-8}\, (S-1)^{0.228}\ (\text{m.s}^{-1}) \tag{5-7}$$

5.2.1.1. Results from Lax-Wendroff

The generated models for the effect of flow rate and disc rotational speed show similar trends to the experimental results obtained from DLS analysis (Figure 5-1). As flow rate and disc rotational speed increase, the PSDs are narrower with peaks shifting towards the left of the size distribution. The modelled results are not in close agreement to the experimental results, which may be a result of agglomeration being left out from the model, despite the experimental results indicating the presence of agglomeration at certain conditions. However, there are errors associated with the conversion of the experimental size distribution from an intensity-based PSD to a number PSD. To ascertain whether the discrepancy between modelled and experimental results is due to agglomeration or a result of conversion of the size distribution, Figure 5-2 also displays the modelled PSD together with TEM PSDs for 18 mL/s and 6 mL/s on the grooved disc. At 18 mL/s, the TEM PSD shows closer agreement with the modelled PSD, however, at 6 mL/s, the modelled size distribution

shows poorer fit with TEM data than the number based DLS size distribution. It seems, both the conversion of the size distribution to a number-based PSD and the exclusion of agglomeration from the model impact the quality of the fit of the model to experimental results.

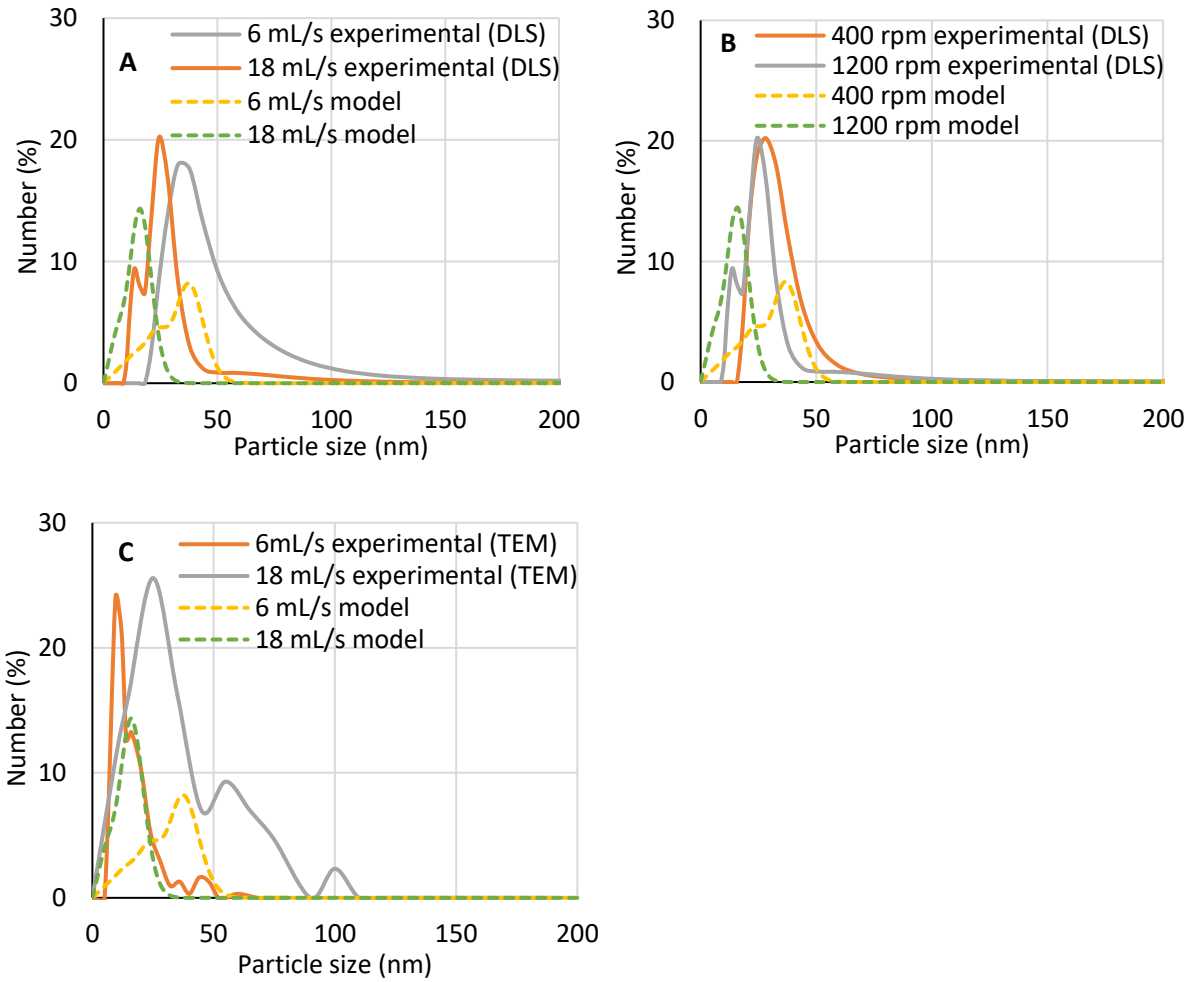

Figure 5-1: Comparison between experimental (DLS) PSDs and model generated through the Lax-Wendroff method for the effect of A) flow rate at conditions of 2 % w/v starch, 1200 rpm, 9:1 ratio, grooved disc, and, B) disc rotational speed at conditions of 2 % w/v starch, 18 mL/s, 9:1 ratio, grooved disc. C) Experimental (TEM) and modelled PSDs for effect flow rate at conditions of 2 % w/v starch, 1200 rpm, 9:1 ratio, grooved disc.

However, when altering antisolvent to solvent ratio, the model does not show a significant change in shape, nor in position of the predicted size distribution (Figure 5-2). The antisolvent to solvent ratio only affects solubility, thus supersaturation and nucleation rate. It does not affect SDR hydrodynamics despite the slight change in viscosities at the different antisolvent to solvent ratios, thus not having a considerable effect on the modelled PSD. Finally, modelled and experimental size distributions are not a close fit, and as highlighted earlier, this may have resulted from the conversion of intensity-based size distributions to

number size distributions for the experimental data, introducing errors, as well as the exclusion of agglomeration from the model.

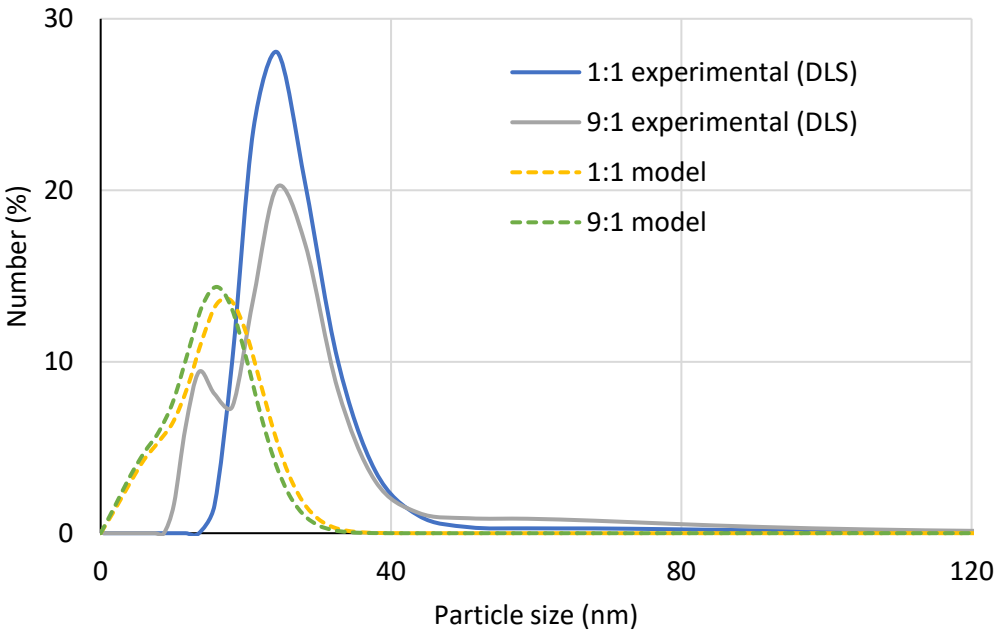

Figure 5-2: Comparison between experimental PSDs and model generated through the Lax-Wendroff method for the effect of antisolvent to solvent ratio at conditions of 2 % w/v starch, 1200 rpm and 18 mL/s on the grooved disc surface.

Although this model fails to predict size distributions close to those from the experimental work, the model does predict nucleation rate close to the values estimated in section 4.4.1. Figure 5-3 shows the modelled and experimental data for the effect of antisolvent to solvent ratio on nucleation rate for smooth and grooved disc surfaces at 1200 rpm and 18 mL/s. The decline in nucleation rate at the 7:1 ratio is a result of agglomeration lowering particle count hence nucleation rate.

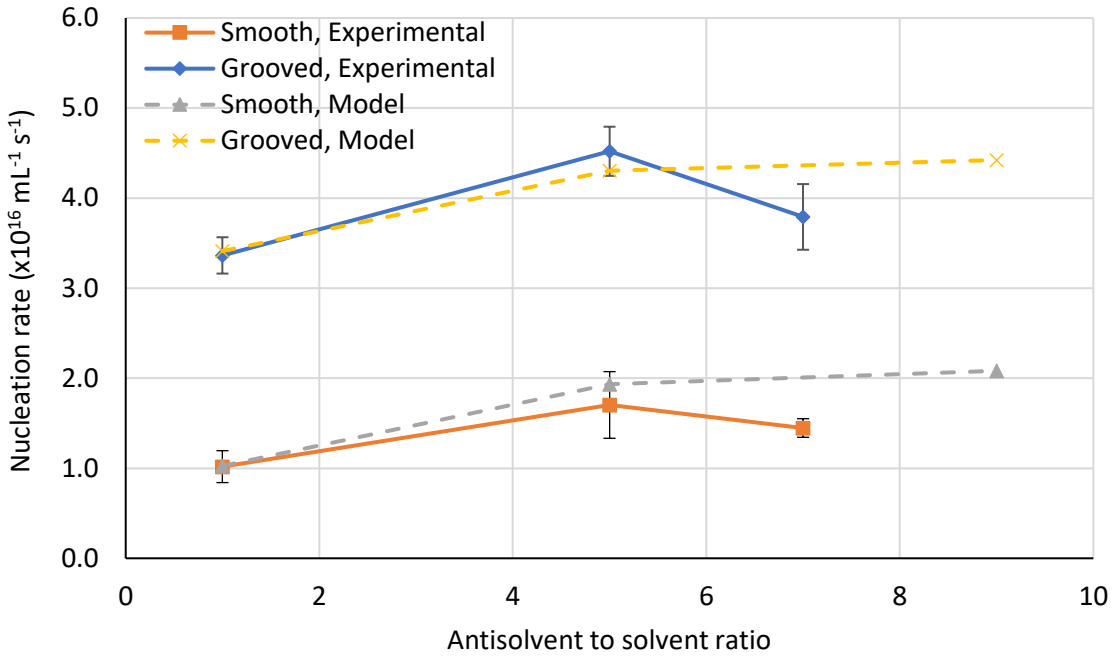

Figure 5-3: Effect of antisolvent to solvent ratio on experimental nucleation rate and nucleation rate from the model at 1200 rpm and 18 mL/s.

Figure 5-4 shows a comparison between the predicted and experimental performances for smooth and grooved disc surfaces. The trend for modelled and experimental PSDs are in agreement, as both show peaks for the smooth surface at the smaller end of the size distribution, whereas the peaks for the grooved discs are present at larger particle sizes. However, the experimental and modelled PSDs do not indicate a close fit. The model only relies on precipitation kinetics obtained earlier (section 4.4.2) to show the effect of the disc surface. The model can benefit from inclusion of residence time distribution data, encompassing the effect of the disc surface, as well as micromixing effects of the SDR in order to obtain a closer fit to the experimental results.

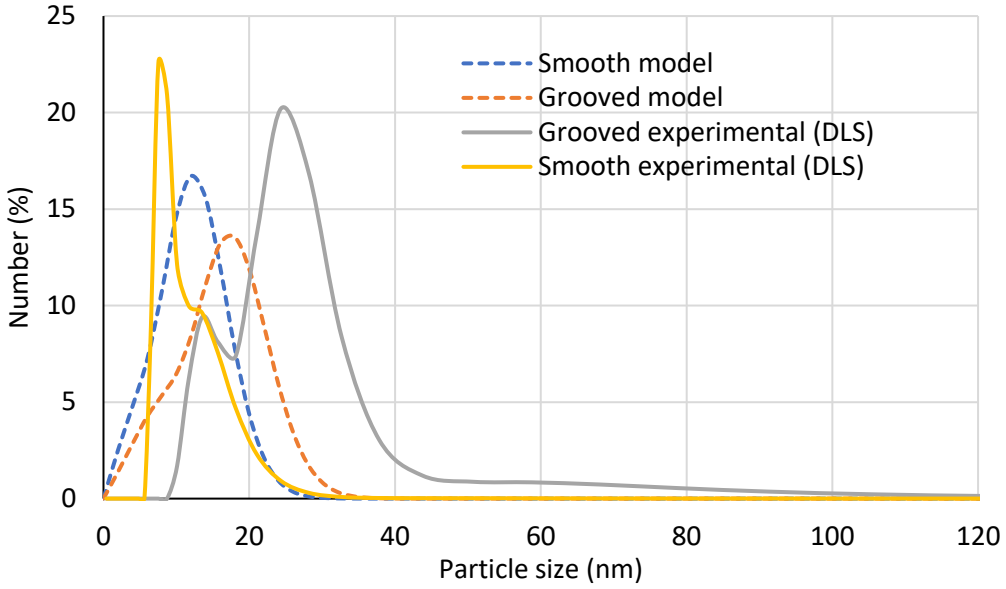

Figure 5-4: Comparison between experimental PSDs and model generated through the Lax-Wendroff for the effect of disc surface textures at 18 mL/s, 1200 rpm and 9:1 ratio.

5.2.2. Hounslow's method of discretisation

Images from TEM have indicated the presence of agglomeration amongst the starch nanoparticles (Figs. 4-2 and 4-10). This has been confirmed by secondary peaks found in PSDs obtained from the DLS technique (Figs. 4-7 and 4-9). Hence the assumption of negligible breakage and agglomeration made for the Lax-Wendroff model is not entirely valid. To accommodate breakage and agglomeration, this section discusses methods adapted from a comprehensive master's report conducted by Manson (2017).

Agglomeration rate is often expressed in terms of a kernel. A number of authors have suggested a size-dependent kernel (Omar and Rohani, 2017), a more complex approach than the assumption of size-independent kernels. For the precipitation of starch nanoparticles in the SDR, agglomeration resulting from Brownian motion has been assumed (Schwarzer and Peukert, 2004). This is known as Perikinetic agglomeration and is the principal mechanism for particles smaller than 1 micron. The rate of collision for such agglomeration is given by the following equations:

$$\beta_{coll,peri} = \frac{2kT}{3\mu}(r_i + r_j)\left(\frac{1}{r_i} + \frac{1}{r_j}\right) \tag{5-8}$$

$$\beta_{i,j} = \frac{1}{W}\beta_{coll} \tag{5-9}$$

where r_i and r_j are the particle radii.

Particle collisions are also affected by particle to particle interactions. This is described by the stability ratio, *W* (Schwarzer and Peukert, 2005).

$$W = 2\int_2^{\infty} \frac{\exp\left(\frac{\Phi_{T,ij}}{k_B T}\right)}{s^2}.ds \qquad (5\text{-}10)$$

$$s = 2R/(r_i + r_j),$$

where $\Phi_{T,ij}$ is the total interaction potential energy. It is the sum of the attractive Van der Waals interaction potential energy, $\Phi_{vdW,ij}$, and the repulsive electrostatic interaction potential energy, $\Phi_{El,ij}$; *R* is the centre to centre distance between the particles (Vold and Vold, 1983, Hunter, 2005, Ohshima, 1995).

$$\Phi_{T,ij} = \Phi_{El,ij} + \Phi_{vdW,ij} \qquad (5\text{-}11)$$

$$\Phi_{vdW,ij} = -\frac{A_H}{6}\left[\frac{2r_i r_j}{R^2 - (r_i + r_j)^2} + \frac{2r_i r_j}{R^2 - (r_i - r_j)^2} + \ln\frac{R^2 - (r_i + r_j)^2}{R^2 - (r_i - r_j)^2}\right] \qquad (5\text{-}12)$$

$$\Phi_{El,ij} = 4\pi\varepsilon\varepsilon_0\psi_0^2\frac{r_i r_j}{r_i + r_j}\ln(1 + exp(-\kappa H)) \qquad \kappa r > 5 \qquad (5\text{-}13)$$

$$\Phi_{El,ij} = 4\pi\varepsilon\varepsilon_0 r_i r_j Y_i Y_j \left(\frac{k_B T}{e}\right)^2 \frac{\exp(-\kappa H)}{H + r_i + r_j} \qquad \kappa r < 5 \qquad (5\text{-}14)$$

where $$Y = \frac{8\tanh(1/4)}{1+\sqrt{[1-[(2\kappa r+1)/(\kappa r+1)^2]tanh^2(1/4)]}} \qquad (5\text{-}15)$$

A_H is the Hamaker constant, *H* is the separation distance between the particles and κ is the inverse of the Debye constant given by:

$$\kappa = \left(\frac{2e^2 N_A}{\varepsilon\varepsilon_0 kT}\right)^{1/2} I \qquad (5\text{-}16)$$

where ε is the relative permittivity estimated to be 77.8 from Piyasena et al. (2003), ε_0 is the electric field constant equal to $8.854 \times 10^{-12}\ C^2 J^{-1} m^{-1}$, ψ_0 is the surface potential, and I is ionic strength given by the following equation:

$$I = \frac{1}{2}\sum_{ions} c_i z_i^2 \qquad (5\text{-}17)$$

To solve the PBE, Hounslow's discretised population balance method has been applied (Hounslow et al., 1988). It is also known as the class method where discrete particle classes are defined. Hounslow suggested a geometric discretisation of the internal coordinate in order to increase resolution for smaller sized particles. The discretisation which is $L_{i+1}/L_i = 2^{1/3}$ is displayed in Figure 5-5.

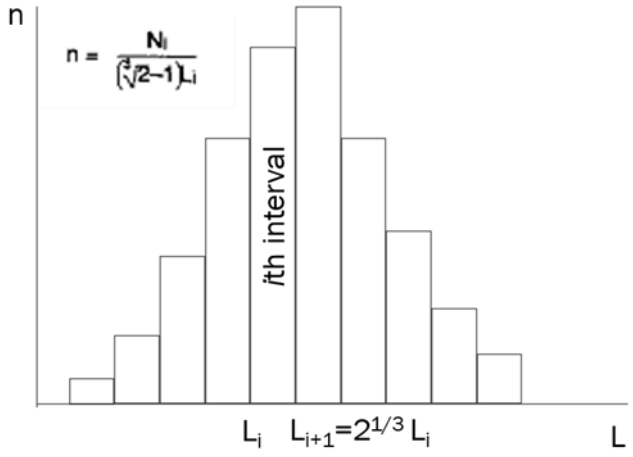

Figure 5-5: The discrete size distributions method adopted from Hounslow et al. (1988).

The rate of change of numbers is given in Equations 5-18 to 5-22 below. The numbers rate equation combines the rate of change in numbers due to nucleation and growth (NCG) and due to agglomeration (AGG). To avoid oscillation and numerical instability, whilst reducing errors, Galbraith and Schneider (2014) proposed a hybrid approach through the introduction of two-term and three-term growth equations (Eq. 5-21 and 5-22). To transition smoothly between the two-term and three-term equations, a weighting factor, α, applied in Equation 5-20 has been used.

$$\frac{dN}{dt} = \frac{dN}{dt}\Big|_{NCG} + \frac{dN}{dt}\Big|_{AGG} - \sum_i \frac{N_i Q_i}{V} \tag{5-18}$$

$$\frac{dN}{dt}\Big|_{AGG} = N_{i-1}\sum_{j=1}^{i-2} 2^{j-i+1}\beta_{i-1,j}N_j + \frac{1}{2}\beta_{i-1,i-1}N_{i-1}^2 - N_i\sum_{j=1}^{i-1} 2^{j-i}\beta_{i,j}N_j - N_i\sum_{j=1}^{N_{eq}} \beta_{i,j}N_j \tag{5-19}$$

$$\frac{dN}{dt}\Big|_{NCG} = (1-\alpha_i)\frac{dN}{dt}\Big|_{2term} + \alpha_i \frac{dN}{dt}\Big|_{3term} \tag{5-20}$$

$$\alpha_i = \frac{1}{1 + (e^i + i_T)}$$

where i_T is the transition interval

$$\left.\frac{dN}{dt}\right|_{2term} = \frac{2}{(r-1)L_i}(rG_{i-1}N_{i-1} - G_iN_i) \quad (5\text{-}21)$$

$$\left.\frac{dN}{dt}\right|_{3term} = \frac{2}{(r+1)L_i}\left(\frac{r}{r^2-1}G_{i-1}N_{i-1} - G_iN_i - \frac{r}{r^2-1}G_{i+1}N_{i+1}\right) \quad (5\text{-}22)$$

The transfer of starch from the aqueous phase to the solid phase can be accounted for through a mass balance. The transfer of material between the phases alters concentration and the thermodynamic driving force, supersaturation. Equation 5-23 describes the change in mass of starch.

$$\frac{dmass_{starch}}{dt} = \dot{m}_{starch,i} - \dot{m}_{starch,o} - k_v\dot{\mu}_3\rho_{crystal}V_{CSTR} \quad (5\text{-}23)$$

where V_{CSTR} is the volume of CSTR in the tank-in-series model discussed below, $\dot{\mu}_3$, is the rate of change of the third moment, calculated through:

$$\dot{\mu}_3 = \int_0^\infty L^3 \frac{dn(L,t)}{dt}.dL \quad (5\text{-}24)$$

k_v is the shape factor which is assumed to be π/6 for spherical particles.

Inclusion of the micromixing effects of the SDR was done through the segregation phenomena as mentioned by Baldyga et al. (1995). The model assumes that the fluid entering the reactor is initially in a segregated state, with the segregation volume, *Vs*, decreasing according to Equation 5-25, as the process continues.

$$-\frac{dV_s}{dt} = \frac{V_s}{t_{micro}} \quad (5\text{-}25)$$

5.2.2.1. Model conditions and simulation

To simplify the otherwise complex model, a few assumptions have been made. Firstly, the precipitation temperature is 25 °C and the disc diameter is 30 cm. There is no seeding and so zero sized nuclei are present at the start; and growth is size independent. In addition, plug flow characteristics are assumed and a tank-in-series approach has been considered to model the SDR process. The number of tanks for the smooth and grooved discs can be linked to the Peclet number correlations given in Equation 5-26 and 5-27 (Mohammadi and

Boodhoo, 2012). The number of tanks is estimated through the inverse of the variance of an RTD plot (Eq. 5-28) (Levenspiel, 1999). This can then be related to the Peclet number through Eq. 5-29 (Levenspiel, 1999), finally giving an expression for number of tanks in series, *N* (Eq. 5-30).

$$Smooth\ Disc: Pe = 10^{2.561}\omega^{0.188}Q^{0.371}v^{-0.136} \quad (5\text{-}26)$$

$$Grooved\ Disc: Pe = 10^{2.765}\omega^{0.203}Q^{0.372}v^{-0.104} \quad (5\text{-}27)$$

$$N = \frac{1}{\sigma(\theta)^2} \quad (5\text{-}28)$$

$$\sigma(\theta)^2 = 2\left(\frac{1}{Pe}\right) + 8\left(\frac{1}{Pe}\right)^2 \quad (5\text{-}29)$$

$$N = \frac{Pe}{2} + 1 \quad (5\text{-}30)$$

The model has been programmed using the MATLAB software. The discretised population balance and the mass balances as mentioned earlier have been solved simultaneously through the MATLAB ODE solvers. The full script for the code is present in Appendix J.

5.2.2.2. Effect of flow rate

Figure 5-6 shows a comparison between the simulated model and the experimental number size distribution for 6 mL/s and 18 mL/s at constant conditions of 1200 rpm, 9:1 ratio and 2 % w/v starch concentration. Trends observed for the model are similar to those for the experimental results. That is, an increase in flow rate results in smaller sized particles with narrower size distributions. The modelled size distributions, however, do not map onto the experimental size distributions.

The R^2 value can be calculated to quantify this closeness of the model to the experimental data. It is defined in terms of the following equation:

$$R^2 = 1 - \frac{SS_{res}}{SS_{tot}}$$

where, SS_{res} is the residual sum of squares and SS_{tot} is the total sum of squares. R^2 values displayed in Fig. 5-6 give values below zero. The negative values, although not typical, indicate a shift in trend between the experimental and modelled data. That is, for example, looking at the results for 6 mL/s, at a particle size of 20 nm, the experimental PSD begins an upward trend, however, at the same particle size, the modelled PSD has reached a peak and

begins to descend following this point. This suggests a poor fit between the model and the experimental results in Figure 5-6.

The size distributions shown here are obtained from the DLS equipment and are prone to errors as the number % values are converted from intensity-based measurements. Although converting the model (instead of the experimental data) to an intensity size distribution was considered, it was deemed to be a very complex process which also introduces errors and so has not been attempted. The model has, however, been compared with size distributions obtained from TEM analysis, which by nature are number-based distributions and so present more accurate data for comparison with the model. This is presented in Figure 5-7. The model and the TEM results are in better agreement. The R^2 values indicate a good fit, as the closer the value is to 1, the better the fit. TEM size distributions are derived from the measurement of a small sample of particles, where roughly between 50 and 150 particles are measured for the generation of a size distribution, and measurement of samples have only been taken once and no repeats have been performed, thus affecting precision of the results. For this reason, both, number size distributions from the DLS technique and TEM size distributions, will be included for comparison with the model.

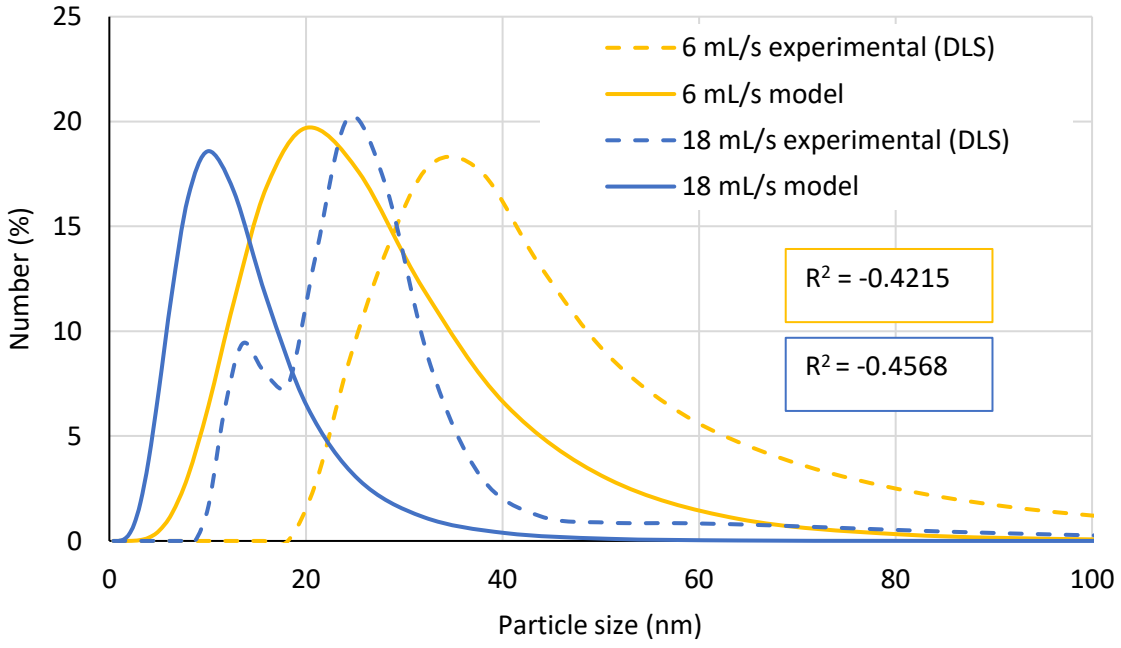

Figure 5-6: Comparison between modelled PSD and experimental results (DLS method) for the effect of flow rate at conditions of 2 % w/v starch, 1200 rpm, 9:1 ratio, grooved disc.

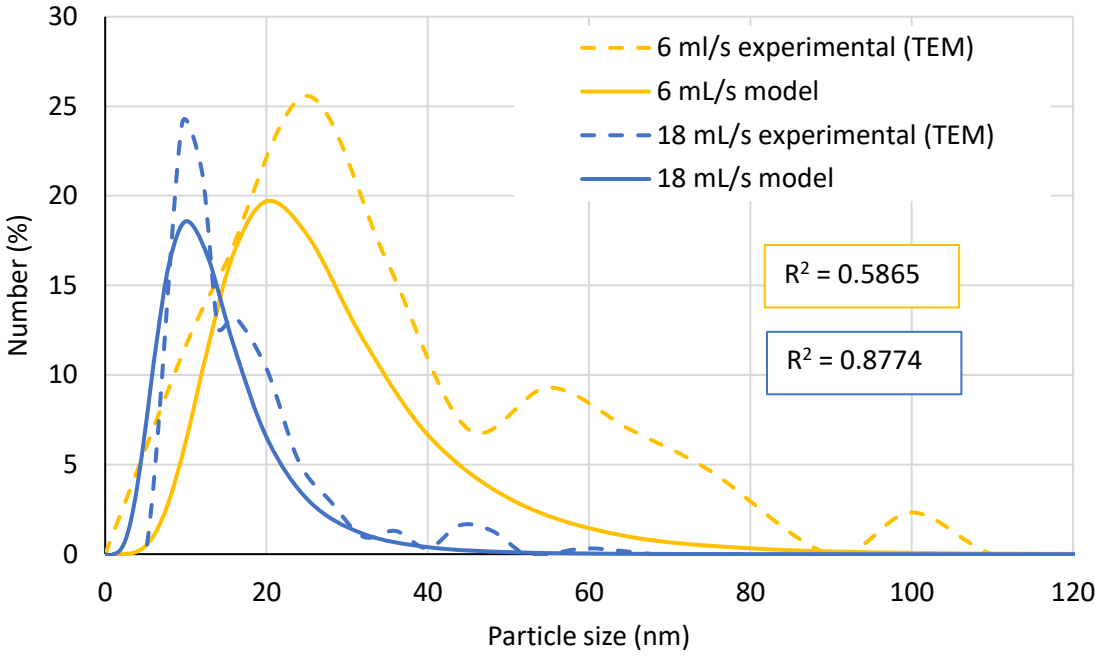

Figure 5-7: Comparison between modelled PSD and experimental results (TEM) for the effect of flow rate at conditions of 2 % w/v starch, 1200 rpm, 9:1 ratio, grooved disc.

5.2.2.3. Effect of disc rotational speed

Figure 5-8 compares the modelled size distribution at 400 rpm and 1200 rpm with the experimental size distribution obtained from the DLS equipment. TEM results are shown with the modelled results in Figure 5-9. The modelled PSD again follows a similar trend as the experimental results, as the simulated model shows the size distribution becoming narrower and shifting towards the smaller end of the distribution as disc speed is increased. R^2 values given in Figure 5-9 demonstrate a good fit between the model and the size distribution obtained from TEM images, although, the R^2 value at 400 rpm is especially low. As the effect of residence time distribution has been accounted for in the model, the discrepancy between modelled and experimental data may possibly be caused by the assumption of size independent growth. At low disc rotational speeds, less ripples and surface waves appear on the film surface, resulting in a less uniform velocity profile. Such deviation from plug flow can cause particles of varying sizes to grow at different rates. This is known as growth rate dispersion (Mohammadi, 2014).

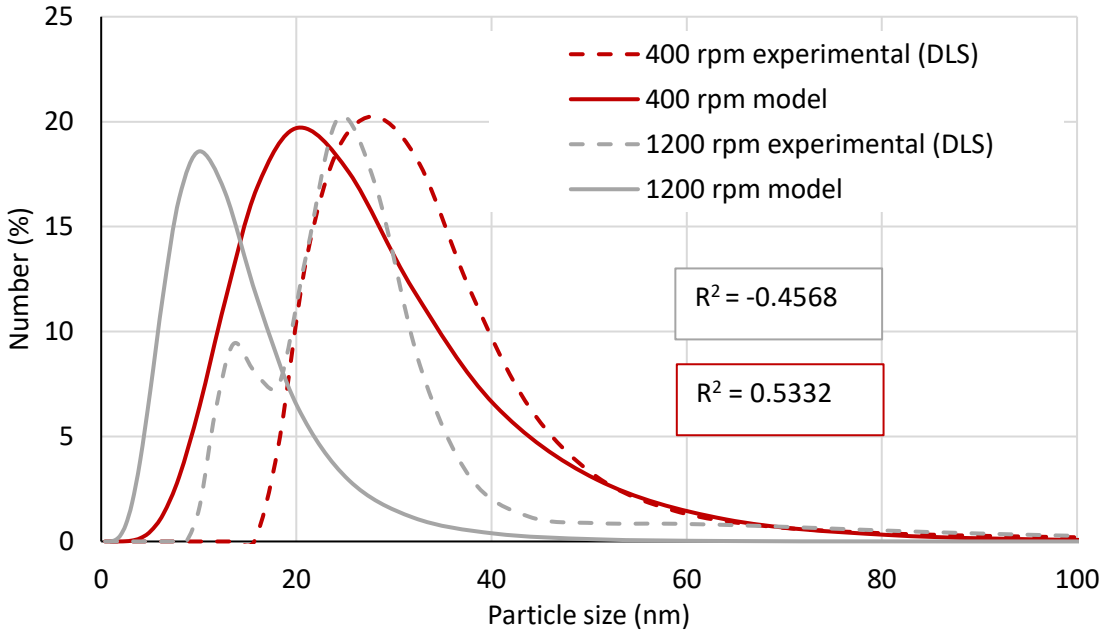

Figure 5-8: Comparison between modelled PSD and experimental results (DLS method) for the effect of disc speed at conditions of 2 % w/v starch, 18 mL/s, 9:1 ratio, grooved disc.

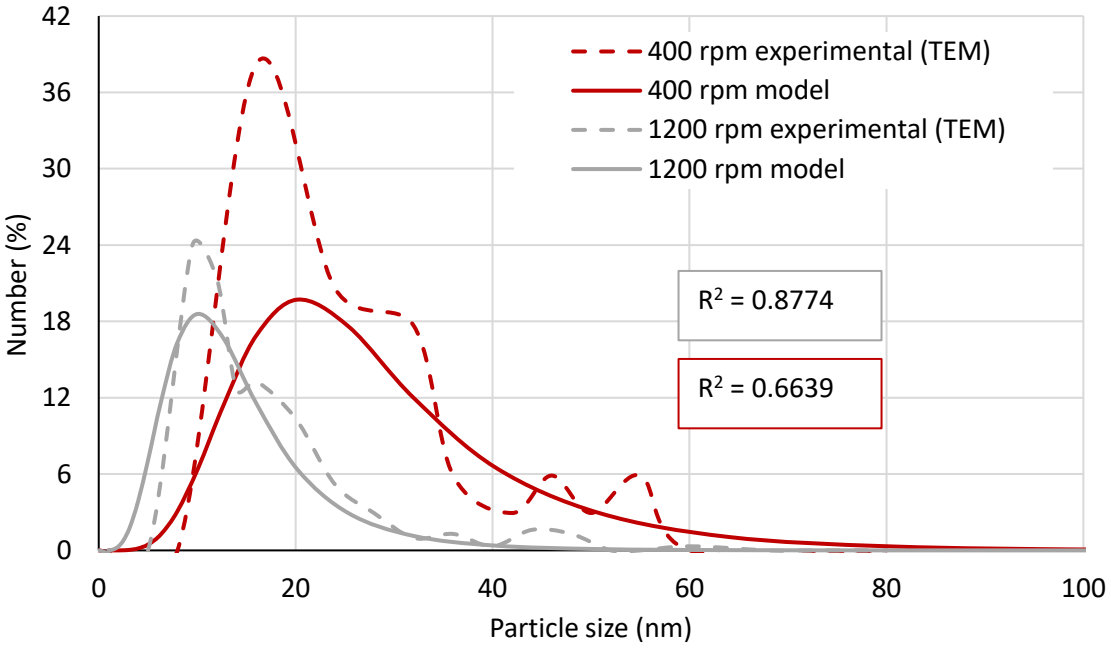

Figure 5-9: Comparison between modelled PSD and experimental results (TEM) for the effect of disc speed at conditions of 2 % w/v starch, 18 mL/s, 9:1 ratio, grooved disc.

5.2.2.4. Effect of antisolvent to solvent ratio

The simulated model showing the effect of increasing the antisolvent to solvent ratio is presented in Figures 5-10 and 5-11 for comparison with DLS size distribution and TEM size distribution, respectively. The models show that increasing the antisolvent to solvent ratio generates narrower size distributions with smaller sized particles. The R^2 values given in Figure 5-11 indicate a very good fit.

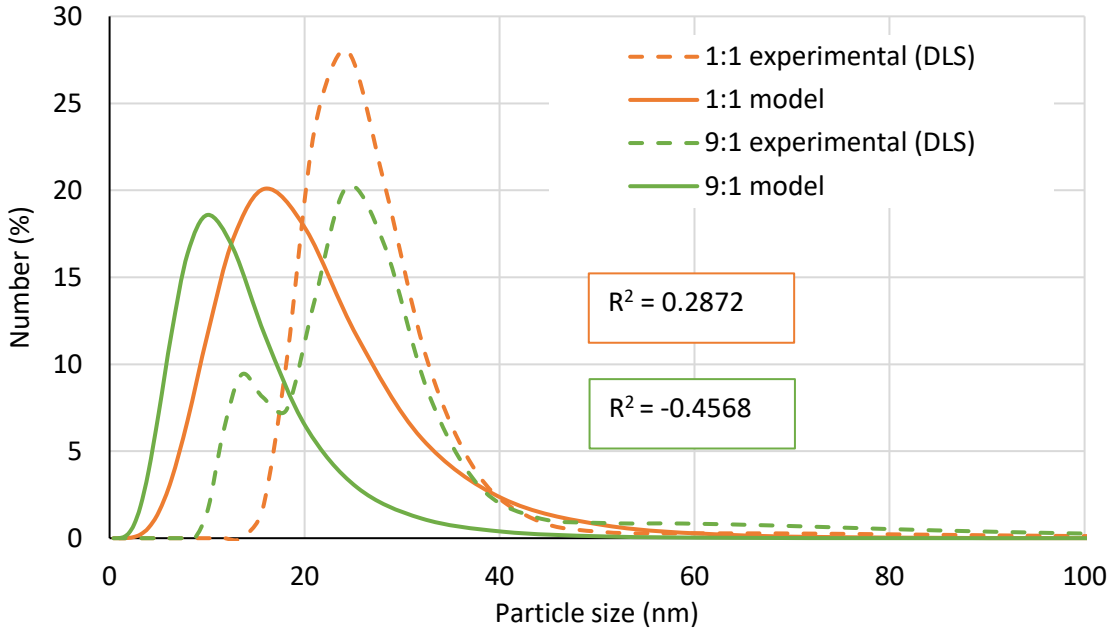

Figure 5-10: Comparison between modelled PSD and experimental results (DLS method) for the effect of antisolvent to solvent ratio at conditions of 2 % w/v starch, 1200 rpm, 18 mL/s, grooved disc.

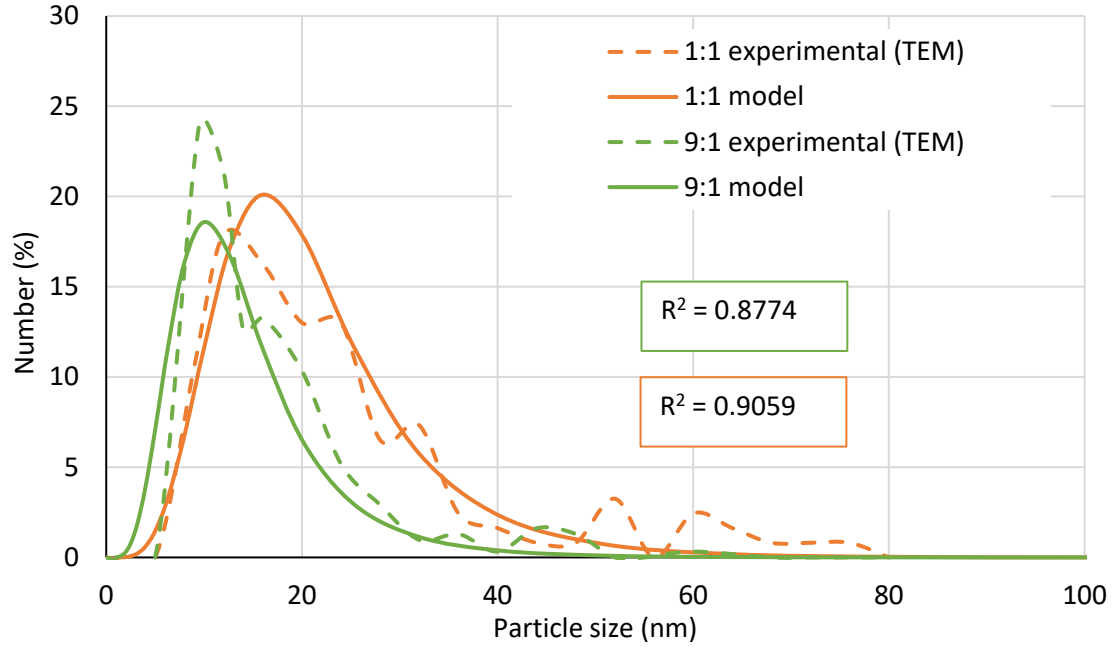

Figure 5-11: Comparison between modelled PSD and experimental results (TEM) for the effect of antisolvent to solvent ratio at conditions of 2 % w/v starch, 1200 rpm, 18 mL/s, grooved disc.

5.2.2.5. Effect of disc surface texture

A comparison between the models generated for the smooth and grooved disc surfaces is shown in Figure 5-12. The results represent conditions of 2 % w/v starch concentration, 1200 rpm, 18 mL/s and 1:1 ratio. Contrary to the experimental results, the modelled results show the smooth disc's size distribution being shifted towards the right of the grooved disc PSD, indicating a lower average particle size obtained using the grooved disc. There are a

number of parameters that are affected by the type of disc which could explain the difference between the model and experimental results. Firstly, the experimental results are not significantly different as has been highlighted earlier in section 4.1.1.4. Secondly, precipitation kinetics used to derive the models indicate greater growth rates on the grooved surface, which would lead to larger particles produced on the grooved disc. In addition to the nucleation and growth kinetics, the residence time distribution in the SDR is also represented in the model through the Peclet number. The equations (Eq. 5-26 and 5-27) for the Peclet number have been taken from Mohammadi and Boodhoo (2012) and have a number of limitations. A high Peclet number suggests a greater number of tanks-in-series, this translates into a tighter residence time distribution bringing the model closer to resemble plug flow. As this occurs, the value of the growth term reduces, hence generating smaller sized particles. The Peclet number for the grooved disc is greater than that for the smooth disc. For example, for the models shown in Figure 5-12, Pe=88 for the smooth disc, and Pe=100 for the grooved disc. Mohammadi and Boodhoo (2012) state that the model is not a good fit beyond certain Peclet numbers. For the smooth disc, this is at Pe>90, and Pe>100 for the grooved disc. Therefore, conditions in the present work are approaching the limits of applicability for accurate Pe representation by the model derived previously (Eq. 5-26 and 5-27). Furthermore, many of the equations specific to the SDR used in the formulation of the model, such as dissipation rate and mean residence time, assume a smooth surfaced disc, not taking grooves into consideration.

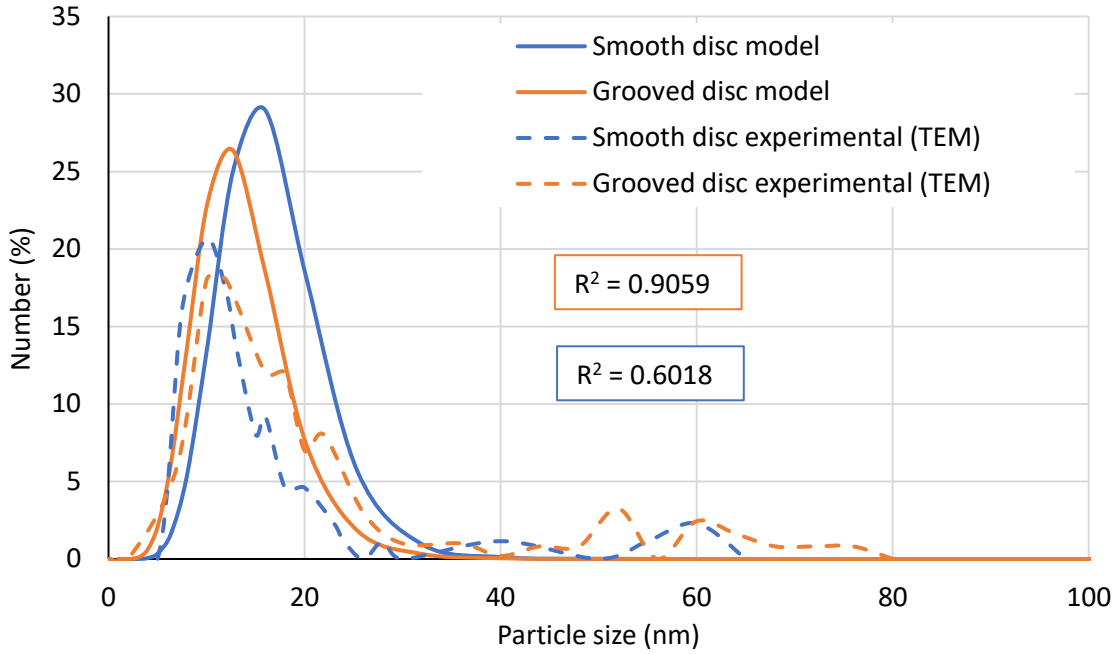

Figure 5-12: Comparison between modelled PSD and experimental results for the effect of disc surface texture at conditions of 2 % w/v starch, 1200 rpm, 18 mL/s and 1:1 ratio.

5.3. Summary

A population balance model for the solvent-antisolvent precipitation of starch nanoparticles in the SDR has been solved using two distinct methods: The Lax-Wendroff method and Hounslow's method of discretisation. Precipitation kinetics, which have been experimentally obtained were included as part of the model. The Lax-Wendroff method based on finite differences method provided a simple and quick solution to the model, neglecting the effects of agglomeration. However, the model and experimental results were a poor fit, as disc hydrodynamics were ignored as well as agglomeration of the particles. The Hounslow's method of discretisation incorporated agglomeration and micromixing effects into the model. Residence time distribution effects were considered through the dimensionless Peclet number, the empirical correlation for which was obtained from literature. The simulated models showed better agreement with experimental results obtained through TEM analysis than with DLS experimental data.

Chapter 6. Conclusions and Recommendations

6.1. Conclusions

The research surrounding the solvent-antisolvent precipitation of starch, to this date has been limited to semi-batch setups, often leading to large particles despite the extra processing time. The SDR has proven to be an effective equipment for the continuous processing of starch nanoparticles through solvent-antisolvent precipitation, generating small particles with a narrow size distribution. Through the operating conditions explored as part of this research, the properties of the nanoparticles in the SDR may be controlled. This has been highlighted in the modelling aspect of the work. Furthermore, a better understanding of the process has been achieved through the attainment of process kinetics.

This research aimed to provide an effective method of starch nanoparticles formation through solvent-antisolvent precipitation in a spinning disc reactor. The approach taken involved both experimental and modelling studies. The following conclusions can be drawn from this research:

1. Particle size and size distribution are impacted by operating conditions such as total flow rate, disc rotational speed, antisolvent to solvent ratio and disc surface texture. These effects can be summarised as follows:

- It has been found that an increase in flow rate and disc rotational speed reduce particle size and PdI values, as shear rate within the thin liquid film increases, intensifying micromixing between the solute/solvent and the antisolvent. There has also been evidence of an increase in agglomeration rate as smaller sized starch nanoparticles are formed.
- The increased antisolvent to solvent ratio has demonstrated a reduction in particle size as a greater proportion of antisolvent reduces solubility, promoting nucleation through increased supersaturation.
- Particle size was not affected significantly by disc texture, however, PdI values were lower for particles produced on the grooved surface as plug flow is promoted as a result of increased turbulent eddies and instabilities in the presence of the grooves.
- An increase in starch concentration showed a reduction in particle size at lower disc speeds and flow rates, however, increasing disc rotational speed and flow rate caused an increase in particle size, indicating greater agglomeration due to increased

supersaturation and mixing conditions. Antisolvent to solvent ratio did not have a profound effect on particle size at the higher starch concentration.

- Yield experiments also showed a similar trend of increases in flow rate, disc speed and antisolvent to solvent ratio resulting in higher yields, more so on the grooved disc.

2. Comparisons were made between starch nanoparticle precipitation in the SDR and a semi-batch system. Power dissipation is higher in an SDR, adding to energy and thus cost for production, however, particle sizes were revealed to be smaller and less agglomerated than those produced in the semi-batch reactor. Additionally, the SDR was successfully used to process high concentrations of starch solutions, whereas issues relating to high viscosities preventing homogenous mixing were attributed to the SBR. Micromixing times were estimated for both systems, with micromixing times being lower in the SDR.
3. XRD patterns have revealed that starch nanoparticles produced through this method are of an amorphous nature. The XRD intensities were found to be affected by antisolvent to solvent ratio, and not disc rotational speed or flow rate.
4. By assigning appropriate dimensionless numbers and through linear regression modelling, an empirical relationship between flow rate, disc rotational speed, antisolvent to solvent ratio and particle size has been established. The following regression models have been obtained, with the first four being in better agreement with the experimental data:

Smooth disc	$Particle\ size\ (\text{microns}) = 10^{0.35} Re^{-0.08} Ta^{-0.06} S^{-0.03}$	R^2 (adj.) = 0.913
Grooved disc	$Particle\ size\ (\text{microns}) = 10^{0.28} Re^{-0.26} Ta^{-0.04}$	R^2 (adj.) = 0.909
Smooth disc	$Particle\ size\ (\text{microns}) = 10^{0.32} Re^{-0.08} {Re_\omega}^{-0.13} S^{-0.03}$	R^2 (adj.) = 0.913
Grooved disc	$Particle\ size\ (\text{microns}) = 10^{0.24} Re^{-0.26} {Re_\omega}^{-0.08}$	R^2 (adj.) = 0.909
Smooth disc	$Particle\ size\ (\text{microns}) = 10^{-0.37} Ro^{0.03} S^{-0.08}$	R^2 (adj.) = 0.734
Grooved disc	$Particle\ size\ (\text{microns}) = 10^{-0.36} Ro^{-0.06} S^{-0.12}$	R^2 (adj.) = 0.830

5. Induction times for the solvent-antisolvent precipitation of starch nanoparticles in the SDR have been estimated through the use of a high-speed camera system. Induction times in the range of 13 ms to 144 ms have been obtained through this method. The induction times along with particle count were used in the estimation of nucleation rates. An increase in nucleation rate was observed with an increase in flow rate, disc

rotational speed and antisolvent to solvent ratio. The maximum average nucleation rate was estimated as 6.44×10^{16} mL^{-1} s^{-1} at conditions of 1200 rpm, 9:1 ratio and 15 mL/s on the smooth disc. The surface texture of the disc also influenced nucleation rate, as at low antisolvent to solvent ratios and low total flow rates, nucleation rates were found to be greater on the grooved disc, whereas at higher flow rates and greater antisolvent concentrations, a 'jumping' effect was observed causing liquid to bounce off the grooves upon entry, thus increasing induction time. In addition, assuming homogeneous nucleation is the dominant mechanism, values for critical radii and interfacial tension have been determined using induction time estimates and compared against values found in literature for solvent-antisolvent systems. Finally, nucleation and growth kinetics have been estimated based on the assumption that nucleation is dominant, consuming the majority of supersaturation for particle formation rather than growth. The following nucleation and growth rate equations have been estimated for starch nanoparticle precipitation in an SDR:

Grooved disc	$J = 1.86 \times 10^{16} S^{0.126}\ (\mathrm{mL^{-1}s^{-1}})$
Smooth disc	$J = 1.24 \times 10^{15} S^{0.437}\ (\mathrm{mL^{-1}s^{-1}})$
Grooved disc	$G = 1.95 \times 10^{-7} (S-1)^{0.088}\ (\mathrm{m.s^{-1}})$
Smooth disc	$G = 7.35 \times 10^{-8} (S-1)^{0.228}\ (\mathrm{m.s^{-1}})$

6. Modelling studies for the solvent-antisolvent precipitation of starch nanoparticles in an SDR were carried out with the aid of the population balance equation (PBE). Two methods were implemented to solve the PBEs. The first method was the Lax-Wendroff method, assuming no agglomeration or breakage. The resulting PSD model did not agree well with experimental PSDs, indicating that agglomeration needs to be considered in the model. The Hounslow's method of discretisation was then applied, incorporating nucleation, growth, agglomeration and breakage into the model. Furthermore, a micromixing model based on the segregation of reactant volumes was used to account for micromixing effects of the SDR. The resulting PSD model is in a close agreement with experimental results determined from TEM measurements.

The SDR has previously been applied to a number of precipitation process, mainly concerning reactive precipitation. However, this is the first thorough research on solvent-antisolvent precipitation in an SDR. Based on the conclusions from this work as well as previous precipitation studies, it seems reasonable to say that the SDR has demonstrated its

capability as an effective crystalliser, both, achieving small particles as well as narrow size distributions through the enhanced micromixing provided in the SDR environment.

6.2. Recommendations for future work

This PhD thesis investigated solvent-antisolvent precipitation in a spinning disc reactor and represents the most thorough research studies carried out within this area. However, to further develop the findings, based on the challenges encountered conducting this research as well as the avenues that were left unexplored due to limited timescales imposed on this project, the following ideas are suggested for future work:

1. Backmixing around the entry point on the disc was prominent at conditions where mixing between solute/solvent and the antisolvent was poor. Studies have shown micromixing is influenced by feed location as well as the number of feed points. It is suggested that future work focuses on the addition of the antisolvent at various locations in the SDR as well as multiple feed points for the antisolvent stream as opposed to the single point distribution as was used in this study.
2. Surfactant concentration has been kept constant throughout this study, as a percentage of the concentration of solute added. However, as the size and number of particles precipitated is affected by the studied operating conditions, the optimum surfactant concentration at each of these conditions would change. Hence a set of experiments are required to investigate the optimum surfactant concentration.
3. Increasing concentration of starch affected particle size and size distribution. However, the experiments conducted in the SDR study employed only two sets of concentrations of starch. To get a better idea of the effect of concentration, a larger range of concentrations may need to be studied, particularly at concentrations greater than 4 % w/v. Furthermore, TEM analysis at the higher concentration was not conducted during the current study, and hence are proposed for future work in order to see the effect of shape, size and extent of agglomeration amongst the nanoparticles.
4. Induction time measurements taken in the SDR have relatively large random errors associated with them. The following have been identified as the possible causes of the errors: (1) particles are too small to measure and the estimated values for induction times represent a maximum value; (2) the residence time equation used assumes fully synchronised flow on the disc which is not true for all conditions. This indicates the need for a more accurate determination of induction time in the SDR perhaps through the use

of a camera with more powerful magnification or an on-line method to monitor changes in turbulence or concentration as supersaturation is developed.

5. Antisolvent to solvent ratio, hence supersaturation values were limited to three levels, and in order to get a better understanding of how supersaturation impacts induction time and nucleation rate, experiments consisting of a broader range of supersaturations are recommended for future work.
6. Many equations applied in this research are based on liquid flow in a smooth disc surface, and thus development of hydrodynamics on a grooved disc needs further attention.
7. Growth rate has not been measured and is based on a few assumptions. It is recommended that growth rate of starch nanoparticles is determined as part of future work as well an investigation into factors affecting nanoparticle growth.
8. Modelling studies can benefit from the inclusion of micromixing models which are better related to the SDR, specifically effects of disc surface on micromixing need to be considered.
9. To relate this work to industrial applications, an evaluation of the starch nanoparticles is recommended in terms of surface area, bioavailability and dissolution rate, with focus on the effect of various experimental conditions in the SDR.
10. Finally, for the application of the SDR as a commercial crystallising technology, further work in the area of scale-up is recommended. As micromixing between the solvent and the antisolvent are crucial in this process, control of film thickness and shear rate are key during scale-up. Furthermore, comparisons with other PI technologies, such as microreactors, are necessary, with particular emphasis on a cost-benefit analysis.

References

AAMIR, E., NAGY, Z. K., RIELLY, C. D., KLEINERT, T. & JUDAT, B. 2009. Combined quadrature method of moments and method of characteristics approach for efficient solution of population balance models for dynamic modeling and crystal size distribution control of crystallization processes. *Industrial and Engineering Chemistry Research,* 48**,** 8575-8584.

AGUIAR, R., MUHR, H., PLASARI, E., BURTY, M. & ROCABOIS, P. 2003. Comparative study of the influence of homogeneous and heterogenous (multi-phase) precipitation processes on the particle size distribution. *Chemical Engineering and Technology,* 26**,** 292-295.

AHOBA-SAM, C., BOODHOO, K. V. K., OLSBYE, U. & JENS, K.-J. 2018. Tailoring Cu Nanoparticle Catalyst for Methanol Synthesis Using the Spinning Disk Reactor. *Materials,* 11**,** 154.

ALI RAZAVI, S. M. & AMINI, A. M. 2016. 8 - Starch nanomaterials: a state-of-the-art review and future trends. *In:* GRUMEZESCU, A. M. (ed.) *Novel Approaches of Nanotechnology in Food.* Academic Press.

ALVAREZ, A. J. & MYERSON, A. S. 2010. Continuous plug flow crystallization of pharmaceutical compounds. *Crystal Growth and Design,* 10**,** 2219-2228.

ALVAREZ, A. J., SINGH, A. & MYERSON, A. S. 2011. Crystallization of cyclosporine in a multistage continuous MSMPR crystallizer. *Crystal Growth and Design,* 11**,** 4392-4400.

AOUNE, A. & RAMSHAW, C. 1999. Process intensification: heat and mass transfer characteristics of liquid films on rotating discs. *International Journal of Heat and Mass Transfer,* 42**,** 2543-2556.

ASSIRELLI, M., BUJALSKI, W., EAGLESHAM, A. & NIENOW, A. W. 2002. Study Of Micromixing in a Stirred Tank Using a Rushton Turbine: Comparison of Feed Positions and Other Mixing Devices. *Chemical Engineering Research and Design,* 80**,** 855-863.

BALDEA, M. 2015. From process integration to process intensification. *Computers and Chemical Engineering,* 81**,** 104-114.

BALDYGA, J., PODGÓRSKA, W. & POHORECKI, R. 1995. Mixing-precipitation model with application to double feed semibatch precipitation. *Chemical Engineering Science,* 50**,** 1281-1300.

BASU, S. & CETEGEN, B. M. 2006. Analysis of hydrodynamics and heat transfer in a thin liquid film flowing over a rotating disk by the integral method. *Journal of Heat Transfer,* 128**,** 217-225.

BECK, C., DALVI, S. V. & DAVE, R. N. 2010. Controlled liquid antisolvent precipitation using a rapid mixing device. *Chemical Engineering Science,* 65**,** 5669-5675.

BEL HAAJ, S., THIELEMANS, W., MAGNIN, A. & BOUFI, S. 2016. Starch nanocrystals and starch nanoparticles from waxy maize as nanoreinforcement: A comparative study. *Carbohydrate Polymers,* 143**,** 310-317.

BENNEMA, P. & SÖHNEL, O. 1990. Interfacial surface tension for crystallization and precipitation from aqueous solutions. *Journal of Crystal Growth,* 102**,** 547-556.

BENNETT, M. K. & ROHANI, S. 2001. Solution of population balance equations with a new combined Lax- Wendroff/Crank-Nicholson method. *Chemical Engineering Science,* 56**,** 6623-6633.

BLANDIN, A. F., MANGIN, D., NALLET, V., KLEIN, J. P. & BOSSOUTROT, J. M. 2001. Kinetics identification of salicylic acid precipitation through experiments in a batch stirred vessel and a T-mixer. *Chemical Engineering Journal,* 81**,** 91-100.

BOODHOO, K. 1999. Process intensification : spinning disc reactor for the polymerisation of styrene. PhD Thesis, Newcastle University.

BOODHOO, K. 2013. Spinning Disc Reactor for Green Processing and Synthesis. *Process Intensification for Green Chemistry.* John Wiley & Sons, Ltd.

BOODHOO, K. & HARVEY, A. 2013. Process Intensification: An Overview of Principles and Practice. *Process Intensification for Green Chemistry.* John Wiley & Sons, Ltd.

BOODHOO, K. V. K. & AL-HENGARI, S. R. 2012. Micromixing Characteristics in a Small-Scale Spinning Disk Reactor. *Chemical Engineering & Technology,* 35**,** 1229-1237.

BOODHOO, K. V. K., DUNK, W. A. E., VICEVIC, M., JACHUCK, R. J., SAGE, V., MACQUARRIE, D. J. & CLARK, J. H. 2006. Classical cationic polymerization of styrene in a spinning disc reactor using silica-supported BF3 catalyst. *Journal of Applied Polymer Science,* 101**,** 8-19.

BOODHOO, K. V. K. & JACHUCK, R. J. 2000. Process intensification: spinning disk reactor for styrene polymerisation. *Applied Thermal Engineering,* 20**,** 1127-1146.

BROWN, C. J., ADELAKUN, J. A. & NI, X. W. 2015. Characterization and modelling of antisolvent crystallization of salicylic acid in a continuous oscillatory baffled crystallizer. *Chemical Engineering and Processing: Process Intensification,* 97**,** 180-186.

BROWN, C. J., LEE, Y. C., NAGY, Z. K. & NI, X. 2014. Evaluation of crystallization kinetics of adipic acid in an oscillatory baffled crystallizer. *CrystEngComm,* 16**,** 8008-8014.

BROWN, C. J. & NI, X. 2011. Online evaluation of paracetamol antisolvent crystallization growth rate with video imaging in an oscillatory baffled crystallizer. *Crystal Growth and Design,* 11**,** 719-725.

BURNS, J. R., RAMSHAW, C. & JACHUCK, R. J. 2003. Measurement of liquid film thickness and the determination of spin-up radius on a rotating disc using an electrical resistance technique. *Chemical Engineering Science,* 58**,** 2245-2253.

CAFIERO, L. M., BAFFI, G., CHIANESE, A. & JACHUCK, R. J. J. 2002. Process Intensification: Precipitation of Barium Sulfate Using a Spinning Disk Reactor. *Industrial & Engineering Chemistry Research,* 41**,** 5240-5246.

CAROSSO, P. A. & PELIZZETTI, E. 1984. A stopped-flow technique in fast precipitation kinetics - The case of barium sulphate. *Journal of Crystal Growth,* 68**,** 532-536.

CHAITANYA, K. K. & SARKAR, D. 2014. Determination of the Metastable Zone Width by a Simple Optical Probe. *Chemical Engineering & Technology,* 37**,** 1037-1042.

CHARWAT, A. F., KELLY, R. E. & GAZLEY, C. 1972. Flow and stability of thin liquid films on a rotating disk. *Journal of Fluid Mechanics,* 53**,** 227-&.

CHEETHAM, N. W. H. & TAO, L. 1998. Variation in crystalline type with amylose content in maize starch granules: An X-ray powder diffraction study. *Carbohydrate Polymers,* 36**,** 277-284.

CHEMALY, Z., MUHR, H. & FICK, M. 1999. Crystallization kinetics of calcium lactate in a mixed-suspension-mixed-product removal crystallizer. *Industrial and Engineering Chemistry Research,* 38**,** 2803-2808.

CHEN, J.-F., ZHOU, M.-Y., SHAO, L., WANG, Y.-Y., YUN, J., CHEW, N. Y. K. & CHAN, H.-K. 2004. Feasibility of preparing nanodrugs by high-gravity reactive precipitation. *International Journal of Pharmaceutics,* 269**,** 267-274.

CHEN, X., ZHENG, B. & LIU, H. 2011. Optical and digital microscopic imaging techniques and applications in pathology. *Analytical cellular pathology (Amsterdam),* 34**,** 5-18.

CHEN, Y. S., TAI, C. Y. D., CHANG, M. H. & LIU, H. S. 2006. Characteristics of micromixing in a rotating packed bed. *Journal of the Chinese Institute of Chemical Engineers,* 37**,** 63-69.

CHIANESE, A., KAREL, M. & MAZZAROTTA, B. 1995. Nucleation kinetics of pentaerythritol. *Chemical Engineering Journal and the Biochemical Engineering Journal,* 58**,** 209-214.

CHIN, S. F., AZMAN, A. & PANG, S. C. 2014. Size Controlled Synthesis of Starch Nanoparticles by a Microemulsion Method. *Journal of Nanomaterials,* 2014**,** 7.

CHIN, S. F., IYER, K. S., RASTON, C. L. & SAUNDERS, M. 2008. Size selective synthesis of superparamagnetic nanoparticles in thin fluids under continuous flow conditions. *Advanced Functional Materials,* 18**,** 922-927.

CHIN, S. F., PANG, S. C. & TAY, S. H. 2011. Size controlled synthesis of starch nanoparticles by a simple nanoprecipitation method. *Carbohydrate Polymers,* 86**,** 1817-1819.

CHIU, T. Y. & CHRISTOFIDES, P. D. 2000. Robust control of particulate processes using uncertain population balances. *AIChE Journal,* 46**,** 266-280.

D' INTINO, A. F., DE CAPRARIIS, B., SANTARELLI, M. L., VERDONE, N. & CHIANESE, A. 2014. Best operating conditions to produce hydroxyapatite nanoparticles by means of a spinning disc reactor. *Frontiers of Chemical Science and Engineering,* 8**,** 156-160.

DABIR, H., DAVARPANAH, M. & AHMADPOUR, A. 2015. Effects of different operating parameters on the particle size of silver chloride nanoparticles prepared in a spinning disk reactor. *Applied Physics A: Materials Science and Processing,* 120**,** 105-113.

DALVI, S. V. & YADAV, M. D. 2015. Effect of ultrasound and stabilizers on nucleation kinetics of curcumin during liquid antisolvent precipitation. *Ultrasonics Sonochemistry,* 24**,** 114-122.

DE CAPRARIIS, B., DI RITA, M., STOLLER, M., VERDONE, N. & CHIANESE, A. 2012. Reaction-precipitation by a spinning disc reactor: Influence of hydrodynamics on nanoparticles production. *Chemical Engineering Science,* 76**,** 73-80.

DEHKORDI, A. M. & VAFAEIMANESH, A. 2009. Synthesis of barium sulfate nanoparticles using a spinning disk reactor: Effects of supersaturation, disk rotation speed, free ion ratio, and disk diameter. *Industrial and Engineering Chemistry Research,* 48**,** 7574-7580.

DOBIE, C. G., MARIJAVICEVIC & BOODHOO, K. V. K. 2013. An evaluation of the effectiveness of continuous thin film processing in a spinning disc reactor for bulk free-radical photo-copolymerisation. *Chemical Engineering and Processing: Process Intensification,* 71**,** 97-106.

DOKI, N., KUBOTA, N., YOKOTA, M., KIMURA, S. & SASAKI, S. 2002. Production of sodium chloride crystals of uni-modal size distribution by batch dilution crystallization. *Journal of Chemical Engineering of Japan,* 35**,** 1099-1104.

DONG, Y., NG, W. K., HU, J., SHEN, S. & TAN, R. B. H. 2010. A continuous and highly effective static mixing process for antisolvent precipitation of nanoparticles of poorly water-soluble drugs. *International Journal of Pharmaceutics,* 386**,** 256-261.

DONG, Y., NG, W. K., SHEN, S., KIM, S. & TAN, R. B. H. 2011. Controlled antisolvent precipitation of spironolactone nanoparticles by impingement mixing. *International Journal of Pharmaceutics,* 410**,** 175-179.

DUFRESNE, A. 2015. Starch and Nanoparticle. *In:* RAMAWAT, G. K. & MÉRILLON, J.-M. (eds.) *Polysaccharides: Bioactivity and Biotechnology.* Cham: Springer International Publishing.

EITZLMAYR, A. 2010. *Numerical simulation of nanoparticle precipitation via the population balance equation.* MSc, Graz University of Technology.

EMSLIE, A. G., BONNER, F. T. & PECK, L. G. 1958. Flow of a Viscous Liquid on a Rotating Disk. *Journal of Applied Physics,* 29**,** 858-862.

ESPIG, H. & HOYLE, R. 1965. Waves in a thin liquid layer on a rotating disk. *Journal of Fluid Mechanics,* 22**,** 671-677.

FALOLA, A., BORISSOVA, A. & WANG, X. Z. 2013. Extended method of moment for general population balance models including size dependent growth rate, aggregation and breakage kernels. *Computers and Chemical Engineering,* 56**,** 1-11.

FUJIWARA, M., CHOW, P. S., MA, D. L. & BRAATZ, R. D. 2002. Paracetamol Crystallization Using Laser Backscattering and ATR-FTIR Spectroscopy: Metastability, Agglomeration, and Control. *Crystal Growth & Design,* 2**,** 363-370.

FURUKAWA, H., KATO, Y., INOUE, Y., KATO, T., TADA, Y. & HASHIMOTO, S. 2012. Correlation of Power Consumption for Several Kinds of Mixing Impellers. *International Journal of Chemical Engineering,* 2012.

GALBRAITH, S. C. & SCHNEIDER, P. A. 2014. Modelling and simulation of inorganic precipitation with nucleation, crystal growth and aggregation: A new approach to an old method. *Chemical Engineering Journal,* 240**,** 124-132.

GHIASY, D., BOODHOO, K. V. K. & THAM, M. T. 2012. Thermographic analysis of thin liquid films on a rotating disc: Approach and challenges. *Applied Thermal Engineering,* 44**,** 39-49.

GHIASY, D., THAM, M. T. & BOODHOO, K. V. K. 2013. Control of a spinning disc reactor: an experimental study. *Industrial & Engineering Chemistry Research,* 52**,** 16832-16841.

GRANBERG, R. A., BLOCH, D. G. & RASMUSON, A. C. 1999. Crystallization of paracetamol in acetone-water mixtures. *Journal of Crystal Growth,* 198**,** 1287-1293.

GRANBERG, R. A., DUCREUX, C., GRACIN, S. & RASMUSON, Å. C. 2001. Primary nucleation of paracetamol in acetone-water mixtures. *Chemical Engineering Science,* 56**,** 2305-2313.

GREEN, D. & PERRY, R. 2007. *Perry's Chemical Engineers' Handbook, Eighth Edition*, McGraw-Hill Education.

HAGENDORFER, H., KAEGI, R., PARLINSKA, M., SINNET, B., LUDWIG, C. & ULRICH, A. 2012. Characterization of silver nanoparticle products using asymmetric flow field flow fractionation with a multidetector approach--a comparison to transmission electron microscopy and batch dynamic light scattering. *Anal Chem,* 84**,** 2678-85.

HASH, J. & OKORAFOR, O. C. 2008. Crystal size distribution (CSD) of batch salting-out crystallization process for sodium sulfate. *Chemical Engineering and Processing: Process Intensification,* 47**,** 622-632.

HEBEISH, A., EL-RAFIE, M. H., EL-SHEIKH, M. A. & EL-NAGGAR, M. E. 2014. Ultra-Fine Characteristics of Starch Nanoparticles Prepared Using Native Starch With and Without Surfactant. *Journal of Inorganic and Organometallic Polymers and Materials,* 24**,** 515-524.

HOLMBÄCK, X. & RASMUSON, Å. C. 1999. Size and morphology of benzoic acid crystals produced by drowning-out crystallisation. *Journal of Crystal Growth,* 198–199, Part 1**,** 780-788.

HOUNSLOW, M. J., RYALL, R. L. & MARSHALL, V. R. 1988. A discretized population balance for nucleation, growth, and aggregation. *AIChE Journal,* 34**,** 1821-1832.

HU, J., CHENG, F., LIN, Y., ZHAO, K. & ZHU, P. 2016. Dissolution of starch in urea/NaOH aqueous solutions. *Journal of Applied Polymer Science,* 133.

HULBURT, H. M. & KATZ, S. 1964. Some problems in particle technology. A statistical mechanical formulation. *Chemical Engineering Science,* 19**,** 555-574.

HUNTER, R. J. 2005. *Foundations of colloid science,* Oxford, Oxford University Press.

JACOBSEN, N. C. & HINRICHSEN, O. 2012. Micromixing Efficiency of a Spinning Disk Reactor. *Industrial & Engineering Chemistry Research,* 51**,** 11643-11652.

JIANG, M. & NI, X. W. 2019. Reactive Crystallization of Paracetamol in a Continuous Oscillatory Baffled Reactor. *Organic Process Research and Development,* 23**,** 882-890.

JIANG, M., ZHU, X., MOLARO, M. C., RASCHE, M. L., ZHANG, H., CHADWICK, K., RAIMONDO, D. M., KIM, K. K. K., ZHOU, L., ZHU, Z., WONG, M. H., O'GRADY, D., HEBRAULT, D., TEDESCO, J. & BRAATZ, R. D. 2014. Modification of crystal shape through deep temperature cycling. *Industrial and Engineering Chemistry Research,* 53**,** 5325-5336.

JIANG, S., LIU, C., HAN, Z., XIONG, L. & SUN, Q. 2016. Evaluation of rheological behavior of starch nanocrystals by acid hydrolysis and starch nanoparticles by self-assembly: A comparative study. *Food Hydrocolloids,* 52**,** 914-922.

JOHN, V., MITKOVA, T., ROLAND, M., SUNDMACHER, K., TOBISKA, L. & VOIGT, A. 2009. Simulations of population balance systems with one internal coordinate using finite element methods. *Chemical Engineering Science,* 64**,** 733-741.

JOHNSON, B. K. & PRUD'HOMME, R. K. 2003. Chemical processing and micromixing in confined impinging jets. *AIChE Journal,* 49**,** 2264-2282.

JONES, A. G. 2002. 3 - Crystallization principles and techniques. *In:* JONES, A. G. (ed.) *Crystallization Process Systems.* Oxford: Butterworth-Heinemann.

KARPINSKI, P. H. & WEY, J. S. 2002. 6 - Precipitation processes. *In:* MYERSON, A. S. (ed.) *Handbook of Industrial Crystallization (Second Edition).* Woburn: Butterworth-Heinemann.

KATAYAMA, K., NOMURA, H., OGATA, H. & EITOKU, T. 2009. Diffusion coefficients for nanoparticles under flow and stop-flow conditions. *Physical Chemistry Chemical Physics,* 11**,** 10494-10499.

KHAN, J. R. 1986. *Heat transfer on a rotating surface with and without phase change.* PhD Thesis, Newcastle University.

KHAN, W. H. & RATHOD, V. K. 2014. Process intensification approach for preparation of curcumin nanoparticles via solvent–nonsolvent nanoprecipitation using spinning disc reactor. *Chemical Engineering and Processing: Process Intensification,* 80**,** 1-10.

KIM, H.-Y., PARK, S. S. & LIM, S.-T. 2015. Preparation, characterization and utilization of starch nanoparticles. *Colloids and Surfaces B: Biointerfaces,* 126**,** 607-620.

KIM, K. J. 2006. Crystal Growth in Drowning-Out Crystallization using a T-Mixer. *Chemical Engineering & Technology,* 29**,** 1267-1272.

KUANG, Y.-Y., ZHANG, Z.-B., XIE, M.-L., WANG, J.-X., LE, Y. & CHEN, J.-F. 2015. Large-Scale Preparation of Amorphous Cefixime Nanoparticles by Antisolvent Precipitation in a High-Gravity Rotating Packed Bed. *Industrial & Engineering Chemistry Research*.

KUBOTA, N. 2008. An interpretation of the metastable zone width concerning primary nucleation in anti-solvent crystallization. *Journal of Crystal Growth,* 310**,** 4647-4651.

KULDIPKUMAR, A., KWON, G. S. & ZHANG, G. G. Z. 2007. Determining the growth mechanism of tolazamide by induction time measurement. *Crystal Growth and Design,* 7**,** 234-242.

KUMAR, S. & RAMKRISHNA, D. 1997. On the solution of population balance equations by discretization - III. Nucleation, growth and aggregation of particles. *Chemical Engineering Science,* 52**,** 4659-4679.

LAFFICHER, R., DIGNE, M., SALVATORI, F., BOUALLEG, M., COLSON, D. & PUEL, F. 2018. Influence of micromixing time and shear rate in fast contacting mixers on the precipitation of boehmite and NH4-dawsonite. *Chemical Engineering Science,* 175**,** 343-353.

LAWTON, S., STEELE, G., SHERING, P., ZHAO, L., LAIRD, I. & NI, X. W. 2009. Continuous crystallization of pharmaceuticals using a continuous oscillatory baffled crystallizer. *Organic Process Research and Development,* 13**,** 1357-1363.

LE CORRE, D. & ANGELLIER-COUSSY, H. 2014. Preparation and application of starch nanoparticles for nanocomposites: A review. *Reactive and Functional Polymers,* 85**,** 97-120.

LEE, F.-M., STOOPS, C. E. & LAHTI, L. E. 1976. An investigation of nucleation and crystal growth mechanism of urea from water-alcohol solutions. *Journal of Crystal Growth,* 32**,** 363-370.

LENEWEIT, G., ROESNER, K. G. & KOEHLER, R. 1999. Surface instabilities of thin liquid film flow on a rotating disk. *Experiments in Fluids,* 26**,** 75-85.

LEVENSPIEL, O. 1999. *Chemical Reaction Engineering,* New York, John Wiley & Sons.

LIM, Y. I., LE LANN, J. M., MEYER, X. M., JOULIA, X., LEE, G. & YOON, E. S. 2002. On the solution of population balance equations (PBE) with accurate front tracking methods in practical crystallization processes. *Chemical Engineering Science,* 57**,** 3715-3732.

LIN, Y., LEE, K. & MATSOUKAS, T. 2002. Solution of the population balance equation using constant-number Monte Carlo. *Chemical Engineering Science,* 57**,** 2241-2252.

LINDENBERG, C. & MAZZOTTI, M. 2011. Continuous Precipitation of L-Asparagine Monohydrate in a Micromixer: Estimation of Nucleation and Growth Kinetics. *AIChE Journal,* 57**,** 942-950.

LINDENBERG, C., SCHÖLL, J., VICUM, L., MAZZOTTI, M. & BROZIO, J. 2008. L-Glutamic acid precipitation: Agglomeration effects. *Crystal Growth and Design,* 8**,** 224-237.

LIU, C., JIANG, S., HAN, Z., XIONG, L. & SUN, Q. 2016a. In vitro digestion of nanoscale starch particles and evolution of thermal, morphological, and structural characteristics. *Food Hydrocolloids,* 61**,** 344-350.

LIU, J. & RASMUSON, Å. C. 2013. Influence of Agitation and Fluid Shear on Primary Nucleation in Solution. *Crystal Growth & Design,* 13**,** 4385-4394.

LIU, Y., XIE, H. & SHI, M. 2016b. Effect of ethanol–water solution on the crystallization of short chain amylose from potato starch. *Starch/Staerke,* 68**,** 683-690.

MAHAJAN, A. J. & KIRWAN, D. J. 1994. Nucleation and growth kinetics of biochemicals measured at high supersaturations. *Journal of Crystal Growth,* 144**,** 281-290.

MAHONEY, A. W., DOYLE III, F. J. & RAMKRISHNA, D. 2002. Inverse problems in population balances: Growth and nucleation from dynamic data. *AIChE Journal,* 48**,** 981-990.

MAISELS, A., EINAR KRUIS, F. & FISSAN, H. 2004. Direct simulation Monte Carlo for simultaneous nucleation, coagulation, and surface growth in dispersed systems. *Chemical Engineering Science,* 59**,** 2231-2239.

MANSON, J. 2017. *Mathematical modelling of TiO2 synthesis in the spinning disc reactor.* Master's thesis, Newcastle University.

MARCHISIO, D. L. & FOX, R. O. 2005. Solution of population balance equations using the direct quadrature method of moments. *Journal of Aerosol Science,* 36**,** 43-73.

MARCHISIO, D. L., PIKTURNA, J. T., FOX, R. O., VIGIL, R. D. & BARRESI, A. A. 2003. Quadrature method of moments for population-balance equations. *AIChE Journal,* 49**,** 1266-1276.

MASON, R. E. A. & STRICKLAND-CONSTABLE, R. F. 1966. Breeding of crystal nuclei. *Transactions of the Faraday Society,* 62**,** 455-461.

MCCARTHY, E. D., DUNK, W. A. E. & BOODHOO, K. V. K. 2007. Application of an intensified narrow channel reactor to the aqueous phase precipitation of barium sulphate. *Journal of Colloid and Interface Science,* 305**,** 72-87.

MCGLONE, T., BRIGGS, N. E. B., CLARK, C. A., BROWN, C. J., SEFCIK, J. & FLORENCE, A. J. 2015. Oscillatory Flow Reactors (OFRs) for Continuous Manufacturing and Crystallization. *Organic Process Research and Development,* 19**,** 1186-1202.

MERSMANN, A. 1990. Calculation of interfacial tensions. *Journal of Crystal Growth,* 102**,** 841-847.
MERSMANN, A. 1999. Crystallization and precipitation. *Chemical Engineering and Processing: Process Intensification,* 38**,** 345-353.
MERSMANN, A. 2001. *Crystallization Technology Handbook*, Taylor & Francis.
MESBAH, A., KRAMER, H. J. M., HUESMAN, A. E. M. & VAN DEN HOF, P. M. J. 2009. A control oriented study on the numerical solution of the population balance equation for crystallization processes. *Chemical Engineering Science,* 64**,** 4262-4277.
MOHAMMADI, S. 2014. *Nano-Tio₂ precipitation in SDRs :experimental and modelling studies.* PhD thesis, Newcastle University.
MOHAMMADI, S. & BOODHOO, K. V. K. 2012. Online conductivity measurement of residence time distribution of thin film flow in the spinning disc reactor. *Chemical Engineering Journal,* 207–208**,** 885-894.
MOHAMMADI, S., HARVEY, A. & BOODHOO, K. V. K. 2014. Synthesis of TiO2 nanoparticles in a spinning disc reactor. *Chemical Engineering Journal,* 258**,** 171-184.
MOHANTY, R., BHANDARKAR, S., ZUROMSKI, B., BROWN, R. & ESTRIN, J. 1988. Characterizing the product crystals from a mixing tee process. *AIChE Journal,* 34**,** 2063-2068.
MORRIS, G., POWER, G., FERGUSON, S., BARRETT, M., HOU, G. & GLENNON, B. 2015. Estimation of Nucleation and Growth Kinetics of Benzoic Acid by Population Balance Modeling of a Continuous Cooling Mixed Suspension, Mixed Product Removal Crystallizer. *Organic Process Research and Development,* 19**,** 1891-1902.
MULLIN, J. W. 2001. Oxford, Butterworth-Heinemann.
MURA, F. & ZACCONE, A. 2016. Effects of shear flow on phase nucleation and crystallization. *Physical Review E,* 93**,** 042803.
MYASNIKOV, S. K., CHIPRYAKOVA, A. P. & KULOV, N. N. 2013. Kinetics, energy characteristics, and intensification of crystallization processes in chemical precipitation of hardness ions. *Theoretical Foundations of Chemical Engineering,* 47**,** 505-523.
MYERSON, A. S. 2002. *In:* MYERSON, A. S. (ed.) *Handbook of Industrial Crystallization (Second Edition).* Woburn: Butterworth-Heinemann.
MYERSON, A. S. & GINDE, R. 2002. 2 - Crystals, crystal growth, and nucleation. *In:* MYERSON, A. S. (ed.) *Handbook of Industrial Crystallization (Second Edition).* Woburn: Butterworth-Heinemann.
NAPPO, V., SULLIVAN, R., DAVEY, R., KUHN, S., GAVRIILIDIS, A. & MAZZEI, L. 2018. Effect of shear rate on primary nucleation of para-amino benzoic acid in solution under different fluid dynamic conditions. *Chemical Engineering Research and Design,* 136**,** 48-56.
NICHOLS, G., BYARD, S., BLOXHAM, M. J., BOTTERILL, J., DAWSON, N. J., DENNIS, A., DIART, V., NORTH, N. C. & SHERWOOD, J. D. 2002. A review of the terms agglomerate and aggregate with a recommendation for nomenclature used in powder and particle characterization. *Journal of Pharmaceutical Sciences,* 91**,** 2103-2109.
NICMANIS, M. & HOUNSLOW, M. J. 1998. Finite-element methods for steady-state population balance equations. *AIChE Journal,* 44**,** 2258-2272.
NIELSEN, A. E. 1961. Homogeneous Nucleation in Barium Sulfate Precipitation. *Acta Chemica Scandinavica,* 15**,** 441-442.
Ó'CIARDHÁ, C. T., FRAWLEY, P. J. & MITCHELL, N. A. 2011. Estimation of the nucleation kinetics for the anti-solvent crystallisation of paracetamol in methanol/water solutions. *Journal of Crystal Growth,* 328**,** 50-57.
O'GRADY, D., BARRETT, M., CASEY, E. & GLENNON, B. 2007. The Effect of Mixing on the Metastable Zone Width and Nucleation Kinetics in the Anti-Solvent Crystallization of Benzoic Acid. *Chemical Engineering Research and Design,* 85**,** 945-952.
OHSHIMA, H. 1995. Effective surface potential and double-layer interaction of colloidal particles. *Journal of Colloid And Interface Science,* 174**,** 45-52.
OMAR, H. M. & ROHANI, S. 2017. Crystal Population Balance Formulation and Solution Methods: A Review. *Crystal Growth and Design,* 17**,** 4028-4041.
OMAR, W. 2006. Effect of Solvent Composition on Crystallization Process of Ascorbic Acid. *Chemical Engineering & Technology,* 29**,** 119-123.

OMAR, W., MOHNICKE, M. & ULRICH, J. 2006. Determination of the solid liquid interfacial energy and thereby the critical nucleus size of paracetamol in different solvents. *Crystal Research and Technology,* 41**,** 337-343.

OOSTERHOF, H., WITKAMP, G. J. & VAN ROSMALEN, G. M. 2001. Antisolvent crystallization of anhydrous sodium carbonate at atmospherical conditions. *Aiche Journal,* 47**,** 602-608.

OXLEY, P., BRECHTELSBAUER, C., RICARD, F., LEWIS, N. & RAMSHAW, C. 2000. Evaluation of spinning disk reactor technology for the manufacture of pharmaceuticals. *Industrial & Engineering Chemistry Research,* 39**,** 2175-2182.

OZAR, B., CETEGEN, B. M. & FAGHRI, A. 2003. Experiments on the flow of a thin liquid film over a horizontal stationary and rotating disk surface. *Experiments in Fluids,* 34**,** 556-565.

PARISI, M. & CHIANESE, A. 2013. Investigation of nucleation kinetics by nephelometric measurements. *Chemical Engineering and Technology,* 36**,** 1335-1340.

PEI, X., ZHAI, K., LIANG, X., DENG, Y., TAN, Y., WANG, P. & XU, K. 2017. Interfacial Activity of Starch-Based Nanoparticles at the Oil-Water Interface. *Langmuir,* 33**,** 3787-3793.

PIYASENA, P., RAMASWAMY, H. S., AWUAH, G. B. & DEFELICE, C. 2003. Dielectric properties of starch solutions as influenced by temperature, concentration, frequency and salt. *Journal of Food Process Engineering,* 26**,** 93-119.

PRIELING, D. 2013. *Computational investigation of liquid film flow on rotating disks.* Doctor of Engineering sciences, Graz University of Technology.

QIN, Y., LIU, C., JIANG, S., XIONG, L. & SUN, Q. 2016. Characterization of starch nanoparticles prepared by nanoprecipitation: Influence of amylose content and starch type. *Industrial Crops and Products,* 87**,** 182-190.

RAMISETTY, K. A., PANDIT, A. B. & GOGATE, P. R. 2013. Ultrasound-Assisted Antisolvent Crystallization of Benzoic Acid: Effect of Process Variables Supported by Theoretical Simulations. *Industrial & Engineering Chemistry Research,* 52**,** 17573-17582.

RAMSHAW, C. 1983. 'HIGEE' Distillation - An example of process intensification. *Chemical Engineer (London)***,** 13-14.

RANDOLPH, A. D. 1964. A population balance for countable entities. *The Canadian Journal of Chemical Engineering,* 42**,** 280-281.

RANE, C. V., GANGULI, A. A., KALEKUDITHI, E., PATIL, R. N., JOSHI, J. B. & RAMKRISHNA, D. 2014. CFD simulation and comparison of industrial crystallizers. *Canadian Journal of Chemical Engineering,* 92**,** 2138-2156.

RAUSCHER, J. W., KELLY, R. E. & COLE, J. D. 1973. An Asymptotic Solution for the Laminar Flow of a Thin Film on a Rotating Disk. *Journal of Applied Mechanics,* 40**,** 43-47.

REAY, D., RAMSHAW, C. & HARVEY, A. 2008. *Process Intensification*.

RIGOPOULOS, S. & JONES, A. G. 2003. Finite-element scheme for solution of the dynamic population balance equation. *AIChE Journal,* 49**,** 1127-1139.

ROBERTS, S. A. & CAMERON, R. E. 2002. The effects of concentration and sodium hydroxide on the rheological properties of potato starch gelatinisation. *Carbohydrate Polymers,* 50**,** 133-143.

ROELANDS, C. P. M., ROESTENBERG, R. R. W., TER HORST, J. H., KRAMER, H. J. M. & JANSENS, P. J. 2004. Development of an Experimental Method to Measure Nucleation Rates in Reactive Precipitation. *Crystal Growth & Design,* 4**,** 921-928.

ROHANI, S. & BOURNE, J. R. 1990. A simplified approach to the operation of a batch crystallizer. *The Canadian Journal of Chemical Engineering,* 68**,** 799-806.

SAW, C. B., ANDERSON, G. K., HOWARTH, C. R. & PORTER, J. E. Application of the spinning disc reactor as an ozone contractor. Proceedings of the Industrial Waste Conference, 1985. 813-823.

SCHALL, J. M., MANDUR, J. S., BRAATZ, R. D. & MYERSON, A. S. 2018. Nucleation and Growth Kinetics for Combined Cooling and Antisolvent Crystallization in a Mixed-Suspension, Mixed-Product Removal System: Estimating Solvent Dependency. *Crystal Growth & Design,* 18**,** 1560-1570.

SCHEICHL, B. & KLUWICK, A. 2019. Laminar spread of a circular liquid jet impinging axially on a rotating disc. *Journal of Fluid Mechanics,* 864**,** 449-489.

SCHWARZER, H. C. & PEUKERT, W. 2004. Combined experimental/numerical study on the precipitation of nanoparticles. *AIChE Journal,* 50**,** 3234-3247.

SCHWARZER, H. C. & PEUKERT, W. 2005. Prediction of aggregation kinetics based on surface properties of nanoparticles. *Chemical Engineering Science,* 60**,** 11-25.

SCHWARZER, H. C., SCHWERTFIRM, F., MANHART, M., SCHMID, H. J. & PEUKERT, W. 2006. Predictive simulation of nanoparticle precipitation based on the population balance equation. *Chemical Engineering Science,* 61**,** 167-181.

SHANG, J. & GAO, X. 2014. Nanoparticle counting: towards accurate determination of the molar concentration. *Chemical Society reviews,* 43**,** 7267-7278.

SHEIKHZADEH, M., TRIFKOVIC, M. & ROHANI, S. 2008. Real-time optimal control of an anti-solvent isothermal semi-batch crystallization process. *Chemical Engineering Science,* 63**,** 829-839.

SHEVCHUK, I. V. 2015. *Modelling of convective heat and mass transfer in rotating flows*.

SHI, D., EL-FARRA, N. H., LI, M., MHASKAR, P. & CHRISTOFIDES, P. D. 2006. Predictive control of particle size distribution in particulate processes. *Chemical Engineering Science,* 61**,** 268-281.

SHIAU, L. D. 2018. Determination of the nucleation and growth kinetics for aqueous L-glycine solutions from the turbidity induction time data. *Crystals,* 8.

SHIN, J., JONES, N., IK LEE, D., FLEMING, P., JOYCE, M., DEJONG, R. & BLOEMBERGEN, S. 2012. *Rheological Properties of Starch Latex Dispersions and Starch Latex-Containing Coating Colors*.

SINHA, B., MÜLLER, R. H. & MÖSCHWITZER, J. P. 2013. Bottom-up approaches for preparing drug nanocrystals: Formulations and factors affecting particle size. *International Journal of Pharmaceutics,* 453**,** 126-141.

SÖHNEL, O. 1992. Precipitation : basic principles and industrial applications*,* Oxford [England], Boston, Oxford England, Boston : Butterworth-Heinemann.

SÖHNEL, O. & MULLIN, J. W. 1978. A method for the determination of precipitation induction periods. *Journal of Crystal Growth,* 44**,** 377-382.

SÖHNEL, O. & MULLIN, J. W. 1982. Precipitation of calcium carbonate. *Journal of Crystal Growth,* 60**,** 239-250.

SRICHUWONG, S., SUNARTI, T. C., MISHIMA, T., ISONO, N. & HISAMATSU, M. 2005. Starches from different botanical sources I: Contribution of amylopectin fine structure to thermal properties and enzyme digestibility. *Carbohydrate Polymers,* 60**,** 529-538.

STANKIEWICZ, A. I. & MOULIJN, J. A. 2000. Process intensification: Transforming chemical engineering. *Chemical Engineering Progress,* 96**,** 22-33.

SUN, Q., LI, G., DAI, L., JI, N. & XIONG, L. 2014. Green preparation and characterisation of waxy maize starch nanoparticles through enzymolysis and recrystallisation. *Food Chemistry,* 162**,** 223-228.

TAI, C. Y., TAI, C.-T., CHANG, M.-H. & LIU, H.-S. 2007. Synthesis of magnesium hydroxide and oxide nanoparticles using a spinning disk reactor. *Industrial & engineering chemistry research,* 46**,** 5536-5541.

TAI, C. Y., WANG, Y. H. & LIU, H. S. 2008. A green process for preparing silver nanoparticles using spinning disk reactor. *Aiche Journal,* 54**,** 445-452.

TAKIYAMA, H., MINAMISONO, T., OSADA, Y. & MATSUOKA, M. 2010. Operation design for controlling polymorphism in the anti-solvent crystallization by using ternary phase diagram. *Chemical Engineering Research & Design,* 88**,** 1242-1247.

TAKIYAMA, H., OTSUHATA, T. & MATSUOKA, M. 1998. Morphology of NaCl crystals in drowning-out precipitation operation. *Chemical Engineering Research & Design,* 76**,** 809-814.

TEYCHENÉ, S. & BISCANS, B. 2008. Nucleation Kinetics of Polymorphs: Induction Period and Interfacial Energy Measurements. *Crystal Growth & Design,* 8**,** 1133-1139.

THOMAS, S., FAGHRI, A. & HANKEY, W. 1991. Experimental analysis and flow visualisation of a thin liquid-film on a stationary and rotating disk. *Journal of Fluids Engineering-Transactions of the Asme,* 113**,** 73-80.

THORAT, A. A. & DALVI, S. V. 2012. Liquid antisolvent precipitation and stabilization of nanoparticles of poorly water soluble drugs in aqueous suspensions: Recent developments and future perspective. *Chemical Engineering Journal,* 181–182**,** 1-34.

TOTH, J., KARDOS-FODOR, A. & HALASZ-PETERFI, S. 2005. The formation of fine particles by salting-out precipitation. *Chemical Engineering and Processing,* 44**,** 193-200.

TSANG, T. H. & RAO, A. 1990. A moving finite element method for the population balance equation. *International Journal for Numerical Methods in Fluids,* 10**,** 753-769.

TUNG, H.-H., PAUL, E. L., MIDLER, M. & MCCAULEY, J. A. 2008a. *Crystallization of Organic Compounds.* John Wiley & Sons, Inc.

TUNG, H.-H., PAUL, E. L., MIDLER, M. & MCCAULEY, J. A. 2008b. Antisolvent Crystallization. *Crystallization of Organic Compounds.* John Wiley & Sons, Inc.

TUNG, H.-H., PAUL, E. L., MIDLER, M. & MCCAULEY, J. A. 2008c. Critical Issues in Crystallization Practice. *Crystallization of Organic Compounds.* John Wiley & Sons, Inc.

VALENTE, I., CELASCO, E., MARCHISIO, D. L. & BARRESI, A. A. 2012. Nanoprecipitation in confined impinging jets mixers: Production, characterization and scale-up of pegylated nanospheres and nanocapsules for pharmaceutical use. *Chemical Engineering Science,* 77**,** 217-227.

VAN GERVEN, T. & STANKIEWICZ, A. 2009. Structure, energy, synergy, time-the fundamentals of process intensification. *Industrial and Engineering Chemistry Research,* 48**,** 2465-2474.

VICEVIC, M., BOODHOO, K. V. K. & SCOTT, K. 2007. Catalytic isomerisation of α-pinene oxide to campholenic aldehyde using silica-supported zinc triflate catalysts: I. Kinetic and thermodynamic studies. *Chemical Engineering Journal,* 133**,** 31-41.

VOLD, R. D. & VOLD, M. J. 1983. *Colloid and interface chemistry,* Reading, Mass., Addison-Wesley.

WANG, H., MUSTAFFAR, A., PHAN, A. N., ZIVKOVIC, V., REAY, D., LAW, R. & BOODHOO, K. 2017. A review of process intensification applied to solids handling. *Chemical Engineering and Processing: Process Intensification,* 118**,** 78-107.

WANG, J., LI, F. & LAKERVELD, R. 2018. Process Intensification for Pharmaceutical Crystallization. *Chemical Engineering and Processing - Process Intensification,* 127.

WEY, J. S. & KARPINSKI, P. H. 2002. 10 - Batch crystallization. *In:* MYERSON, A. S. (ed.) *Handbook of Industrial Crystallization (Second Edition).* Woburn: Butterworth-Heinemann.

WONG, S. H., WARD, M. C. L. & WHARTON, C. W. 2004. Micro T-mixer as a rapid mixing micromixer. *Sensors and Actuators B: Chemical,* 100**,** 359-379.

WOODS, W. P. 1995. The Hydrodynamics of Thin Liquid Films Flowing Over a Rotating Disc*.* PhD Thesis, Newcastle University.

WU, X., CHANG, Y., FU, Y., REN, L., TONG, J. & ZHOU, J. 2016. Effects of non-solvent and starch solution on formation of starch nanoparticles by nanoprecipitation. *Starch - Stärke,* 68**,** 258-263.

XIANG, Y., WEN, L., CHU, G., SHAO, L., XIAO, G. & CHEN, J. 2010. Modeling of the Precipitation Process in a Rotating Packed Bed and Its Experimental Validation. *Chinese Journal of Chemical Engineering,* 18**,** 249-257.

YANG, H., YU, X., RAVAL, V., MAKKAWI, Y. & FLORENCE, A. 2016. Effect of Oscillatory Flow on Nucleation Kinetics of Butyl Paraben. *Crystal Growth & Design,* 16**,** 875-886.

YANG, Y. C., XIANG, Y., PAN, C., ZOU, H. K., CHU, G. W., AROWO, M. & CHEN, J. F. 2015. Influence of Viscosity on Micromixing Efficiency in a Rotating Packed Bed with Premixed Liquid Distributor. *Journal of Chemical Engineering of Japan,* 48**,** 72-79.

YU, Z. Q., TAN, R. B. H. & CHOW, P. S. 2005. Effects of operating conditions on agglomeration and habit of paracetamol crystals in anti-solvent crystallization. *Journal of Crystal Growth,* 279**,** 477-488.

ZAUNER, R. & JONES, A. G. 2002. On the influence of mixing on crystal precipitation processes-application of the segregated feed model. *Chemical Engineering Science,* 57**,** 821-831.

ZHANG, Y., JIANG, Y., ZHANG, D., QIAN, Y. & WANG, X. Z. 2015. Metastable zone width, crystal nucleation and growth kinetics measurement in anti-solvent crystallization of β-artemether in the mixture of ethanol and water. *Chemical Engineering Research and Design,* 95**,** 187-194.

ZHAO, H., WANG, J.-X., WANG, Q.-A., CHEN, J.-F. & YUN, J. 2007. Controlled Liquid Antisolvent Precipitation of Hydrophobic Pharmaceutical Nanoparticles in a Microchannel Reactor. *Industrial & Engineering Chemistry Research,* 46**,** 8229-8235.

ZHAO, H., WANG, J., ZHANG, H., SHEN, Z., YUN, J. & CHEN, J. 2009. Facile Preparation of Danazol Nanoparticles by High-Gravity Anti-solvent Precipitation (HGAP) Method. *Chinese Journal of Chemical Engineering,* 17**,** 318-323.

ZHI, M., WANG, Y. & WANG, J. 2011. Determining the primary nucleation and growth mechanism of cloxacillin sodium in methanol–butyl acetate system. *Journal of Crystal Growth,* 314**,** 213-219.

Appendices

Appendix A – Design of experiments

Table A-1: Experimental design for SDR experiments.

Run no.	Total flow rate (mL/s)	Antisolvent to solvent ratio	Disc rotational speed (rpm)	Antisolvent flow rate (mL/s)	Solvent flow rate (mL/s)
1	6	1	400	3	3
2	6	1	800	3	3
3	6	9	400	5.4	0.6
4	6	9	800	5.4	0.6
5	18	9	400	16.2	1.8
6	6	5	1200	5	1
7	6	5	400	5	1
8	6	9	1200	5.4	0.6
9	6	1	1200	3	3
10	6	5	800	5	1
11	18	9	800	16.2	1.8
12	18	9	1200	16.2	1.8
13	18	5	400	15	3
14	12	9	1200	10.8	1.2
15	18	5	1200	15	3
16	18	5	800	15	3
17	12	9	400	10.8	1.2
18	12	9	800	10.8	1.2
19	12	1	800	6	6
20	12	1	1200	6	6
21	18	1	800	9	9
22	12	5	1200	10	2
23	18	1	400	9	9
24	12	5	800	10	2
25	12	5	400	10	2
26	12	1	400	6	6
27	18	1	1200	9	9

Following repeats were carried out to assess the reproducibility of the experiments:

Run no.	Total flow rate (mL/s)	Antisolvent to solvent ratio	Disc rotational speed (rpm)	Antisolvent flow rate (mL/s)	Solvent flow rate (mL/s)
28	6	1	400	3	3
29	6	1	400	3	3
30	18	9	400	16.2	1.8
31	18	9	400	16.2	1.8
32	12	5	800	10	2
33	12	5	800	10	2
34	12	9	1200	10.8	1.2
35	12	9	1200	10.8	1.2

Appendix B – Sample calculations

B.1. Yield calculation

Sample calculation of yield for the conditions of 6 mL/s, 1200 rpm and 9:1 ratio, on a grooved disc.

Volume of sample collected = 14 mL

Mass of dried sample = 0.0155 g

Concentration = 0.0155 g / 14 mL = 0.0011 g/mL

Run time = 30 s

Assuming there is no loss, gain or reaction between solvents,

NaOH = 0.6 mL/s x 30 s = 18 mL

Ethanol = 5.4 mL/s x 30 s = 162 mL

Total volume = 180 mL

Mass of starch produced in 30s = 0.0011 g/mL x 180 mL = 0.199 g

Initial mass of starch = 0.02 w/v x 18 mL = 0.36 g

$$Yield\ (\%) = \frac{Mass\ of\ dried\ product}{Mass\ of\ starch\ in\ original\ solution} \times 100$$

Yield = (0.199 g / 0.36 g) x 100 = 55.36 %

B.2. Particle count calculation

Sample calculation of particle count for the conditions of 6 mL/s, 1200 rpm and 9:1 ratio, on a grooved disc.

Volume of sample collected = 14 mL

Mass of total dried starch sample = 0.0155 g

Concentration = 0.0155 g / 14 mL = 0.0011 g/mL

Average particle size estimated from TEM = 17.93 nm = 1.793×10^{-8} m

Density of starch = 1.5 g/mL

Mass of a single starch nanoparticle (Shang and Gao, 2014) = particle volume x density

$$= \frac{\pi\,(\text{diameter})^3}{6}\rho$$

$$= \frac{(1.793 \times 10^{-8})^3\,\pi}{6} \times 1.5 \times 10^6 = 4.53 \times 10^{-18}\ \text{g}$$

$$\text{Particle count} = \frac{\text{Mass of dried product}}{\text{Mass of single particle}}$$

$$= \frac{0.0155\ \text{g}}{4.53 \times 10^{-18}\ \text{g}}$$

$$= 3.42 \text{ x } 10^{15} \text{ particles in } 14 \text{ mL}$$

$$= \frac{3.42 \times 10^{15}}{14\ \text{mL}} = 2.45 \times 10^{14} \text{ particles / mL}$$

B.3. Solubility calculation

The sample calculation used to calculate solubility features 0.2 g ethanol/g NaOH as an example. The following equation has been applied:

$$Solubility\ (g\ starch/g\ NaOH) = \frac{Initial\ mass\ of starch\ (g) - Mass\ of\ starch\ retained\ (g)}{Mass\ of\ 0.5\ M\ NaOH\ solution\ (g)}$$

Initial starch mass (g) = 3.5 g

Undissolved starch mass on filter paper after drying (g) = 0.334 g

Dissolved starch (g) = 3.5 g – 0.334 g = 3.166 g

Volume of 0.5M NaOH = 100 mL

Mass of 0.5 M NaOH = 100 mL x 1.0216 g/mL = 102.16 g

Solubility (g starch/g NaOH) = 3.166 g / 102.16 g = 0.031 g starch/g NaOH

Appendix C – Solubility of starch and supersaturation

C.1: Solubility

Solubility of starch in 0.5 M sodium hydroxide at various concentrations of ethanol has been measured to obtain the plot shown in Figure C-1. Below the concentration of 0.1 g ethanol/g NaOH the mixture would become highly viscous and obtaining a solubility value for starch was not possible through the filtration method employed. Similarly, above 5 g ethanol/g NaOH the solubility was too low to be measurable via this method.

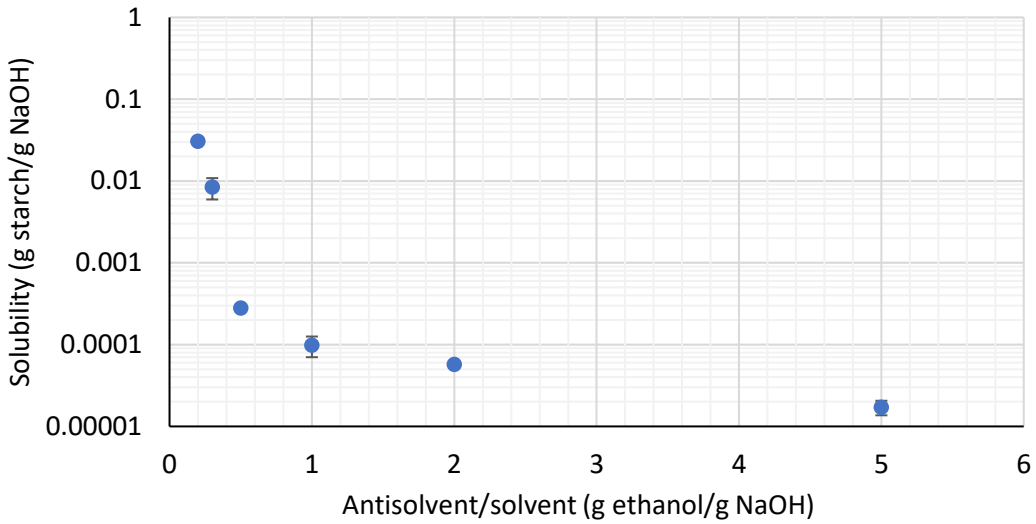

Figure C-1: Solubility of 2 % w/v starch at different concentrations of antisolvent

The data was linearized by taking the logarithm of the dependent variable, solubility, to fit a trendline to the points in Figure C-1. SigmaPlot software was then used to generate a regression line, presented by the solubility curve in Figure C-2. An R^2 value of 0.9737 achieved suggests a good fit of the regression model to the experimental data. The solubility curve can be defined by the following equation:

$$\ln\ (solubility)\ =\ -11.208 + \frac{2.067}{AS} - \frac{0.098}{AS^2} \qquad \text{(C-1)}$$

where AS is the concentration of ethanol in g ethanol/g NaOH.

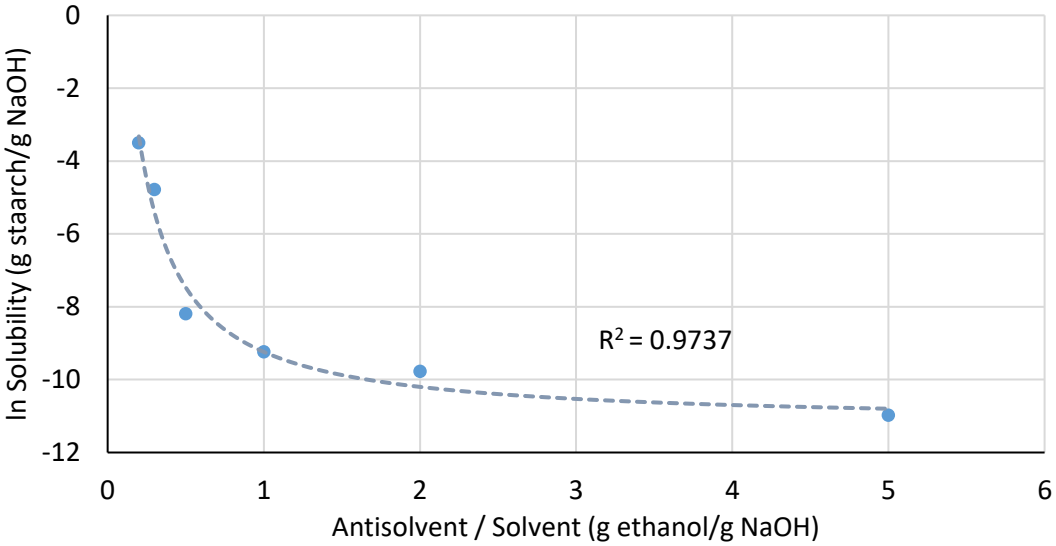

Figure C-2: Solubility curve fitted with trendline as predicted in Eq. C-1

C.2 Supersaturation

Supersaturation is a function of solubility and can be calculated through the following equation:

$$S = {}^{C}/_{C^*} \qquad \text{(C-2)}$$

where *C* is solution concentration, and *C** is equilibrium concentration or solubility.

Using the solubility data, the initial supersaturation values have been calculated for 2 % w/v starch. The results are presented in Table C-1.

Table C-1: Solubility data and supersaturation for various antisolvent to solvent ratios

Antisolvent to solvent ratio	Antisolvent concentration (g ethanol/g NaOH)	Solubility, *C** (g starch/g NaOH)	Initial supersaturation
1:1	0.77	1.69×10^{-04}	116
5:1	3.90	2.29×10^{-05}	855
7:1	5.41	1.98×10^{-05}	988
9:1	6.96	1.82×10^{-05}	1074

Appendix D - Comparison between TEM and DLS results for the grooved disc

A comparison between the average particle size from the DLS equipment, measuring the overall Z-average, and TEM has been made to ensure that despite the variation in particle size due to measuring technique, the trend is similar.

The graph demonstrating the mean sizes for the two methods of sizing as flow rate is increased is presented in Figure D-1. The graph shows the DLS and TEM results following a similar trend, which is, as discussed earlier, an increase in flow rate, causing a decrease in particle size, which slows down between 12 mL/s and 18 mL/s. There is also a slight increase in particle size at 18 mL/s for both methods, as a result of agglomeration. Figures D-2 and D-3 show TEM and DLS particle size trends for the effect of disc rotational speed and antisolvent to solvent ratio, respectively. The graphs show that the two sizing methods are in agreement with each other when it comes to the trend of average particle size.

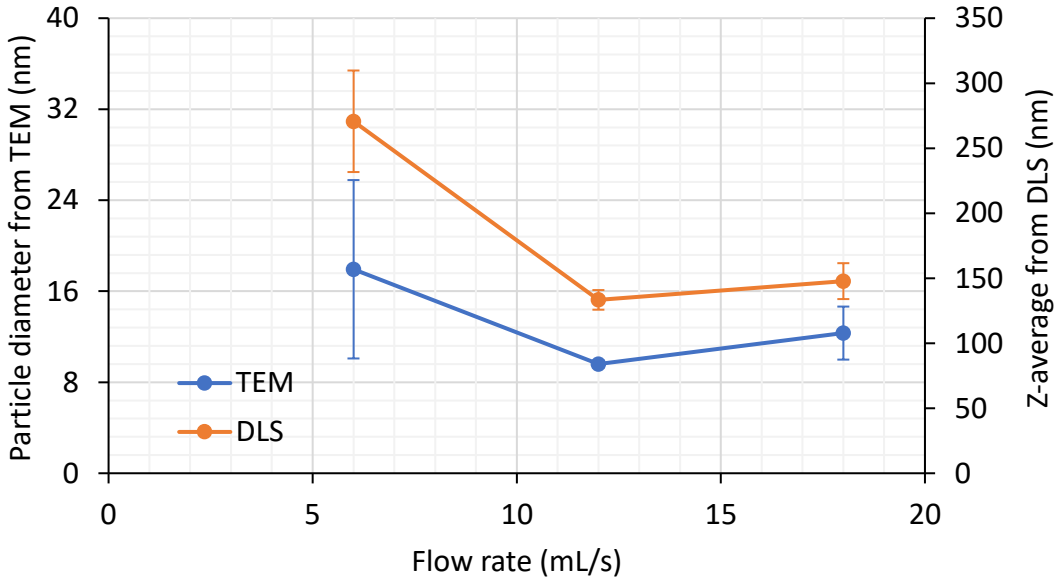

Figure D-1: Comparison between sizing from DLS and TEM methods for the effect of flow rate (1200 rpm, 9:1 ratio).

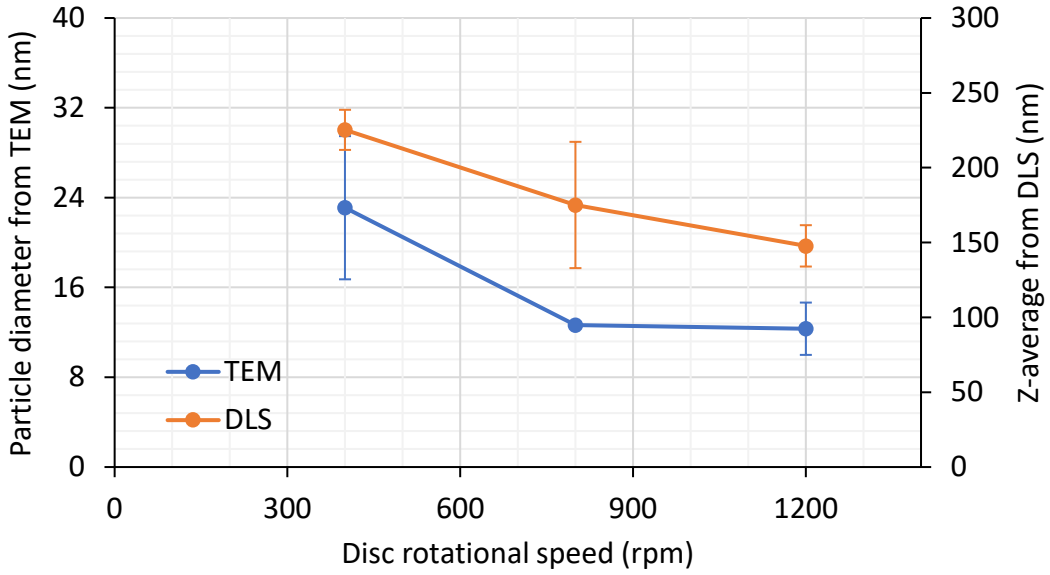

Figure D-2: Comparison between sizing from DLS and TEM methods for the effect of disc rotational speed (18 mL/s, 9:1 ratio).

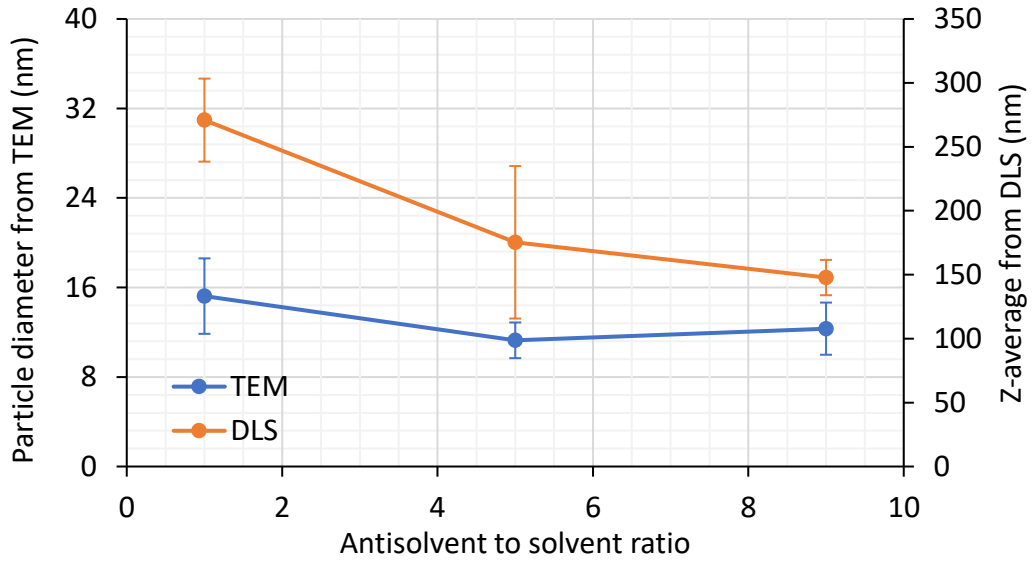

Figure D-3: Comparison between sizing from DLS and TEM methods for the effect of antisolvent to solvent ratio (1200 rpm, 18 mL/s).

Appendix E – Rheological characterisation of starch

The shear rates for the experimental conditions studied in the SDR using a 2 % w/v starch concentration are presented in Figure E-1. The following equation has been used to calculate shear rate (Boodhoo, 1999):

$$\dot{\gamma} = \frac{\omega^2 r}{\nu}(\delta - z) \tag{E-1}$$

where δ is film thickness, and z is the vertical distance along the z axis.

The values presented here for shear rate have been calculated at the edge of the disc, and at z = 0, hence representing the maximum shear rate. Equation E-1 thus becomes:

$$\dot{\gamma} = \frac{\omega^2 r \delta}{\nu} \tag{E-2}$$

It is observed that very high shear rates, in the range of 5905 to 54048 s^{-1}, are generated in the SDR. Starch is known to be a shear thickening fluid (Stankiewicz and Moulijn, 2000), however, this needs to be verified through experimental analysis for the conditions of the current work.

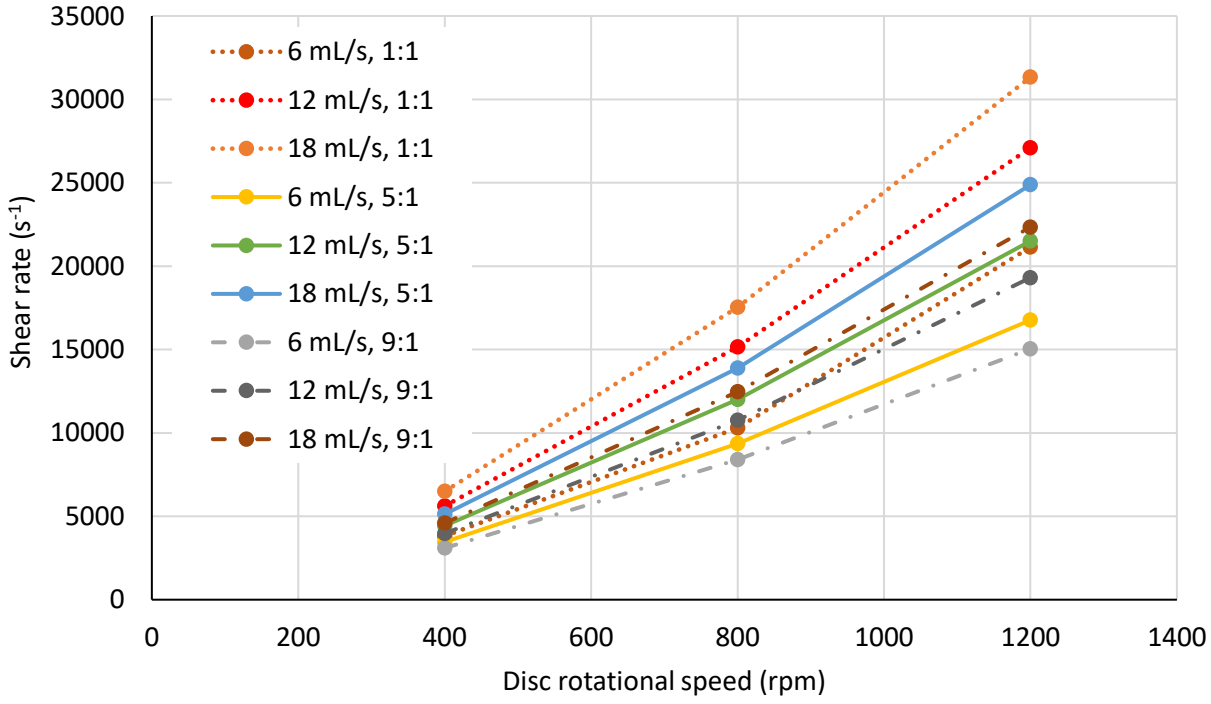

Figure E-1: Effect of disc rotational speed on shear rate at various experimental conditions for power-law model of starch using shear rate expression given in Eq. E-2.

The effect of high shear rates on the behaviour of starch has been investigated using a Bohlin Visco 88 viscometer with a cup and bob attachment. The viscosities for 2 % w/v and 4

% w/v starch in 0.5 M sodium hydroxide solutions were measured at shear rates between 66.67 s^{-1} to 1220 s^{-1} at a temperature of 25°C. The results are shown in Figure E-2. Interestingly, the viscosity for 2 % w/v begins at 13.84 mPa s at a shear rate of 66.67 s^{-1}, whereas the viscosity measured for 2 % w/v starch solution using an Ostwald viscometer without the exertion of intense shear was lower at 6 mPa s. This is not the case for 4 % w/v, for which the viscosity using an Ostwald Viscometer was found to be 59.7 mPa s, higher than the viscosities measured under the influence of shear. This points towards a possible shear thickening behaviour at low shear rates for low starch concentrations. As this research is mainly concerned with the effect of shear at high shear rates, further deliberation on this shall not be made, and so a shear thinning behaviour has been assumed.

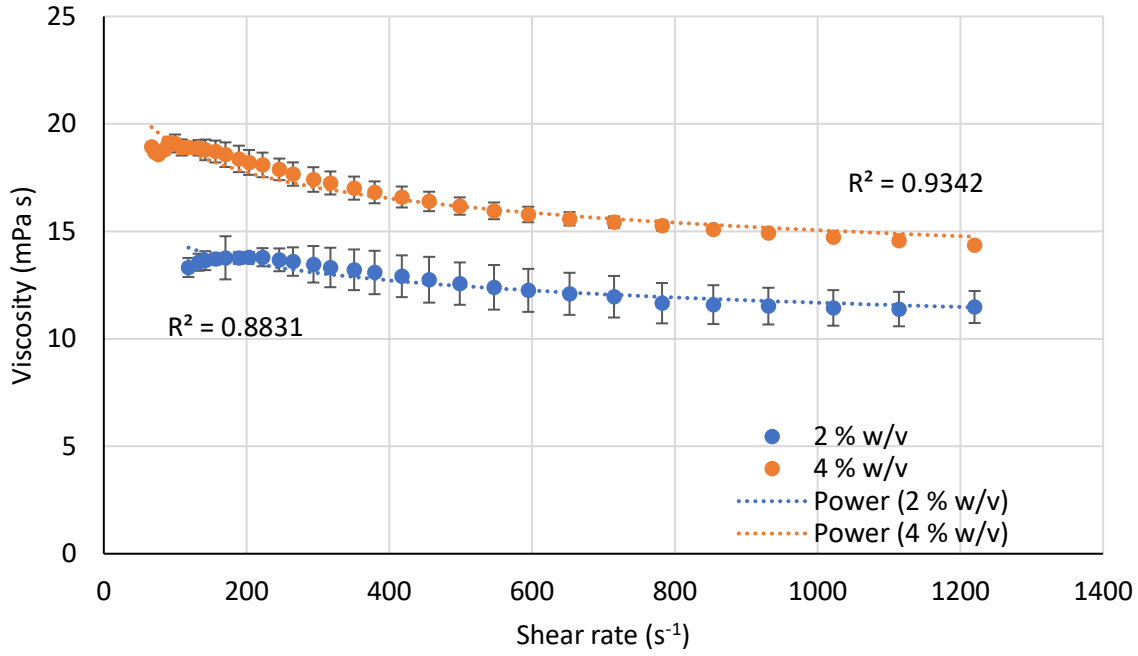

Figure E-2: Shear rate against viscosity at 2 % w/v starch and 4 % w/v starch, measured by Bohlin viscometer.

The SDR operates at shear rates beyond the range of the viscometer, and the graph in Figure E-2 does not give enough insight into the rheological behaviour of starch at higher shear rates. This means further evidence is required to confirm the shear thinning behaviour of starch. Further evaluation has been carried out by looking into literature. A particular study by Shin et al. (2012) presents data for 14 % v/v starch, equivalent to 21 % w/v, at lower and higher shear rates, collected at 24 °C. These data together with the data obtained experimentally for 2 % and 4 % w/v starch is shown in Figure E-3. A similar trend can be seen in this plot, confirming shear thinning behaviour of starch at 2 % w/v and 4 % w/v.

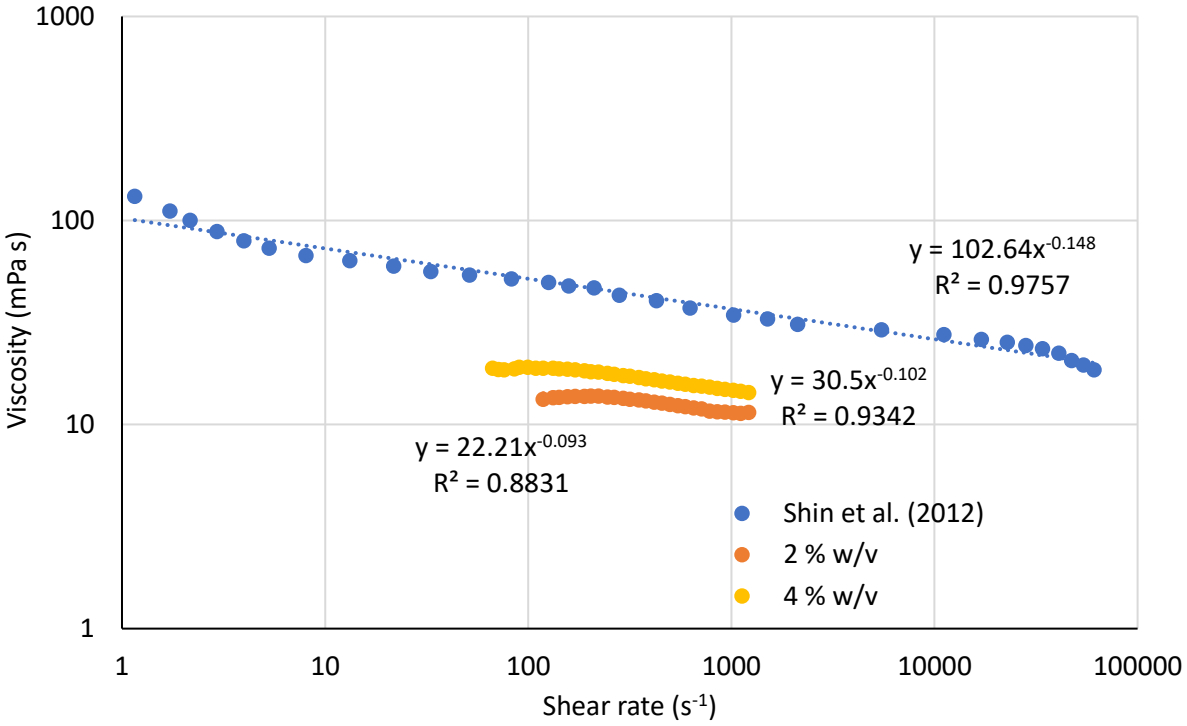

Figure E-3: Comparison of shear rate vs. viscosity plots with published data (Shin et al., 2012).

From the plot in Figure E-3, a power law expression can be obtained, relating the dynamic viscosity to shear rate:

$$\eta = k\dot{\gamma}^{n-1} \tag{E-3}$$

The values for the consistency index, *k* and the power law index are presented in Table E-1 for 2 % w/v and 4 % w/v concentrations of starch, as well as for 21 % w/v.

Table E-1: Power law parameters for starch at concentrations of 2 % w/v, 4 % w/v and 21 % w/v.

Starch concentration (% w/v)	Consistency index, k (mPa)	Power law index, n	Source
2	22.2	0.907	This work
4	30.5	0.898	This work
21	102.6	0.852	Shin et al. (2012)

From the table the following deductions can be made: As expected, the consistency of the starch solution increases as concentration is increased, as to some extent it is analogous to apparent viscosity. The power law index on the other hand is virtually similar for the three concentrations. It represents the behaviour of the fluid, and a value of n < 1 signifies shear thinning behaviour. It has been reported in an earlier study to be independent of starch concentration and temperature (Roberts and Cameron, 2002).

The film thickness equation can be modified to incorporate the power-law model for the flow of non-Newtonian liquids on the spinning disc reactor (Boodhoo, 1999). The film thickness has been obtained through the following equation:

$$\delta = \left(\frac{1+2n}{2\pi n}\right)^{\frac{n}{1+2n}} \left(\frac{Q}{r}\left[\frac{k}{\rho\omega^2 r}\right]^{\frac{1}{n}}\right)^{\frac{n}{1+2n}} \quad \text{(E-4)}$$

The shear rate has been calculated for the film thickness obtained from Eq. E-4, and viscosities are calculated from Eq. E-3. For 2 % w/v starch solution the shear in the SDR increases from 3095 s^{-1} to 31332 s^{-1}, viscosity at these shear rates decreases from 10.50 mPa s to 8.48 mPa s (Figure E-1). The change in viscosity on the disc due to increasing shear is very small and therefore considered to be negligible in terms of having any effect on the precipitation process. For a 4 % w/v concentration the viscosity ranges from 13.92 mPa s to 10.96 mPa s for shear rates of 2183 s^{-1} and 22745 s^{-1}. Despite the high viscosity at rest, the 4 % w/v solution falls drastically with increasing shear, which would mean that a more concentrated solution of starch is affected more strongly to increasing shear. However, these conclusions are based on the validation of the power law model obtained through extrapolation of the experimental data. The data from Shin et al. (2012) through which this model is established shows a downward trend of viscosity at increasing shear rates, however, there are certain factors that need to be considered which may influence the model. The data from Shin et al. (2012) has been obtained at a temperature of 24 °C for starch dissolved in water. The research presented here involves experiments carried out at 25 °C, with starch dissolved in a solution of 0.5 M sodium hydroxide. A 1 °C difference is considered acceptable and just within the standard deviation for the experiments carried out throughout this research. Also, as mentioned earlier, power law index, *n* is not affected by temperature. Other than this, starch is known to dissolve better in solutions of sodium hydroxide as the degree of swelling in NaOH solutions is far greater than it is in water (Hu et al., 2016). For this reason, the intrinsic viscosity of the starch solution is reduced in the alkali solution. However, as mentioned earlier, the shear thinning behaviour, expressed by the constant power law index, is not affected (Roberts and Cameron, 2002). It may be considered that if the 21 % w/v dissolution were to be carried out in a solution of sodium hydroxide rather than water, the literature data would be positioned lower in the plot for

shear rate against viscosity. However, it is to be noted that the concentration of sodium hydroxide used in the present study is very low and may not have quite a significant impact.

Appendix F – SBR results

The conditions for the experiments carried out in a semi-batch setup are presented in Table F-1. The concentration was limited to a maximum of 2 % w/v, as beyond this concentration the high viscosity of the starch solution prevented effective mixing in the SBR. The effect of agitation rate can be seen in Figures F-1 and F-2. In theory, an increase in agitation should result in the formation of smaller nanoparticles and a narrower size distribution. However, this was not that case, particularly for concentrations of 2 % w/v starch. An explanation for this is that at the lower agitation speed of 200 rpm the particles were not fully suspended and settled below the impeller (as observed in Figure F-3), prohibiting the collection of any larger particles and thereby erroneously shifting the measured size distribution towards the smaller size. However, at the lower concentration of 1 % w/v, starch nanoparticles produced are of a smaller size and have narrower size distribution, indicated by the PdI value, at high agitation rates, as shown in Figure F-1.

Table F-1: SBR conditions for precipitation of starch nanoparticles.

Factor	Low	High
Starch concentration (% w/v)	1	2
Ethanol addition rate (mL/s)	1	12
Agitation rate (rpm)	200	800

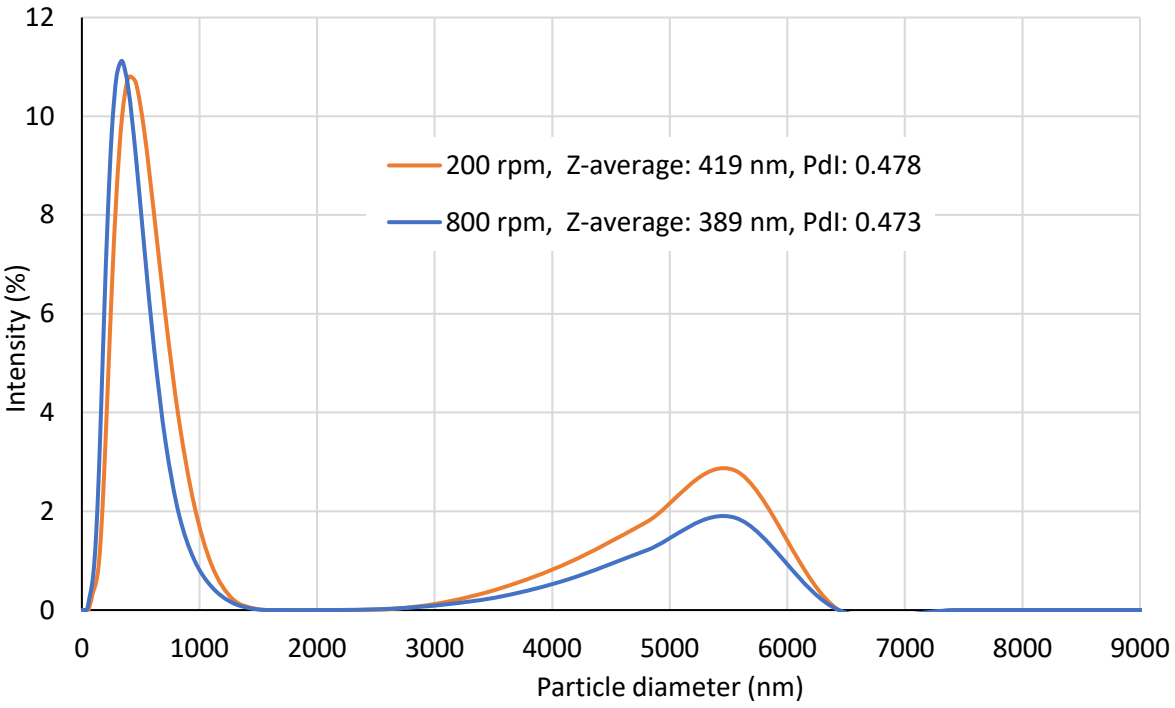

Figure F-1: Effect of agitation rate in SBR set-up at 1 % w/v concentration and 1mL/s ethanol addition.

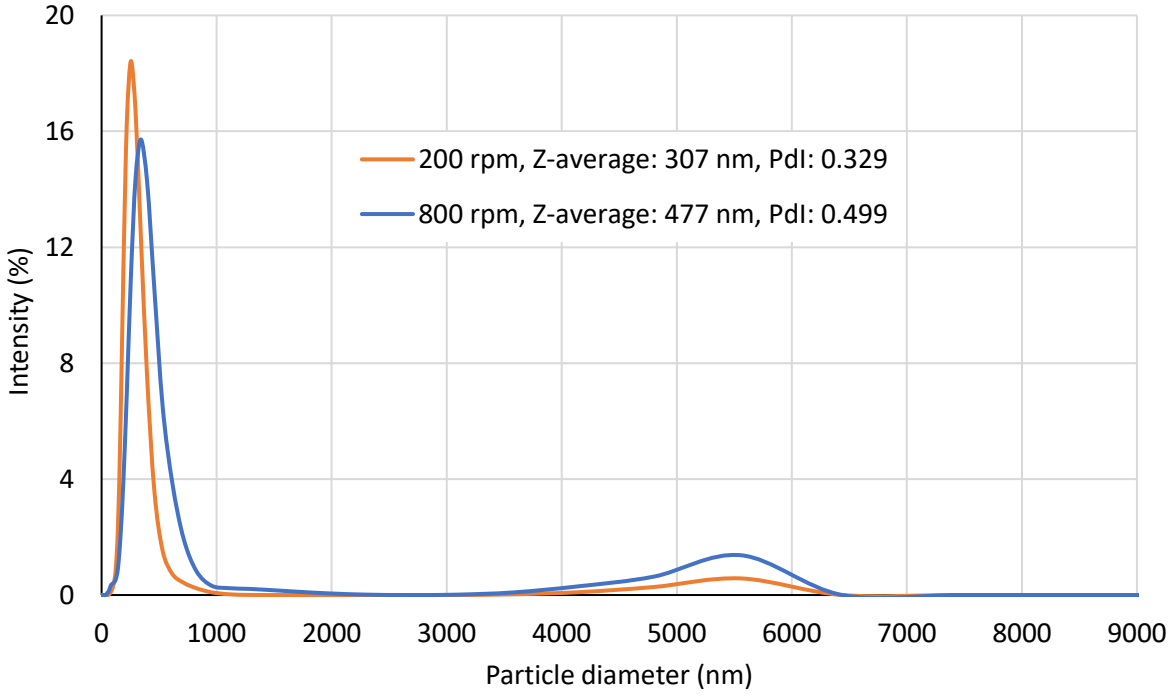

Figure F-2: Effect of agitation rate in SBR set-up at 2 % w/v concentration and 1mL/s ethanol addition.

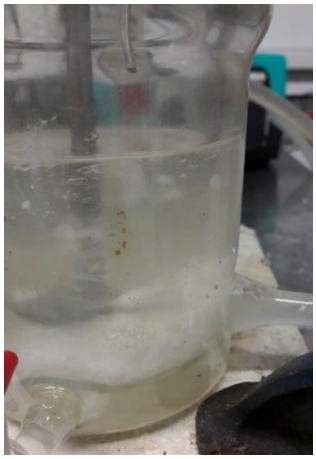

Figure F-3: Particles settling in the SBR vessel at low agitation rates of 200 rpm.

The effect of starch concentration can be seen in the particle size distributions presented in Fig. F-4. An increase in concentration does not show a significant impact on the PSD, as there does not appear to be much of a difference between the major peaks. However, there is a difference in the Z-averages, as the agglomerated peaks also contribute to these values. The major peaks are at 373 nm and 364 nm for 1 % w/v starch and 2 % w/v starch, respectively, which indicates lower sized particles produced at the higher concentration. This could be because a higher concentration results in higher supersaturation, leading to faster nucleation and the formation of nanoparticles. As the smaller particles are more likely to agglomerate, the particles produced at 2 % w/v are more likely to agglomerate and thus increase the Z-average. The PdI values support this theory as the PdI is higher for 2 % w/v starch, indicating a broad size distribution which could be attributed to the agglomeration of particles. Previous studies with starch have indicated that an increase in concentration caused an increase in particle size. This has been explained as a consequence of increased viscosity at higher concentration, causing penetration of the antisolvent through the starch/solvent mixture to be challenging (Hebeish et al., 2014). However, at the two concentrations presented in this study, the viscosity is not significantly different which may be the reason behind the concentration not having a substantial effect on particle size. This is displayed in Figure F-5. Experiments carried out at concentrations above 2 % w/v of starch were too viscous to process in the SBR at the selected agitation rates, which is why 2 % w/v concentrations were used in the SDR experiments for an accurate comparison of the two technologies.

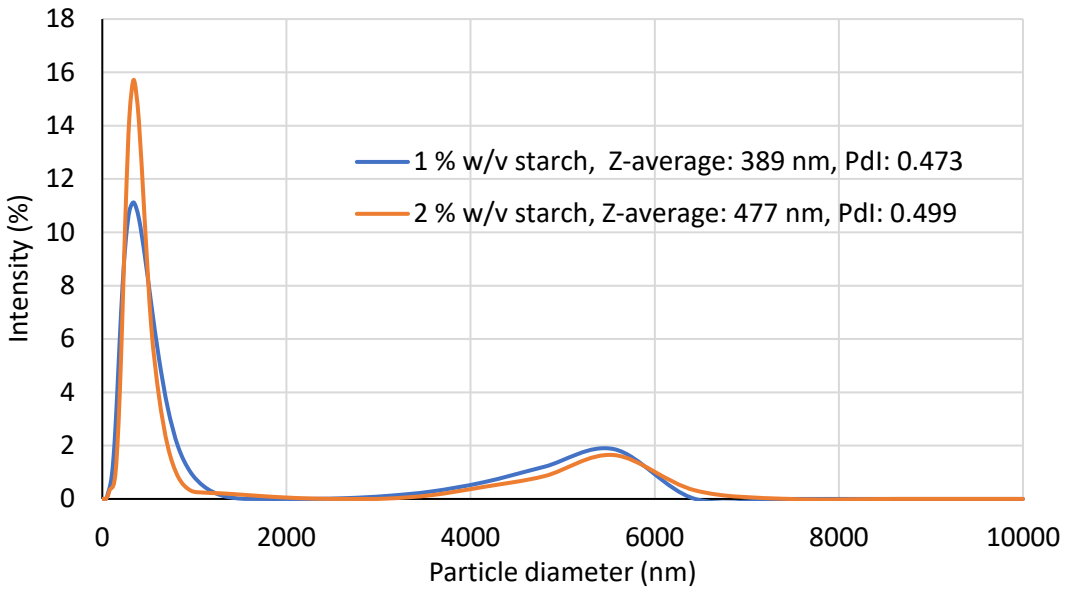

Figure F-4: PSD for effect of starch concentration in SBR set-up at 800 rpm agitation and 1 mL/s ethanol addition.

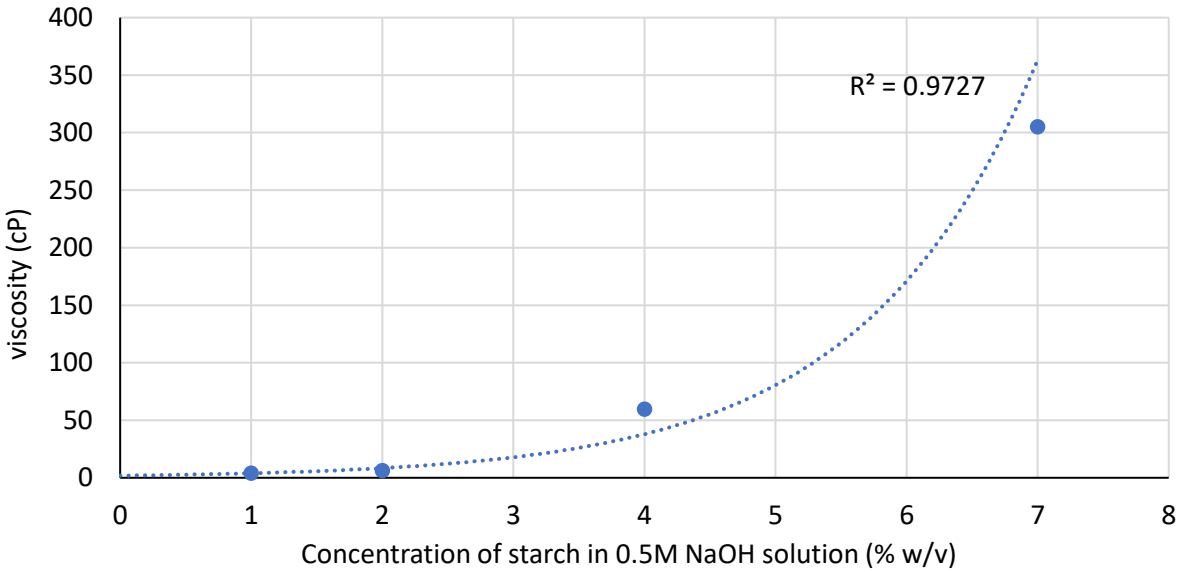

Figure F-5: Effect of starch concentration on viscosity.

At a high ethanol addition rate, the starch nanoparticles produced are of a larger size, signified by a peak at 364 nm at an addition rate of 1 mL/s, as opposed to the peak at 434 nm at a 12 mL/s addition rate. This is due to insufficient local mixing between the solvent and the antisolvent at the higher flow rate. With regards to precipitation, this can cause uneven supersaturation especially near the feed point, leading to particles precipitating out at different times (O'Grady et al., 2007). Such a phenomenon can be seen

in the PSD in Figure F-6, displayed in the form of a smaller peak before the major peak for the size distribution at 12 mL/s. This is quantified through the high PdI of 0.516 at 12 mL/s.

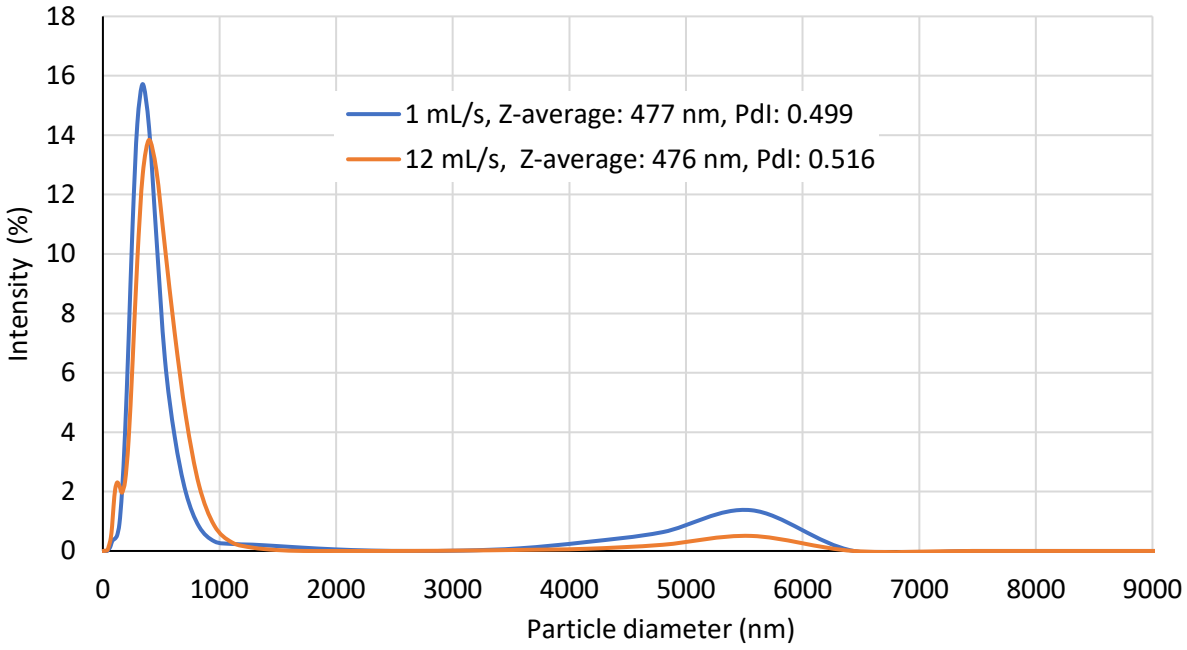

Figure F-6: PSD showing the effect of antisolvent addition rate at 800 rpm and 2 % w/v starch.

The results for the SBR experiments can be summed up in the form of a main effect plot and an interaction plot, as displayed in Figure F-7 and Figure F-8. It should be noted that the means calculated in these graphs are from the major peak and not the Z-average as this is a better representative of the individual particles formed and does not consider agglomerated particles. Figure F-7 shows the effect of agitation rate, concentration and antisolvent addition rate on the mean particle size. In summary, increase in agitation shows an increase in particle size, increase in concentration reduces particle size, and an increase in addition rate increases particle size. These results have been explained earlier in detail. It is vital to look at the interactions plot to get a better understanding of these findings. Figure F-8 shows the interactions between the three parameters and how they affect the particle size. The agitation rate and concentration interaction profile show smaller particles being formed at higher starch concentration, as well as an increase in particle size at 2 % w/v as agitation rate increases, which is again a result of larger particles settling due to the low agitation rate. For the agitation rate and ethanol addition rate profile, 1 mL/s addition rate produced smaller sized particles which increase as agitation rate is increased, whereas, at a 12 mL/s addition rate the mean particle size reduces slightly. However, these changes are small, hence negligible. Lastly, the interaction between concentration and ethanol addition rate shows a

decrease in particle size as concentration increases, which is true at both, 1 mL/s and 12 mL/s addition rates.

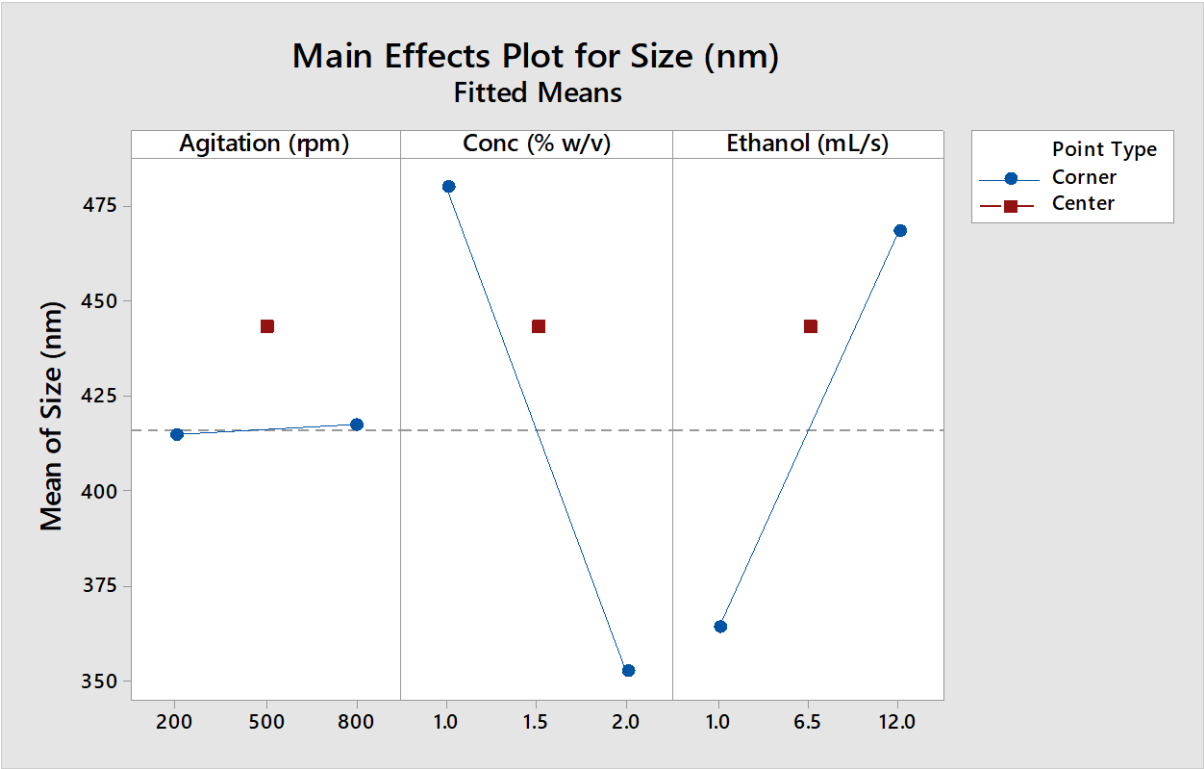

Figure F-7: Main effects plot showing effect of agitation rate, concentration and ethanol addition rate in the SBR experiments.

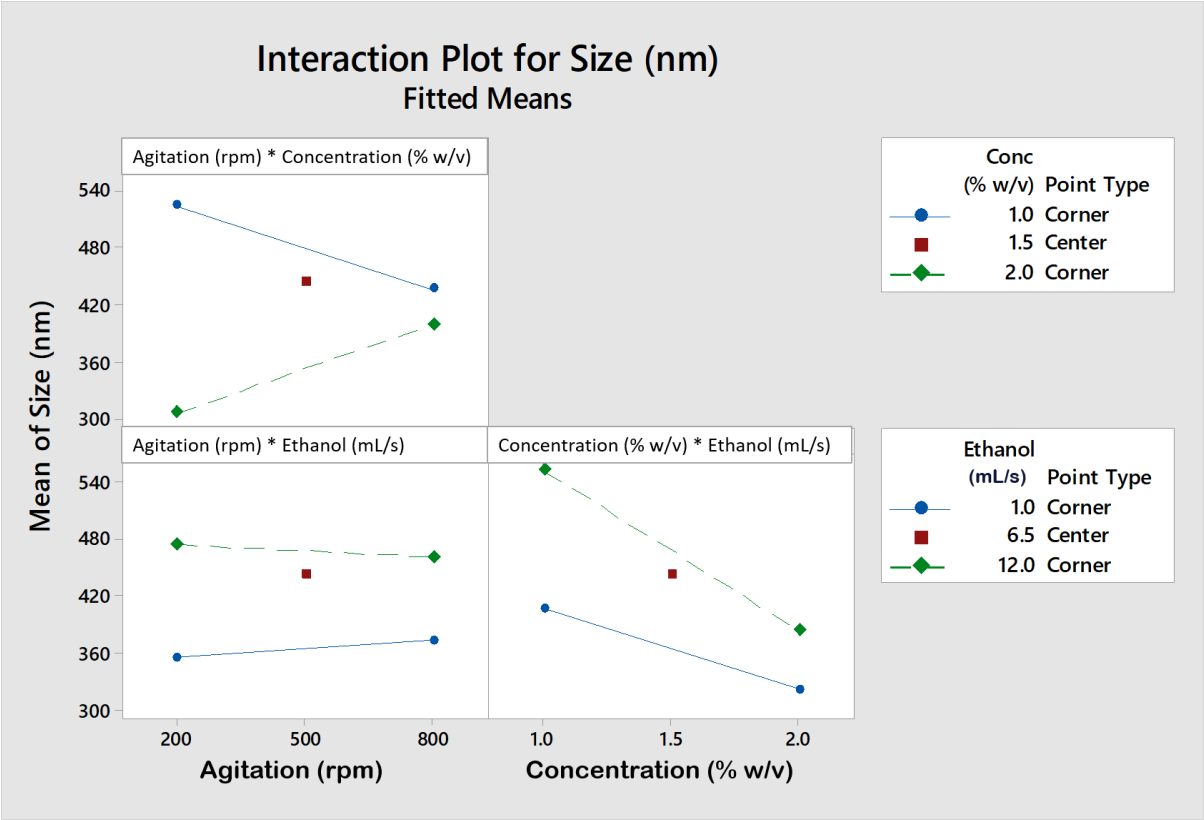

Figure F-8: Interactions plot for SBR experiments.

Concentration, ethanol addition rate and the interaction between agitation rate and concentration are statistically significant at 0.05 significance level. According to the Pareto chart in Figure F-9, the agitation rate parameter is not significant, however, that is not the case and the data for particle size has been affected by errors during sampling as mentioned earlier, a result of particles settling.

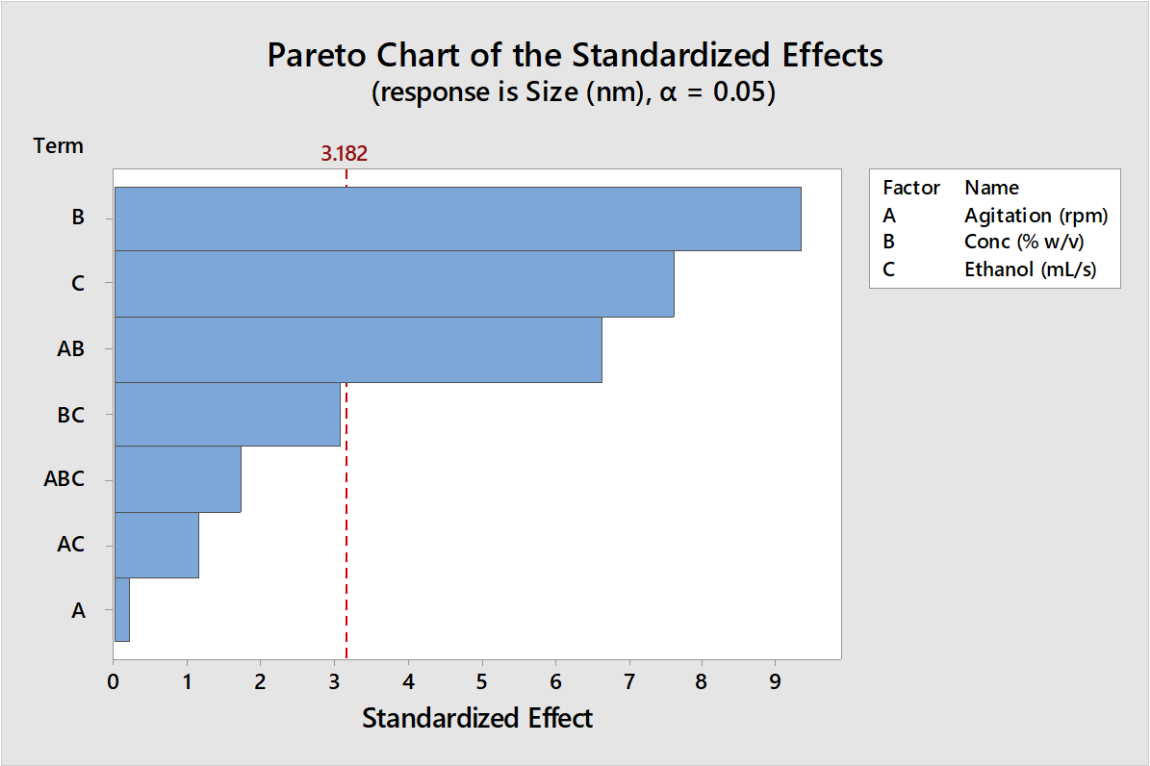

Figure F-9: Pareto chart for SBR experiments.

Appendix G – Validation of centrifugal model

For the centrifugal model to be valid, Coriolis forces must be negligible, and the following condition must be satisfied:

$$\nu \gg \omega\delta^2 \qquad \text{(G-1)}$$

Table G-1 presents the values for the term $\omega\delta^2$ at various operating conditions in the SDR alongside the kinematic viscosity, *v*. Film thickness, δ, at the edge of the disc and halfway across the disc are used to test the validity of the centrifugal model. To summarise, all conditions suggest negligible Coriolis forces.

Table G-1: Table showing validation of condition G-1 at various operating conditions in the SDR, halfway across the disc and at the edge of the disc.

Flow rate, Q (mL/s)	Disc speed (rpm)	Antisolvent to solvent ratio	ν (m^2/s)	Film thickness, δ – edge of disc (m)	$\omega\delta^2$ – edge of disc	Film thickness, δ – middle of disc (m)	$\omega\delta^2$ – middle of disc
6	400	1:1	3.10×10^{-6}	5.69×10^{-5}	1.35×10^{-7}	9.03×10^{-5}	3.41×10^{-7}
6	800	1:1	3.00×10^{-6}	3.58×10^{-5}	1.08×10^{-7}	5.69×10^{-5}	2.71×10^{-7}
6	1200	1:1	2.92×10^{-6}	2.73×10^{-5}	9.39×10^{-8}	4.34×10^{-5}	2.37×10^{-7}
18	400	1:1	3.05×10^{-6}	8.20×10^{-5}	2.82×10^{-7}	1.30×10^{-4}	7.10×10^{-7}
18	800	1:1	2.94×10^{-6}	5.17×10^{-5}	2.24×10^{-7}	8.20×10^{-5}	5.64×10^{-7}
18	1200	1:1	2.88×10^{-6}	3.94×10^{-5}	1.95×10^{-7}	6.26×10^{-5}	4.92×10^{-7}
12	400	1:1	3.06×10^{-6}	7.16×10^{-5}	2.15×10^{-7}	1.14×10^{-4}	5.42×10^{-7}
12	800	1:1	2.95×10^{-6}	4.51×10^{-5}	1.71×10^{-7}	7.16×10^{-5}	4.30×10^{-7}
12	1200	1:1	2.89×10^{-6}	3.44×10^{-5}	1.49×10^{-7}	5.47×10^{-5}	3.76×10^{-7}
6	400	5:1	1.66×10^{-6}	4.84×10^{-5}	9.80×10^{-8}	7.68×10^{-5}	2.47×10^{-7}
6	800	5:1	1.65×10^{-6}	3.05×10^{-5}	7.78×10^{-8}	4.84×10^{-5}	1.96×10^{-7}
6	1200	5:1	1.64×10^{-6}	2.33×10^{-5}	6.79×10^{-8}	3.69×10^{-5}	1.71×10^{-7}
18	400	5:1	1.66×10^{-6}	6.98×10^{-5}	2.04×10^{-7}	1.11×10^{-4}	5.14×10^{-7}
18	800	5:1	1.64×10^{-6}	4.39×10^{-5}	1.62×10^{-7}	6.98×10^{-5}	4.08×10^{-7}
18	1200	5:1	1.63×10^{-6}	3.35×10^{-5}	1.41×10^{-7}	5.32×10^{-5}	3.56×10^{-7}
12	400	5:1	1.66×10^{-6}	6.09×10^{-5}	1.56×10^{-7}	9.67×10^{-5}	3.92×10^{-7}
12	800	5:1	1.64×10^{-6}	3.84×10^{-5}	1.23×10^{-7}	6.09×10^{-5}	3.11×10^{-7}
12	1200	5:1	1.63×10^{-6}	2.93×10^{-5}	1.08×10^{-7}	4.65×10^{-5}	2.72×10^{-7}
6	400	9:1	1.48×10^{-6}	4.69×10^{-5}	9.23×10^{-8}	7.45×10^{-5}	2.33×10^{-7}
6	800	9:1	1.47×10^{-6}	2.96×10^{-5}	7.32×10^{-8}	4.69×10^{-5}	1.85×10^{-7}
6	1200	9:1	1.46×10^{-6}	2.26×10^{-5}	6.40×10^{-8}	3.58×10^{-5}	1.61×10^{-7}
18	400	9:1	1.47×10^{-6}	6.77×10^{-5}	1.92×10^{-7}	1.07×10^{-4}	4.84×10^{-7}
18	800	9:1	1.46×10^{-6}	4.26×10^{-5}	1.52×10^{-7}	6.77×10^{-5}	3.84×10^{-7}
18	1200	9:1	1.46×10^{-6}	3.25×10^{-5}	1.33×10^{-7}	5.17×10^{-5}	3.35×10^{-7}
12	400	9:1	1.47×10^{-6}	5.91×10^{-5}	1.46×10^{-7}	9.39×10^{-5}	3.69×10^{-7}
12	800	9:1	1.47×10^{-6}	3.73×10^{-5}	1.16×10^{-7}	5.91×10^{-5}	2.93×10^{-7}
12	1200	9:1	1.46×10^{-6}	2.84×10^{-5}	1.02×10^{-7}	4.51×10^{-5}	2.56×10^{-7}

Appendix H – Spin-up radius calculations

The following equation has been taken from Burns et al. (2003) and applied to estimate the spin-up radius, r_s for the current starch nanoparticles solvent-antisolvent precipitation system in the SDR:

$$r_s = 0.93\lambda\left(\frac{d}{2\lambda}\right)^{-0.025} {K_1}^{0.11}{K_2}^{-0.37} \quad \text{(H-1)}$$

where *d* is the distributor diameter, λ is the characteristic radial length scale $\lambda = (Q^2/\omega\nu)^{0.25}$, and the viscosity correction factors, $K_1 = 0.61$ and $K_2 = \frac{\lambda}{\lambda_0}$ with $\lambda_0 = 10.8$ cm. The correction factors are strongly influenced by operating conditions such as flow rate and disc rotational speed, particularly K_2. K_1 does not vary significantly and an average value of 0.61 has been assigned. (Burns et al., 2003).

The results are displayed in Table H-1. Beyond the spin-up radius, flow is synchronised and the Nusselt model can be applied. Most induction radii are above their respective spin-up radii with a few exceptions, occurring at high disc speeds combined with high flow rates. It is also worth noting that Eq. H-1 is derived from data obtained on the smooth disc and may not be applicable to the grooved disc. In addition to this, the residence time equation does not consider the disc's surface texture, hence errors may have incurred whilst calculating induction time on the grooved disc.

Table H-1: Spin-up radius for various experimental conditions in the SDR

Flow rate (mL/s)	Disc speed (rpm)	Antisolvent to solvent ratio	Average radial distance for induction – smooth (cm)	Average radial distance for induction – grooved (cm)	Spin -up radius (cm)
18	400	9:1	7.00	6.03	5.32
6	1200	9:1	7.83	4.63	3.23
18	800	9:1	5.07	7.17	4.79
12	1200	9:1	5.27	5.77	3.99
18	1200	5:1	5.60	4.87	4.45
18	1200	1:1	5.03	4.57	4.13
18	1200	7:1	5.83	4.23	4.48
15	1200	9:1	2.00	3.63	4.26
18	1000	9:1	4.77	5.63	4.63
18	600	9:1	6.67	6.87	5.00

Appendix I – Lax-Wendroff MATLAB code

```
% Clear all
%{
_____________________________________________________________________________
                              LAX-WENDROFF METHOD
_____________________________________________________________________________
%}

close all
clear all;
for kb = [2.046*10^15 1.89*10^16] %[smooth grooved] particles/ml. s
for Qt = [6 12 18]
% Specify model parameters
nm = 1*10^-9;
Length_upper = 100;
Ll = 0; Lu = Length_upper*nm; % Lchar domain [Ll,:Lu] [metres]
K = 100; % number of divisions
dL = (Lu-Ll) / K; % dL: Lchar step size
r_inner = 0.0015;
radius = 0.15; % radius, metres
Nx = 100; % Nx: number of reactor length steps
dr = radius/Nx; % reactor length step size
r = 0:(radius/Nx):radius; % reactor position vector
mu = dr/dL;
ratio = 9;
nu0 = 1.425*10^-6;

N = 1200;
w = 2*N*pi/60;
Q = Qt*1*10^-6; % flow rate [m3/sec]
rho_solution = 1026; % kg/m3

uav=(Q^2*w^2/(12*(pi^2)*nu0*radius))^0.333;
tres = (3/4)*(((12*(pi^2)*nu0)/(Q^2*w^2))^(1/3))*(radius^(4/3)-
r_inner^(4/3));
t = tres/K;
%smooth
if kb == 2.046*10^15;
b = 0.3319;
kg = 5.44*10^-8;
g = 0.0375;
else
    b = 0.1216; %grooved
    kg = 5.44*10^-8;
    g = 0.0797;
end

Q_naoh = Q/(ratio+1);
Q_etoh = Q - Q_naoh;
rho_etoh = 0.789*1000; %(kg/m3)
rho_naoh = 1.02*1000; %kg/m3
rho_starch = 1.5*1000; %kg/m3
kv=1;

AS_conc = (Q_etoh*rho_etoh)/Q_naoh*rho_naoh; %g ethanol / g NaOH
sat_conc = exp (-11.2077+((2.0667/AS_conc)-(0.0979/AS_conc^2))); %g starch
/ g NaOH

C0 = 0.019577; %g starch/g naoh
S0 = C0/sat_conc;
```

```
%zero vectors
B = zeros(1,Nx+1); % nucleation rate vector
G = zeros(1,Nx+1); % growth rate vector
C = zeros(1,Nx+1); % concentration vector
C(1,1:2)=C0;
S = zeros(1,Nx+1); %supersaturation
S(1,1:2)=S0;
dC = zeros (1,Nx+1);
L = Ll:dL:Lu; % Lchar vector
Lsq = L.^2; % Lchar vector squared
A = zeros(1,Nx+1); % surface area
% Population density
n = zeros(K+1,Nx+1);
%Iterations
for m = 1:Nx+1
B(1,m) = kb *(S(1,m).^b); %particles/mL.s
G(1,m) = kg *((S(1,m)-1).^g); %m/s
% B, G, concentration calculations go here
if m==1 % first column (entrance to reactor)
for k=1:K+1 % for all Lchar
n(k,m) = 0; % pop.dens. = 0 (no seeding)
end
else % positions after the entrance
for k=1 % for size 0 crystals
n(k,m) = B(1,m)/G(1,m); % pop.dens. = B/G
end
for k=K+1 % for max size crystals
n(k,m) = 0; % pop.dens. = 0
end
for k=2:K % for other size crystals

n(k,m) = n(k,m-1) + ((-G(1,m)*dr/uav)*((n(k+1,m-1)-n(k-1,m-1))/(2*dL)))...
+ (0.5*((-G(1,m)*dr/uav)^2)*((n(k+1,m-1)-2*n(k,m-1)+n(k-1,m-1))/(dL^2))); %
pop.dens. = B/G


end

A(1,m) = trapz(Lsq,n(:,m));
dC(1,m) =
((3*rho_starch*kv*G(1,m)*dr*A(1,m)/uav)*Q)/((1/(ratio+1))*rho_naoh);
if dC(1,m) >= C(1,m);
   break
end
%

C(1,m+1) = C(1,m)-dC(1,m);
%}

S(1,m+1) = C(1,m+1)/sat_conc;
Sfinal(1,m) = S(1,m+1);


%


end

end
```

```
hold on;

L2 = L';

CSD = n(:,Nx).*L2;
sum_CSD = sum(CSD);
PSD = (CSD/sum_CSD)*100;

Diameter = L/nm;
hold on
if kb == 2.046*10^15
if Qt==6
  p1=plot(Diameter,PSD,'r');
hold on
 elseif Qt==12
  p2=plot(Diameter,PSD,'b');
else
  p3=plot(Diameter,PSD,'g');
hold all
end
hold on
else
    if Qt==6
  p4=plot(Diameter,PSD,'r.');
hold on
 elseif Qt==12
  p5=plot(Diameter,PSD,'b.');
else
  p6=plot(Diameter,PSD,'g.');
hold all
    end
end
end
end

legend([p1,p2,p3,p4,p5,p6],'6 mL/s smooth','12 mL/s smooth','18 mL/s
smooth','6 mL/s grooved','12 mL/s grooved','18 mL/s
grooved','Location','northeast')
 xlabel('Particle size (nm)');
 ylabel('Frequency (%)');
 title('1200 rpm. 9:1 antisolvent to solvent ratio');
```

Appendix J – Hounslow's method MATLAB code

J.1. Main script

```
%%                          Model Description


%{
This script uses the folllowing functions

Function                                              Details
PopBalance.m    The function calculates the       number, mass and moment
                                                  derivatives for the
modelled
                                                  system

StabilityRatioEstimate.m                          Estimates the stability
                                                  ratio when agglomeration
                                                  is being considered
_____________________________________________________________________________
_____________________________________________________________________________
MATLAB PREPARATION

%}

clear variables                 % clear MatLab Workspace
clear global                    % clear MatLab global variables

clc                             % clear MatLab Command Window

close all                       % close any open graph windows

dbstop if error                 % set MatLab debug options to stop if error

%%                          MODEL PARAMETERS

%{
_____________________________________________________________________________
Specify fundamental constants
%}
% Boltzmann
Qt = 18;
global boltz   InitialConcentration S
boltz = 1.38064852 * 10^-23;    % J/K

% Avogadro's Number
global Na
Na = 6.02214*10^23;     % /mol

% Molecular Diffusivity
global D
D = 1.1*10^-12;  % m2/s


%{
_____________________________________________________________________________
Specify reactor dimentions
%}
DiscDiameter = 0.3;          %m
InletRadius = 0.0015;       %m
```

```
%{
_____________________________________________________________________
Specify physical properties
%}
global NumberComponents
NumberComponents = 4;

global CrystalDensity
CrystalDensity = 1500;                  % kg/m3

global Density
Density(1) = 1026;                      % kg/m3 stach
Density(2) = 785;                       % kg/m3 ethanol
Density(3) = Density(1);                % kg/m3 mixed
Density(4) = Density(2);                % kg/m3 mixed


global viscosity
viscosity = 1.47*10^-6;                 % m2/s ratio 1:1->2.97 5:1->1.65 9:1-
>1.47

% Molecular Weight
global Mw
Mw(1) = 692;    %  starch
Mw(2) = 46.07; %  ethanol
Mw(3) = Mw(1);
Mw(4) = Mw(2);


% Molar Volume
global Vm
Vm = Mw / (1000*Na*CrystalDensity);

global kh
kh = 8.5*10^-6;

global flowrate
flowrate = Qt/1000000;  % m3/s

global ratio
ratio = 9;                % VolumetricRatio

global Solubility

Q_naoh = (Qt/(ratio+1))/1000000; %m3/s
Q_etoh = (Qt - Q_naoh)/1000000;
AS_conc = (((Q_etoh*(Density(2)))/Mw(2))/(Q_naoh));    %kmol/m3
Solubility = exp (-10.6905+((43.9396/AS_conc)-(42.848964/AS_conc^2)));
%kmol/m3
%{
_____________________________________________________________________
Specify operating conditions
%}
N_rpm = 1200;                             % rpm
global Omega
Omega = ( 2 * pi() * N_rpm )/60;         % rad/s


global Temperature
Temperature = 273 + 25;                  % K
```

```
%{
_____________________________________________________________________________
Specify discretisation settings, geometric grid for hounslow technique
Number of CSTRs, class width etc.
%}
Pe = 10^2.561*Omega^0.188*flowrate^0.371*viscosity^-0.136; %grooved ->
10^2.765*Omega^0.203*flowrate^0.372*viscosity^-0.104;
10^2.561*Omega^0.188*flowrate^0.371*viscosity^-0.136 smooth

global NumberCSTRs
NumberCSTRs =  10;%round((Pe^2)/((2*Pe)+8));

% Initial Particle Size
global Di
Di = 1*10^-9;

global r q
q =1;
r = 2^(1/(3*q));

global NumberClasses
NumberClasses = 35;

global ParticleSizeRange
ParticleSizeRange = zeros(1,NumberClasses+1);

for n = 1 : NumberClasses + 1
    switch n
        case 1
            ParticleSizeRange(n) = Di;
        otherwise
            ParticleSizeRange(n) = ParticleSizeRange(n-1) * r;
    end
end

%{
_____________________________________________________________________________
Calculate reactor volume and film thickness
%}

Width = ((DiscDiameter-2*InletRadius)/(2*NumberCSTRs))*(1/(100));

global RadiusVector
for j = 1 : (NumberCSTRs * 100) + 1
    switch j
        case 1
            RadiusVector(j)=InletRadius;
        otherwise
            RadiusVector(j)=RadiusVector(j-1)+Width;
    end
end

global FilmThickness

for j = 1 : length(RadiusVector)
    FilmThickness(j) = (((3*viscosity*flowrate)/...
                        (2*pi()*Omega^2*RadiusVector(j)^2))^(1/3));
end
```

```
global Volume
global CSTRVolume
CSTRVolume=zeros(1,NumberCSTRs);

for jj = 1:NumberCSTRs
for j = 1 + 100*(jj-1) : 100*jj
    Volume(j) = (1/3)*pi()*(RadiusVector(j)^2+RadiusVector(j+1)^2+...
                    RadiusVector(j)*RadiusVector(j+1))*...
                    (FilmThickness(j)-FilmThickness(j+1)) + ...
                    pi()*FilmThickness(j+1)*RadiusVector(j+1)^2 - ...
                    pi()*FilmThickness(j)*RadiusVector(j)^2;
   CSTRVolume(jj)=CSTRVolume(jj)+Volume(j);
end
end

%{
_____________________________________________________________________________
Define nucleation constants
%}

% Interfacial Energy
global gamma
gamma=10.33/1000;

% Numcleation Constant
global Bn kg b g B G

Bn = 1.86*10^22 ; %m-3s-1 grooved->1.86*10^22 smooth->1.24*10^21
b = 0.1238; % grooved-> 0.126 smooth->0.4365
kg = 194.98; %grooved->194.98 smooth->73.49 %nm/s
g = 0.0877; %grooved->0.0877 smooth->0.2284;



% Convert particle size to nanometers
ParticleSizeRange = ParticleSizeRange * 10^9;


%{
_____________________________________________________________________________
                          AGGLOMERATION
%}
%

% Define Agglomeration Kernel
global Kern
Kern=zeros(NumberClasses);
for j = 1 : NumberClasses
    for i = 1:NumberClasses

        Kern(j,i) = (2*boltz*Temperature/(3*viscosity*Density(3)))* ...
            (((ParticleSizeRange(j)*10^-9)/2) + ((ParticleSizeRange(i)*10^-
9)/2)) * ...
            ((1/((ParticleSizeRange(j)*10^-
9)/2))+(1/((ParticleSizeRange(i)*10^-9)/2)));
        % }
    end
end

% Calculate Stability Ratio
```

```
W= zeros(NumberClasses);
for i = 1 : NumberClasses
    xi = ParticleSizeRange(i)*1e-9;
    for j = 1 :NumberClasses
        xj = ParticleSizeRange(j)*1e-9;
        ftot=0;
        for jj = 1:100000
            H = jj*1e-11;
            f = StabilityRatioEstimate(xi,xj,H);
            ftot = ftot + f;
            f=0;
        end
        W(i,j)=ftot;
    end
end

Kern = Kern ./ W;

%}

%{
_____________________________________________________________________
Calculate micromixing time for mixing supersaturation model
%}

Sc = viscosity / D;
CSTRWidth = (DiscDiameter/2 - InletRadius)/NumberCSTRs;
for j = 1 : NumberCSTRs + 1
    switch j
        case 1
    WidthVector(j) = InletRadius;
        otherwise
            WidthVector(j) = WidthVector(j-1) + CSTRWidth;
    end
end
% Calculate Velocities
u = ((flowrate^2 * Omega^2) ./(12*pi()^2 * WidthVector *
viscosity)).^(1/3);
% Calculate Energy Dissipation and Micromixing Time
global tmicro
global EnergyDiss
for j = 1 : NumberCSTRs
    tres(j) = (81*pi^2*viscosity/(16*Omega^2*flowrate^2))^(1/3) *
(WidthVector(j+1)^(4/3)-WidthVector(j)^(4/3));
    EnergyDiss(j) =
abs(0.5*(1/tres(j))*((WidthVector(j+1)^2*Omega^2+u(j+1)^2)-
(WidthVector(j)^2*Omega^2+u(j)^2)));
    tmicro(j) = 2*(viscosity/EnergyDiss(j))^0.5 * asinh(0.05*Sc);
end

%{
_____________________________________________________________________
Specify initial conditions
%}
global Starch
Starch = ((16/Mw(1))/((800)))*1000; %kmol/m3
InitialConcentration = [Starch AS_conc 0 0];    %

InitialNumberDensity(NumberClasses,NumberCSTRs) = 0;

InitialMass(NumberComponents,NumberCSTRs) = 0;                    % g
for j = 1:NumberCSTRs
```

```
    for jj = 1: NumberComponents
InitialMass(jj,j) =
(1/(ratio+1))*CSTRVolume(j)*Mw(jj)*1000*InitialConcentration(jj);
    end
end

InitialMoment = zeros(4,NumberCSTRs);


%%                              INITIALISE SIMULATION
%{
_____________________________________________________________________________
Time Interval
%}

time = sum(tres(1,:))*3;       % seconds

EndTime = time;

ispan = [0 EndTime];

ispan = [ispan];

ispan = sort(ispan);

ispan = unique(ispan);

%{
INITIALISE the Dependent Variables
%}
InitialNumberDensity = reshape(InitialNumberDensity, 1, []);
InitialMass = reshape(InitialMass, 1, []);
InitialMoment = reshape(InitialMoment,1,[]);


y0= [InitialNumberDensity InitialMass InitialMoment];

% SET INTEGRATOR OPTIONS

options = odeset('NonNegative', 1:length(y0));
%options = odeset('MaxStep', 1e-8);


%%                            INTEGRATION MANAGER
%{
RUN THE SIMULATION
%}

for j = 1:length(ispan) - 1


    [tSection, ySection] = ode45 (@PopBalance, ...
                                  [ispan(j): 0.0001 :ispan(j+1)], ...
                                  y0, ...
                                  options);
    if  j == 1
        t = tSection;
        y = ySection;
    else
        t = [t; tSection(2:end)];
```

```
        y = [y; ySection(2:end,:)];
    end
     y0 = ySection(end,:);

end

%%                                Output Results

% Define Number Output from derivative function output
Number = y(:,1:NumberCSTRs*NumberClasses);

% Calculate Number Fraction
ND=zeros(length(t),NumberCSTRs);
for j = 1 : NumberCSTRs
for l  = 1 : length(t)
for i = 1 : NumberClasses
ND(l,j) = ND(l,j) + Number(l, (i+NumberClasses*(j-1)));
end
end
end
NumberDensity=zeros(length(t),(NumberClasses*NumberCSTRs));
for l = 1 : length(t)
for j = 1 : NumberCSTRs
for i = 1 : NumberClasses
a = i + (j-1)*NumberClasses;
NumberDensity(l,a) = (Number(l,a) / ND(l,j))*100;
end
end
end

hold on

% Graphical outputs of PSD exiting the reactor

 figure(1)


plot(ParticleSizeRange(1:NumberClasses),NumberDensity(end,(NumberClasses*Nu
mberCSTRs - NumberClasses + 1)...
    :(NumberClasses*NumberCSTRs)),'r+')


h = findobj(gca,'Type','line');
x=get(h,'Xdata');
y=get(h,'Ydata');

figure(2)
semilogx(ParticleSizeRange(1:NumberClasses),Number(end,(NumberClasses*Numbe
rCSTRs - NumberClasses + 1)...
   :(NumberClasses*NumberCSTRs)),'LineStyle','none','Marker','+')
h = findobj(gca,'Type','line');
x1=get(h,'Xdata');
y2=get(h,'Ydata');

%}
```

J.2. Population Balance script

```
%{

PopBalance.m

This function calculates the derivatives of the dependent variables

The number derivatives are based of work by Hounslow and Lister and
Galbraith and Schnider

Micromixing model based upon segregated volume mixing
%}

function [dy_dt] = PopBalance( t , y )

%{
INPUTS

t                   Time (s)
y                   Vector of initial number, mass and moment values
_____________________________________________________________________________
OUTPUT

dy_dt               Derivative output for number density, mass and moment


_____________________________________________________________________________
global variables

%}
global NumberCSTRs Concentration
global NumberClasses
global ParticleSizeRange
global CrystalDensity
global NumberComponents
global Density
global flowrate
global CSTRVolume
global r q
global ratio
global Mw
global kg b g
global Bn
global B
global G
global Solubility
global tmicro
global EnergyDiss
global viscosity
global S InitialConcentration
global Kern

%{
local variables
%}
B = zeros(NumberClasses,NumberCSTRs);
G = zeros(NumberClasses,NumberCSTRs);
dMoment_dt = zeros(4,NumberCSTRs);
dMoment_NCG_dt = zeros(4,NumberCSTRs);
dNumber_dt_NCG3term = zeros(NumberClasses,NumberCSTRs);
dNumber_dt_NCG2term = zeros(NumberClasses,NumberCSTRs);
dNumber_dt_NCG = zeros(NumberClasses,NumberCSTRs);
```

```
dNumber_dtAGG = zeros(NumberClasses,NumberCSTRs);
alpha = zeros(NumberClasses,NumberCSTRs);
dNumber_dt = zeros(NumberClasses,NumberCSTRs);
NumberFlowIn = zeros(NumberClasses,NumberCSTRs);
NumberFlowOut = zeros(NumberClasses,NumberCSTRs);
VolumetricRate=zeros(1,NumberCSTRs);
ResidenceTime=zeros(1,NumberCSTRs);
Concentration=zeros(1,NumberCSTRs);
VolumeChange =zeros(1,NumberCSTRs);
dMass_dt=zeros(NumberComponents,NumberCSTRs);
MassOutflowRate=zeros(NumberComponents,NumberCSTRs);
MassAdditionRate(1,1)= flowrate * (1/(ratio+1)) * Density(1);
%starch/NaOH
MassAdditionRate(2,1)= flowrate * (ratio/(ratio+1)) * Density(2); % ethanol
MassAdditionRate(3,1)= 0;
MassAdditionRate(4,1)= 0;
R1 = zeros ( NumberClasses , NumberCSTRs);
R2 = zeros ( NumberClasses , NumberCSTRs);
R3 = zeros ( NumberClasses , NumberCSTRs);
R4 = zeros ( NumberClasses , NumberCSTRs);
Volume = zeros (NumberComponents,NumberCSTRs);
VolumeFraction = zeros (NumberComponents,NumberCSTRs);
S = zeros(1,NumberCSTRs);
Term1 = zeros (NumberClasses,NumberCSTRs);
Term2 = zeros (NumberClasses,NumberCSTRs);
Term3 = zeros (NumberClasses,NumberCSTRs);
Term4 = zeros (NumberClasses,NumberCSTRs);
Term5 = zeros (NumberClasses,NumberCSTRs);
Term6 = zeros (NumberClasses,NumberCSTRs);
Term2Sum2 = zeros (NumberClasses,NumberCSTRs);
Term2Sum1 = zeros (NumberClasses,NumberCSTRs);
Term4Sum1 = zeros (NumberClasses,NumberCSTRs);
Term4Sum2 = zeros (NumberClasses,NumberCSTRs);
E = zeros(1,NumberCSTRs);
SegregatedVolume = zeros(1,NumberCSTRs);
dV_dt = zeros(NumberComponents,NumberCSTRs);
dVs_dt = zeros(1,NumberCSTRs);
dn_dt = zeros(NumberComponents,NumberCSTRs);


%{
_____________________________________________________________________
Copy dependent variables into local storage

y0=[ ];

May need to reshape to required format
%}
N = reshape(y(1:NumberCSTRs*NumberClasses),[],NumberCSTRs);
Mass = reshape(y((NumberCSTRs*NumberClasses) + 1: ...
               (NumberCSTRs*NumberClasses) +
(NumberCSTRs*NumberComponents)),...
               [],NumberCSTRs);

% Enter for loop to calculate derivates for each CSTR
for j = 1:NumberCSTRs

        %{
        Calculate residence time
        %}
        for jj = 1 : (NumberComponents)
            switch j
```

```
                case 1
                    VolumetricRate(j) = VolumetricRate(j) +
MassAdditionRate(jj,j) / Density(jj);
                otherwise
                    VolumetricRate(j) = VolumetricRate(j) +
(MassOutflowRate(jj,j-1)/1000) / Density(jj);
            end
        end



        %{
        Calculate Concentrations of components for rate equations
        %}
        for jj = 1 : NumberComponents
        Volume(jj,j) = (Mass(jj,j)/(Density(jj)*1000));
        end
        for jj = 1 : NumberComponents
            if j==1
            Concentration(jj,j) = InitialConcentration(jj);
            else
            Concentration(jj,j) = (Mass(jj,j)/Mw(jj)) / (1000*Volume(1,j));
            end
        end
        for jj = 1 : NumberComponents
            VolumeFraction(jj,j) = Volume(jj,j) / sum(Volume(:,j));
        end

        % Calculate Residence time through each modelled CSTR
        ResidenceTime(j) = CSTRVolume(j) / VolumetricRate(1);

        % Calculate Supersaturation for modelled CSTR section
           Solubility(j)= exp (-10.6905+((43.9396/Concentration(2))-
(42.848964/Concentration(2)^2)));
           S(j) = (Concentration(1,j))/(Solubility(j));

   % Enter for loop to calculate growth and nucleation rate for each size
classification
    for i = 1:NumberClasses

        %{
        ____________________________________________________________________
        Calculate Nucleation Rate
        Nucleation only occurs in the smallest size interval
        %}
        % {

        if i == 1 && S(j) >= 1

          B(i,j) = Bn *(S(j).^b);
        else
               B(i,j) = 0;

        end

        %}

        %{
        ____________________________________________________________________
        Calculate Growth Rate
        %}
```

```
        if S(j)>=1
        G(i,j)  = kg *(((Concentration(1,j)/Solubility(j))-1).^g) ;
        else
            G(i,j)=0;
        end
        if G(i,j)<0
            G(i,j)=0;
        else
        end

        %}
        %}

        %{
        ____________________________________________________________________
        Calculate Number Outflow from modelled CSTR section
        %}

        NumberFlowOut(i,j) = N(i,j) / ResidenceTime(j);
        switch j
            case 1
        NumberFlowIn(i,j) = 0;
            otherwise
                NumberFlowIn(i,j) = NumberFlowOut(i,j-1);
        end
    end
    %{
    ____________________________________________________________________
    Re-do number class for loop this time calculating the number
    derivatives
    %}
    for i = 1 : NumberClasses

        %{
        Calculate number derivatives
        %}
        switch i
            case 1

        dNumber_dt_NCG3term(i,j) = B(i,j) + ( 2
/((1+r)*ParticleSizeRange(1)))...
            * ((1-(r^2/(r^2-1)))*N(1,j)*G(1,j) - (r/(r^2-
1))*N(2,j)*G(2,j));

        dNumber_dt_NCG2term(i,j) = B(i,j) - ((G(i,j)*N(1,j))/((r-
1)*ParticleSizeRange(1)));

            case NumberClasses
        dNumber_dt_NCG3term(i,j) = ( 2 /((1+r)*ParticleSizeRange(i)))...
            * ((r/(r^2-1))*N(i-1,j)*G(i-1,j) + N(i,j)*G(i,j));

        dNumber_dt_NCG2term(i,j) = (1/((r-1)*ParticleSizeRange(i)))...
            * (r * N(i-1,j)*G(i-1,j) - N(i,j)*G(i,j));


            otherwise

        dNumber_dt_NCG3term(i,j) = ( 2 /((1+r)*ParticleSizeRange(i)))...
            * ((r/(r^2-1))*N(i-1,j)*G(i-1,j) + N(i,j)*G(i,j) - (r/(r^2-
1))*N(i+1,j)*G(i+1,j));
```

```
        dNumber_dt_NCG2term(i,j) = (1/((r-1)*ParticleSizeRange(i)))...
            * (r * N(i-1,j)*G(i-1,j) - N(i,j)*G(i,j));
        alpha(i,j) = 1 / (1 + exp(-i + (20)));

        dNumber_dt_NCG(i,j) = (1 - alpha(i,j)) *
dNumber_dt_NCG2term(i,j)...
                              + alpha(i,j) * dNumber_dt_NCG3term(i,j);

         %{
_____________________________________________________________________
Calculate Agglomeration number change
         %}
   % Hounslows Agglomeration Kernel
             %
        for z = 1 : (i - 2)
            if i == 1
                R1(i,j)=0;
            else
             R1(i,j) = R1(i,j) + 3 * 2^(z-i) * Kern(i,z) * N(i-1,j) *
N(z,j);
            end
        end
        if i == 1
                R2(i,j)=0;
        else
                R2(i,j) = 0.5 * Kern(i-1,i-1) * N(i-1,j)^2;
        end
        for z = 1 : (i - 1)
        R3(i,j) = R3(i,j) + 3 * 2^(z-i-1) * Kern(i,z) * N(z,j);
        end
        R3(i,j) = R3(i,j) * N(i,j);
        for z = i : NumberClasses
        R4(i,j) = R4(i,j) + Kern(i,z) * N(z,j);
        end
        R4(i,j) = N(i,j) * R4(i,j);

        dNumber_dtAGG(i,j) = (2/3) * (R1(i,j) - R3(i,j)) + R2(i,j) -
R4(i,j);
       %}


%{
        _____________________________________________________________
         Define total number derivates for each size classification
%}
dNumber_dt(i,j) = dNumber_dt_NCG(i,j) + dNumber_dtAGG(i,j) -
NumberFlowOut(i,j) + NumberFlowIn(i,j);

        % Calculate change in moments for mass calculation
        for k = 1:4
         dMoment_dt(k,j) = dMoment_dt(k,j) + ParticleSizeRange(i)^(k-1) *
dNumber_dt(i,j);
        end
        for k = 1:4
         dMoment_NCG_dt(k,j) = dMoment_NCG_dt(k,j) +
ParticleSizeRange(i)^(k-1) * dNumber_dt_NCG(i,j);
        end
    end

    %{
    Calculate the mass derivative considering change due to pop balance
    %}
```

```
    VolumeChange(j) = (dMoment_NCG_dt(4,j) * pi()/6) * 1*10^-27; % convert
from nm3 to m3 for mass calculation 1*10^-27

   dMass_dt(1,j) = dMass_dt(1,j) - (VolumeChange(j) * CrystalDensity *
sum(Volume(:,j))) * 1000;



    %{
    Adjust mass derivative for outflow and inflow.
    %}

    for jj = 1 : NumberComponents
        MassOutflowRate(jj,j) = Mass(jj,j) / ResidenceTime(j);
        switch j
            case 1
       dMass_dt(jj,j) = dMass_dt(jj,j) - MassOutflowRate(jj,j) +
MassAdditionRate(jj)*1000;
            otherwise
       dMass_dt(jj,j) = dMass_dt(jj,j) - MassOutflowRate(jj,j) +
MassOutflowRate(jj,j-1);
        end
    end

    %{
    Micromixing Model
    %}
    E(j) = 0.058 * (EnergyDiss(j)/viscosity)^0.5;

    % {
    SegregatedVolume(j) = Volume(1,j) + Volume(2,j);

    if  SegregatedVolume(j)~= 0

    dVs_dt(j) = - SegregatedVolume(j) / tmicro(j);  % Rate of change of
segregated volume

    dV_dt(1,j) = dVs_dt(j) ;
    dV_dt(2,j) = dVs_dt(j) ;
    dV_dt(3,j) = - dV_dt(1,j);
    dV_dt(4,j) = - dV_dt(2,j);

    else
    dV_dt(1,j) = 0;
    dV_dt(2,j) = 0;
    dV_dt(3,j) = 0;
    dV_dt(4,j) = 0;
    end
    %}

    % Convert to moles
    for jj = 1 : (NumberComponents)
        dn_dt(jj,j) = dV_dt(jj,j) * Density(jj) * 1000 / Mw(jj);
    end



    % Convert back to mass


    for jj = 1:(NumberComponents)
```

```
            dMass_dt(jj,j) = dMass_dt(jj,j) + dn_dt(jj,j)*Mw(jj);
        end

    end
    % Reshape output derivates to required format
    dNumber_dt = reshape(dNumber_dt,1,[]);
    dMass_dt = reshape(dMass_dt,1,[]);
    dMoment_dt = reshape(dMoment_dt,1,[]);

    dy_dt = [dNumber_dt dMass_dt dMoment_dt]';

    end
```

J.3. Stability ratio script

```
%{
Stability Ratio Estimate based upon DLVO theory accounting for van der
waals and electrostatic repulsion
%}

function f = StabilityRatioEstimate(xi,xj,H)
A = 3.5e-20; %JK-1
Na = 6.022e+26;
kb = 1.3806e-23;
T=273+25;
zeta=0.04;
epsilono=8.8541e-12;
epsilon=77.8;
e=1.602e-19;
I=0.00316228;
kappa=(2*e^2*Na*I/(epsilon*epsilono*kb*T))^0.5;
ri=xi./2;
rj=xj./2;
Yi=8*tanh(1/4)/(1+(1-
((2*kappa.*ri+1)./(kappa.*ri+1)^2).*tanh(1/4)^2).^0.5);
Yj=8*tanh(1/4)/(1+(1-
((2*kappa.*rj+1)./(kappa.*rj+1)^2).*tanh(1/4)^2).^0.5);
R=H+ri+rj;
S=2*R./(ri+rj);
VdW=-(A/6)*(2*ri.*rj./(R.^2-(ri+rj).^2)+2*ri.*rj./(R.^2-(ri-
rj).^2)+log((R.^2-(ri+rj).^2)./(R.^2-(ri-rj).^2)));
if kappa*max(ri,rj)<5
    VEDL=4*pi()*epsilon*epsilono*ri*rj*Yi*Yj*(kb*T/e)^2*(exp(-
H*kappa)/(H+ri+rj));
else
    VEDL=4*pi()*epsilon*epsilono*zeta^2*(ri.*rj./(ri+rj)).*log(1+exp(-
kappa.*H));
end
VT= VdW + VEDL;
f = exp(VT/(kb*T))./S.^2;
end
```

Appendix K – Presentations and publications

Presentations:

- Poster presentation: "Process intensification of solvent-antisolvent precipitation in a spinning disc reactor" – SCI meeting: Reactors, Scale-up and Separations, 2019, London.
- Oral presentation: "Production of starch nanoparticles through solvent-antisolvent precipitation in a spinning disc reactor" – 6th International Congress on Green Process Engineering (GPE) 2018, Toulouse.
- Oral presentation: "Solvent-antisolvent precipitation in a spinning disc reactor" - 26th Process Intensification Network (PIN) meeting 2018, Newcastle University.
- Poster presentation: "Exploiting the spinning disc technology for solvent-antisolvent precipitation of starch nanoparticles" – 10th World Congress of Chemical Engineering (WCCE) 2017, Barcelona.

Publications:

- Sana S, Boodhoo K, Zivkovic V. Production of starch nanoparticles through solvent-antisolvent precipitation in a spinning disc reactor. *Green Processing and Synthesis. 8(1), 507-515, 2019.*